

**APPLIED  
COMPUTATIONAL  
ELECTROMAGNETICS  
SOCIETY  
JOURNAL**

November 2014  
Vol. 29 No. 11  
ISSN 1054-4887

**The ACES Journal is abstracted in INSPEC, in Engineering Index, DTIC, Science Citation Index Expanded, the Research Alert, and to Current Contents/Engineering, Computing & Technology.**

The illustrations on the front cover have been obtained from the research groups at the Department of Electrical Engineering, The University of Mississippi.

# THE APPLIED COMPUTATIONAL ELECTROMAGNETICS SOCIETY

<http://www.aces-society.org>

## EDITOR-IN-CHIEF

**Atef Elsherbeni**

Colorado School of Mines, EECS Dept.  
Golden, CO 80401, USA

## ASSOCIATE EDITORS-IN-CHIEF

**Sami Barmada**

University of Pisa, EE Dept.  
Pisa, Italy, 56126

**Mohammed Hadi**

Kuwait University, EE Dept.  
Safat, Kuwait

**Paolo Mezzanotte**

University of Perugia  
I-06125 Perugia, Italy

**Yasushi Kanai**

Niigata Inst. of Technology  
Kashiwazaki, Japan

**Alistair Duffy**

De Montfort University  
Leicester, UK

**Antonio Musolino**

University of Pisa  
56126 Pisa, Italy

**Ozlem Kilic**

Catholic University of America  
Washington DC, 20064, USA

**Mohamed Bakr**

McMaster University, ECE Dept.  
Hamilton, ON, L8S 4K1, Canada

**Marco Arjona López**

La Laguna Institute of Technology  
Coahuila 27266, Mexico

**Fan Yang**

Tsinghua University, EE Dept.  
Beijing 100084, China

**Abdul Arkadan**

Rafik Hariri University  
Chouf 2010, Lebanon

## EDITORIAL ASSISTANTS

**Matthew J. Inman**

University of Mississippi, EE Dept.  
University, MS 38677, USA

**Shanell Lopez**

Colorado School of Mines, EECS Dept.  
Golden, CO 80401, USA

## EMERITUS EDITORS-IN-CHIEF

**Duncan C. Baker**

EE Dept. U. of Pretoria  
0002 Pretoria, South Africa

**Ahmed Kishk**

University of Mississippi, EE Dept.  
University, MS 38677, USA

**Allen Glisson**

University of Mississippi, EE Dept.  
University, MS 38677, USA

**Robert M. Bevensee**

Box 812  
Alamo, CA 94507-0516, USA

**David E. Stein**

USAF Scientific Advisory Board  
Washington, DC 20330, USA

## EMERITUS ASSOCIATE EDITORS-IN-CHIEF

**Mohamed Abouzahra**

MIT Lincoln Laboratory  
Lexington, MA, USA

**Erdem Topsakal**

Mississippi State University, EE Dept.  
Mississippi State, MS 39762, USA

**Levent Gurel**

Bilkent University  
Ankara, Turkey

**Alexander Yakovlev**

University of Mississippi, EE Dept.  
University, MS 38677, USA

## EMERITUS EDITORIAL ASSISTANTS

**Khaled ElMaghoub**

University of Mississippi, EE Dept.  
University, MS 38677, USA

**Christina Bonnington**

University of Mississippi, EE Dept.  
University, MS 38677, USA

**Anne Graham**

University of Mississippi, EE Dept.  
University, MS 38677, USA

**Mohamed Al Sharkawy**

Arab Academy for Science and Technology, ECE Dept.  
Alexandria, Egypt

## NOVEMBER 2014 REVIEWERS

**Ahmed Abdelrahman**

**Ercument Arvas**

**Hany Atallah**

**Rahul Bakore**

**Mohamed Bakr**

**Bastian Bandlow**

**Istvan Bardi**

**Pabitra Biswas**

**Ahmed Boutejdar**

**Claudio Curcio**

**Pasquale Dottorato**

**Apostolos Georgiadis**

**Andrey Grigoryev**

**Xiangyu Guan**

**Yan-Jie Guo**

**Osama Haraz**

**Ahsan Illahi**

**Ulrich Jakobus**

**Hu Jun**

**Arkom Kaewrawang**

**Darko Kajfez**

**Majid Karimipour**

**Ali Lalbakhsh**

**Angelo Liseno**

**Ali Lotfi**

**Jugal Lotiya**

**Olusegun Ogundapo**

**Yasser Ojaroudi**

**Andrew Peterson**

**C. J. Reddy**

**Mehdi Salehi**

**Ashish Singh**

**Sellakkutti Suganthi**

**Fernando Teixeira**

**Gang Zhang**

**Francesco Zirilli**

**Valiallah Zomorrodian**



**THE APPLIED COMPUTATIONAL ELECTROMAGNETICS SOCIETY**  
**JOURNAL**

Vol. 29 No. 11

November 2014

**TABLE OF CONTENTS**

“Metal Strip Grating on Grounded Dielectric Slab and PEC/PMC Shielded Interconnect: Modal Relationships” Kun Chen, Jiming Song, and Telesphor Kamgaing.....	828
“Numerical Investigation of Monitoring Antenna Influence on Shielding Effectiveness Characterization” T. Cvetković, V. Milutinović, N. Dončov, and B. Milovanović .....	837
“Development of a Broadband Substrate Integrated Waveguide Cavity Backed Slot Antenna Using Perturbation Technique” Elham Baghernia and Mohammad H. Neshati .....	847
“Using the Best Uniform Approximation with Compression for Efficient Computation of Monostatic Scattering” Zhiwei Liu, Shan He, Xiaoyan Zhang, Yingting Liu, and Yueyuan Zhang .....	856
“Fabrication of a Novel Diplexer Using Folded Open-Loop Ring Resonators and Microstrip Lines” Chia-Mao Chen, Shoou-Jinn Chang, and Cheng-Fu Yang.....	864
“High Gain Dielectric Loaded Exponentially Tapered Slot Antenna Based on Substrate Integrated Waveguide for V-Band Wireless Communications” S. Ramesh and T. Rama Rao .....	870
“Modified Broadband Half Mode Substrate Integrated Waveguide Cruciform Coupler” Zahra Mansouri, Mitsuyoshi Kishihara, Ferdows B. Zarrabi, and Fatemeh Geran.....	881
“An Improved Combination of IE-ODDM and MLFMA” Jun Hu .....	887
“Real-Time Implementation of UWB-OFDM SAR Imaging System Using Shared Memory Based FPGA” Md Anowar Hossain, Ibrahim Elshafiey, and Majeed A. S. Alkanhal.....	895
“Normal Directional NURBS Arithmetic of Conformal PML” Y. J. Zhang and X. H. Zhang .....	904

“Diamond Shaped Ring Antenna for UWB Applications with Inherent Band-Notched Functionality” Majid Shokri, Zhaleh Amiri, Somayeh Asiaban, and Bal Virdee .....	911
“Electromagnetic Force Calculation of Conductor Plate Double Halbach Permanent Magnet Electrodynamic Suspension” Yin Chen and Kunlun Zhang .....	916
“A Novel Fractal Monopole Antenna with Wide Bandwidth Enhancement for UWB Applications” Bahman Heydari, Zakarya Sanaati, Vorya Waladi, and Yashar Zehforoosh .....	923
“60-GHz 3-D Cavity Bandpass Filter for V-Band Gigabit Wireless Systems” Gang Zhang, Jianpeng Wang, Hui Gu, and Xin Xu .....	928

# Metal Strip Grating on Grounded Dielectric Slab and PEC/PMC Shielded Interconnect: Modal Relationships

Kun Chen <sup>1</sup>, Jiming Song <sup>1</sup>, and Telesphor Kamgaing <sup>2</sup>

<sup>1</sup>Department of Electrical and Computer Engineering  
Iowa State University, Ames, IA 50011, USA  
{kunc, jisong}@iastate.edu

<sup>2</sup>Intel Corporation, Chandler, AZ 85226, USA  
telesphor.kamgaing@intel.com

**Abstract** — This paper employs the spectral domain approach for full wave analysis of metal strip grating on grounded dielectric slab and microstrips shielded with either Perfect Electric Conductor (PEC) or Perfect Magnetic Conductor (PMC) walls. The modal relations between these structures are revealed by exploring their symmetries. It is derived analytically and validated numerically that all the even and odd modes of the latter two (when they are mirror symmetric) find their correspondence in the modes of metal strip grating on grounded dielectric slab when the phase shift between adjacent two unit cells is  $0$  or  $\pi$ . Extension to non-symmetric case is also made. Several factors, including frequency, grating period, slab thickness and strip width, are further investigated for their impacts on the effective permittivity of the dominant mode of PEC/PMC shielded microstrips. It is found that the PMC shielded microstrip generally has a larger wave number than the PEC shielded microstrip.

**Index Terms** — Grounded dielectric slab, metal strip grating, perfect electric conductor, perfect magnetic conductor, periodic boundary condition, shielded microstrip.

## I. INTRODUCTION

In modern integrated circuits, interconnects play such an important role that accurate and efficient modeling of them is a must. For example, COMS circuits see the responsibility of interconnects for more than half of the on-chip

capacitance and dynamic power dissipation, significant delay to critical paths, and noise and jitter to signals [1]. However, there are many challenges in successful modeling of interconnects: firstly, the state-of-the-art 3D circuits usually come as multilayered structures, the modeling of which is quite involved [2]; secondly, high density of integration leads to millions of interconnects within a very limited space; thirdly, high frequency means we can no longer take neglect of conduction loss and metal thicknesses as granted.

Faced with such a complexity, it is natural and beneficial for us to abstract some key features of the interconnects and give priorities to some typical structures, as this simplifies the problem and allows for the employment of reliable simulation techniques. The study of multilayered structure can be considered the generalization of the single layered structure. Also, many layouts of interconnects are well approximated with periodic structures. In this work, we consider the single layered microstrip with PEC/PMC walls as well as Metal Strip Grating on Grounded Dielectric Slab (MSG-GDS).

Microstrip transmission lines, as we know, are key building blocks for interconnects. Microstrips shielded with Perfect Electric Conductors (PECs) draw attention in that they can model the effect of packaging such as providing isolation between different elements as well as mechanic support for the integrated circuit [3]. As a dual of the PEC shielded case, the Perfect Magnetic Conductor

(PMC) shielded microstrip is also worth investigation. Metal Strip Grating on Grounded Dielectric Slab (MSG-GDS), which is a grounded dielectric slab loaded with one-dimensional periodic metal strips, is another classic structure which has seen various applications in electronic engineering. For instance, the behaviors of the waves travelling in the direction perpendicular to the strips are utilized to design leaky wave antennas [4]. Strip-element phased arrays [5] and polarizers with low cross-polarization [6] also account for some important applications of MSG-GDS. In fact, we can treat the three structures mentioned above as only one: a microstrip, but with different boundary conditions. It is not unfamiliar to us that the PEC and PMC boundary conditions are used to truncate the simulation domain or analyze periodic structures in high frequency electromagnetic field solvers. But what exactly is the relationships between the PEC, the PMC and the periodic boundary conditions? Though for each of these structures, there exists an abundance of literatures, it is hardly seen in the literature an explicit elaboration of this relation. As far as we are concerned, only the literature [7] bears a short discussion about the relationships between the modes of the PEC/PMC shielded microstrips and the MSG-GDS, but it is restricted to the case in the absence of phase shift between adjacent periods.

Based on our previous work [8], we aim in this paper to reveal more comprehensively the modal relationships between MSG-GDS and the PEC/PMC shielded microstrips. To this end, we perform a full wave analysis for these structures using the spectral domain approach [9]. Two variations of these structures will be considered: one with a top PEC shield, and the other without, as illustrated in Fig. 1 (a) and (b). We first consider the structures when they are symmetric, then extensions to non-symmetric ones are carried out. Furthermore, we also look at the impacts of frequency, grating period and slab thickness on the wave number of the dominant mode of PEC/PMC shielded microstrips. Numerical results are presented to validate our conclusions.

## II. SPECTRAL DOMAIN APPROACH

The MSG-GDS is drawn in Fig. 1 (a). The

structure obtained by adding a top PEC shield, illustrated in Fig. 1 (b), will be considered together. A coordinate system is created in Fig. 1 (c), added with some assisting dash lines locating symmetry planes. As shown in the figure, a dielectric slab of thickness  $h$  is grounded by an infinite PEC plane, and topped by a grating (with period  $P$ ) of perfect conducting strips of widths  $w$ . We assume that the thickness of the metal strips is zero. The permittivity and permeability for the slab are  $\epsilon_1$  and  $\mu_1$ , and for the region above the slab are  $\epsilon_2$  and  $\mu_2$ . If there is a top shield, the distance to the top slab surface is  $d$ . The shielded microstrips can be obtained by placing PEC (or PMC) walls at  $x = \pm P/2$ , so we save their illustrations for book-keeping. For the MSG-GDS, the waves can be guided in arbitrary horizontal directions, but we focus on the case when the wave propagates along the strips.

The spectral domain approach [9] is a very accurate and efficient method to solve the eigenproblem for microstrip structures, hence, it will be adopted in this work. Given the periodicity of the structure, the Floquet theorem enables us to confine our scope to the first unit cell (between  $x = \pm P/2$ ). The tangent electric fields at the top surface of the slab can be determined by the current on the metal strip and expressed in the form of a Fourier series as:

$$\sum_{n=-\infty}^{\infty} \sum_s \tilde{G}_{rs}(k_{xn}, k_y; h) \tilde{J}_s(k_{xn}) e^{-jk_{xn}x} = E_r(x, h), \quad (1)$$

where  $k_{xn}$  and  $k_y$  are the wave numbers in  $x$  and  $y$  directions, with the Bloch wave number  $k_{xn} = (\phi_0 + 2n\pi)/P$  ( $n \in Z$ ), where  $\phi_0$  is the phase shift between adjacent periods,  $r, s \in \{x, y\}$ ,  $\tilde{J}_s$  is the Fourier transform of the current in the unit cell,  $\tilde{G}_{rs}$  is the spectral dyadic Green's function available in simple analytic form [9]:

$$\begin{aligned} \tilde{G}_{xx}(k_{xn}, k_y) &= j\eta_2(k_2\Delta)^{-1} [\mu_r \gamma_1 (k_{xn}^2 - k_2^2) \tanh(\gamma_1 h) \\ &\quad + \gamma_2 (k_{xn}^2 - k_1^2) \Theta] \\ \tilde{G}_{xy}(k_{xn}, k_y) &= \tilde{G}_{yx}(k_{xn}, k_y) = j\eta_2 k_{xn} k_y (k_2\Delta)^{-1} \\ &\quad \times [\mu_r \gamma_1 \tanh(\gamma_1 h) + \gamma_2 \Theta] \\ \tilde{G}_{yy}(k_{xn}, k_y) &= j\eta_2(k_2\Delta)^{-1} [\gamma_1 \mu_r (k_y^2 - k_2^2) \tanh(\gamma_1 h) \\ &\quad + \gamma_2 (k_y^2 - k_1^2) \Theta], \end{aligned} \quad (2)$$

with

$$\Delta = [\gamma_1 \coth(\gamma_1 h) + \mu_r \gamma_2 \Theta^{-1}] [\gamma_1 \tanh(\gamma_1 h) + \varepsilon_r \gamma_2 \Theta], \quad (3)$$

where we have  $\varepsilon_r = \varepsilon_1 / \varepsilon_2$ ,  $\mu_r = \mu_1 / \mu_2$ ,  $\eta_i = \sqrt{\mu_i / \varepsilon_i}$ ,  $k_i = \omega \sqrt{\mu_i \varepsilon_i}$  and  $\gamma_i = \sqrt{k_{x_i}^2 + k_y^2 - k_i^2}$ ,  $\Theta = 1$  for Fig. 1 (a) and  $\Theta = \tanh(\gamma_2 d)$  for Fig. 1 (b). When  $\gamma_2 d > 9$ , which is approximately guaranteed when  $d > 3P/2$ , the two Green's functions has little difference if single precision is used. Since the Green's functions for the two cases are so close, they can be handled together. Then we apply Galerkin's method to solve (1), which leads us eventually to the following homogeneous linear system:

$$\begin{bmatrix} K^{xx} & K^{xy} \\ K^{yx} & K^{yy} \end{bmatrix} \begin{bmatrix} A \\ B \end{bmatrix} = \mathbf{0}, \quad (4)$$

where  $K^{rs}$  ( $r, s \in \{x, y\}$ ) is a matrix with elements given by:

$$K_{pq}^{rs} = \sum_{n=-\infty}^{\infty} \tilde{J}_{rp}(-k_{x_n}) \tilde{J}_{sq}(k_{x_n}) \tilde{G}_{rs}(k_{x_n}, k_y), \quad (5)$$

where  $p = 1, \dots, N_x$ ,  $q = 1, \dots, N_y$  ( $N_x$  and  $N_y$  are the number of basis functions for  $J_x$  and  $J_y$ ),  $\tilde{J}$  is the Fourier transform of the current basis function, for which we have chosen the Chebyshev polynomials of the first and second kind for  $J_y$  and  $J_x$  respectively [10].  $A = [A_1, \dots, A_{N_x}]^T$ ,  $B = [B_1, \dots, B_{N_y}]^T$  are the unknown expansion coefficients for  $J_x$  and  $J_y$ . To solve the eigenvalue problem, we require vanishing of the determinant of the matrix in (4). In general, we need to find both  $\phi_0$  and  $k_y$ , but in this paper we would fix  $\phi_0$ , and just find  $k_y$  using a root-finding procedure. The series in (5) can be slowly convergent, so the leading asymptotic terms are extracted and summed with some fast convergent series, while the remaining part is summed directly, which, after this process, exhibits good convergence [10]. Notice that, when  $k_y = 0$ , we have  $K^{xy} = K^{yx} = 0$ , so the modes decouple into TE and TM waves, and  $k_{x_0}$  is the eigenvalue to be found.

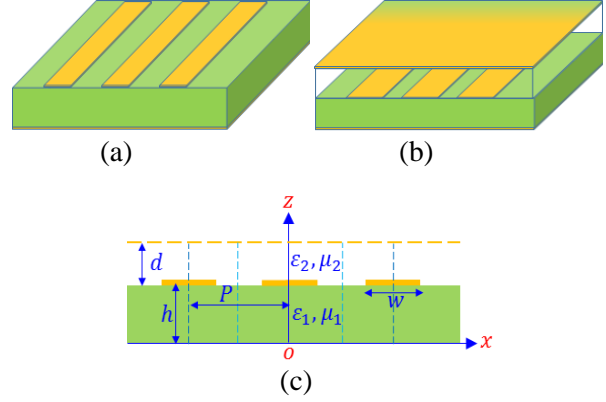


Fig. 1. Metal strip grating on grounded dielectric slab: (a) 3D view without top shield, (b) 3D view with top shield, and (c) edge view.

### III. RELATIONS WITH PEC/PMC SHIELDED MICROSTRIPS

#### A. Symmetric case

Figure 2 shows the symmetric and non-symmetric shielded microstrips. On the two sides, the shields can be PEC walls, or PMC walls. The top shield may be absent when we consider their relationships with the MSG-GDS in Fig. 1 (a). Let's first consider the symmetric case. In the periodic structure, we place phase shift walls (PSWs) at the boundary of the first unit cell and obtain a shielded structure as well. The electric and magnetic fields for this structure can be expressed in Fourier series as:

$$\mathbf{F}(x, z) = \sum_{n=-\infty}^{\infty} \tilde{\mathbf{F}}(k_{x_n}, z) e^{-jk_{x_n} x}, \quad (6)$$

where  $\mathbf{F} \in \{\mathbf{E}, \mathbf{H}\}$  and  $\exp(-jk_y y)$  variation has been suppressed. In fact, the expressions for the fields in Fig. 2 are in the same form as (6), but the values of  $k_{x_n}$  are different. Considering the mirror symmetry of the structure with respect to the  $yoz$  plane, one can classify the modes into two categories: even and odd [11]. To better under the parity of the modal fields, we first express the components of the spectral currents using the magnetic and electric vector potentials  $\Phi_i^{(e)}$  and  $\Phi_i^{(h)}$  as follows [12]:

$$\begin{aligned}\tilde{J}_x(k_{xn}) &= jk_y^{-1} \begin{bmatrix} (k_2^2 - k_y^2)\Phi_2^{(h)}(k_{xn}, h) \\ -(k_1^2 - k_y^2)\Phi_1^{(h)}(k_{xn}, h) \end{bmatrix} \\ \tilde{J}_y(k_{xn}) &= -jk_{xn}[\Phi_2^{(h)}(k_{xn}, h) - \Phi_1^{(h)}(k_{xn}, h)] \\ &\quad - \frac{\omega}{k_y} \frac{\partial}{\partial z} [\varepsilon_2 \Phi_2^{(e)}(k_{xn}, z) - \varepsilon_1 \Phi_1^{(e)}(k_{xn}, z)]_{z=h}, \quad (7)\end{aligned}$$

where  $\omega$  is the angular frequency and  $i$  indicates the  $i^{\text{th}}$  region. The above equations inform us that for a given mode, either even or odd, the currents in  $x$  and  $y$  directions have different parities in terms of  $k_x$ . Given the parity of a mode, parity of the current is specified, and then we can determine the parities of the potentials at the upper surface of the dielectric slab, which should be identical for all constant  $z$  planes. This would in turn allow us to identify the parities of all the components of the electric and magnetic fields. If we separately consider the two types of modes, and check the expressions for the electric and magnetic fields, we find that  $\tilde{E}_y$  and  $\tilde{E}_z$  have the same parity in terms of  $k_x$ , which differs from that of  $\tilde{E}_x$ ;  $\tilde{H}_y$  and  $\tilde{H}_z$  have the same parity, but different from that of  $\tilde{H}_x$ . The parity of the fields in spectral domain, according to the properties of Fourier transform, is the same as that in spatial domain. With these in mind, we are ready to distinguish two types of modes, and define the modes as even modes if  $J_y, E_y, E_z, H_x$  are even and  $J_x, E_x, H_y, H_z$  are odd; the modes are odd modes if the converse is true. Now let's make use of (6), and examine the tangential fields at the PSWs ( $x = \pm P/2$ ). For  $\phi_0 = 0$ , indicating the absence of phase shift between adjacent periods, we yield:

$$F_{y/z}(\pm P/2, z) = \tilde{F}_{y/z}(0, z) + \sum_{n=1}^{\infty} (-1)^n \begin{bmatrix} \tilde{F}_{y/z}(2n\pi/P, z) \\ + \tilde{F}_{y/z}(-2n\pi/P, z) \end{bmatrix}, \quad (8)$$

where  $F \in \{E, H\}$ . Obviously it vanishes if  $F_{y/z}$  is an odd function of  $x$ . While for  $\phi_0 = \pi$ , we acquire:

$$F_{y/z}(\pm P/2, z) = \mp j \sum_{n=0}^{\infty} (-1)^n \begin{Bmatrix} \tilde{F}_{y/z}[(2n+1)\pi/P, z] \\ - \tilde{F}_{y/z}[-(2n+1)\pi/P, z] \end{Bmatrix}, \quad (9)$$

which again vanishes if  $F_{y/z}$  is even. The implication of the vanishing of tangential fields is that we can place PEC or PMC walls at the boundary and the modal profiles would remain unperturbed. Now if we take into account the

parities of the modal fields as have been defined above, we conclude that the Periodic Boundary Condition (PBC) reduces to PEC boundary condition for the odd modes if  $\phi_0 = 0$ , for even modes if  $\phi_0 = \pi$ ; it reduces to PMC boundary condition for odd modes if  $\phi_0 = \pi$ , for even modes if  $\phi_0 = 0$ . Think the other way around: Are all the modes of the PEC or PMC shielded microstrips included in the modes of the MSG-GDS with phase shift  $\phi_0 = 0, \pi$ ? The answer is yes, because we can extend the domain of the PEC or PMC shielded structures to periodic ones by introducing infinite number of images according to the image theory. Then we are assured that the PEC and PMC boundary conditions are indeed special cases of the PBC for the symmetric structure under consideration. It should be noted that the above conclusions are not limited to the case when the strip thickness is 0, but also apply when the strips are of finite thickness, since our derivation only assumes mirror symmetry of the structure in this section and is independent of the zero-thickness assumption.

Since the structure is also mirror symmetric with respect to the plane  $x = P/2$ , we can also place PSWs at  $x = 0$  and  $x = P$ . Thus, a corresponding PEC or PMC shielded microstrip is obtained if PEC or PMC walls are placed. In this circumstance, the parity of a mode is defined in the same way as in the case for symmetry about  $x = 0$ , but referred with respect to the central plane of the shielded microstrip at  $x = P/2$ . The modal relations between the three structures can be analyzed similarly. We tabulate the relations for both cases in Table 1. For the modes in the same row, they have the same propagation constant along the longitudinal direction. We can see that when  $\phi_0 = 0$ , the same walls are placed and the parities are the same for both symmetric cases, while when  $\phi_0 = \pi$ , different walls are placed and the parities are opposite.

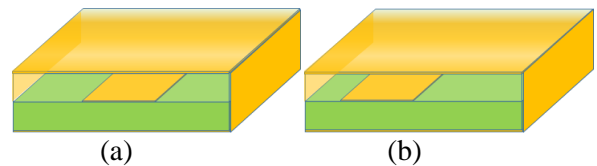


Fig. 2. Shielded microstrips: (a) symmetric, and (b) non-symmetric.

Table 1: Summary of modal relations

	$x = 0$ symmetry		$x = P/2$ symmetry	
	PEC	Odd	PEC	Odd
$\phi_0 = 0$	PMC	Even	PMC	Even
$\phi_0 = \pi$	PEC	Even	PMC	Odd
	PMC	Odd	PEC	Even

### B. Non-symmetric case

For non-symmetric case, the modes of the PEC/PMC shielded microstrips can no longer be divided into even and odd modes. But we can perform periodic extension in this case. As shown in Fig. 3 (a), where the arrows are used to illustrate the direction of current, we perform odd extension for the modes of PEC shielded microstrip, and all the modes of the original non-symmetric structure now correspond to the odd modes of the extended symmetric PEC shielded structure whose width has doubled. For the PMC shielded microstrip, we conduct even extension, and all the modes of the original structure has correspondence to the even modes of the extended structure. Now we make up a MSG-GDS with the extended structure in Fig. 3 (taking away the PEC or PMC walls) as the unit cell. Based on our previous discussions, we know the odd modes of the extended PEC shielded microstrip correspond to the modes with  $\phi_0 = 0$  in the MSG-GDS (with extended unit cell), which means all the modes of the original non-symmetric PEC shielded microstrip correspond to the modes of MSG-GDS with  $\phi_0 = 0$ . Similarly, we have the correspondence between the modes of the non-symmetric PMC shielded microstrip and those of the MSG-GDS.

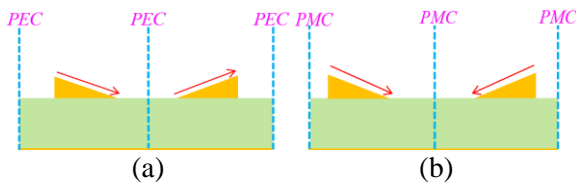


Fig. 3. Periodic extension for non-symmetric shielded microstrip: (a) PEC shielded, and (b) PMC shielded.

## IV. NUMERICAL EXAMPLES

The first numerical experiment is about the PEC shielded microstrip as illustrated by Fig. 2 (a). Following the reference [13], we set the parameters as follows:  $\varepsilon_{r1} = 8.875$ ,  $\mu_{r1} = 1$ ,

$\varepsilon_{r2} = \mu_{r2} = 1$ ,  $f = 20$  GHz,  $h = 1.27$  mm,  $w = h$ ,  $d = 11.43$  mm and  $P = 10h$ . The first 5 modes are calculated and tabulated in Table 2, where the normalized wavenumbers are  $k_y/k_2$ . We can see that agreement of 8-10 digits is achieved, and we only use 4 terms in the expansion of the currents in  $x$  and  $y$  directions. It is to be noted that our results are obtained not by solving the eigenproblem of the shielded microstrip directly, but by solving that for the MSG-GDS. We pick up the modes of the shielded microstrip from the set of modes of MSG-GDS by letting  $\phi_0 = 0$  or  $\pi$  and using basis functions with proper parities according to our previous conclusions. The good agreement achieved confirms our claims about the relationships between the MSG-GDS and shielded microstrip.

Table 2: Normalized wavenumbers in  $y$  direction

Mode	Reference [13]	Calculated
1 (even)	2.7102057109	2.7102057101
2 (odd)	1.2894527450	1.2894527434
3 (even)	1.1026365889	1.1026365888
4 (odd)	0.9223133480	0.9223133479
5 (even)	0.7250996002	0.7250996009

In practice, the shield for the microstrips may be used to model the packaging effect. Then one question arises: Which one captures the physics better, the PEC shielded microstrip, or the PMC shielded? So it is beneficial for us to compare the behavior of the two structures. Again, we do this by finding their eigen modes from a calculation of the MSG-GDS. Figure 4 shows the dispersion curves for the dominant modes of the PEC and PMC shielded microstrips in the range from 1 GHz to 25 GHz, where the effective permittivity is defined as the square of the normalized wave number. The parameters are:  $\varepsilon_{r1} = 9.7$ ,  $\mu_{r1} = 1$ ,  $\varepsilon_{r2} = \mu_{r2} = 1$ ,  $w = 1.219$  mm,  $h = 1.27$  mm and  $P/w = 5$ . Here we assume there is no top shield. As indicated by the legend, both modes are even modes. It can be seen first that both effective permittivities increase with the frequency. Also, notice that the PMC shielded microstrip has a larger effective permittivity than the PEC shielded microstrip, and the difference between the two permittivities decreases with frequency and

eventually almost vanishes at high frequency. The reason for this is that the electromagnetic fields aggregate more in the vicinity of the metal strip, whose width is just 1/5 of the period. Therefore, we are grounded to treat the shields on both sides as far from the region where most energy rests, and it makes little difference whether we put a PEC or PMC wall.

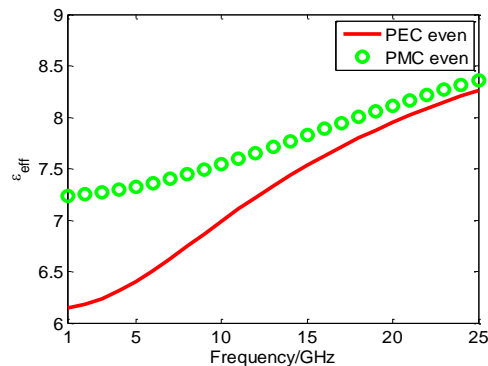


Fig. 4. Effective permittivity for the PEC/PMC shielded microstrip vs. frequency. Parameters:  $\epsilon_{r1}=9.7$ ,  $\mu_{r1}=1$ ,  $\epsilon_{r2}=\mu_{r2}=1$ ,  $w=1.219$  mm,  $h=1.27$  mm and  $P/w=5$ .

In Fig. 5, the geometric parameters  $P$ ,  $h$ ,  $w$  are explored. Parameters common to Fig. 5 (a-c) are:  $\epsilon_{r1}=9.7$ ,  $\mu_{r1}=1$ ,  $\epsilon_{r2}=\mu_{r2}=1$ ,  $w=1.219$  mm. In Fig. 5 (a),  $w$  is very close to  $h$ , and the effective permittivities are plotted against the ratio  $P/w$  at 10 GHz. It is observed that the PMC shielded microstrip still has a larger effective dielectric constant than the PEC shielded microstrip, and the two permittivities approach each other when frequency is increased. At  $P=1.5w$ , the electric field distributions in the two structures are drawn in Fig. 6. The fields are calculated by convoluting the dyadic Green's function with the eigen-current, which can be found by solving (4) with the normalization that the  $l_2$ -norm of the expansion coefficients equals unity. The arrows in the graphs represent a snapshot of the vector fields, and color plot conveys the amplitude of the fields. It is very clear that the PEC shielded microstrip has the fields mostly confined around the two edges of the metal strip, and decays very quickly into the dielectric region and air region. Nevertheless, the PMC shielded microstrip drives most of the electric fields into the high dielectric region, and the

distribution is also rather uniform. This implies that the PMC shielded microstrip in this configuration has a larger capacitance for storing electric energy, which is equivalently interpreted as a larger effective permittivity. But when  $P/w$  goes high, the PEC/PMC walls on both sides play a lesser role, which leads to very close effective permittivities.

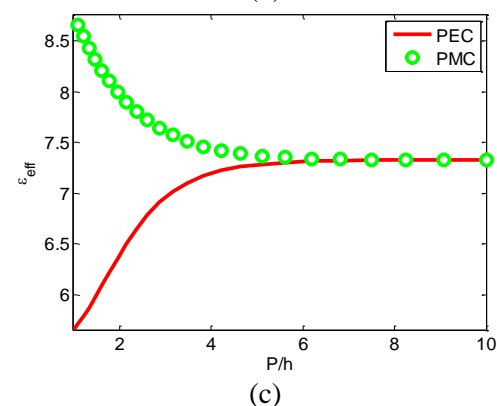
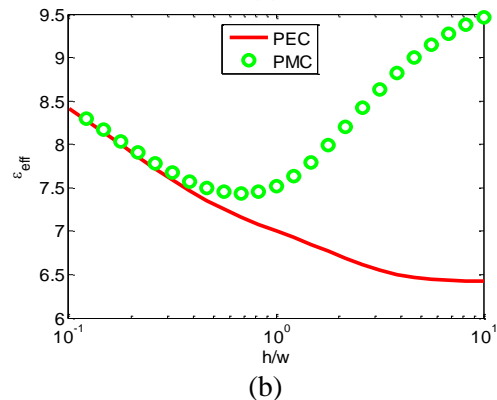
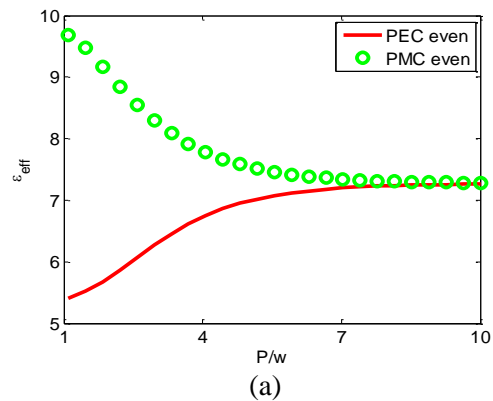


Fig. 5. Effective permittivity for the PEC/PMC shielded microstrip vs. geometry, with parameters:  $\epsilon_{r1}=9.7$ ,  $\mu_{r1}=1$ ,  $\epsilon_{r2}=\mu_{r2}=1$ ,  $w=1.219$  mm. (a)  $h=1.27$  mm and  $f=10$  GHz, (b)  $f=10$  GHz and  $P/w=5$ , and (c)  $h=5w$ , and  $f=5$  GHz.

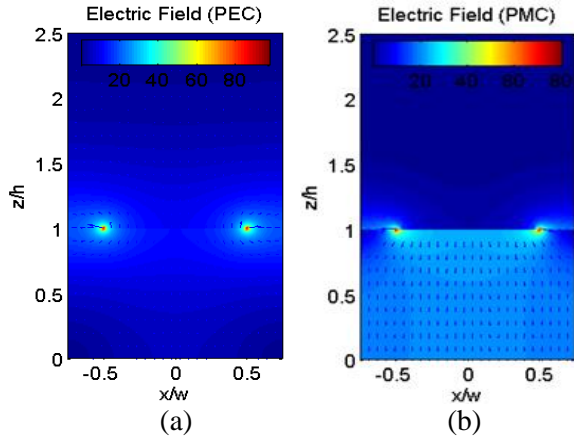


Fig. 6. Electric field (in V/m) distributions for PEC/PMC shielded microstrips. Parameters follow the two points at  $P = 1.5w$  in Fig. 5 (a).

The influence of the slab thickness is more complicated, as illustrated in Fig. 5 (b). For the PEC shielded microstrip, the effective permittivity keeps going down when the slab becomes thicker, while that for the PMC shielded microstrip descends to a valley before its rise. When  $h$  is very small, the two have almost the same effective permittivity. In this situation, we can think of a very thin parallel capacitor formed between the metal strip and the metal ground, and this capacitor has a large capacitance to store the energy in the small region near the metal strip. As a result, the fields can hardly reach the boundary on the two sides, shedding light on why the two permittivities are very close. For this point, we are confirmed by the field distribution in Fig. 7, where the field distributions for the two structures at  $h = w$  are close to each other, and most of the fields are in the slab region. Besides, the fields decay to a very weak level at the PEC/PMC walls. When  $h$  is very large, the PMC shielded microstrip has a much larger effective permittivity than the PEC shielded microstrip. To make sense of this, we look at the (magnetic) field distributions at  $h = 10w$  in Fig. 8. We can see that for the PEC shielded microstrip, the fields decay away from the metal strip, but for the PMC shielded, things are different; there are peaks and valleys in the high dielectric region. The PMC shields influence the field distribution such that

the mode is very close to a TEM wave in the slab region, and much more energy is stored in the slab. That is why it exhibits a larger dielectric constant.

In Fig. 5 (c), the dispersion curves of the PEC and PMC shielded microstrip are plotted against  $P/h$ , where  $h = 5w$  and  $f = 5$  GHz. Similar phenomena are observed as in Fig. 5 (a). From the above discussions, we are led to claim that the PMC shielded microstrip in general has a larger effective dielectric constant than the PEC shielded microstrip, given that the frequency is not too high, the slab not too thin, and the width  $P$  is not significantly larger than the slab thickness  $h$  and strip width  $w$ .

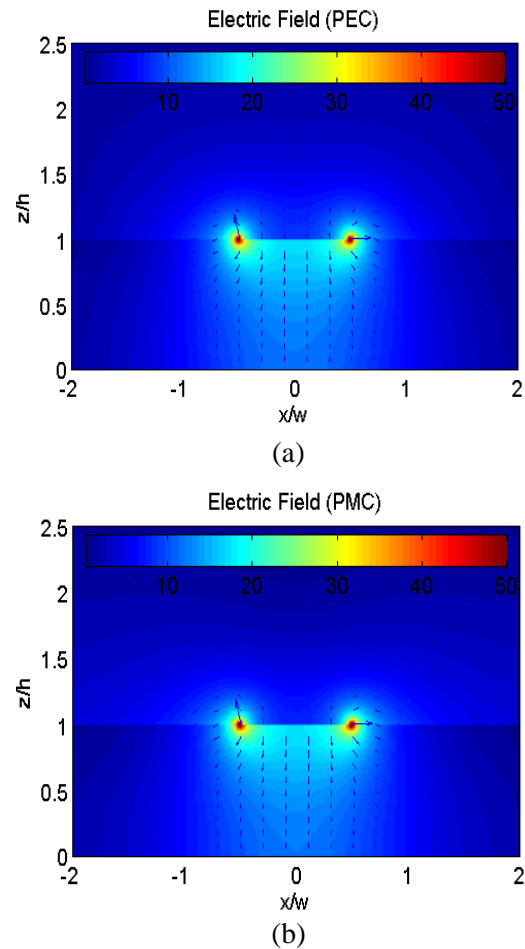


Fig. 7. Electric field (in V/m) distributions for PEC/PMC shielded microstrips. Parameters follow the two points at  $h = w$  in Fig. 5 (b).

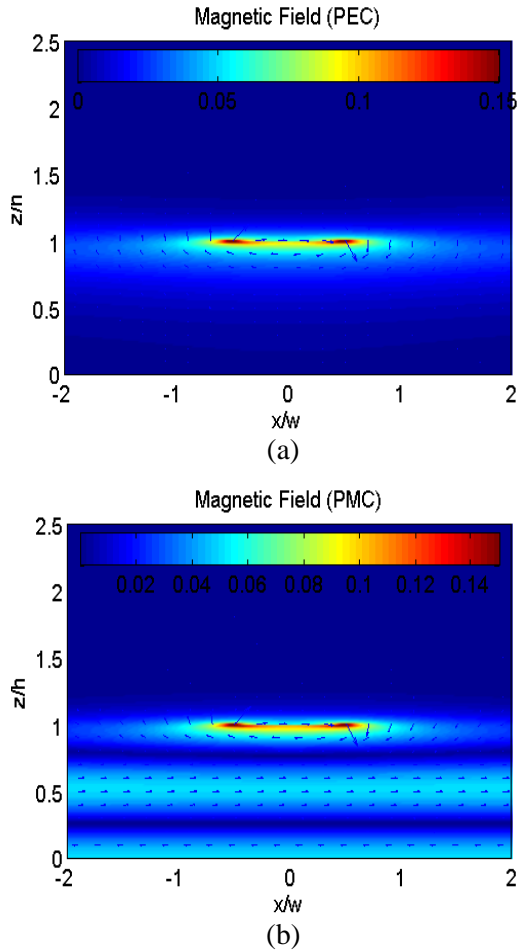


Fig. 8. Magnetic field (in A/m) distributions for PEC/PMC shielded microstrips. Parameters follow the two points at  $h=10w$  in Fig. 5 (b).

## V. CONCLUSION

To summarize, this paper has investigated the modal relationships between Metal Strip Grating on Grounded Dielectric Slab (MSG-GDS) and PEC/PMC shielded microstrip by virtue of full wave spectral domain approach. By exploring symmetry of these structures and examining the tangential fields at the boundary, we have found that the PEC and PMC boundary conditions are special cases for the periodic boundary conditions. To be specific, it has been revealed and verified that all the even and odd modes of the mirror symmetric PEC/PMC shielded microstrip find their correspondence in the modes of metal strip grating on grounded dielectric slab when the phase shift between adjacent two unit cells is  $0$  or  $\pi$ . By performing a periodic extension for the non-symmetric shielded structures and making up a

new MSG-GDS, all the modes for the original non-symmetric shielded structures also correspond to those of the MSG-GDS with  $0$  or  $\pi$  phase shift between adjacent unit cells. Through a calculation for the MSG-GDS and the use of the relations between the PEC/PMC shielded microstrips and MSG-GDS, we conduct a comparison of the PEC and PMC shielded microstrips. The effect of frequency and geometric parameters on the dominant modes for the PEC and PMC shielded microstrips have been studied. We found that the dominant (even) mode of the PMC shielded microstrip has in general a larger effective dielectric constant than the dominant (even) mode of the PEC shielded microstrip, due to a stronger capacity to drive more electromagnetic energy into the high dielectric region.

## ACKNOWLEDGMENT

This work was supported in part by the Intel Corporation and the National Science Foundation CAREER Grant ECS-0547161.

## REFERENCES

- [1] S. Rakheja and A. Naeemi, "Interconnects for novel state variables: performance modeling and device and circuit implications," *IEEE Trans. Electron. Devices*, vol. 57, no. 10, pp. 2711-2718, 2010.
- [2] W. C. Chew, "Waves and fields in inhomogeneous media," *IEEE Press*, New York, 1995.
- [3] A. A. Melcón and J. R. Mosig, "Two techniques for the efficient numerical calculation of the green's functions for planar shielded circuits and antennas," *IEEE Trans. Microwave Theory Tech.*, vol. 48, no. 9, pp. 1492-1504, 2000.
- [4] R. E. Collin and F. J. Zucker, "Antenna theory," *McGraw-Hill*, New York, chapters 19-20, 1969.
- [5] C. P. Nehra, A. Hessel, J. Shmoys, and H. J. Stalzer Jr., "Probe-fed strip-element microstrip phased arrays: E- and H-plane scan resonances and broadbanding guidelines," *IEEE Trans. Antennas Propag.*, vol. 43, no. 11, pp. 1270-1280, November 1995.
- [6] N. K. Das and A. Mohanty, "Infinite array of printed dipoles integrated with a printed strip grating for suppression of cross-polar radiation. part I: rigorous analysis," *IEEE Trans. Antennas Propag.*, vol. 45, no. 6, pp. 960-972, June 1997.
- [7] P. Baccarelli, P. Burghignoli, F. Frezza, A. Galli, P. Lampariello, G. Lovat, and S. Paulotto, "Modal properties of surface and leaky waves propagating at arbitrary angles along a metal strip grating on a grounded slab," *IEEE Trans. Antennas Propag.*,

vol. 53, no. 1, pp. 36-46, 2005.

- [8] K. Chen, J. M. Song, and T. Kamgaing, "Modal relationship between PEC/PMC shielded interconnect and grounded dielectric slab loaded with periodic metal strips," *Annual Review of Progress in Applied Computational Electromagnetics*, Monterey, CA, pp. 904-909, March 2013.
- [9] T. Itoh, "Numerical techniques for microwave and millimeter-wave passive structures," Wiley, New York, NY, 1989.
- [10] S. Jain, J. M. Song, T. Kamgaing, and Y. Mekonnen, "Acceleration of spectral domain approach for generalized multilayered shielded microstrip interconnects using two fast convergent series," *IEEE Trans. Components, Packaging, Manufacturing Tech.*, vol. 3, no. 3, pp. 401-410, 2013.
- [11] J. D. Joannopoulos, S. G. Johnson, J. N. Winn, and R. D. Meade, "Photonic crystals: molding the flow of light," (second edition), chapter 3, *Princeton University Press*, Princeton and Oxford, 2008.
- [12] R. Mittra and T. Itoh, "A new technique for the analysis of the dispersion characteristics of microstrip lines," *IEEE Trans. Microwave Theory Tech.*, vol. 19, no. 1, pp. 47-56, 1971.
- [13] J. L. Tsalamengas and G. Fikioris, "Rapidly converging spectral-domain analysis of rectangularly shielded layered microstrip lines," *IEEE Trans. Microwave Theory Tech.*, vol. 51, no. 6, pp. 1729-1734, 2003.



**Kun Chen** received the B.S. degree from The University of Electronic Science and Technology of China, Chengdu, China. He is currently pursuing the Ph.D. degree at Iowa State University. His current research interests are integral equation methods for electromagnetics and elastics, and non-destructive evaluation.



**Jiming Song** received the B.S. and M.S. degrees in Physics from Nanjing University, China, in 1983 and 1988, respectively, and the Ph.D. degree in Electrical Engineering from Michigan State University, East Lansing, in 1993.

From 1993 to 2000, he worked as a Postdoctoral Research Associate, a Research Scientist and Visiting Assistant Professor at The University of Illinois at Urbana-Champaign. From 1996 to 2000, he worked as a Research Scientist at SAIC-DEMCO. He was the Principal Author of the Fast Illinois Solver Code (FISC), which has been distributed to more than 400 government and industrial users. From 2000 to 2002, he was a Principal Staff Engineer/Scientist at Digital DNA Research Lab., Semiconductor Products Sector of Motorola, Tempe, Arizona. In 2002, he joined the Department of Electrical and Computer Engineering, Iowa State University, Ames, as an Assistant Professor and is currently an Associate Professor. His research has dealt with modeling and simulations of interconnects on lossy silicon and RF components, wave scattering using fast algorithms, wave propagation in metamaterials, and transient electromagnetic field. He has co-edited one book and published seven book chapters, 55 journal papers and 146 conference papers.

Song received the NSF Career Award in 2006 and the Excellent Academic Award from Michigan State University in 1992. He is an IEEE Fellow and was selected as a National Research Council/Air Force Summer Faculty Fellow in 2004 and 2005.

# Numerical Investigation of Monitoring Antenna Influence on Shielding Effectiveness Characterization

T. Cvetković<sup>1</sup>, V. Milutinović<sup>1</sup>, N. Dončov<sup>2</sup>, and B. Milovanović<sup>2</sup>

<sup>1</sup> Republic Agency for Electronic Communications  
Belgrade, 11000, Republic of Serbia  
tatjana.cvetkovic@ratel.rs, vesna.milutinovic@ratel.rs

<sup>2</sup> Faculty of Electronic Engineering  
University of Niš, Niš, 18000, Republic of Serbia  
nebojsa.doncov@elfak.ni.ac.rs, bratislav.milovanovic@elfak.ni.ac.rs

**Abstract** — This paper deals with an impact of receiving antenna placed in a metal enclosure on an electromagnetic field distribution within the enclosure, and thus on its shielding effectiveness. In an experimental setup, a frequently used tool for measuring the electromagnetic field level at certain points within the enclosure is a dipole antenna connected to a measuring instrument via a coaxial cable. For modeling a coupling between the electromagnetic field and antenna in the protective enclosure we use the Transmission-Line Matrix (TLM) method, enhanced with the compact wire model. The numerical model is verified through comparison with the available experimental results and then used to investigate the influence of physical dimensions of dipole antenna and its cable connection on the detected level of shielding effectiveness.

**Index Terms** — Dipole antenna, enclosure, shielding effectiveness, TLM wire model.

## I. INTRODUCTION

For correct operation of electronic equipment, its proper protection is of key significance. Metal enclosures represent the most frequent form of protection. The performances of any electronic system placed in a protective enclosure, in terms of Electromagnetic Compatibility (EMC) [1], depend on the character of the source of external/internal Electromagnetic (EM) radiation, the configuration of wire and dielectric structures within the system, as well as the existence and

nature of coupling paths, through which the coupling of EM source energy and sensitive parts of the electronic system is realized. The performance of metal enclosures is usually assessed by the Shielding Effectiveness (SE), defined as a ratio between the field strength with and without an enclosure, at the same observed point. The value of this parameter, and thus the entire resistance of the system, depends on the structure and form of the enclosure and characteristics of the materials the enclosure is made of.

In practical use, there are apertures on the enclosure walls whose purpose is the access to the system and its control, laying of power supply and by-pass cables, ventilation, cooling, etc. EM radiation penetrating through the apertures has an adverse effect on the enclosure's protective function. It is therefore necessary to perform an analysis and determine the nature and level of the EM emission originating from different parts of the system, as well as the impact of externally generated EM disturbances on the functionality of the overall system; i.e., to determine the enclosure SE and undertake steps for elimination/reduction of coupling paths.

Numerous techniques are currently available for the calculation of the SE, from analytical methods to numerical simulations. Analytical methods represent fast tools, but their application is usually limited to simplified problems. One of analytical approaches used the Mendez method based on solving the problem of scattering [2].

Analytical solution based on an equivalent waveguide circuit was proposed in [3] and enhanced in [4] to allow for considering oblique incidence and polarization of incident plane wave and arbitrary location of apertures on enclosure walls. The numerical methods were also used for the SE calculation; e.g., the Finite Difference Time Domain (FDTD) method in [5], the Methods of Moments (MoM) in [6] and the Transmission Line Matrix (TLM) method in [7,8,9]. Various factors, such as aperture patterns (dimensions, number and orientation of apertures) and plane wave excitation parameters, and their impact on shielding properties of enclosure have been numerically considered at high frequencies.

The shielding performances of enclosure may also be characterized by experimental measurements. In that case, a small receiving dipole antenna is placed within the enclosure in order to measure the level of EM field at some characteristic points. Antenna is connected via a coaxial cable to an instrument that records measurement results (most frequently it is a network analyzer). Antenna of finite dimensions could significantly affect the EM field distribution in closed environment as already shown in [10] for resonant cavity-based microwave applicators. It is also mentioned in [4] as an explanation for some differences between the results obtained by presented equivalent circuit model, which does not include antenna presence, and the experimental SE results.

Therefore, the aim of this paper is to numerically investigate the influence of dipole antenna during experimental procedure for SE characterization. The TLM method is used here as a numerical tool due to the integrated solution introduced in this method in the form of compact wire model [11] and later extended in [12] for cylindrical mesh. Such enhanced TLM method allows to create a numerical model capable to efficiently take into account the dipole presence without resorting to an extremely fine mesh and to describe its two-way coupling with the EM field inside the enclosure. The model is first verified through comparison with the available experimental SE results for a rectangular enclosure with various rectangular apertures on its front wall [4]. Then it is used to calculate the SE of enclosure considering different physical dimensions of dipole antenna and its cable connection in order to

analyze their impact on detected EM field level.

## II. TLM MODELING OF ENCLOSURE WITH DIPOLE ANTENNA INSIDE

The TLM method [13] is a numerical modeling technique based on temporal and spatial sampling of EM fields. In the TLM method, a Three-Dimensional (3D) EM field distribution in enclosure is modeled by filling the space with a network of transmission link lines. EM properties of a medium inside the enclosure are described by using a network of interconnected nodes. A typical node structure is the Symmetrical Condensed Node (SCN), which is shown in Fig. 1. Additional stubs are attached to SCN to model inhomogeneous and lossy materials and/or a modified SCN, so-called hybrid SCN [13] is usually used to operate simulations at a higher time-step. External boundaries of arbitrary reflection coefficient of enclosures are modeled in the TLM by terminating the link lines at the edge of the problem space with an appropriate load. Individual apertures on enclosure walls are usually described by a finer mesh; i.e., using several TLM nodes across each aperture dimension, while in the case of higher number of apertures, so-called airvent model [8] can be used.

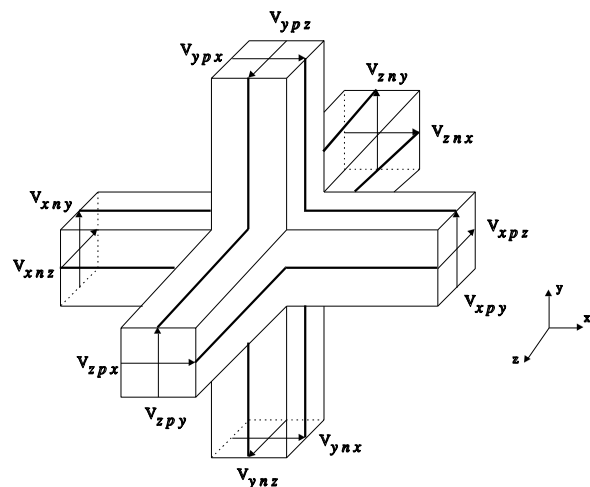


Fig. 1. Symmetrical condensed node.

Wire structures inside the enclosure can be efficiently represented by a compact TLM wire model [11], which considers wires as new elements that increase the capacitance and inductance of the medium in which they are

placed. This model allows for accurate modeling of wires with a considerably smaller diameter than the node size. It uses a special wire network formed by additional link and stub lines (Fig. 2) whose characteristic impedance parameters,  $Z_w$  and  $Z_{ws}$ , are chosen to model the capacitance and inductance increased by the wire presence, while at the same time maintaining synchronism with the rest of the transmission line network. This wire network is embedded within the TLM nodes (Fig. 3) to model signal propagation along the wires, while allowing for interaction with the EM field. Coupling between the additional link and stub lines with the rest of the TLM node is achieved through points A and B.

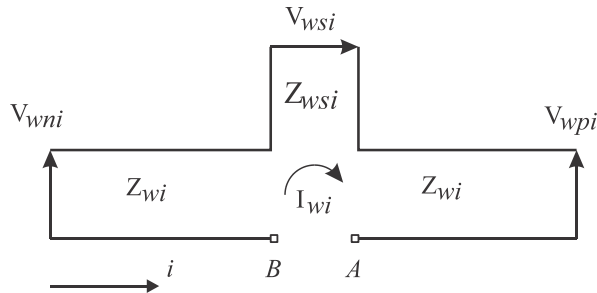


Fig. 2. Wire network for a straight wire running in the  $i$ -direction.

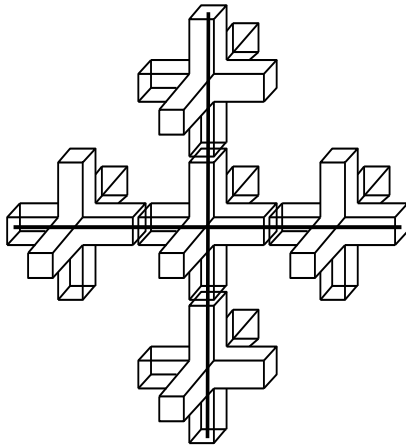


Fig. 3. Wire network embedded within the TLM nodes.

The single column of TLM nodes, through which wire conductor passes, can be used to approximately form the fictitious cylinder which represents capacitance and inductance of wire per

unit length. Its effective diameter, different for capacitance and inductance, can be expressed as a product of factors empirically obtained by using known characteristics of TLM network and the mean dimensions of the node cross-section in the wire running direction [11].

For an example, for the node containing  $i$ -directed straight wire segment, as depicted in Fig. 2, the effective diameters of fictitious cylinder for wire capacitance and inductance can be defined as:

$$d_{Ci} = 2k_{Ci}\Delta i_c, \quad (1)$$

$$d_{Li} = 2k_{Li}\Delta i_c, \quad (2)$$

respectively, where  $\Delta i_c$  represents mean cross-section dimensions of the TLM node in  $i$  direction,  $\Delta i_c = (\Delta j + \Delta k)/2$ . Empirically found factors  $k_{Ci}$  and  $k_{Li}$  for the wire located in free space are:

$$k_{Ci} = 0.0511k_i^2 + 0.0194k_i + 0.617, \quad (3)$$

$$k_{Li} = 0.34, \quad (4)$$

and for the wire above the ground:

$$k_{Ci} = 0.0223k_i^2 + 0.024k_i + 0.606, \quad (5)$$

$$k_{Li} = 0.347. \quad (6)$$

Parameter  $k_i$  depends on time- and space-step discretization and EM properties of medium represented by the TLM node and it can be calculated as:

$$k_i = 2\Delta t / (\sqrt{\epsilon\mu}\Delta i_c). \quad (7)$$

Once the effective diameters are known, the per-unit length wire capacitance and inductance can be calculated as:

$$C'_{wi} = 2\pi\epsilon / \ln(d_{Ci} / d_w), \quad (8)$$

$$L'_{wi} = \mu \ln(d_{Li} / d_w) / 2, \quad (9)$$

where  $d_w$  is a real wire diameter. Wire per-unit length capacitance is then modeled by the link line of characteristic impedance  $Z_{wi}$ :

$$Z_{wi} = \frac{\Delta t}{\Delta i C'_{wi}}, \quad (10)$$

while the wire per-unit length inductance is modeled by short-circuit stub of characteristic impedance  $Z_{wsi}$ :

$$Z_{wsi} = L'_{wi} \frac{\Delta i}{\Delta t} - Z_{wi}. \quad (11)$$

Resistive load termination at the end of wire can be treated in two ways. In the first case, lossy termination is shifted to the centre of the last wire segment, causing changes in scattering procedure of the wire node. Also, resistive load can be

defined exactly at the wire end, and in that case, a Thevenin equivalent circuit (Fig. 4) is used to determine the required reflection coefficient. A resistor  $R$  is used to connect one end of wire to a nearby ground or metal. The required reflection coefficient  $\rho$  for this wire termination is given by:

$$\rho = \frac{R - Z_{wi}}{R + Z_{wi}} \quad (12)$$

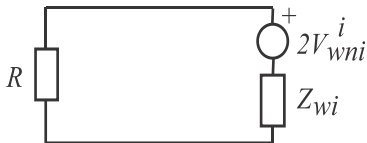


Fig. 4. Resistive load termination at one wire end.

All the mentioned models are incorporated into 3D SCN TLM mesh and implemented in 3D TLMscn solver, developed at the Microwave Lab at the Faculty of Electronic Engineering in Nis, Serbia.

### III. NUMERICAL ANALYSIS

Impact of receiving dipole antenna on the SE is considered here, on the example of rectangular enclosure with dimensions:  $l_x=300$  mm,  $l_y=400$  mm and  $l_z=200$  mm (Fig. 5). The frontal wall of the enclosure is made of 2 mm thick Al conducting material with different patterns and numbers of rectangular apertures as shown in Fig. 6. A plane wave of normal incidence to the frontal panel and with vertical electric polarization is used as an excitation. Choice of enclosure geometry, aperture dimensions and patterns, excitation and output was governed by experimental arrangements in [4].

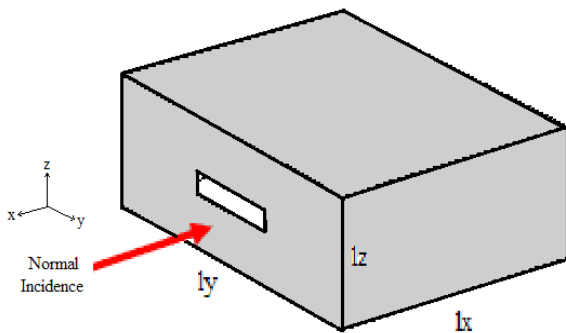


Fig. 5. Enclosure with a rectangular cross-section.

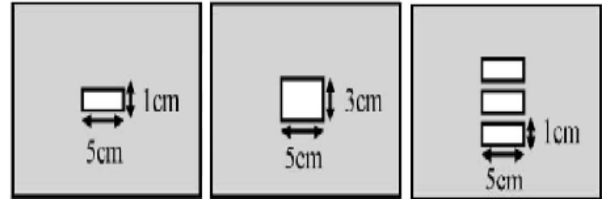


Fig. 6. Frontal panel with one or three apertures of different size.

First, it is assumed that the space inside the enclosure is empty. TLM method is used to calculate the level of EM field with and without enclosure. The frequency dependence of the SE for all aperture patterns is presented in Fig. 7.

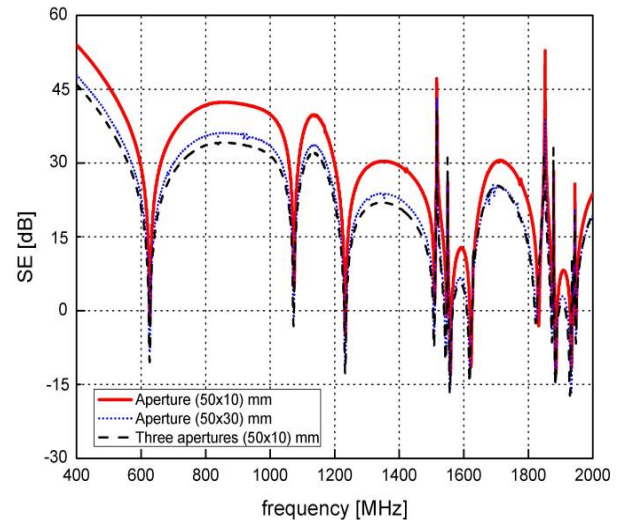


Fig. 7. SE of enclosure with various aperture patterns on the front wall-TLM model of enclosure without antenna.

As it can be seen from Fig. 7, the shape of the SE curve is similar for all considered patterns of apertures, including the values of resonant frequencies. This indicates that the patterns and the number of apertures mostly affect the level of attenuation to which EM field propagating through apertures is exposed. As expected, the level of the SE decreases with the increase of area covered by apertures. It should be also pointed out that the numerical results are in good agreement with the results obtained by equivalent circuitual model presented in [4], as it can be seen from Fig. 8 for an aperture (50x10 mm). Similar agreement is obtained for the other two aperture patterns.

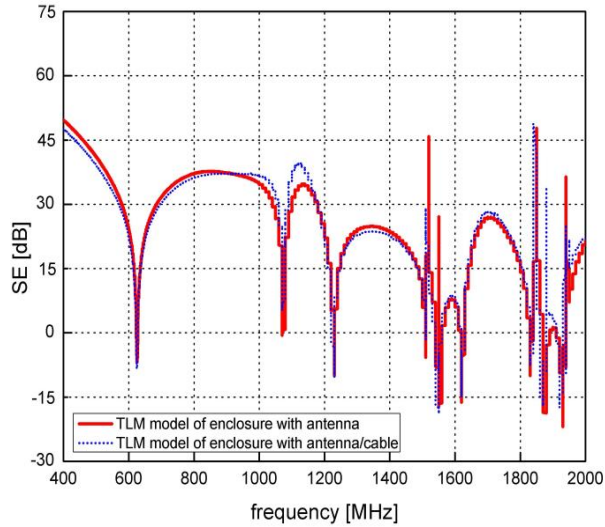


Fig. 8. SE of enclosure with one aperture (50x10 mm) on the front wall-TLM model of enclosure without antenna and equivalent circuitual model presented in [4].

Further, the physical presence of the dipole antenna in the enclosure is considered, as well as the impact of the different radii of the dipole antenna on the SE of the enclosure. For this SE calculation, the compact wire model described in Section II is used to model the dipole antenna. Dipole antenna is represented as two z-directed 50 mm long wires, both having the radius of 0.1 mm, and mutually separated by 2 mm. Their position within the enclosure is defined at the point slightly off the enclosure center in x-direction as specified in [4]. The electric field is directly taken at the point in space between two wires instead of picking up signal directly from the antenna. The SE results obtained by TLM simulations are compared to the experimental results [4] and shown in Figs. 9-11. Good agreement between numerical and experimental results can be observed.

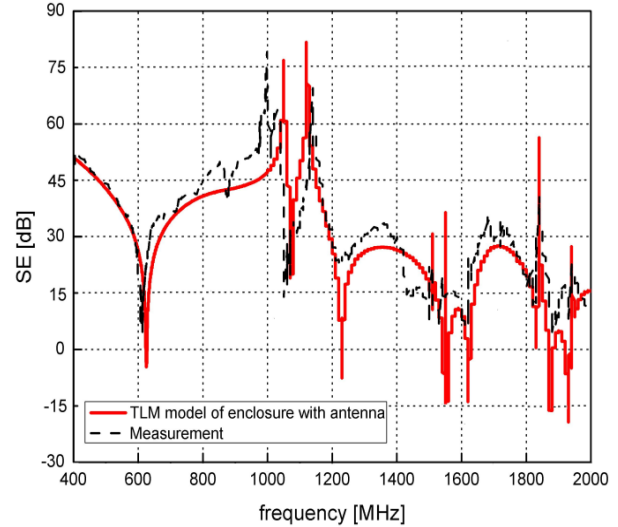


Fig. 9. SE of enclosure with one aperture (50x10 mm) on the front wall-TLM model of enclosure with antenna and measurements [4].

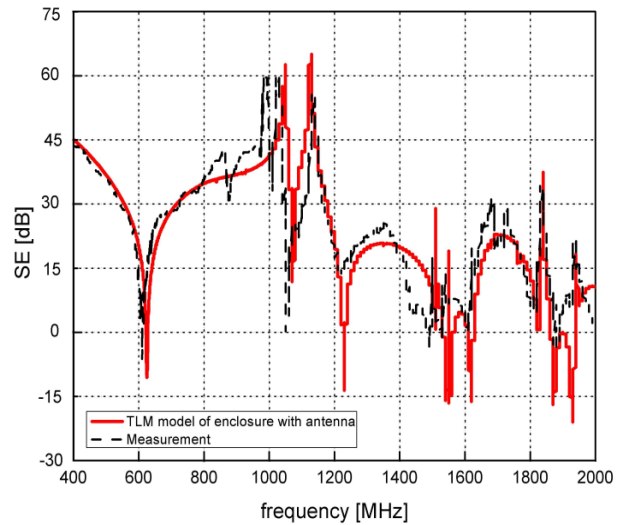


Fig. 10. SE of enclosure with one aperture (50x30 mm) on the front wall-TLM model of enclosure with antenna and measurements [4].

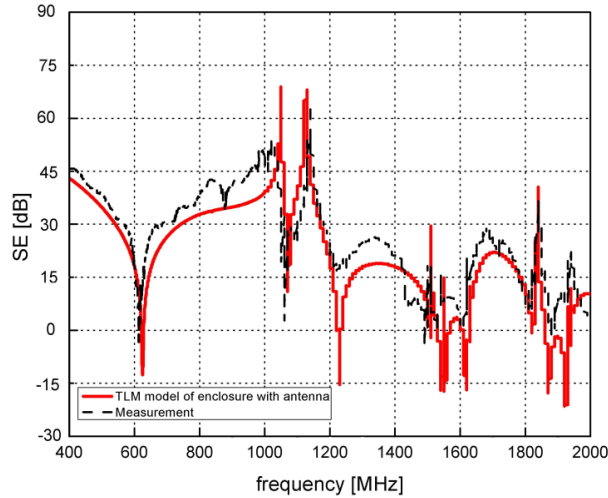


Fig. 11. SE of enclosure with three apertures (50x10 mm) on the front wall-TLM model of enclosure with antenna and measurements [4].

The SE results obtained by TLM simulations for different radii of dipole antenna within the enclosure with one aperture (50x10 mm) on the front wall are shown in Fig. 12. It can be noticed that the level of the SE decreases with the increase of wire radius while the resonant frequencies shift towards lower frequencies. When wire radius is decreasing, the resonant frequencies are approaching to the case when antenna is excluded from the numerical model. Values of the first resonant frequency for different radii of the antenna are given in Table 1.

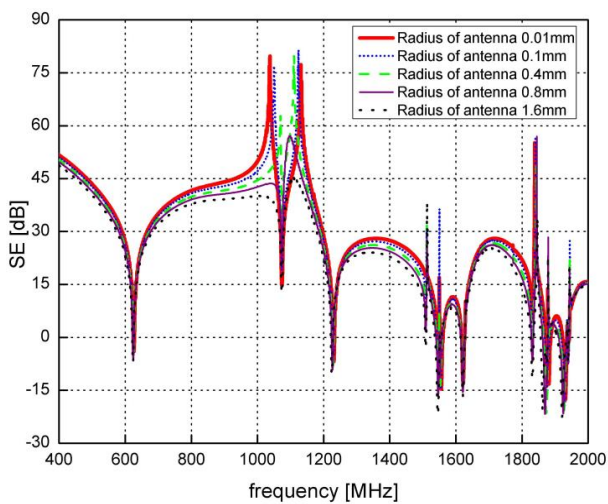


Fig. 12. Impact of the increase of wire radius on the SE of enclosure with one aperture (50x10 mm) on the front wall.

Table 1: Value of the first resonant frequency for different radii of the dipole antenna

Radius of Antenna (mm)	First Resonant Frequencies (MHz)
0.001	626.095
0.1	625.600
0.4	624.981
0.8	624.485
1.6	623.619

The SE results obtained by TLM simulations for different length of dipole antenna of radius 0.1 mm within enclosure with one aperture (50x10 mm) on frontal wall are shown in Fig. 13. The same effects can be observed as in the case of different wire radii. Level of the SE decreases and the resonant frequencies shift toward lower frequencies with the increase of antenna length, due to stronger influence of antenna as a second emitter on total EM field inside the enclosure. Change of antenna length also influences the location of the first dipole antenna resonance. The same conclusions regarding the impact of physical dimensions of the antenna on the SE can be reached if the TLM method enhanced with wire model is applied to the enclosure with other considered aperture patterns on the front wall.

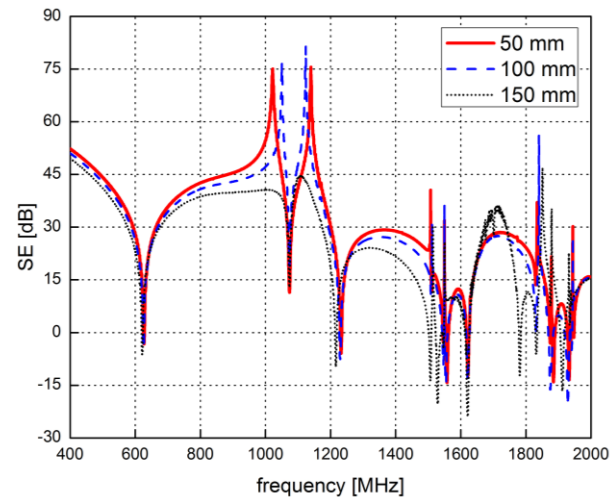


Fig. 13. Impact of the increase of wire length on the SE of enclosure with one aperture (50x10 mm) on the front wall.

The same effects can be observed as in the case of different wire radii. Level of the SE

decreases and the resonant frequencies shift toward lower frequencies with the increase of antenna length due to stronger influence of antenna as a second emitter on total EM field inside the enclosure. Change of antenna length also influences the location of the first dipole antenna resonance. The same conclusions regarding the impact of physical dimensions of the antenna on the SE can be reached if the TLM method enhanced with wire model is applied to the enclosure with other considered aperture patterns on the front wall.

In previous cases, the SE is calculated based on the EM field level directly taken in space between two wires. However, during the experimental measurement of the SE, signal is picked up directly from the antenna and via a coaxial cable transferred to the network analyzer. In order to create a numerical model that will correspond to the experimental case, both 50 mm long wires of 0.1 mm radius are connected in their mutually nearest points by resistor  $R$  equal to the impedance of the coaxial cable. Physical presence of coaxial cable is not taken into account as cable can be placed in such position (closed to enclosure wall and with minimal running length) not to disturb the EM field distribution inside the enclosure. Impact of balun usually placed between antenna and cable is also neglected.

Current induced in the dipole antenna is shown in Fig. 14 for the case of the enclosure with three apertures (50x10 mm) on the front wall. It can be used to find the voltage induced between wires ends; i.e., in the centre of the dipole antenna, with and without the enclosure in order to calculate the SE.

Numerical results for the SE together with the results of the case when only dipole antenna is considered (without the cable connection) and experimental results are shown in Figs. 15-17. The position of the dipole antenna is the same as in the

previously considered case.

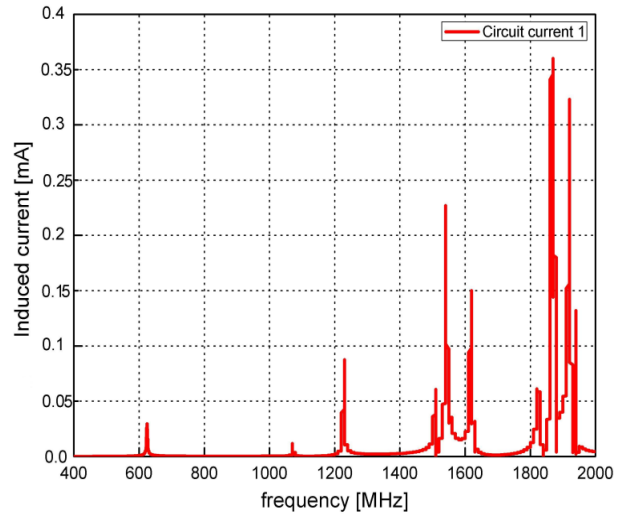


Fig. 14. Induced dipole antenna current as a function of frequency.

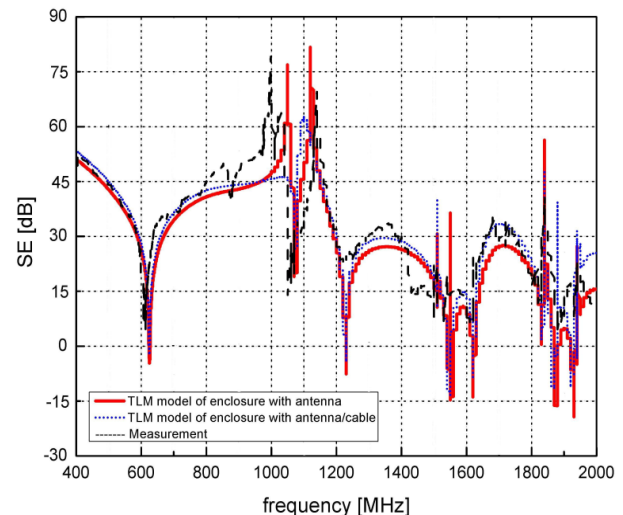


Fig. 15. SE of enclosure with one aperture (50x10 mm) on the front wall-TLM models of enclosure with antenna/cable and with antenna and measurements [4].

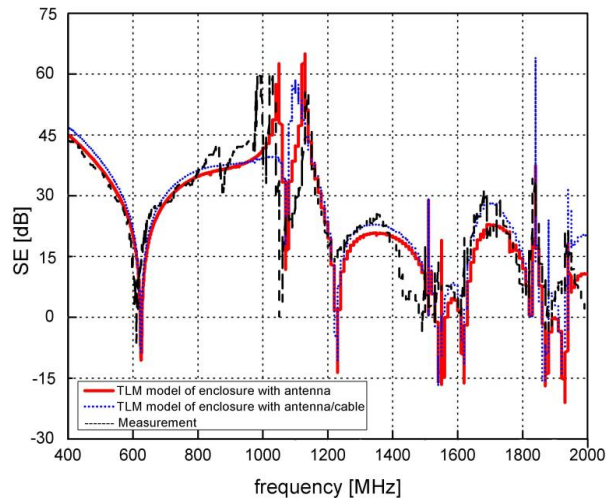


Fig. 16. SE of enclosure with one aperture (50x30 mm) on the front wall-TLM models of enclosure with antenna/cable and with antenna and measurements [4].

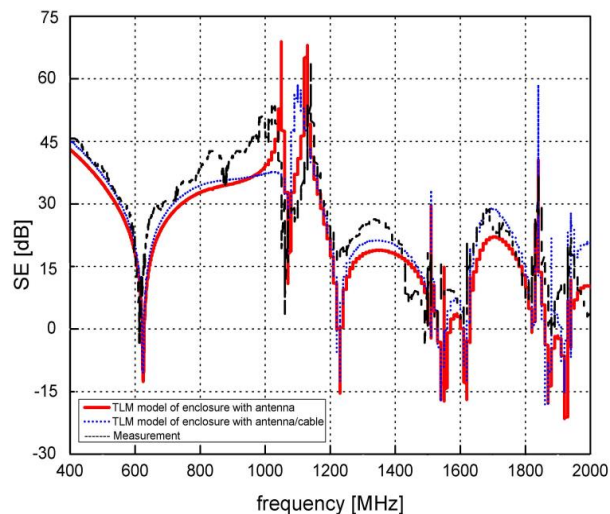


Fig. 17. SE of enclosure with three apertures (50x10 mm) on the front wall-TLM models of enclosure with antenna/cable and with antenna and measurements [4].

From Figs. 15-17 it can be noticed that in the case when antenna and cable influences are taken into account, the results for the SE are similar to the case when only physical presence of the dipole antenna in the enclosure is taken into account. However, in some parts of considered frequency range, TLM model of enclosure with antenna/cable provides slightly better agreement with the experimental results [4].

#### IV. CONCLUSION

In this paper, a numerical model based on TLM method with compact wire description is used to calculate the SE of metal enclosure with dipole antenna inside. The modeling case is in line with practical measurement conditions for SE characterization. Physical dimensions of dipole antenna and its cable connection are considered with respect of their influence on the level of EM field detected by the antenna. The obtained results confirm that the antenna presence affects the distribution of the EM field within the enclosure, and thus also the SE parameter value. Therefore, this impact has to be taken into account during the experimental SE characterization in order to correctly estimate the shielding properties of metal enclosure. Future research will comprise of more detailed analysis of this impact in order to empirically derive a factor that should correct the measured level of SE due to antenna and other equipment presence inside the enclosure.

#### ACKNOWLEDGMENT

This work has been partially supported by the Ministry for Education, Science and Technological Development of Serbia, project number TR32052.

#### REFERENCES

- [1] C. Christopoulos, "Principles and techniques of electromagnetic compatibility," *CRC Press*, 2007.
- [2] H. A. Mendez, "Shielding theory of enclosures with apertures," *IEEE Trans. Electromagn. Compat.*, vol. 20, no. 2, pp. 296-305, 1978.
- [3] M. P. Robinson, T. M. Benson, C. Christopoulos, J. F. Dawson, M. D. Ganley, A. C. Marvin, S. J. Porter, and D. W. P. Thomas, "Analytical formulation for the shielding effectiveness of enclosures with apertures," *IEEE Trans. Electromagn. Compat.*, vol. 40, no. 3, pp. 240-248, 1998.
- [4] J. Shim, D. G. Kam, J. H. Kwon, and J. Kim, "Circuit modeling and measurement of shielding effectiveness against oblique incident plane wave on apertures in multiple sides of rectangular enclosure," *IEEE Trans. Electromagn. Compat.*, vol. 52, no. 3, pp. 566-577, 2010.
- [5] L. J. Nuebel, J. L. Drewniak, R. E. DuBroff, T. H. Hubing, and T. P. Van Doren, "EMI from cavity modes of shielding enclosures-FDTD modeling and measurements," *IEEE Trans. Electromagn. Compat.*, vol. 42, no. 1, pp. 29-38, 2000.
- [6] S. Ali, D. S. Weile, and T. Clupper, "Effect of near field radiators on the radiation leakage through

- perforated shields,” *IEEE Trans. Electromagn. Compat.*, vol. 47, no. 2, pp. 367-373, 2005.
- [7] B. L. Nie, P. A. Du, Y. T. Yu, and Z. Shi, “Study of the shielding properties of enclosures with apertures at higher frequencies using the transmission-line modeling method,” *IEEE Trans. Electromagn. Compat.*, vol. 53, no. 1, pp. 73-81, 2011.
- [8] N. Dončov, B. Milovanović, and Z. Stanković, “Extension of compact TLM air-vent model on rectangular and hexagonal apertures,” *Applied Computational Electromagnetic Society (ACES) Journal*, vol. 26, no. 1, pp. 64-72, 2011.
- [9] V. Milutinović, T. Cvetković, N. Dončov, and B. Milovanović, “Analysis of enclosure shielding properties dependence on aperture spacing and excitation parameters,” *In Proceedings of the IEEE TELSIKS Conference*, Niš, Serbia, vol. 2, pp. 521-524, 2011.
- [10] J. Joković, B. Milovanović, and N. Dončov, “Numerical model of transmission procedure in a cylindrical metallic cavity compared with measured results,” *Int. Journal of RF and Microwave Computer-Aided Engineering*, vol. 18, no. 4, pp. 295-302, 2008.
- [11] A. J. Włodarczyk, V. Trenkic, R. Scaramuzza, and C. Christopoulos, “A fully integrated multiconductor model for TLM,” *IEEE Trans. Microwave Theory Tech.*, vol. 46, no. 12, pp. 2431-2437, 1998.
- [12] T. Dimitrijević, J. Joković, B. Milovanović, and N. Dončov, “TLM modeling of a probe-coupled cylindrical cavity based on compact wire model in the cylindrical mesh,” *Int. Journal of RF and Microwave Computer-Aided Engineering*, vol. 22, no. 2, pp. 184-192, 2012.
- [13] C. Christopoulos, “The transmission-line modelling (TLM) method,” *IEEE/OUP Series*, Piscataway, NJ, 1995.

**Tatjana Cvetković** graduated in 1989 at the Military-Technical Faculty, in Zagreb, Croatia, with the Department of Electronics and Telecommunications. Doctoral studies at the University of Niš, Faculty of Electronics, Department of Telecommunications, enrolled in 2008. She is employed in the Republic Agency for Electronic Communications, for activities related to the regulations in the area of electronic communications. She is an author and co-author of many conference works in the field of analyzing and calculation of shielding effectiveness of metal enclosures, and also in fields of regulation, realization and quality of electronic communication services.

**Vesna Milutinović** graduated in 2000 at the Faculty of Electronics in Niš, with the Department of Electronics and Telecommunications. Doctoral studies at the Faculty of Electronics in Niš, Department of Telecommunications, under the supervision of Professor Bratislav Milovanović, enrolled in October 2008. She has worked in planning, development and design of telecommunication networks. Since April 2007 she has been employed in RATEL for activities related to the control of radio communications. The author works in the field of telecommunication networks and systems.

**Nebojša Dončov** received the Dipl.-Ing. degree in Electrical Engineering and Ph.D. degree in Telecommunication Engineering from the University of Niš, Niš, Serbia in 1995 and 2002, respectively.

From 1998 to 2001, he was a Research Assistant with the Faculty of Electronic Engineering, University of Niš. From 2001 to 2004, he was a Research and Development Engineer with the Electromagnetics Division of Flomerics Ltd., Nottingham, UK. Since 2004, he has been with the Department of Telecommunications, Faculty of Electronic Engineering, University of Niš, Serbia where he is now a Full Professor. His research interests include computational and applied electromagnetics with a particular emphasis on TLM and network methods applications in microwaves and EMC.

Dončov was a recipient of the International Union of Radio Science (URSI) Young Scientist Award in 2002.

**Bratislav Milovanović** received the Dipl.-Ing., M.Sc. and Ph.D. degrees from the Faculty of Electronic Engineering, University of Nis, Serbia, in 1972, 1975 and 1979, respectively.

From 1972 onwards he was promoted, with the Faculty of Electronic Engineering to all academic positions to Full Professor (1990). He was the Head of the Department of Telecommunications in the period from 1994-2000 and 2004-2010, and the Dean of the Faculty of Electronic Engineering from 1994-1998. Also, he was President of Serbia and Montenegro IEEE MTT Chapter from 2004-2008. His present research work is in the field of telecommunications, particularly in the field of microwave theory and techniques, computational electromagnetic and neural networks applications. He is a General Chairman of series of IEEE TELSIKS conferences, a Member of Serbian Scientific Society since 1999, a Full Member of the Academy of Engineering Sciences of Serbia and Montenegro since 2000, President of national MTT Society since 2002.

Milovanović's awards and honors include the Octobar Prize of the City of Niš, the Annual Prizes of

Radio Television of Serbia, the Distinguished Prize (YU IEEE Society for Microwave Technique and Technology), the Diplomas of Academy of Engineering Sciences of Serbia and Montenegro, the Tesla Award (Nikola Tesla foundation in Serbia) and a number of certificates of appreciation.

# Development of a Broadband Substrate Integrated Waveguide Cavity Backed Slot Antenna Using Perturbation Technique

Elham Baghernia and Mohammad H. Neshati

Department of Electrical Engineering  
Ferdowsi University of Mashhad, 91779-48974, Mashhad, Iran  
elham.baghernia@stu-mail.um.ac.ir, neshat@um.ac.ir

**Abstract** — A novel method for bandwidth enhancement of Substrate Integrated Waveguide (SIW) cavity-backed slot antenna is introduced for a single element and an array configuration. Using a corner cut in the SIW square cavity, resonant frequency of two degenerate  $TE_{210}$  and  $TE_{120}$  modes of a square cavity are separated and impedance bandwidth is improved. The simulated and measured results of the antennas show at least 140% and 220% wider bandwidth compared to the bandwidth of a conventional single cavity antenna for single and two element array antennas, respectively. The presented antennas provide a few advantages including low profile, light weight, easy fabrication with low cost and convenient integration with planar circuits.

**Index Terms** — Antenna array, cavity-backed antenna, slot antenna, Substrate Integrated Waveguide (SIW).

## I. INTRODUCTION

Wireless communication systems have been rapidly growing up in recent years and low profile, low cost antenna with high performance radiation characteristics are in a great demand, especially in some applications such as satellite, aircraft and radar systems.

Slot antennas exhibits favorable characteristics including compact size, low cost, conformability and easy integration with planar circuits, so they are highly suitable for wireless communication applications. However, one evident drawback of the slot antenna is its bidirectional radiations [1], which limit its performance in some applications. Cavity backed slot antennas eliminate backward radiation and provide high performance radiation

characteristics. The conventional metallic cavity backed antennas are bulky and it is not easy to integrate them with planar circuits. So they are not suitable for many applications.

Recently Substrate Integrated Waveguide (SIW) technology has been greatly suggested due to its useful substitute to the conventional bulky metallic waveguide, and therefore, implementation of microwave circuits and antennas by SIW technique is easy using low cost Printed Circuit Board (PCB) process. SIW technology firstly proposed by Wu [2], is an integrated waveguide structure fabricated using two rows of vias, metallic cylinders, embedded in dielectric substrate. These vias connect two parallel metal plates of PCB. SIW waveguides provide same propagation characteristic as the propagation properties of the metallic waveguides [3]. They also allow the integration of planar and non-planar structures on a same substrate.

Low profile cavity backed slot antennas based on Substrate Integrated Waveguide (SIW) technology have been proposed in [4] and [5]. These antennas have good radiation performance and provide the advantages of low cost fabrication, low profile and easy integration with planar circuit. There are some inherent drawbacks in using a thin substrate in a cavity backed slot antenna. The height of the substrate affects  $Q$ , quality factor, of the slot and cavity. A low height substrate increases  $Q$  of the antenna, which causes to obtain narrow bandwidth [4]. Overcoming these problems is an important issue in designing a low profile cavity backed slot antenna. Various methods have been proposed to enhance bandwidth of the cavity backed slot antennas.

A dual mode cavity backed slot antenna has

been investigated in [5], in which two hybrid modes are simultaneously excited. By merging the two hybrid modes, cavity bandwidth could be enhanced. In [6], by removing the substrate under the slot and in turn, by decreasing  $Q$  of the slot, 24% wider bandwidth compared to those of the conventional cavity backed slot antenna has been achieved. The proposed technique is more useful for substrate, which have high relative permittivity or high loss tangent. Bandwidth enhancement of SIW cavity backed slot antenna using a via hole above the slot has been demonstrated in [7], in which the via hole is used to create the second resonate frequency. By adjusting the location of the via hole, the second resonate can be moved to improve bandwidth of the antenna.

Despite the fact that this antenna provides high radiation performance, obtaining higher gain is realized by array structure. A  $2 \times 2$  SIW cavity backed slot array antenna has been proposed in [8]. The presented antenna provides high gain and radiation efficiency of 12.1 dBi and 87% respectively. However, its impedance bandwidth is about 1%.

In this paper, a perturbation technique using a corner cut in the SIW square cavity is used to enhance impedance bandwidth of the cavity backed slot antennas. Furthermore, in order to increase gain of the proposed antenna, a two element antenna array is introduced. The presented antennas show dual resonance due to splitting of resonant frequency of the two degenerate modes. The proposed antenna structures are fabricated on single layer substrate using ordinary low cost Printed Circuit Board (PCB) process. The design and simulation of the proposed antenna is performed using full wave software High Frequency Simulator Structures (HFSS) based on Finite Element Method (FEM). The simulated and measured results show the impedance bandwidth of the both antennas is greatly enhanced.

## II. THEORY OF OPERATION

### A. Square SIW cavity

Figure 1 (a) shows a square SIW cavity. It is made by four rows metalized via arrays made on a single layer board. Length of the cavity is designated by  $a$  and diameter of the metallic vias

and distance between the centre of two adjacent vias is nominated by  $d$  and  $p$ , respectively. In order to make the SIW cavity to be equivalent to a conventional metallic cavity, two conditions  $d/p \geq 0.5$  and  $d/\lambda_o \leq 0.1$  must be satisfied and  $\lambda_o$  represent free space wavelength [9].

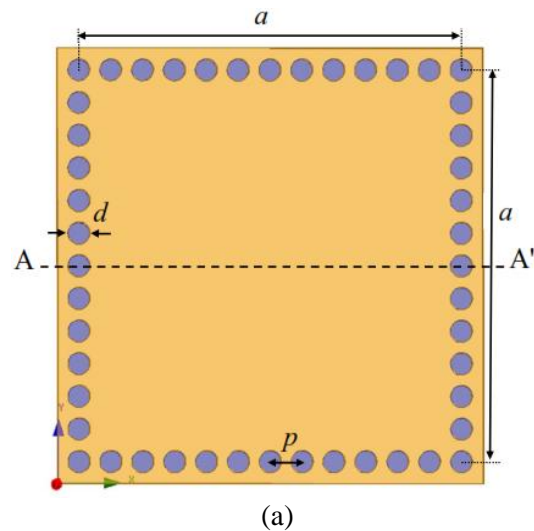
The equivalent width of the SIW cavity is approximately expressed by equation 1 [10]:

$$a_e \approx a - \frac{d^2}{0.95p}, \quad (1)$$

where  $a_e$  is the effective width of the equivalent conventional metallic cavity. In a square SIW cavity only  $TE_{mn0}$  modes can be excited and their resonant frequency is determined by equation (2) [11]:

$$f_{mn0} = \frac{c}{2a_e \sqrt{\epsilon_{rs}}} \sqrt{m^2 + n^2}, \quad (2)$$

where  $c$  is light velocity in free space and  $\epsilon_{rs}$  is permittivity of the filled material inside the cavity. The simulated electric field distribution for the first three modes in the square SIW cavity with a length of  $a=17.8$  mm using full wave electromagnetic Eigen mode of HFSS is shown in Fig. 1 (b). It can be seen that  $TE_{120}$  and  $TE_{210}$  modes provide odd and even symmetric field distribution with respect to  $AA'$  plane. Moreover, using equation (2), it can be calculated that these modes resonate at 13.2 GHz, and so they are decoupled degenerate modes with the same resonate frequency [12].



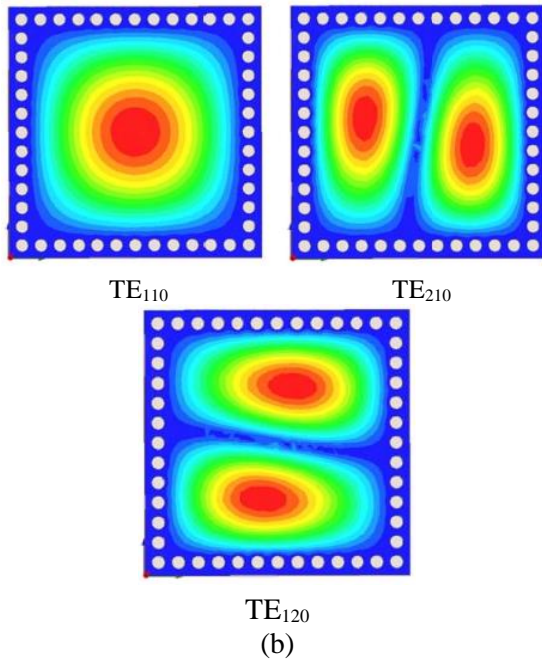


Fig. 1. (a) Geometry of a square cavity, and (b) electric field distribution at three first modes.

### B. Perturbed square SIW cavity

Figure 2 (a) shows a perturbed square SIW cavity. In fact, this cavity is same as the square cavity which is perturbed by a corner cut. By perturbing the square cavity using the corner cut, two degenerate modes will be coupled to each other, and their resonate frequencies will split [13]. Based on the symmetry of the structure with respect to diagonal  $BB'$  plane, field distributions of degenerate modes is symmetric. This is verified by simulated E-field distribution of  $TE_{210}$  and  $TE_{120}$  modes, using Eigen mode analysis, as is shown in Fig. 2 (b). It can be seen that electric field distribution is symmetric for odd and even modes with respect to  $BB'$  plane. To study the splitting of resonate frequency of degenerate modes due to the corner cut, a parametric study was carried out for the perturbed SIW cavity using HFSS software. The variation of resonate frequency of the degenerate modes,  $TE_{210}$  and  $TE_{120}$ , versus cut size  $l$ , is shown in Fig. 3. It can be concluded that resonant frequency of odd mode remains almost fixed, but for even modes resonant frequency is increased by increasing  $l$ . This is due to the location of perturbation, which is at null position of electric field, whereas for even mode, the corner cut is located at maximum of magnetic field.

Furthermore, the effective volume of the cavity is decreased by increasing the cut size.

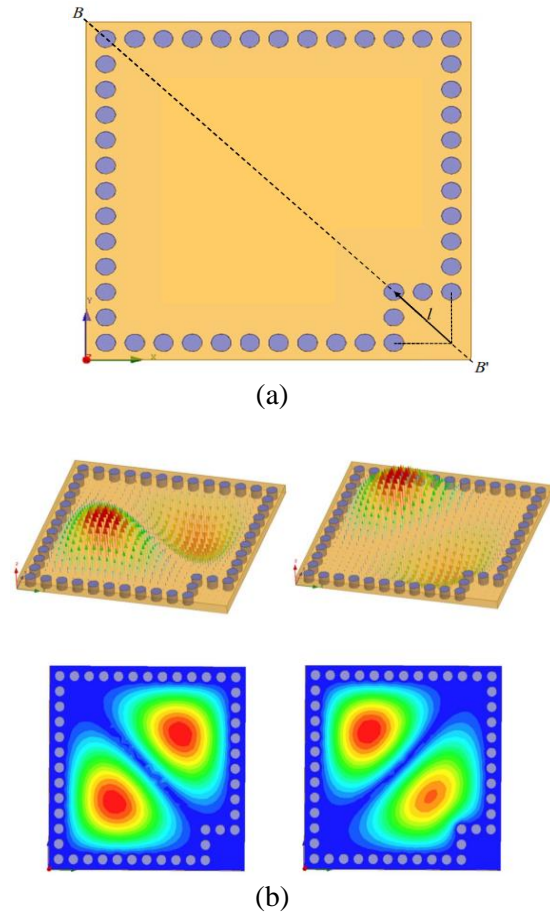


Fig. 2. (a) Geometry of the perturbed square cavity, and (b) simulated electric field distribution at  $TE_{210}$  and  $TE_{120}$ .

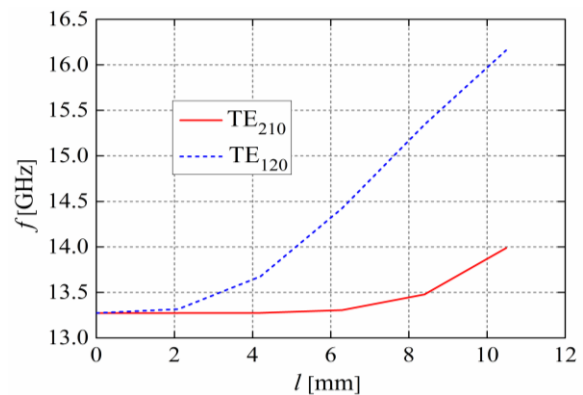


Fig. 3. Variation of the simulated resonate frequency of the degenerate modes versus perturbation size  $l$ .

### III. ANTENNA STRUCTURE

#### A. Single element antenna

Figure 4 shows a perturbed square SIW cavity as a single element antenna. A non-resonant slot with a length  $L_s$ , far more than a half resonant wavelength, and width of  $W_s$  is placed at the distance  $y_s$  from the centre of the cavity as the radiating element. In order to isolate the spurious radiation from the feed line, radiating slot is etched at the ground plane of the structure. Moreover, a  $50 \Omega$  microstrip inset feed line is adopted as the feeding network to excite the cavity. For measurement convenience, a section of  $50 \Omega$  microstrip line is added at the end of inner conductor of the feed line with the same width. All the presented antennas are designed and made on a single TLY031 substrate with permittivity of 2.2, thickness of  $h=0.787$  mm and loss tangent of 0.001. The detailed geometrical parameters of the single element antenna are summarized in Table 1.

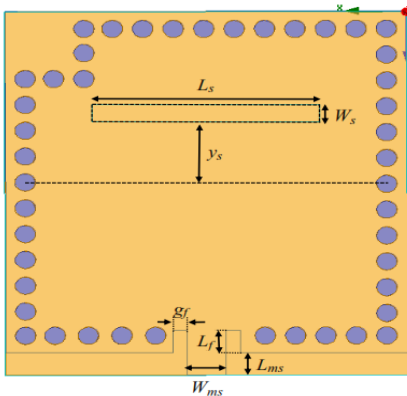


Fig. 4. Single element antenna structure.

Table 1: Geometrical parameters of the proposed antennas (units in mm)

Parameter	Single Antenna	Antenna Array	Power Divider	
$L_t$	17.8	17.8	$L_1$	9.6
$L_{ms}$	1.3	1.3	$L_2$	4.15
$W_{ms}$	1.9	1.9	$L_3$	7.96
$L_f$	1.3	1.3	$L_4$	7.9
$l$	4.1	4.1	$L_c$	0.9
$L_s$	11	11.2	$W_1$	3
$W_s$	1	1	$W_2$	1.13
$y_s$	3.6	3.6	-	-
$g_f$	0.7	0.7	-	-
$d$	1	1	-	-

A full wave simulation of the proposed antenna has been investigated using HFSS. To study the effect of size perturbation  $l$ , a parametric study was carried out and  $S_{11}$  of the proposed antenna was considered for different values of  $l$ . The simulated result of reflection coefficient versus frequency for different values of  $l$  is shown in Fig. 5. It can be seen that by increasing  $l$ , two separate resonance frequencies are obtained, while only the second resonance frequency is increased by  $l$ . Therefore, dual mode operation is achieved and by merging these two, wideband operation can be obtained. Furthermore, for a square cavity without corner cut,  $l=0$  mm, simulated bandwidth, for return loss of +10 dB, is nearly 100 MHz, which shows fractional bandwidth of 0.76%. In case of perturbed cavity with  $l=4.1$  mm, simulated impedance bandwidth is 240 MHz, from 13.13 GHz to 13.37 GHz, provides fractional bandwidth of 1.8%.

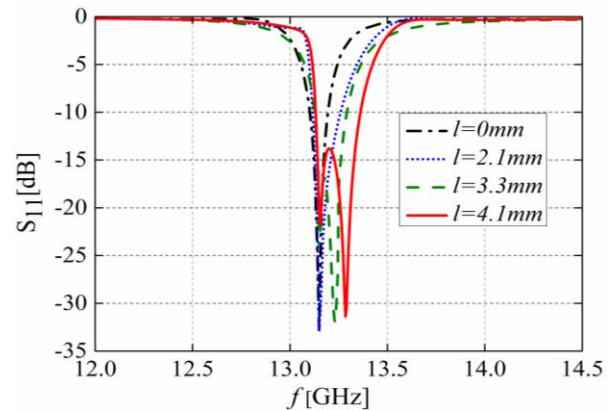


Fig. 5. Simulation results of  $S_{11}$  versus frequency for a perturbed cavity and different values of  $l$ .

#### B. Two elements array

In order to increase gain and to obtain narrower beamwidth, a two element antenna array is formed by placing two perturbed cavity side by side as shown in Fig. 6. The array elements are similar to that of the designed single perturbed cavity, whereas, the distance between the elements is nearly  $d_x \approx 0.7\lambda_o$  and  $\lambda_o$  is free space wavelength at the centre frequency.

To excite the cavities, a microstrip T junction in phase power divider is adopted as the feed network, which is symmetric to its horizontal axis, so input power is divided equally between its two arms. The  $50 \Omega$  microstrip line split into two

quarter wave transformers lines using T junction. In fact, there are  $100 \Omega$  lines before these  $70.7 \Omega$  lines, but their length is considered to be zero. The feed network with the removed  $100 \Omega$  lines works exactly same as the feed network with non-zero length of  $100 \Omega$  lines [14]. The geometrical parameters of the array are listed in Table 1.

For antenna array, a parametric study was investigated and its reflection coefficient is studied for different values of the beveled line size  $L_c$ . Simulated results are shown in Fig. 7, which can be seen that  $L_c$  has an important effect on  $S_{11}$  and impedance bandwidth. From this figure, it can be found that when  $L_c$  increases, the impedance matching improves because the effective width around the corners becomes smaller. However if  $L_c$  becomes greater than a special value, the effective width around the corners will be too small, so impedance matching gets worse.

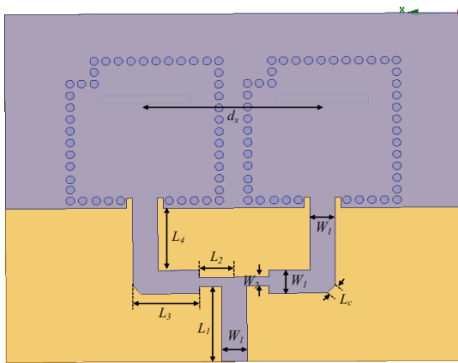


Fig. 6. Two elements antenna array.

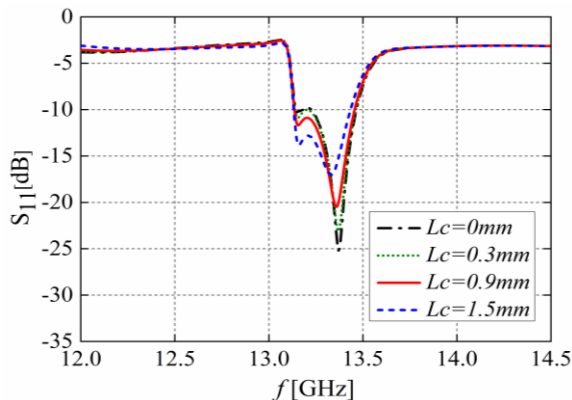


Fig. 7. Simulation results of  $S_{11}$  for the proposed array versus frequency and different values of  $L_c$ .

## IV. EXPERIMENTAL RESULTS AND DISCUSSION

### A. Single element antenna

In order to validate the design method, a sample of the proposed single element antenna has been made on a single layer of TLY031 substrate by the low cost PCB process. To improve ground connection, the connector legs are soldered to the substrate ground. The photo of the fabricated antenna is shown in Fig. 8, in which the detailed geometrical parameters in Table 1 are used.

Measured  $S_{11}$  of the proposed antenna is shown in Fig. 9 (a), compared with full wave simulated results. It can be seen that measured results are in a good agreement with those obtained by simulation. Measured impedance bandwidth is 220 MHz, with a fractional bandwidth of 1.65%, which is slightly less than the predicted value of 1.8%. Measured and simulated gain of the antenna at boresight direction,  $\theta=180^\circ$ , versus frequency is also plotted in Fig. 9 (b). It can be seen that the proposed antenna provides almost uniform gain throughout the operating bandwidth within the range of 3.25 dBi to 5.2 dBi. The simulated maximum gain is of 6.1 dBi, which is slightly more than the measured maximum gain. The slight discrepancy between measured and simulated results is due to imperfection in fabrication process and transmission loss in measurement.

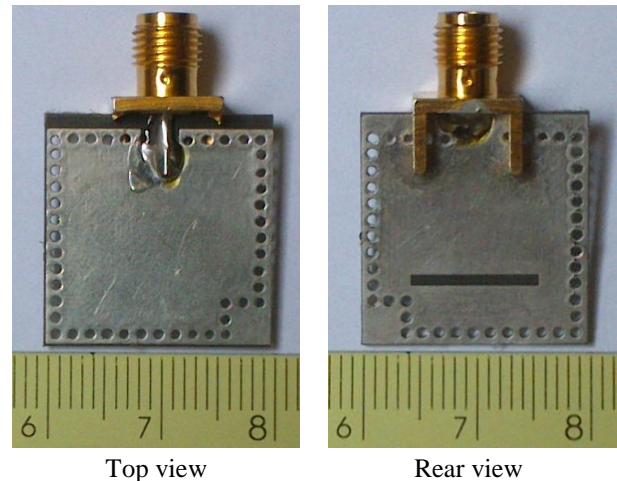


Fig. 8. Photo of the fabricated proposed single element antenna.

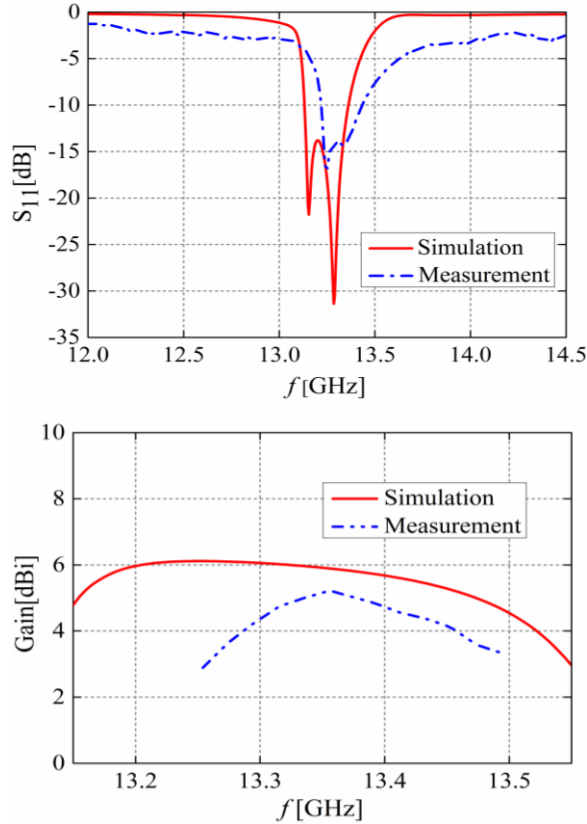


Fig. 9. Measured and simulated results of the single element antenna at boresight direction of: (a)  $S_{11}$ , and (b) gain.

Measured and simulated far-field E- and H-plane co-polarized radiation patterns of the proposed antenna at 13.15 GHz and 13.29 GHz are shown in Fig. 10. The largest radiation direction of the perturbed square cavity is offset from boresight direction by nearly  $15^\circ$  for its structure asymmetry along  $y$ -direction. Measured results also show that the proposed antenna has very low level cross-polarized radiation at  $\theta=180^\circ$ . This is due to structure symmetry in  $x$ -direction. Measured Front to Back Ratio (FTBR) of the antenna is nearly 18 dB. Apart from deviation of measured and simulated radiation patterns, it can be found that the proposed perturbed SIW cavity antenna provides high radiation performance of the conventional cavity backed antenna with a significantly reduction in profile.

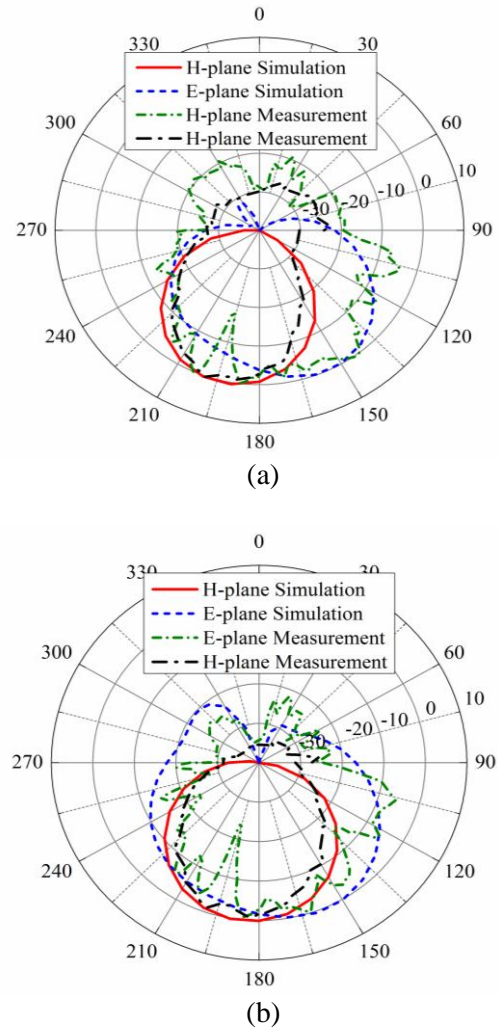


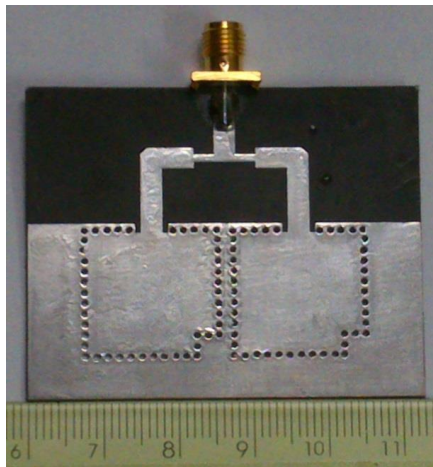
Fig. 10. Measured and simulated radiation patterns of the single antenna at: (a) 13.15 GHz, and (b) 13.29 GHz.

## B. Antenna array

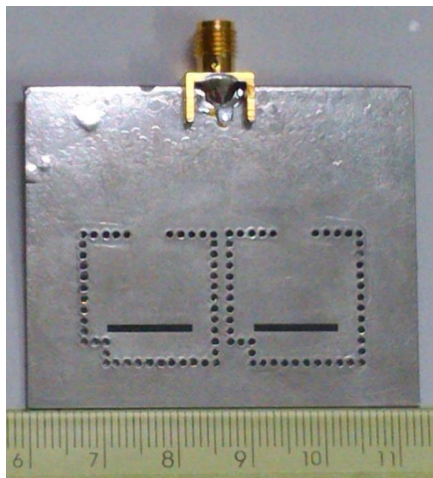
The photo of the fabricated antenna array is shown in Fig. 11. Figure 12 (a) and 12 (b) show measured  $S_{11}$  and gain of the proposed array compared with the simulation results. Apart from a shift in frequency response of  $S_{11}$ , a good agreement between measured and simulated results is obtained. The small shift at high frequencies of the provided  $S_{11}$  parameter may be attributed to the considered permittivity value of the substrate. Measured impedance bandwidth is

410 MHz, provides fractional bandwidth of 3%, which is more than the predicted value of 2.4%. The increasing bandwidth is due to coupling between the two elements and array configuration of the structure. Moreover, it can be seen that for the antenna array, the simulated and measured peak gain of 8.8 dBi and 8.4 dBi are obtained respectively at boresight direction  $\theta=180^\circ$ . Both of the results show that the antenna array provides 2.7 dBi more gain compared to the gain of the single antenna.

The simulated radiation efficiency of the presented antennas is also shown in Fig. 13. From this figure, it can be found that the simulated peak efficiency of 84% and 91% are achieved for proposed single and antenna array, respectively.

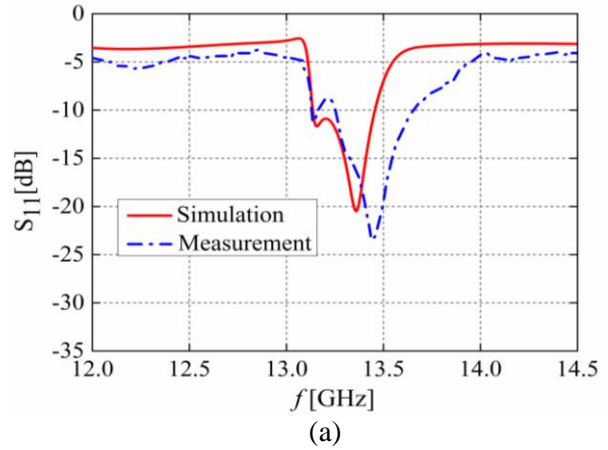


Top view

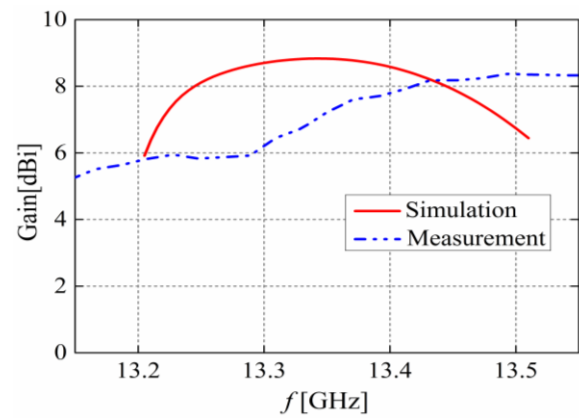


Rear view

Fig. 11. Photo of the fabricated proposed two elements antenna array.



(a)



(b)

Fig. 12. Simulated and measured results of the proposed antenna array versus frequency: (a) reflection coefficient, and (b) gain.

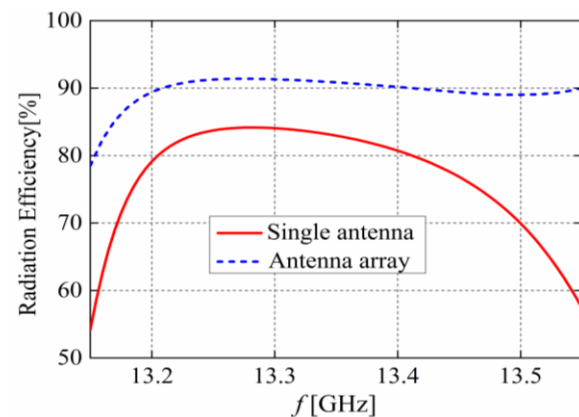


Fig. 13. Simulated radiation efficiency of the proposed single and antenna array.

Radiation patterns of the array are illustrated in Fig. 14 in two principal E- and H-planes at two

resonate frequencies. It can be observed that radiation patterns are in boresight direction ( $\theta=180^\circ$ ), perpendicular to the ground plane of the structures. As it expected, the H-plane radiation pattern of the array antenna is narrower than the H-plane beamwidth of the single antenna. Some of the specifications of designed antenna structures such as resonate frequencies, reflection coefficient

and impedance bandwidth are summarized in Table 2. The presented antennas maintain good radiation performance of the SIW cavity backed slot antenna, although their bandwidth are greatly enhanced. Table 3 compares the detailed characteristics of the proposed single antenna with the antenna specifications of recently published research in literature.

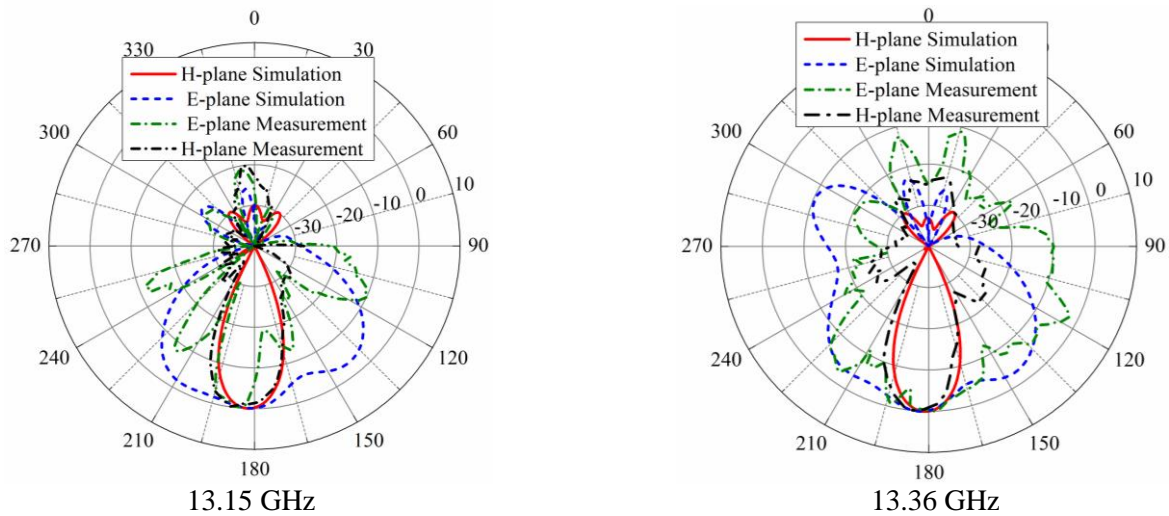


Fig. 14. Measured and simulated radiation patterns of the antenna array at two frequencies.

Table 2: Summary of the simulated and measured results of the proposed antennas

Parameter	Single Antenna		Antenna Array	
	Simulation	Measurement	Simulation	Measurement
$f_1$ (first resonate frequency, GHz)	13.16	13.24	13.15	13.14
$f_2$ (first resonate frequency, GHz)	13.26	13.34	13.36	13.44
$S_{11}$ at $f_1$ (dB)	-22	-17	-12	-12
$S_{11}$ at $f_2$ (dB)	-31	-14	-20	-24
Gain (dBi)	6.1	5.2	8.8	8.4
Bandwidth (%)	1.8%	1.65%	2.4%	3%
Antenna size (mm <sup>2</sup> )	20×21		44.5×54.5	

Table 3: Comparison between the presented single antenna and recently published antennas

Antenna	Operating Frequency (GHz)	Bandwidth (MHz)	Gain (dBi)	Radiation Efficiency (%)
Single proposed	13.2	220	6.1	84
Antenna in Ref. [4]	10	140	5.5	86
Antenna in Ref. [5]	10	630	6	92
Antenna in Ref. [6]	2.45	53	-	50.6
Antenna in Ref. [7]	2.45	91	5.9	89

## V. CONCLUSION

A new technique to improve bandwidth of a SIW cavity backed slot antenna is presented in this paper. With the perturbation method, employing a corner cut in the square SIW cavity, resonant frequency of the two degenerated modes are separated, and in turn, impedance bandwidth of the antenna is enhanced. The proposed method has been experimentally and numerically investigated. Compared with SIW cavity backed slot antenna with no corner cut, impedance bandwidth of the proposed antenna is greatly improved. By employing proposed antenna in array configuration, at least 33% wider bandwidth and 44% higher gain compared to that of a single cavity backed slot antenna is achieved. The presented structures show favorable radiation performance and provide other advantages such as low cost, light weight and easy integration with planar circuits.

## REFERENCES

- [1] R. Elliott, "Antenna theory and design," Wiley, New York, 2003.
- [2] F. Xu and K. Wu, "Guided-wave and leakage characteristics substrate integrated waveguide," *IEEE Transactions on Microwave Theory and Techniques*, vol. 53, pp. 66-73, 2005.
- [3] M. Bozzi, A. Georgiadis, and K. Wu, "Review of substrate-integrated waveguide circuits and antennas," *IET Microwaves Antennas & Propagation*, vol. 5, pp. 909-920, 2011.
- [4] G. Luo, Z. Hu, L. Dong, and L. Sun, "Planar slot antenna backed by substrate integrated waveguide cavity," *IEEE Antennas and Wireless Propagation Letters*, vol. 7, pp. 236-239, 2008.
- [5] G. Luo, Z. Hu, W. Li, X. Zhang, L. Sun, and J. Zheng, "Bandwidth enhanced low-profile cavity-backed slot antenna by using hybrid SIW cavity modes," *IEEE Antennas and Wireless Propagation Letters*, vol. 60, pp. 1698-1704, 2012.
- [6] S. Yun, D. Kim, and S. Nam, "Bandwidth and efficiency enhancement of cavity-backed slot antenna using a substrate removal," *IEEE Antennas and Wireless Propagation Letters*, vol. 11, pp. 1458-1461, 2012.
- [7] S. Yun, D. Kim, and S. Nam, "Bandwidth enhancement of cavity-backed slot antenna using a via-hole above the slot," *IEEE Antennas and Wireless Propagation Letters*, vol. 11, pp. 1092-1095, 2012.
- [8] K. Jiang, G. Luo, W. Li, G. Huang, P. Li, and L. Sunm, "A 2x2 antenna array consisting of low profile cavity backed slot antennas," *CJMW Proceedings*, pp. 1-3, 2011.
- [9] F. Xu and K. Wu, "Guided-wave and leakage characteristics of substrate integrated waveguide," *IEEE Transactions on Microwave Theory and Techniques*, vol. 53, pp. 66-73, 2005.
- [10] L. Yan, W. Hong, G. Hua, J. Chen, K. Wu, and T. Cui, "Simulation and experiment on SIW slot array antennas," *IEEE Antennas and Wireless Propagation Letters*, vol. 14, pp. 446-448, 2004.
- [11] P. Rizzi, "Microwave engineering passive circuits," *Prentice-Hall International Press*, 1998.
- [12] C. Chuang, H. Lin, and C. Wang, "Design of dual-mode SIW cavity filters," *TENCON, IEEE Region 10 Conference*, pp. 1-4, 2007.
- [13] X. Liang, K. Zaki, and A. Atia, "Dual mode coupling by square corner cut in resonators and filters," *IEEE Transactions on Microwave Theory and Techniques*, vol. 40, pp. 2294-2302, 1994.
- [14] C. A. Balanis, "Antenna theory analysis and design," Wiley, New York, 2005.



**Elham Baghernia** was born in Mashhad, Iran, in 1987. She received her B.Sc. degree in Electrical Engineering from Sadjad University of Technology, Mashhad, Iran, in 2010; the M.Sc. degree from Ferdowsi University of Mashhad, Iran, in 2014. Her current research interests include antenna design and microwave and millimeter wave passive devices.



**Mohammad Hassan Neshati** was born in Yazd, Iran. He received his B.Sc. in Electrical Engineering from Isfahan University of Technology, Isfahan, Iran; M.Sc. degree from Amir-Kabir University of Technology, Tehran, Iran and Ph.D. degree from the University of Manchester (UMIST), England in 2000. He was with Sistan and Baluchistan University, Zahedan, Iran from 1988 to 2006.

Since 2006 he has been with the Department of Electrical Engineering of Ferdowsi University of Mashhad Iran, where he is Associate Professor. He is a Senior Member of IEEE and also Member of Antennas and Propagation Society (AS-P) and Microwave Theory and Techniques Society (MTT-S). His current research works include electromagnetic, antenna theory and design, microwave active and passive circuit design.

# Using the Best Uniform Approximation with Compression for Efficient Computation of Monostatic Scattering

Zhiwei Liu<sup>1,2</sup>, Shan He<sup>1</sup>, Xiaoyan Zhang<sup>1,2</sup>, Yingting Liu<sup>1</sup>, and Yueyuan Zhang<sup>1</sup>

<sup>1</sup>East China Jiaotong University, Nanchang, 330013, China  
lucky-shan@163.com, yingtingmm@163.com, aney0360\_cn@sina.com

<sup>2</sup>The State Key Laboratory of Millimeter Wave, Nanjing, 210096, China  
zwliu1982@hotmail.com, xy\_zhang3129@sohu.com

**Abstract** — The best uniform approximation method hybridized with Singular Value Decomposition (SVD) is proposed to reduce the time requirement for computation of monostatic Radar Cross Section (RCS). In contrast to our previous work, the traditional best uniform approximation technique is applied to compute the key excitation vectors instead of electric current vectors. Reduction of the number of multiple excitation vectors can lead to significantly reduced computation time. Furthermore, with low-rank property, the key excitation vectors could be further compressed by SVD, resulting in a more efficient method. Numerical results demonstrate that the proposed method is efficient for monostatic RCS calculation with high accuracy.

**Index Terms** — Best uniform approximation, monostatic scattering, radar cross-section, Singular Value Decomposition (SVD).

## I. INTRODUCTION

Analysis of electromagnetic wave scattering from electrically large objects using conventional Method of Moment (MoM) [1,2] requires a mass of computation time and storage, because the Electrical Field Integral Equation (EFIE) matrix associated with the resulting linear systems is large, dense, and ill-conditioned. To solve integral equations by applying traditional MoM, the computation complexity for the iterative solver is  $O(kN^2)$  and the memory requirement is  $O(N^2)$ , where  $N$  refers to the number of unknowns and  $k$  refers to the number of iterative steps. Obviously, it is impractical to use a personal computer to

solve equations with more than 10,000 unknowns. This difficulty can be overcome by using the multi-level fast multi-pole algorithm (MLFMA) [2,3] while accelerating the operation of matrix-vector product. The computation complexity can be reduced to  $O(N\log N)$  and the memory requirement to  $O(N\log N)$ . Moreover, preconditioning techniques [4-8] can speed up convergence of iterative solvers by improving spectral properties of the EFIE matrix. However, it is still time- and memory-consuming for calculation of monostatic RCS since it requires repeated solution of EFIE at each incident direction and frequency.

The Model-Based Parameter Estimation (MBPE) technique is presented by Miller and Burke to accurately compute the wide band response with a few direct calculations [9,10]. In this technique, the electric current or field is expanded as a rational function. The coefficients of the rational function are obtained using either frequency/angular data or the related derivative data [22]. In [11,12], an adaptive sampling method to obtain the optimal samples for monostatic RCS calculation with wide angular band. The adaptive technique is employed to generate new sampling points automatically by using a coarse-to-fine hierarchy.

As an alternative technique, the best uniform approximation [13] has been introduced. The best uniform approximation are important in approximation theory since the roots of the Chebyshev polynomials of the first kind, which are also called Chebyshev nodes, are used as nodes in polynomial interpolation. The resulting

interpolation polynomial minimizes the problem of Runge's phenomenon and provides an approximation that is close to the polynomial of best approximation to a continuous function under the maximum norm. In [13], the best uniform approximation is proposed to optimally select the most informative angles in monostatic RCS curve, resulting in an efficient computation of monostatic scattering.

In [14], it is reported that multiple excitation vectors or right hand side vectors can be compressed by use of the low-rank property. Accordingly, the optimal excitation vectors corresponding to the selected angles can be compressed by Singular Value Decomposition (SVD). In this paper, the combination of SVD and best uniform approximation is applied to efficient computation of monostatic RCS. The numerical simulations demonstrate that this framework can reduce the computation time significantly.

The remainder of this paper is organized as follows. Section II demonstrates the basic theory and formulations of integral equations. The theory of the best uniform approximation and using SVD to achieve compression will be discussed in section III. Numerical experiments of several geometries are presented to demonstrate the efficiency of this proposed method in Section IV.

## II. EFFICIENT COMPUTATION OF MONOSTATIC RCS BY BEST UNIFORM APPROXIMATION

### A. Theory of moment method

For electromagnetic scattering from a Perfect Electrical Conductor (PEC), the Combined Field Integral Equation (CFIE) which consists of EFIE and MFIE is widely used for closed structures [1]. The CFIE formulation of electromagnetic wave scattering problems using planar Rao-Wilton-Glisson (RWG) basis functions for surface modeling is presented in [15,16]. Once the resulting linear systems from the CFIE formulation after Galerkin's test are solved by numerical matrix equation solvers, the CFIE matrix equation can be symbolically rewritten as:

$$\mathbf{Ax}=\mathbf{b}. \quad (1)$$

Here,  $\mathbf{A}$  refers to the impedance matrix.  $\mathbf{x}$  is the column vector containing the unknown coefficients of the surface current expansion with RWG basis functions and it can be used to

calculate the scattered field and RCS.  $\mathbf{b}$  devotes the right hand side which generated by the incident wave.

To solve the above matrix equation by an iterative method, the matrix-vector products are required at each iteration step. Physically, a matrix-vector product corresponds to one cycle of iterations between the basis functions. The basic idea of the Fast Multi-pole Method (FMM) is to convert the interaction of element-to-element to the interaction of group-to-group. Here a group includes the elements residing in a spatial box. The mathematical foundation of the FMM is the addition theorem for the scalar Green's function in free space. Using the FMM, the matrix-vector product  $\mathbf{Ax}$  can be written as:

$$\mathbf{Ax}=\mathbf{A}_N\mathbf{x}+\mathbf{A}_F\mathbf{x}. \quad (2)$$

Here  $\mathbf{A}_N$  is the near part of  $\mathbf{A}$  and  $\mathbf{A}_F$  is the far part of  $\mathbf{A}$ . In the FMM, the calculation of matrix elements in  $\mathbf{A}_N$  remains the same as in the MoM procedure. However, those elements in  $\mathbf{A}_F$  are not explicitly computed and stored. Hence, they are not numerically available in the FMM. It has been shown that the operation complexity of FMM to perform  $\mathbf{Ax}$  is  $O(N^{1.5})$ . If the FMM is implemented in multilevel, the total cost can be reduced further to  $O(N\log N)$  [2,3]. However, it is still time consuming for the computation of a monostatic RCS since it requires repeated solution of CFIE for each incident direction. As a result, new methods are required to circumvent this difficulty.

### B. Accelerated by best uniform approximation

In order to compute the monostatic RCS of arbitrary geometry, MoM solver and MLFMA have to be applied angle by angle over a given angular band. To accelerate it by the best uniform approximation, the specific algorithm is as follows:

For a given angular band  $[\theta_m, \theta_n]$ , let:

$$k = \frac{2\theta - (\theta_m + \theta_n)}{\theta_n - \theta_m}. \quad (3)$$

Accordingly, the surface current vector can be written as:

$$\mathbf{I}(k) = \mathbf{I} \left[ \frac{k(\theta_n - \theta_m) + (\theta_m + \theta_n)}{2} \right], \quad (4)$$

where  $k$  belongs to  $[-1, 1]$ .

Assume that  $T_l(k)$  ( $l=1,2,\dots,n$ ) as the  $l$ -order Chebyshev polynomials and it is defined as:

$$T_0(k)=1, \quad (5a)$$

$$T_1(k)=k, \quad (5b)$$

$$T_{l+1}(k)=2kT_l(k)-T_{l-1}(k), 2 \leq l \leq n. \quad (5c)$$

So the Chebyshev Approximation of  $\mathbf{I}(k)$  can be expressed as:

$$\mathbf{I}(k) \approx \sum_{l=0}^{n-1} \mathbf{c}_l T_l(k) - \frac{\mathbf{c}_0}{2}. \quad (6)$$

Suggest  $k_i$  ( $i=1,2,\dots,n$ ) as the  $i$ -th zero point of  $T_n(k)$ , so,

$$k_i = \cos\left(\frac{i-0.5}{n} \pi\right), i=1,2,\dots,n, \quad (7)$$

$$\mathbf{c}_l = \frac{2}{n} \sum_{i=1}^n \mathbf{I}(\theta_i) T_l(k_i). \quad (8)$$

Here,  $\theta_i$  is called the Chebyshev samples in  $[\theta_m, \theta_n]$ . Where:

$$\theta_i = \frac{k_i(\theta_n - \theta_m) + (\theta_m + \theta_n)}{2}, i=1,2,\dots,n. \quad (9)$$

Above all, we summarize the algorithm of the best uniform approximation about the target surface current, which is presented as follows.

#### **The best uniform approximation algorithm**

- Step 1: Calculate the zero points  $k_i$  of  $T_n(k)$ .
- Step 2: Transform the zero points to Chebyshev samples. That is transform  $k_i$  to  $\theta_i$  using formulation (9).
- Step 3: Using MoM and MLFMA to compute current vector  $\mathbf{I}(\theta_i)$ . Then apply the formula of (8) to get the coefficients  $\mathbf{c}_l$ .
- Step 4: Using the formula of (6) to calculate the approximate current throughout the whole angular band  $[\theta_m, \theta_n]$ .
- Step 5: Using the approximated current vector to compute the monostatic RCS.

### **III. BEST UNIFORM APPROXIMATION WITH SVD COMPRESSION**

Theoretically, the combination of MoM and MLFMA is able to accurately analyze the scattering of any geometry. Improved by the best uniform approximation, the computation of a monostatic RCS can be accelerated greatly. However, in some cases, the number of coefficients of the interpolation polynomials is so large as to compromise the efficient calculation of monostatic scattering. This process can be computationally prohibitive for electrically large objects. In order to alleviate this difficulty, a singular value decomposition based method is proposed and discussed in this section.

Firstly, a brief review of compression of right hand sides is given. The computation of monostatic RCS can be considered as linear equations with multiple right hand sides:

$$\mathbf{A}\mathbf{X}=\mathbf{B}, \quad (10)$$

where  $\mathbf{A}$  is the impedance matrix,  $\mathbf{X}$  is the multiple complex coefficient vector of RWG basis and  $\mathbf{B}$  is the multiple right hand side generated by the incident wave. In addition,

$$\mathbf{X}=[\mathbf{x}(\theta_1), \mathbf{x}(\theta_2), \dots, \mathbf{x}(\theta_n)], \quad (11)$$

$$\mathbf{B}=[\mathbf{b}(\theta_1), \mathbf{b}(\theta_2), \dots, \mathbf{b}(\theta_n)], \quad (12)$$

where  $\theta_i$  is the  $i^{\text{th}}$  incident angle. Using traditional singular value decomposition, the matrix  $\mathbf{B}$  can be described in the form of an eigenvalue and eigenvector:

$$\mathbf{B}=\mathbf{U}\mathbf{\Sigma}\mathbf{V}^H. \quad (13)$$

The superscript ‘H’ denotes the conjugate transpose. If the dimension of  $\mathbf{B}$  is  $N \times M$ , the dimension of matrices  $\mathbf{U}$ 、 $\mathbf{\Sigma}$  and  $\mathbf{V}$  are  $N \times M$ ,  $M \times M$ ,  $M \times M$ , respectively.  $N$  is the number of unknowns.  $\mathbf{\Sigma}$  is a diagonal matrix including all the eigenvalues of  $\mathbf{B}$  while  $\mathbf{U}$  and  $\mathbf{V}$  contain all the eigenvectors of  $\mathbf{B}$ . When  $\mathbf{B}$  is the multiple right hand sides in the linear system connecting with the SIE used for monostatic RCS, the matrix  $\mathbf{B}$  is low-rank and can be approximately described as a low-rank SVD form:

$$\mathbf{B}=\mathbf{U}_k \mathbf{\Sigma}_k \mathbf{V}_k^H, \quad (14)$$

where the dimension of matrices  $\mathbf{U}_k$ 、 $\mathbf{\Sigma}_k$  and  $\mathbf{V}_k$  are  $N \times k$ ,  $k \times k$ ,  $M \times k$ , respectively. Only the  $k$  largest eigenvalues and corresponding eigenvectors are reserved. Substituting (14) into (10), the linear equations can be rewritten as:

$$\mathbf{X} \approx (\mathbf{A}^{-1} \mathbf{U}_k) \mathbf{\Sigma}_k \mathbf{V}_k^H. \quad (15)$$

Here,  $\mathbf{A}^{-1} \mathbf{U}_k$  can be computed by any iterative solver. If using a direct solver to compute the inversion of matrix  $\mathbf{A}$  [17], the proposed method will become useless. Therefore, the number of repeated solutions of  $\mathbf{A}\mathbf{x}=\mathbf{b}$  is  $k$  for SVD method. Using traditional method, the number is  $M$ . Generally,  $k$  is much smaller than  $M$  which leads to an efficient method for computation of monostatic RCS over a wide angular band.

Using the best uniform approximation, we can write the induced current into the sum of the samples shown in (14). We rewrite this formulation in matrix form:

$$\mathbf{X}=\mathbf{A}^{-1} \mathbf{B}_s \mathbf{C}, \quad (16)$$

where  $\mathbf{X}$  is a matrix containing all induced currents over the whole angular band.  $\mathbf{C}$  is the

coefficient matrix of the non-uniform interpolation method with the dimension of  $s \times M$ .  $\mathbf{B}_s$  contains all the key samples of the excitation vectors. According to formulation (16), the required number of repeated solution of  $\mathbf{Ax}=\mathbf{b}$  is  $s$ , where  $s$  is the number of required terms of Chebyshev Polynomials. Using singular value decomposition for matrix  $\mathbf{B}_s$ :

$$\mathbf{B}_s = \mathbf{U}_{sk} \mathbf{\Sigma}_{sk} \mathbf{V}_{sk}^H. \quad (17)$$

Then,

$$\mathbf{X} = (\mathbf{A}^{-1} \mathbf{U}_{sk}) \mathbf{\Sigma}_{sk} \mathbf{V}_{sk}^H \cdot \mathbf{C}. \quad (18)$$

As a result, the required number of repeated solution is reduced to  $sk$ .

Above all, we can summarize the algorithm of the compressed best uniform approximation, which is presented as follows.

#### *The compressed best uniform approximation algorithm*

- Step 1: Calculate the zero points  $k_i$  of  $T_n(k)$ .
- Step 2: Transform the zero points to Chebyshev samples. That is transform  $k_i$  to  $\theta_i$  using formulation (9).
- Step 3: Computing the right hand sides  $\mathbf{V}(\theta_i)$  using MoM formulation. Apply the formula of (8) to get the coefficients  $\mathbf{c}_i$ . Then put all the Chebyshev basis into matrix  $\mathbf{B}_s$ .
- Step 4: Transfer  $\mathbf{B}_s = [\mathbf{B}_{s1}, \mathbf{B}_{s2}, \dots, \mathbf{B}_{sn}]$  into the form of  $\mathbf{U}_k \mathbf{\Sigma}_k \mathbf{V}_k^H$  by singular value decomposition, where  $k$  is the rank of  $\mathbf{B}_s$ .
- Step 5: Computing the value  $\mathbf{A}^{-1} \mathbf{U}_{sk}$ . Then using formulation (18) to get the value of current vector  $\mathbf{I}$ .
- Step 6: Using the formula of (6) to calculate the approximate current throughout the whole angular band  $[\theta_m, \theta_n]$ .
- Step 7: Using the approximated current vector to compute the monostatic RCS.

Considering the accuracy of the proposed method, the error control is very important in SVD. The Convergence Error (CE) is defined here to control the error of SVD. That is, some rows of matrix  $\mathbf{U}$  and some columns of  $\mathbf{V}$  should be truncated in SVD when the corresponding eigenvalue over the largest eigenvalue is smaller than CE. In order to reduce the numerical error, CE is required to be sufficiently small. However, large CE is needed for efficiency. The value of CE is chosen as  $CE=10^{-2}$  in this paper, and this will be

discussed in the next session.

## IV. NUMERICAL RESULTS

In this section, a number of numerical results are presented to demonstrate the accuracy and efficiency of the proposed method for fast calculation of monostatic RCS over a wide angular band. The Flexible General Minimal Residual (FGMRES) [18,19,20] algorithm is applied to solve linear systems. The dimension size of the Krylov subspace is set to be 30 for outer iteration and the dimension is set to be 10 for inner iteration. The tolerance of the inner iteration is 0.1 in this paper. All experiments are conducted on a Quad-Core AMD Opteron (tm) with 4.00 GB local memory and run at 2.31 GHz in single precision. The iteration process is terminated when the 2-norm residual error is reduced by  $10^{-3}$ , and the limit of the maximum number of iterations is set as 1000.

Four geometries are applied to illustrate the performance of our proposed method. They consist of a NASA Almond with 1815 unknowns [23], a Reentry Vehicle (RV) with 26566 unknowns [21], a Cube with 49260 unknowns and the VFY-218 model [3] with 40725 unknowns. The NASA Almond is used for testing the value of CE, while the last three geometries is used for testing the accuracy and efficiency of the proposed method.

As shown in Fig. 1, the NASA Almond is one of the most popular geometry in electromagnetics and its structure is define in [23]. The RV has a blunt nose as well as a deeply recessed rear cavity that are expected to be significant sources of backscatter. The three-dimensional shape of the RV is illustrated in Fig. 2 (unit: wavelength). As the third geometry, the length of the Cube is 1 m. The VFY-218 is a well-known model in the field of electromagnetic scattering and its geometry is shown in Fig. 3. The VFY-218 is 15.5 m from nose to tail, 8.9 m from one wing to another, and 4.1 m from top to bottom.

In our numerical experiments, the geometries are illuminated by a plane wave with the incident pitch angles range from 0 to 180 deg. The frequency is 1.0 GHz for the RV, 300 MHz for Cube and 300 MHz for VFY-218. For all cases the azimuth angle is 0 deg. Firstly, the factor 'CE' must be determined. In Fig. 3, the NASA almond is used for testing the value of CE since it has a

small number of unknowns. The results of the monostatic RCS of by four different CE are compared with the reference result (the direct method). The frequency is 3.0 GHz for the almond geometry. The reference result is the RCS curve computed with repeated solution without compression at each angle. Other curves are computed by our proposed method. We select a part of the curve where the difference is much bigger with the incident pitch angles range from 20 to 100 deg. From this figure, when CE is set to be 0.1 or 0.05, although the decrease of computation time meets the requirement, the RCS curve is not accurate enough. When CE is set to be 0.01 and 0.001, the proposed method will be able to perform a good result. The time of the comparison is listed in Table 1. As is shown, the CPU time is 338s when CE is set to be 0.001, and 232s when CE is set to be 0.01. Therefore, CE=0.001 leads to larger computation time than 0.01. If using the proposed method without compression, which means CE is set to be 0, it would spend 5 times longer than CE is set to be 0.01 for the high-rank. That is, there is a tradeoff between accuracy and efficiency. In this paper, the value of CE is set to be 0.01 to keep the RCS curve accurate enough.

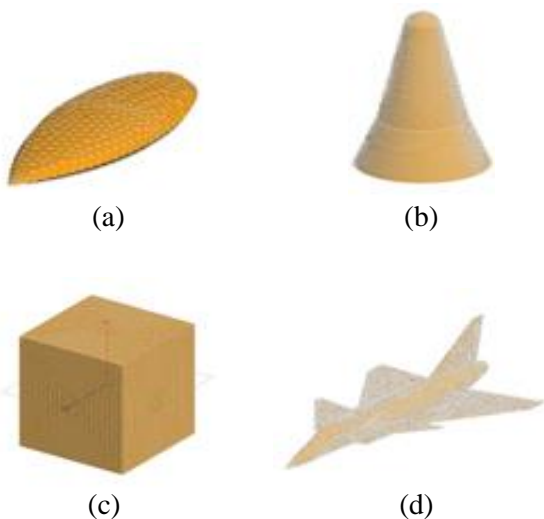


Fig. 1. Four geometries used in this paper: (a) NASA Almond, (b) Reentry Vehicle, (c) Cube, and (d) VFY-218.

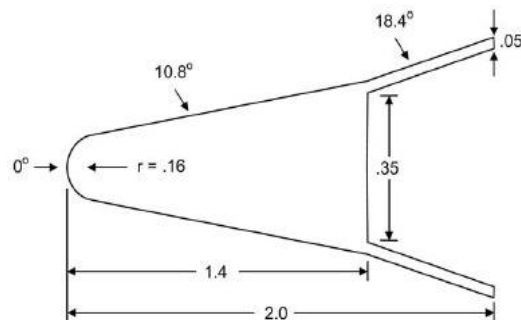


Fig. 2. Reentry vehicle model (unit: wavelength).

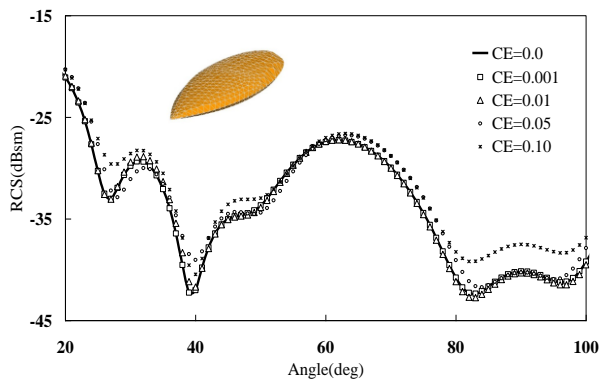


Fig. 3. Comparison of the results by proposed method with different CE.

Table 1: Computation time of monostatic RCS with different CE (time: second)

CE	0	0.001	0.01	0.05	0.1
Time	1386	338	232	152	78

As is shown in Figs. 4-6, the monostatic RCS curve of RV, Cube, and VFY-218 which computed by the proposed method is compared with the curve computed by the reference result repeatedly. “Reference” refers to the results computed by the MLFMA without interpolation, while “proposed method” denotes results computed by proposed method in section III. The CE is set to be 0.01 and the SVD is used to compress the multiple vectors generated by the best uniform approximation. It is obvious that the results matched very well. Consequently, the proposed method is accurate since there is no significant difference between the RCS result obtained by the reference result and the proposed

method. As is shown in Table 2, when compared with the reference results, the proposed method provides great advantage on total computation time since the number of right hand side is small. For reference results, the total computation time is 351497s, 53497s and 594576s, respectively, and the number of linear equation solutions is 721 since the space for angle sweep is 0.25 degree. It is time consuming for repeated solution of linear systems. In order to demonstrate the efficiency, it is applied for comparison. When SVD compression is used, the multiple vectors for these three geometries can be compressed. Consequently, the CPU time is reduced to 12004s, 1672s and 95838s. By using the proposed method, it saved time much than 29 times for RV, 31 times for Cube and 6 times for VFY-218, which is mentioned before while contrasting with the direct method. For different geometries, the saving time is different due to their complexity of the structures and the frequency.

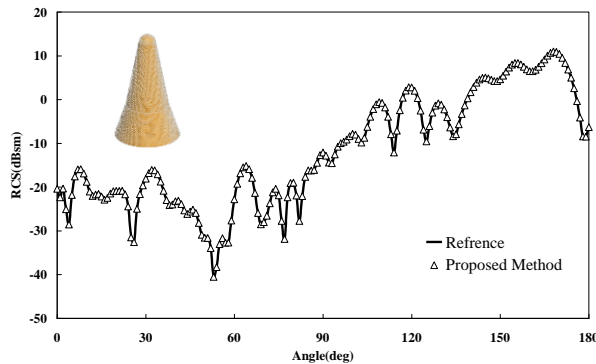


Fig. 4. The monostatic RCS results for RV.

Table 2: Computation time of monostatic RCS with different methods

Geometry	Unknown	f	$\theta$ (deg)	$\varphi$ (deg)	Computation Time (s)	
					Repeated Solution	Proposed Method
RV	26566	1.0 GHz	0~180	0	351497	12005
Cube	49260	300 MHz	0~180	0	53498	1672
VFY-218	40725	300 MHz	0~180	0	594577	95838

## V. CONCLUSIONS

In this paper, combining singular value decomposition with the best uniform approximation has been proposed for efficient analysis of monostatic scattering. Unlike interpolation of the electric current, the best uniform approximation algorithm is used to approximate the multiple right hand sides on a set of non-uniform sampling angles and SVD is

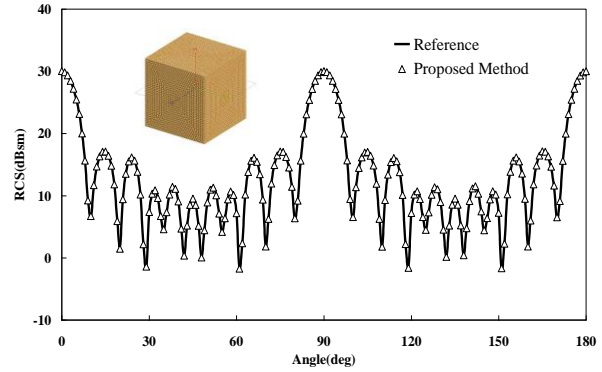


Fig. 5. The monostatic RCS results for Cube.

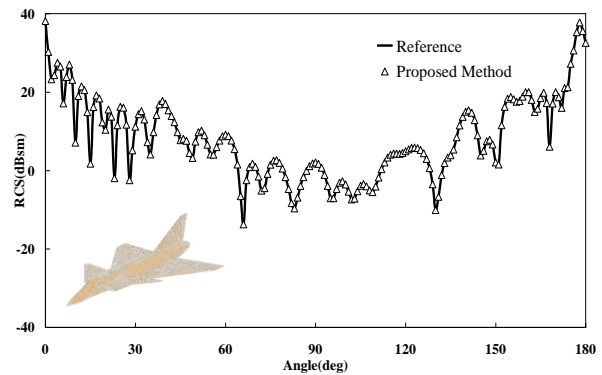


Fig. 6. The monostatic RCS results for VFY-218.

From Table 2, it is concluded that when compared with traditional method, the solution times for the linear system are reduced greatly and total computation time can be reduced significantly with this proposed method. As a result, our proposed method can be considered as an accurate and efficient method.

employed to reduce the consumption time automatically. The most informative angles may be selected by this procedure. Moreover, applying SVD to compute the eigenvectors of the selected vectors leads to reduced times for the iterative solutions of linear systems. Numerical experiments demonstrate that the proposed method is more efficient when compared with the traditional direct method.

## ACKNOWLEDGEMENTS

The authors would like to thank the support of National Science Foundation of China (No: 61261005, 61061002); Open Project of State Key Laboratory of Millimeter Wave (No: K201326).

## REFERENCES

- [1] R. F. Harrington, "Field computation by moment methods," *Malabar, Fla.: R. E. Krieger*, 1968.
- [2] W. C. Chew, J. M. Jin, E. Michielssen, and J. M. Song, "Fast and efficient algorithms in computational electromagnetics," *Boston, MA: Artech House*, 2001.
- [3] J. M. Song, C. C. Lu, and W. C. Chew, "Multilevel fast multipole algorithm for electromagnetic scattering by large complex objects," *IEEE Trans. Antennas Propagation*, vol. 45, no. 10, pp. 1488-1493, October 1997.
- [4] R. S. Chen, E. K. N. Yung, C. H. Chan, and D. G. Fang, "Application of SSOR preconditioned conjugate gradient algorithm to edge FEM for 3-dimensional full wave electromagnetic boundary value problems," *IEEE Trans. Microwave Theory Technology*, vol. 50, pp. 1165-1172, 2002.
- [5] R. S. Chen, X. W. Ping, and E. K. N. Yung, "Application of diagonally perturbed incomplete factorization preconditioned CG algorithms for edge FEM analysis of helmholtz equations," *IEEE Trans. Antennas Propag.*, vol. 54, pp. 1064-1068, 2006.
- [6] J. Lee, J. Zhang, and C. C. Lu, "Sparse inverse preconditioning of multilevel fast multipole algorithm for hybrid integral equations in electromagnetics," *IEEE Trans. Antennas Propag.*, vol. 52, pp. 2277-2287, 2004.
- [7] P. L. Rui and R. S. Chen, "An efficient sparse approximate inverse preconditioning for FMM implementation," *Microwave Optical Technology Letter*, vol. 49, pp. 1746-1750, 2007.
- [8] P. L. Rui, R. S. Chen, D. X. Wang, and E. K. N. Yung, "Spectral two-step preconditioning of multilevel fast multipole algorithm for the fast monostatic RCS calculation," *IEEE Trans. Antennas Propagation*, vol. 55, pp. 2571-2577, 2007.
- [9] E. K. Miller and G. J. Burke, "Using model-based parameter estimation to increase the physical interpretability and numerical efficiency of computational electromagnetics," *Computer Physics Communications*, vol. 68, pp. 43-75, 1991.
- [10] E. K. Miller, "Model-based parameter estimation in electromagnetics-part I: background and theoretical development," *IEEE Antennas Propag. Mag.*, vol. 40, no. 1, pp. 42-52, February 1998.
- [11] Z. W. Liu, R. S. Chen, and J. Q. Chen, "Adaptive sampling cubic-spline interpolation method for efficient calculation of monostatic RCS," *Microwave Optical Technology Letter*, vol. 50, no. 3, pp. 751-755, 2008.
- [12] Z. W. Liu, D. Z. Ding, Z. H. Fan, and R. S. Chen, "Adaptive sampling bicubic spline interpolation method for fast computation of monostatic RCS," *Microwave Optical Technology Letter*, vol. 50, no. 7, pp. 1851-1857, 2008.
- [13] C. Tian, Y. J. Xie, Y. Y. Wang, and Y. H. Jiang, "Fast solutions of wide-band RCS pattern of objects using MLFMA with the best uniform approximation," *Journal of Electronics & Information Technology*, vol. 31, no. 11, pp. 2772-2775, November 2009.
- [14] Z. Peng, M. B. Stephanson, and J. F. Lee, "Fast computation of angular responses of large-scale three-dimensional electromagnetic wave scattering," *IEEE Trans. Antennas Propagation*, vol. 58, no. 9, pp. 3004-3012, September 2010.
- [15] S. M. Rao, D. R. Wilton, and A. W. Glisson, "Electromagnetic scattering by surfaces of arbitrary shape," *IEEE Trans. Antennas Propagation*, vol. 30, no. 3, pp. 409-418, 1982.
- [16] G. K. Carvajal, D. J. Duque, and A. J. Zozaya, "RCS estimation of 3D metallic targets using the moment method and rao-wilton-glisson basis functions," *Applied Computational Electromagnetic Society Journal*, vol. 24, no. 5, pp. 487-492, October 2009.
- [17] J. Shaeffer, "Direct solve of electrically large integral equations for problem sizes to 1 M unknowns," *IEEE Trans. Antennas Propagation*, vol. 56, no. 8, pp. 2306-2313, August 2008.
- [18] C. Rorres and H. Anton, "Application of linear algebra." *New York: John Wiley and Sons*, 1984.
- [19] Y. Saad and M. Schultz, "GMRES: a generalized minimal residual algorithm for solving nonsymmetric linear systems," *SIAM J. Sci. Stat. Comput.*, vol. 7, no. 3, pp. 856-869, 1986.
- [20] V. Simoncini and D. B. Szyld, "Flexible inner-outer krylov subspace methods," *SIAM J. Numer. Anal.*, vol. 40, no. 6, pp. 2219-2239, 2003.
- [21] W. C. Gibson, "The method of moments in electromagnetics," *Boca Raton: Chapman & Hall/CRC*, 2008.
- [22] X. Y. Zhang and X. Q. Sheng, "Fast RCS computation in both spatial and frequency domains using adaptive MBPE technique," *ICMTCE*, 2009.
- [23] A. C. Woo, H. T. G. Wang, M. J. Schuh, and M. L. Sanders, "EM programmer's notebook-benchmark radar targets for the validation of computational electromagnetics programs," *IEEE Antennas and Propagation Magazine*, vol. 35, no. 1, pp. 84-89, February 1993.



**Zhiwei Liu** was born in Nanchang, Jiangxi, China in 1982. He received his B.S. degree in Computer Science from Nanjing University of Science and Technology in 2003, his M.S. degree from Nanjing Institute of Electronics and Technology in 2006, and his Ph.D. degree from Nanjing University of Science and Technology in 2011, respectively. He was with the Department of Electrical and Computer Engineering, Iowa State University, as a Visiting Scholar in 2009. He is currently working at the School of Information Engineering, East China Jiaotong University. His research interests focus on the theory of electromagnetic scattering and inverse scattering.



**Shan He** was born in Anqing, Anhui, China in 1989. She received her B.S. degree with the Institute of Electrical and Information from Anhui University of Technology in 2011. She is currently working towards her M.S. degree at the School of Information Engineering, East China Jiaotong University. Her research interests focus on the theory of electromagnetic scattering and inverse scattering.

# Fabrication of a Novel Diplexer Using Folded Open-Loop Ring Resonators and Microstrip Lines

Chia-Mao Chen <sup>1</sup>, Shoou-Jinn Chang <sup>2</sup>, and Cheng-Fu Yang <sup>3\*</sup>

<sup>1</sup>Department of Electrical Engineering  
National Cheng Kung University, Tainan 70101, Taiwan, R.O.C.  
jmchen0813@gmail.com

<sup>2</sup>Institute of Microelectronics and the Department of Electrical Engineering  
Advanced Optoelectronic Technology Center, Center for Micro/Nano Science and Technology  
National Cheng Kung University, Tainan 70101, Taiwan, R.O.C.  
changsj@mail.ncku.edu.tw

<sup>3\*</sup>Department of Chemical and Materials Engineering  
National University of Kaohsiung, Kaohsiung 811, Taiwan, R.O.C.  
cfyang@nuk.edu.tw

**Abstract** — A simple and novel low-loss diplexer with two folded Open-Loop Ring Resonators (OLRRs) that couple three microstrip lines is proposed. The first passband and second passband of the designed diplexer could be easily and accurately shifted to a desired frequency and construct the bandpass filters by adjusting the physical dimensions of the OLRRs. These results suggested that the proposed diplexer had the frequency-adjustable characteristics. The longer OLRR is placed between the upper and middle microstrip lines to generate a 2.4 GHz resonant frequency and the shorter OLRR is placed between the middle and lower microstrip lines to generate a 5.2 GHz resonant frequency. By adjusting the positions of the two OLRRs, the resonant frequencies can be tuned.

**Index Terms** — Diplexer, microstrip lines, microwave components, Open-Loop Ring Resonator (OLRR), standing wave.

## I. INTRODUCTION

Modern wireless communication systems require radio-frequency devices operating in multiple frequency bands. Planar diplexer with compact circuit size, low insertion loss, high isolation, and flexible passband frequencies is an

important component in the multi-band and multi-service wireless communication systems. Low-cost microstrip diplexers can be easily mounted on a dielectric substrate and allow for flexible circuit layout design [1]. Many studies have attempted to reduce the size and improve the performance of microstrip diplexers [2-10].

To reduce size, many complex resonators, such as stepped-impedance open-loop resonators [2], miniaturized open-loop resonators [3], square open-loop with stepped-impedance resonators [4], stepped-impedance coupled-line resonators [5], H-type resonators [6], and artificial transmission lines [7] have been utilized in diplexer design. In [8], a compact diplexer based on double-sided parallel microstrip lines was developed, but it requires a multilayer structure. In [9], a microstrip electromagnetic band gap structure was used to obtain a wide stopband of the diplexer, but the selectivity was poor. In [10], the diplexer with resistor-loaded resonator can suppress harmonics near the two passbands. The performance of microstrip diplexers is also important. However, the above diplexers have one or more performance problems, such as low selectivity, low isolation, large harmonic suppression, and fixed frequency ratio range of the two passbands. In addition, their circuits have problems such as high complexity,

sensitivity to the dimensions of designed patterns, and difficulty of duplication.

A folded coupled-line structure and dual-mode stripline ring resonators have been utilized to produce transmission zeros to improve the selectivity of diplexers [11,12]. If the unloaded quality factor of harmonics can be greatly reduced, the harmonics can be well suppressed. For diplexers with a wide stopband, it is easy to control the frequency ratio of the two passbands of the diplexer, because the harmonic of the lower passband is far from that of the higher passband, and thus, adjusting one does not affect the other. OLRRs have been applied to planar bandpass and bandstop filter design [13,14].

In the present study, a novel and simple low-loss diplexer with two folded Open-Loop Ring Resonators (OLRRs) with different physical dimensions that couple three microstrip lines, shown in Fig. 1, is proposed. Each OLRR is placed between two microstrip lines and has a perimeter of about a half wavelength of the designed resonant frequency. Each of the fold OLRRs has its maximum electric field density near the open ends of the line and has its maximum magnetic field density around the center valley of the line at resonance. The resonant frequencies can be adjusted via the length of the OLRRs to provide a high-performance passband response. The proposed diplexer has low insertion loss, a wide tunable range of either passband, transmission zeros, simple design, and no external impedance-matching block. A high-performance diplexer with dual-band frequencies of 2.4/5.2 GHz for WLAN band system is designed here to demonstrate the proposed structure.

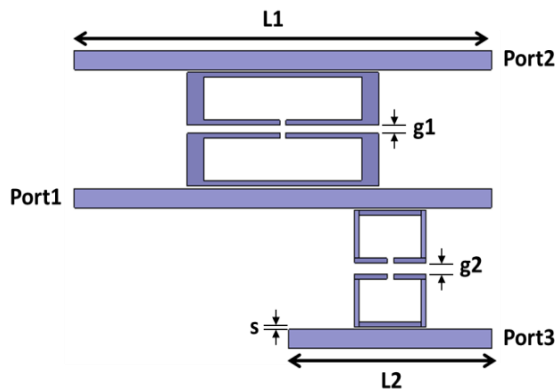


Fig. 1. Proposed diplexer based on OLRRs.

## II. DESIGN METHODOLOGY

The diplexer with dual-band frequencies of 2.4/5.2 GHz for WLAN band system is designed here to demonstrate the proposed structure. In the past, the diplexer using OLRRs was accompanied by using the discriminating coupling technique [15-17]. Each of the open-loop ring resonators is essentially a folded half-wavelength resonator. Those coupled structures result from different orientations of a pair of open-loop resonators, which are separated by a spacing  $S_{OLRR}$ . It is obvious that any coupling in those structures is in close proximity coupling, which is, basically, through fringe fields.

The nature and the extent of the fringe fields determine the nature and the strength of the coupling. It can be shown that at resonance of the fundamental mode, each of the open-loop ring resonators has the maximum electric field density at the side with an open gap ( $g_{OLRR}$ ) and the maximum magnetic field density at the opposite side. Because the fringe field exhibits an exponentially decaying character outside the region, the electric fringe field is stronger near the side having the maximum electric field distribution, whereas, the magnetic fringe field is stronger near the side having the maximum magnetic field distribution. It follows that the electric coupling can be obtained if the open sides of two coupled resonators are proximately placed, as shown in Fig. 2.

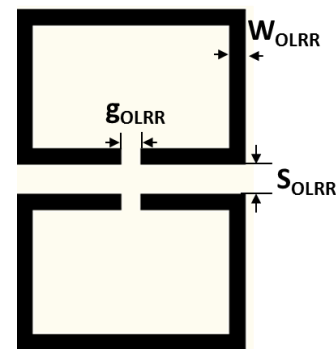


Fig. 2. Folded open-loop ring resonators.

To obtain the maximum magnetic coupling, the center valley of the OLRRs must be positioned in the proper location along the microstrip line with the maximum magnetic field intensity, which can be determined by studying wave motions on a

microstrip line. For the Transverse Electromagnetic (TEM) field structure, it is assumed that both the electric and magnetic field vectors lie in the transverse plane perpendicular to the uniform propagation axis. Under the assumptions of the TEM mode of propagation and a lossless line, the fields are uniquely related to voltage and current, respectively. Based on transmission line theory, the magnitude of the voltage and current on the microstrip line can be expressed in terms of the incident wave and the reflection coefficient:

$$|V(z)| = |V_0^+| |1 + \Gamma| e^{j(\theta - 2\beta l)}, \quad (1)$$

$$|I(z)| = \frac{|V_0^+|}{Z_0} |1 - \Gamma| e^{j(\theta - 2\beta l)}, \quad (2)$$

where  $l = -z$  is measured away from the load at  $z=0$ , and  $\theta$  is the phase of the reflection coefficient. When  $\theta - 2\beta l$  has a magnitude of zero or any multiple of  $2\pi$  radians, the quantities in (1) and (2) are at their maximum and minimum magnitudes, respectively. For the case of an open-circuited line, (1) and (2) respectively become:

$$|V(z)| = |V_0^+| |1 + e^{j(\theta - 2\beta l)}|, \quad (3)$$

$$|I(z)| = \frac{|V_0^+|}{Z_0} |1 - e^{j(\theta - 2\beta l)}|. \quad (4)$$

At a distance of a quarter wavelength from the receiving end, the voltage becomes zero while the current is maximal. If the line is half a wavelength long, the current distribution near the center of the transmission line is maximal. High magnetic coupling results from a high conduction current. Once the points of  $I_{max}$  are found, the points of  $H_{max}$  can be easily determined. Figure 3 shows a uniform section of a transmission line of length  $L1/L2$ , where  $L1/L2$  is about  $0.5\lambda$  under operation frequencies of 2.4/5.2 GHz. Similarity, with an operation frequency of 5.2 GHz applied to  $L1$ ,  $I_{max}$  or  $H_{max}$  occurs at distances of  $0.135\lambda$  and  $0.385\lambda$  from the receiving end. These results suggest that the resonant frequencies of the designed diplexer can be adjusted by changing the layout dimension of the OLRRs.

To demonstrate the proposed structure, two bandpass filters are designed using OLRRs. To excite two passbands, two different pairs of guided half-wavelength OLRRs must be located between two transmission lines terminated at the open end. Each OLRR provides a path coupled signal energy

from one microstrip to another at around resonance. At above and below resonance, most of the signal energy is reflected back and standing waves are said to exist on the line. The diplexer was simulated using the HFSS simulator with loss factors (conductor loss and dielectric loss) included in the simulated response. The coupling paths shown in Fig. 4 were generally chosen specifically for each resonant frequency.

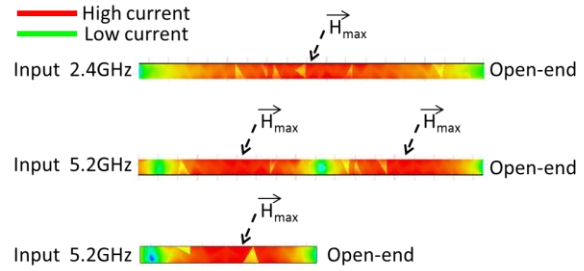


Fig. 3. Current distribution in microstrip line with an open end.

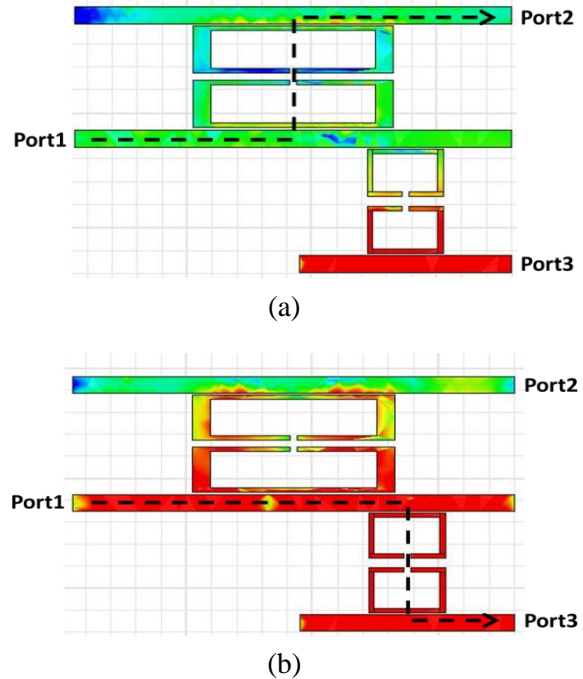


Fig. 4. Simulations of current distribution and coupling paths oscillating at: (a) 2.4 GHz, and (b) 5.2 GHz.

### III. DESIGN OF DIPLEXER

The simulated frequency responses of 2.4-GHz and 5.2-GHz single-band filters are shown in

Fig. 5 with layout patterns shown in the inset. Each of the designed bandpass filters is based on a pair of half-wavelength OLRRs. Electric coupling can be obtained if the open sides of the two coupled resonators are placed near each other, and magnetic coupling can be obtained if the sides with the maximum magnetic field of two coupled resonators are placed near each other. The coupling spacing  $s$  between the main line and OLRRs is 0.2 mm and the spacing  $g1/g2$  between two resonators is 0.61/0.81 mm. The simulation results of 2.4-GHz and 5.2-GHz filters are shown in Fig. 4. The center frequency of the designed filter can be accurately controlled to a desired frequency band once the right position is chosen. The simulation results of the designed diplexer show an adjustable frequency, good selectivity, high isolation, and a wide passband.

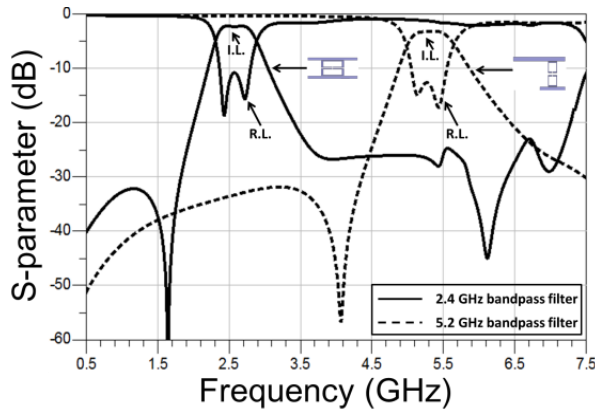


Fig. 5. Amplitude response of bandpass filters with center frequencies of 2.4 and 5.2 GHz.

The diplexer using OLRRs was fabricated on an FR4 substrate with a relative permittivity of 4.4 and a thickness between the two electrodes was 1.2 mm. The electrode's material was Cu foil with a thickness of 35  $\mu\text{m}$ . The dimensions for the proposed diplexer are about 35x23.16 mm, as shown in Fig. 6 (a). A photograph of the designed 2.4/5.2-GHz diplexer is shown in Fig. 6 (b). Measurements were carried out using an Agilent N5071C network analyzer. The measured S-parameters of the fabricated diplexer are compared to the simulation results in Fig. 7. The measured responses show a reasonably good agreement with the simulated responses. The isolation between the two channels is larger than 25 dB. The lower and higher bands are located at 2.65 and 5.4 GHz with

respective insertion losses of 1.94 and 2.55 dB, respectively. The measured return losses at lower and higher bands are less than -15 dB. Table 1 shows the comparisons of the superiority of the insertion loss (I.L.), circuit size, and bandwidth between the proposed diplexer and other literatures. As the table shows, the proposed diplexer had wider bandwidth and acceptable insertion loss, circuit size, and isolation.

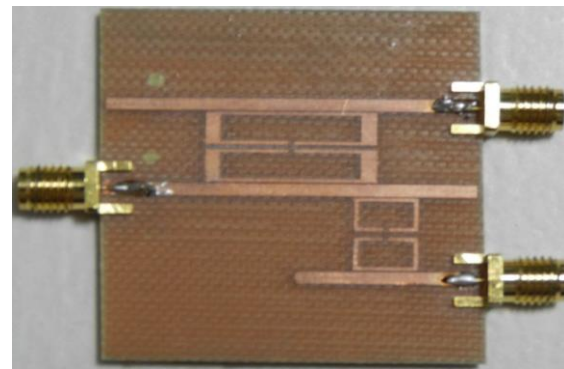
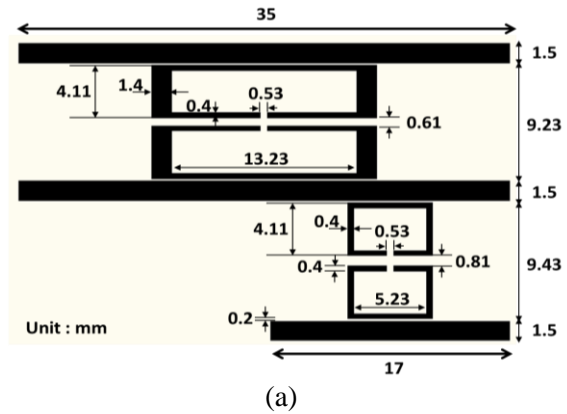


Fig. 6. (a) Layout pattern, and (b) photograph of designed 2.4/5.2-GHz diplexer.

Table 1: Results comparison between the proposed diplexer and the references [18,19]

	This work	Ref. 18	Ref. 19
Circuit Size (mm <sup>2</sup> )	35x23.16	44x11	26x56
Passbands (GHz)	2.65/5.4	1.98/2.23	1.5/2/2.4/3.5
I.L. (dB)	1.94/2.55	1.8/3.01	0.8/1/0.7/1.5
FBW (%)	12.5/5.9	6.3/4.3	8/4/6/2
Isolation (dB)	>25	>40	>3

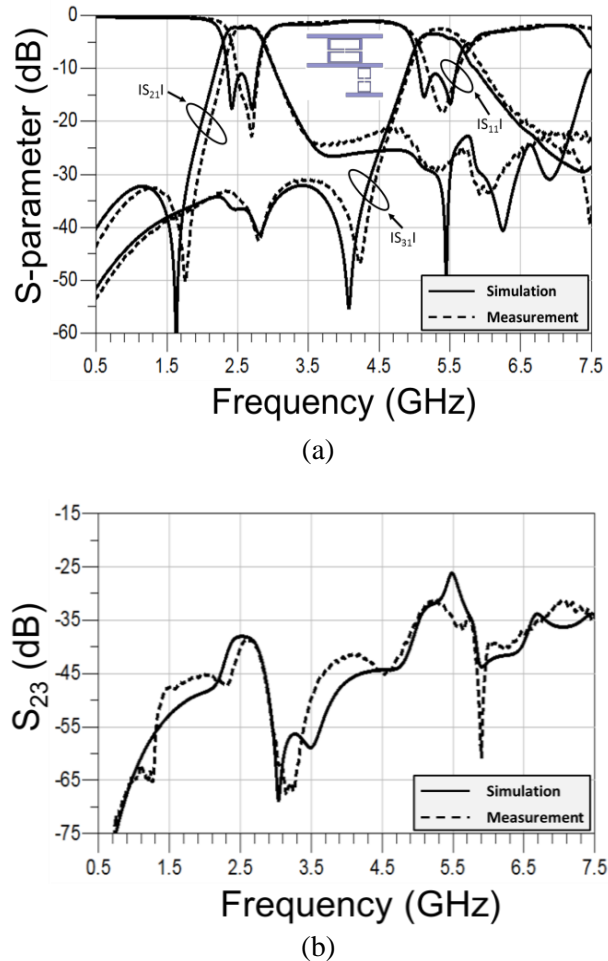


Fig. 7. (a) Measured and simulated S-parameters ( $S_{21}$ ,  $S_{11}$ , and  $S_{31}$ ), and (b) isolation ( $S_{23}$ ) of diplexer. Diagram of the fabricated diplexer is shown in the inset.

#### IV. CONCLUSION

A simple and effective method based on standing waves and coupling for designing a microstrip diplexer was proposed. The electric and magnetic couplings between microstrip lines and two folded OLRs are simultaneously provided to produce high-performance band-pass filters. By adjusting the physical dimensions of the OLRs, the center frequencies of the diplexer can be tuned separately over a wide range. A 2.4/5.2-GHz diplexer was fabricated and measured to demonstrate the proposed structure. The rejection between the two passbands was lower than 25 dB and the insertion loss for each band was lower than 3 dB. The measurement results are in good agreement with the simulation results.

#### ACKNOWLEDGMENT

The authors acknowledge financial supports of NSC 101-2221-E-005-065, NSC 102-2622-E-390-002-CC3, and NSC 102-2221-E-390-027.

#### REFERENCES

- [1] D. M. Pozar, "Microwave engineering," 2<sup>nd</sup> edition, ch. 8, Wiley, New York, 1998.
- [2] S. S. Oh and Y. S. Kim, "A compact duplexer for IMT-2000 handsets using microstrip slow-wave open-loop resonators with high-impedance meander lines," *Radio Wireless Conf.*, 177-180, August 2001.
- [3] E. Goron, J. P. Coupez, C. Person, Y. Toutain, H. Lattard, and F. Perrot, "Accessing to UMTS filtering specifications using new microstrip miniaturized loop-filters," *IEEE MTT-S Int. Microw. Symp. Dig.*, 1599-1602, June 2003.
- [4] J. Konpang, "A compact diplexer using square open loop with stepped impedance resonators," *Asia-Pacific Microwave Conference*, 1-4, 2008.
- [5] S. Srisathit, S. Patisang, R. Phromlounsri, S. Bunnjaveht, S. Kosulvit, and M. Chongcheawchamnan, "High isolation and compact size microstrip hairpin diplexer," *IEEE Microw. Wireless Compon. Lett.*, vol. 15, no. 2, 101-103, February 2005.
- [6] H. A. Cabral, S. T. G. Bezerra, and M. T. de Melo, "A diplexer for UMTS applications," *IEEE MTT-S International Microwave and Optoelectronics Conference*, 215-217, 2009.
- [7] K. H. Li, C. W. Wang, and C. F. Yang, "A miniaturized diplexer using planar artificial transmission lines for GSM/DCS applications," *Asia-Pacific Microwave Conference*, 1-4, 2007.
- [8] Q. Xue and J. X. Chen, "Compact diplexer based on double-sided parallel-strip line," *Electronics Letters*, vol. 44, no. 2, 123-124, January 2008.
- [9] X. W. Chen, W. M. Zhang, and C. H. Yao, "Design of microstrip diplexer with wide band-stop," *International Conference on Microwave and Millimeter Wave Technology*, 1-3, 2007.
- [10] Shi, J., J.-X. Chen, and Z.-H. Bao, "Diplexers based on microstrip line resonators with loaded elements," *Progress In Electromagnetics Research*, Vol. 115, 423-439, 2011.
- [11] C. M. Tsai, S. Y. Lee, C. C. Chuang, and C. C. Tsai, "A folded coupled-line structure and its application to filter and diplexer design," *IEEE MTT-S Int. Microw. Symp. Dig.*, 1927-1930, June 2002.
- [12] W. Q. Xu, M. H. Ho, and C. G. Hsu, "UMTS diplexer design using dual-mode stripline ring resonators," *Electronics Letters*, vol. 43, no. 13, 721-722, June 2007.

- [13] C. Y. Chen and C. Y. Hsu, "A simple and effective method for microstrip dual-band filters design," *IEEE Microw. Wireless Compon. Lett.*, vol. 16, no. 5, pp. 246-248, May 2006.
- [14] J. S. Hong and M. J. Lancaster, "Couplings of microstrip square open-loop resonators for cross-coupled planar microwave filters," *IEEE Trans. Microw. Theory Tech.*, vol. 44, no. 12, pp. 2099-2108, December 1996.
- [15] J. S. Hong, "Microstrip filters for RF/microwave applications," 2<sup>nd</sup> edition, Wiley, New York, 2011.
- [16] X. Y. Zhang and Q. Xue, "Harmonic-suppressed bandpass filter based on discriminating coupling," *IEEE Microw. Wireless Compon. Lett.*, vol. 19, no. 11, pp. 695-697, November 2009.
- [17] Y. C. Li, X. Y. Zhang, and Q. Xue, "Bandpass filter using discriminating coupling for extended out-of-band suppression," *IEEE Microw. Wireless Compon. Lett.*, vol. 20, no. 7, pp. 369-371, July 2010.
- [18] V. K. Velidi, U. Prabhakaran, A. V. G. Subramanyam, D. Sivareddy, and V. V. Srinivasan, "Design of compact microstrip diplexer with high selectivity," *International Conference on Signal Processing and Communications (SPCOM)*, 10.1109/SPCOM.2012.6290012, 2012.
- [19] H. W. Wu, S. H. Huang, and Y. F. Chen, "Design of new quad-channel diplexer with compact circuit size," *IEEE Microw. Wireless Compon. Lett.*, vol. 23, no. 5, pp. 240-242, May 2013.



**Chia-Mao Chen** was born in Kaohsiung, Taiwan, on August 13, 1979. He received his B.S. degree from Kao Yuan University, Luzhu, Taiwan, in 2002, his M.S. degree from National Kaohsiung University of Applied Science (KUAS), Kaohsiung, Taiwan, in 2004, and is currently working towards his Ph.D. degree at National Cheng Kung University (NCKU), Tainan, Taiwan. His current research interests include design of antennas and microwave circuits.



**Shoou-Jinn Chang (M'06-SM'10)** was born in Taipei, Taiwan, on January 17, 1961. He received his B.S. degree from National Cheng Kung University (NCKU), Tainan, Taiwan, in 1983, his M.S. degree from the State University of New York, Stony Brook, NY, USA, in 1985, and his Ph.D. degree from the University of California, Los Angeles, USA, in 1989; all in Electrical Engineering. From 1989 to 1992, he was a Research Scientist with Nippon Telegraph and Telephone Basic Research Laboratories, Musashino, Tokyo, Japan. He joined the Department of Electrical Engineering, NCKU, in 1992 as an Associate Professor, where he was promoted to Full Professor in 1998. He is currently the Deputy Director of the Advanced Optoelectronic Technology Center, NCKU. From August to September 2001, he was a Visiting Scholar with the Institute of Microstructural Science, National Research Council, Canada; from August to September 2002, he was a Visiting Scholar with the Institute of Physics, Stuttgart University, Stuttgart, Germany; and from July to September 2005, he was a Visiting Scholar

with the Faculty of Engineering, Waseda University, Tokyo. He is also an Honorary Professor with the Changchun University of Science and Technology, China. His current research interests include semiconductor physics, optoelectronic devices, and nanotechnology. Chang received the Outstanding Research Award from the National Science Council, Taiwan, in 2004. He is a Fellow of the Optical Society of America and the International Society for Optical Engineers.



**Cheng-Fu Yang** was born in Taiwan on July 12, 1964. After graduating in the "Department of Electrical Engineering" from Cheng Kung University in 1986, Yang also gained his Master and Ph.D. degrees in 1988 and 1993 from the "Department of Electrical Engineering" of Cheng Kung University. After he obtained the Ph.D. degree, Yang entered academic life in 1993, first with the "Department of Electronic Engineering, Chinese Air Force Academy," and since February 2000 as a Professor at the Chinese Air Force Academy, Taiwan. In February 2004 he joined the Faculty of the National University of Kaohsiung (NUK). Currently, he is a Professor of Chemical and Materials Engineering at NUK. His current research interests are focused on fine ceramics, microwave ceramics, dielectric thin films, optical materials, transparent conducting oxides, solar cell materials, microwave antennas, and microstrip filters. So far, he has published over 250 SCI and EI international journal papers and also has published over 250 domestic and international conference papers.

# High Gain Dielectric Loaded Exponentially Tapered Slot Antenna Based on Substrate Integrated Waveguide for V-Band Wireless Communications

S. Ramesh and T. Rama Rao

RADMIC, Department of Telecommunication Engineering  
SRM University, Chennai 603203, India  
rameshsvk@gmail.com, ramaraotr@gmail.com

**Abstract** — The conception of Substrate Integrated Waveguide (SIW) technology and Exponentially Tapered Slot (ETS) antenna are together used to design a high gain, and efficient planar dielectric loaded antenna for V-band wireless communications. To increase the gain of the antenna, a dielectric loaded portion is used in front of the antenna which works as a dielectric guiding structure and SIW is used to feed the proposed antenna. The dielectric loaded ETS antenna and compact SIW feed are fabricated on a single substrate, resulting in low cost and easy fabrication. The antenna with elliptical shaped dielectric loaded is fabricated using printed circuit board process. The measured gain of the single element antenna is 10.2 dB, while the radiation efficiency of 96.84% is obtained at 60 GHz. The Y-junction SIW power divider is used to form a 1×2 array structure. Measured gain of the 1×2 array antenna is 11.2 dB, while the measured radiation pattern and gain are almost constant within the wide bandwidth of the antenna.

**Index Terms** — 60 GHz, antenna, ETS dielectric loading, millimeter waves, SIW.

## I. INTRODUCTION

Millimeter (Mm) wave technology, system, and applications have been one of the newest topical discussions in academic laboratories, technical sessions, and commercial boardrooms since the early time [1,2]. Strong and growing interest in this specific electromagnetic spectrum is being fueled by a popular recognition that this frequency range allows effectively bridging the

gap of well apparent technology between electronics and wireless communication. We will focus specifically on 60 GHz antenna, which has emerged as one of the most encouraging contenders for multi gigabit wireless communication systems. The 60 GHz technology offers various recompenses over present wireless communication systems. One of the deciding aspects that mark 60 GHz technology gaining significant interest recently is due to the huge unrestricted bandwidth (up to 7 GHz) available worldwide [3]. This huge bandwidth represents great potentials in terms of capacity and flexibility that makes 60 GHz technology mainly attractive for gigabit wireless applications.

Antennas with excellent design can improve the performance of communication. Many types of antenna structures are considered not suitable for 60 GHz WLAN/WPAN applications due to the requirements for low cost, small size, and light weight [4]. In addition, 60 GHz antennas also require to be operated with constant gain and high efficiency over the broad frequency range. Recently, the technology of planar integrated antenna [5] has been developed for Mm wave applications due to the trend of the integration in radio frequency front-end circuits and systems. As the operating frequency of wireless systems move into Mm wave range in order to provide gigabits per second service, there is an increasing demand of high gain antennas used for consumer devices. The desired antenna has to be compatible with integrated circuits, and possess high gain and small side lobe. When integrated into consumer devices, should also have the benefits of small size

and low production cost [6].

The concept of SIW technology makes it possible to realize the waveguide in a substrate and provides a sophisticated way to integrate the waveguide with microwave and millimeter wave planar circuits using the conventional low-cost printed circuit technology. In particular, a number of SIW based slot antennas have been reported in recent years. These antennas consist of single layer of dielectric substrate and are fed from one end through a coplanar feed network which significantly increases the size of the antenna. Furthermore, radiation from microstrip feed lines and junctions severely negotiate the low side-lobe level of the slot antenna and increases cross-polarization [7-10].

Therefore, this work targets on addressing challenges in designing dielectric loaded ETS antenna using SIW technology for the realization of V-band wireless communications, particularly at 60 GHz utilizing 3D electromagnetic software CST Microwave Studio, and comparison with Ansys HFSS validates the design procedure. The work in this paper is organized as follows; Section II deals with step by step design procedure for the ETS antenna, simulation, measurement results and discussions. Section III deals with ETS array antenna simulation and measurement results obtained in our present work and discussions. Finally, Section IV gives conclusions.

## II. DIELECTRIC LOADED EXPONENTIALLY TAPERED SLOT ANTENNA DESIGN

The ETS antenna is also known as flared notch or Vivaldi antenna, is among one of the most promising antenna satisfying all requirements described in the technical challenges [11]. It is fundamentally a planar traveling wave antenna with end fire radiation. The flared notch antenna comprising a plurality of flared disposed immediately adjacent each other, each having a direction of maximum gain which is directed in a different direction. The ETS antenna containing a two flares in the same plane providing the gain in specific direction with wider main lobe. This antenna is the preferred candidate for Mm Wave applications due to its wide bandwidth, low cross-polarization and highly directive patterns. A major advantage of this antenna type is that the wide bandwidth and maximum gain can be achieved

using exponentially tapered profiles with dielectric loading [12]. The proposed dielectric scheme provides an interesting alternative. This antenna is integrated by using a single substrate. It is easy to fabricate and the structure is compact [13]. To eliminate the higher order modes in the waveguide, the thickness of the substrate is restricted. The loaded dielectric slab in front of the antenna can be considered as a dielectric guiding structure excited by the exponential flare resulting in a wider beamwidth and maximum gain. The compact Mm wave antenna with dielectric loading can achieve a broadband performance and offer several advantages over other counterparts such as relatively low insertion loss, better VSWR, good design tolerance and circuit size compactness [14,15].

### A. Replacing waveguides with equivalent SIW

The conventional waveguide technology still plays an important role in Mm wave circuits and systems, which takes the advantages of low loss, high Q-factor and high power handling capability. But its bulky structure makes it difficult to fabricate it at low cost and integrate it into planar structure. So the SIW technology makes it possible to realize the waveguide in a substrate and provides a sophisticated way to integrate the waveguide with Mm wave planar circuits using the conventional low cost printed circuit technology [16-19]. Here, the dielectric filled waveguide is transformed to SIW by the support of vias for the side walls of the waveguide. In the SIW design, the following conditions are required. The metalized via hole diameter is:

$$d < \lambda_g / 2. \quad (1)$$

The spacing between the via holes is:

$$P < 2d. \quad (2)$$

The physical width of SIW is:

$$a = a_d + (d^2 / (0.95p)). \quad (3)$$

The calculated values of the physical width of SIW is 2.0 mm, metalized via hole diameter is 0.30 mm, and space between via holes is 1.0 mm.

### B. Microstrip to SIW transition

The microstrip line is used to transfer the power to antenna. This transmission line is connected to the feed waveguide in the bottom layer. The transition between microstrip line and SIW is critical for achieving good impedance

matching and small return loss. A tapered transition was suggested, which is useful in most applications [20].

In order to make a good transition from the microstrip to the SIW, first of all, it is necessary to calculate the guide impedance of the SIW which is given by:

$$Z_g = Z_{TE}(\pi^2 b / 8a). \quad (4)$$

For the calculation of the guide impedance, it is also necessary to calculate the wave impedance of TE mode which is given by:

$$Z_{TE} = j\omega\mu / \gamma = \sqrt{\mu / \xi} \times (\lambda_g / \lambda). \quad (5)$$

In our transition, the width of 50 Ω microstrip line is like to the width of SIW physical width to achieve impedance matching with low insertion loss and nullify the higher order modes. The width of the 50 Ω microstrip line is 2 mm, is calculated from above equations.

### C. Design of the antenna

The ETS antenna radiating tapered profile is described by an exponential function. The antenna is excited via the microstrip line to SIW transition. The transition construction exploits wideband features of a microstrip radial stub used as a virtual wideband short. The microstrip is virtually shunted to the second half of the strip line metallization, while the first half serves as a ground metallization for the microstrip line. It is necessary to transform the impedance of the input feeding microstrip line to the input impedance of the transition. Therefore, the linear microstrip taper is used as the input impedance transformer [21]. Instead of using the wideband balun, a SIW has been employed to feed an ETS antenna.

Antenna tapers is defined as exponential curves in the x-y plane. To comply with the antenna board dimensions and slot line parameters, the following exponential taper curve definition equation is used [22,23]:

$$y = C_1 e^{ax} + C_2, \quad (6)$$

where ‘a’ is the rate of opening the exponential taper, and C<sub>1</sub> and C<sub>2</sub> can be calculated by the starting and ending points of the taper P1(x<sub>1</sub>, y<sub>1</sub>) and P2(x<sub>2</sub>, y<sub>2</sub>):

$$C_1 = (y_2 - y_1) / (e^{ax_2} - e^{ax_1}), \quad (7)$$

$$C_2 = (y_1 e^{ax_2} - y_2 e^{ax_1}) / (e^{ax_2} - e^{ax_1}). \quad (8)$$

The antenna length L<sub>A</sub>, aperture width W<sub>A</sub>, and substrate thickness t, all directly affect the radiation performance of the ETSA. The flare angle is distinctive to linear tapered designs and determines the antenna’s input impedance. The directivity increases as the length L<sub>A</sub> of an antenna is increased. For lengths between three and eight wavelengths, the increase is linear according to below equation:

$$D = 10L_A / \lambda_o. \quad (9)$$

The performance of antenna depends upon the thickness t and the dielectric permittivity ξ<sub>r</sub> [24] as given in (10):

$$f_{substrate} = \frac{t(\sqrt{\xi_r} - 1)}{\lambda}. \quad (10)$$

For enhanced performance it should lie within a range given by:

$$0.005 \leq f_{substrate} \leq 0.03. \quad (11)$$

The EM surface wave in the antenna substrate is attached to the metal tapers in the antenna. Primarily, when for most taper profiles the separation is moderately small, the EM wave is closely bound to the tapers. As the taper separation increases, the EM wave becomes progressively less attached to the metal tapers. This continues until after a taper separation of a half wavelength has been reached and the EM wave begins to radiate into free space. This means that the aperture width W<sub>A</sub> must be greater than a half wavelength in any ETS antenna design in order to efficiently radiate.

The antenna designed to radiate at 60 GHz. Figures 1, 2 and 3 illustrate layout of a modeled SIW based ETS antenna without dielectric loading, rectangular dielectric loading and elliptical dielectric loading respectively by using CST Microwave Studio.

Table 1 shows the parameters of the antenna obtained using equations (1)-(11). The shape of the curvature influences the traveling wave in two main areas. First is the beginning of the taper and the second is the wide end of the taper. On both places, a reflection of the traveling wave is likely to occur. Therefore, smoother taper in the neck minimizes the reflection there [25,26]. This can be achieved with higher value of ‘a’. The beamwidth in the H-plane can be controlled through the flare in the H-plane. The beamwidth in the E-plane is determined by the flare in the E-plane that is

limited. In some Mm wave applications, a wider beamwidth in the E-plane is also desired. For this purpose, a dielectric slab is placed in front of the flare of the ETS antenna. This slab serves as the dielectric guiding structure in the E-plane. In the H-plane, for an ETS antenna with maximum gain, the flare phase distribution along the H-plane is nearly uniform without the dielectric loading.

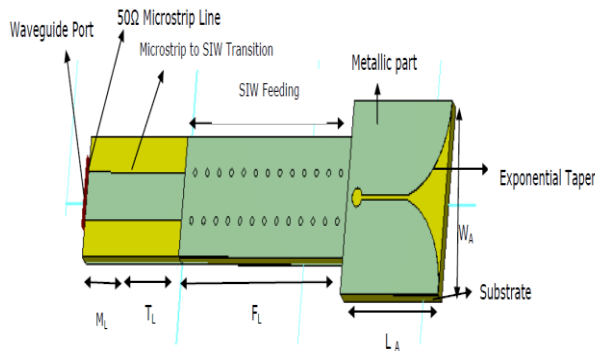


Fig. 1. ETS antenna without dielectric loading.

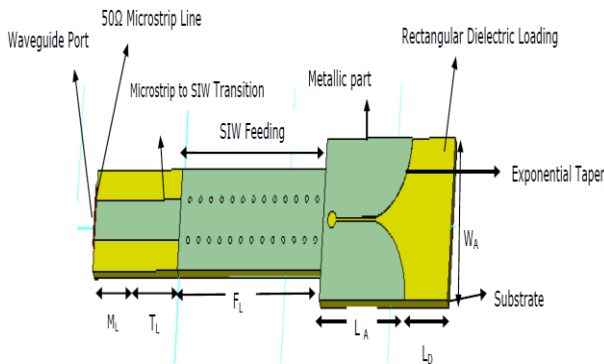


Fig. 2. ETS antenna with rectangular dielectric loading.

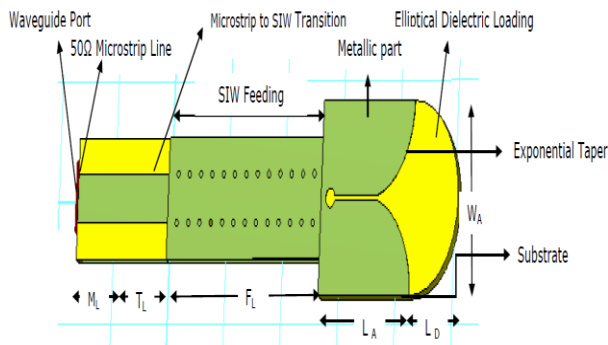


Fig. 3. ETS antenna with elliptical dielectric loading.

Table 1: Dimension of the antenna (unit: mm)

Symbol	Value (mm)
$L_A$	8
$W_A$	8
$L_D$	4
$F_L$	13.5
$T_L$	5
$M_L$	3

#### D. Optimization of ETS antenna

The SIW based ETS antenna with elliptical dielectric loading modeled utilizing CST Microwave Studio. Once the model has been formulated, an optimization algorithm can be used to find its best solution. The newly implemented trust region framework algorithm can work the sensitivity information to cut down optimization time dramatically. The yield analysis for complex three dimensional models is now available at virtually no additional computational rate. Trust-region methods define a region around the current iterate within which they trust the model to be an adequate representation of the objective function, and then choose the step to be the approximate minimizer of the model in this region. In effect, they choose the direction and length of the step simultaneously. If a step is not acceptable, reduce the size of the region and find a new minimizer. In general, the direction of the step changes whenever the size of the trust region is altered. According to the target of this antenna at 60 GHz, the radius of vias was modified to provide a better return loss. The parameter ' $d$ ' was swept from 0.135 to 0.165 mm using trust region framework algorithm in CST to find the best performance of the antenna. A new trust region framework algorithm is very efficient for a direct 3D EM optimization, especially in conjunction with the sensitivity analysis [27].

#### E. Simulation and measurement

The antenna structure is simulated without dielectric loading using 3D electromagnetic software CST Microwave Studio as shown in Fig. 1, the gain is 7.2 dB, main lobe direction is  $81^\circ$ , return loss is -12.07 dB, VSWR is 1.66 and side lobe level is -4.0 dB. A rectangle and elliptical dielectric loading is placed in front of the antenna flare works as dielectric guiding structure to increase the gain, reduce the side lobe level of the

antenna and respective structures are shown in Figs. 2 and 3. Figure 4 shows that the elliptical dielectric loading gives higher gain compared to the rectangle dielectric loading with the same length.

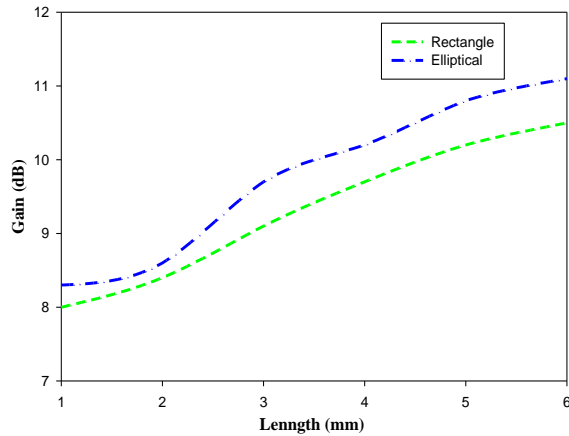


Fig. 4. Gain versus length of the dielectric loading.

When the length of dielectric loading is 4 mm, gain of rectangle and elliptical is 8.3 dB and 10.2 dB respectively. Further, the rectangle and elliptical dielectric loading are explored. Table 2 shows the performance comparison of the dielectric loading at 60 GHz. The dielectric loaded antenna was suggested in [28], which are useful in high gain applications. However, in the dielectric loaded antenna using SIW technology provides slightly higher gain with wider main lobe directions at 60 GHz.

Table 2: Performance comparison of the dielectric loading at 60 GHz

Dielectric Loading	Gain (dB)	Main Lobe (degree)	S <sub>11</sub> (dB)	VSWR	Side Lobe (dB)
Without	7.2	80	-12.07	1.66	-4.0
Rectangle	8.3	82	-11.43	1.73	-3.8
Elliptical	10.2	84	-12.23	1.64	-6.2

The simulated results of 3D radiation pattern, S<sub>11</sub> parameter, and VSWR for the antenna with elliptical dielectric loading is shown in Figs. 5, 6 and 7. Compared with elliptical dielectric loaded antenna, the gain of the antenna without dielectric loading is increased by 3.0 dB, S<sub>11</sub> parameter has decreased by -0.16 dB and main lobe direction is increased by 4° with less side lobe level.

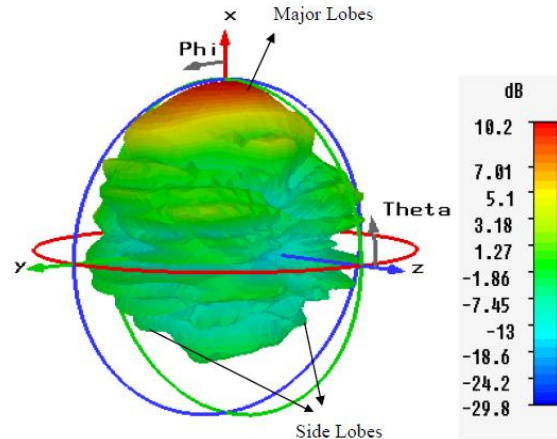


Fig. 5. Simulated 3D radiation pattern of antenna with elliptical dielectric loading.

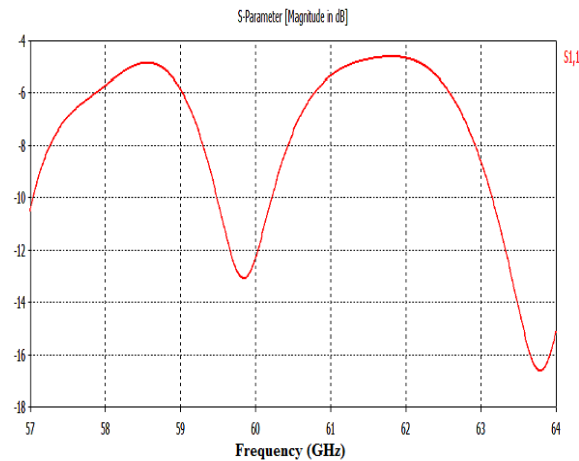


Fig. 6. Simulated S<sub>11</sub> parameter of antenna with elliptical dielectric loading.

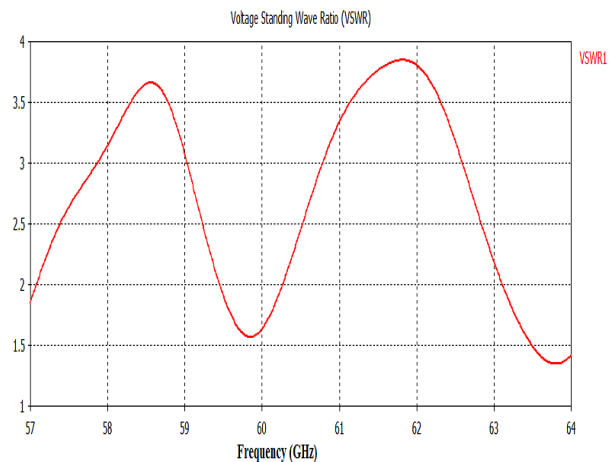


Fig. 7. Simulated VSWR of antenna with elliptical dielectric loading.

From these results it is seen that elliptical dielectric loading with the antenna gives higher gain with marginally broader main lobe direction at 60 GHz. The ETS antenna provides high gain and main lobe direction depending on the length dielectric loading.

Figures 8, 9 and 10 prove the validation of the designed elliptically dielectric loaded antenna. A slight difference in the two simulated values is because of the two different numerical methods employed in CST and HFSS. The CST employs FDTD (Finite Difference Time Domain) and HFSS employs FEM (Finite Element Method).

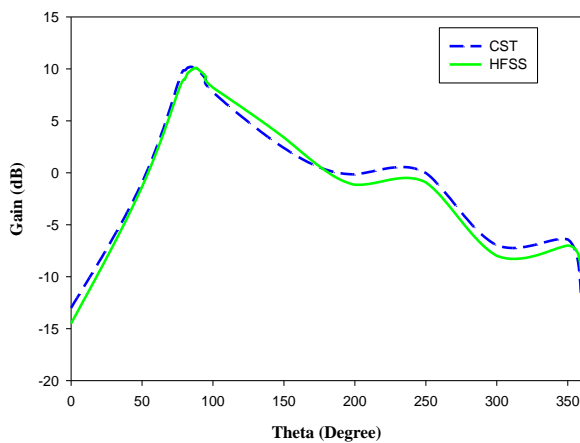


Fig. 8. Simulated gain comparison between CST and HFSS for antenna with elliptical dielectric loading.

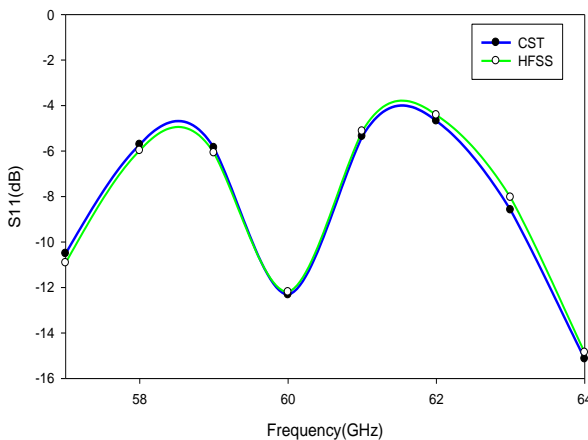


Fig. 9. Simulated  $S_{11}$  parameter comparison between CST and HFSS for antenna with elliptical dielectric loading.

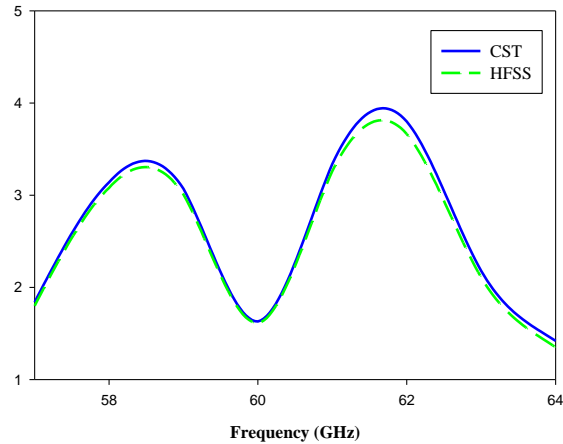


Fig. 10. Simulated VSWR comparison between CST and HFSS for antenna with elliptical dielectric loading.

The performance comparison of antenna with elliptical dielectric loading using 3D electromagnetic software CST and comparisons with HFSS validate the design procedure based on antenna gain,  $S_{11}$  and VSWR. It is perceived that there is good agreement in the simulated results between the gain,  $S_{11}$  and VSWR.

A slight difference in the two simulated values is basically because of the two different numerical methods employed in CST and HFSS. Further, the SIW based ETS antenna efficiency with elliptical dielectric loading is also analyzed and found that the radiation efficiency is 96.84% and total efficiency is 91.05%.

The antenna without dielectric loading and elliptical dielectric loading with optimized dimensions are fabricated on Rogers RT Duroid 5880 high frequency substrate with a thickness of 0.787 mm, relative permittivity of 2.2, relative permeability of 1 and loss tangent of 0.0009. The top side of the antenna having radiating flare and other side is ground plane. The photograph of fabricated antenna without dielectric loading and elliptical dielectric loaded ETS antenna is shown in Figs. 11 and 12.

The measurements were carried out in Sub Millimeter Wave Laboratory (SMWL) at RCI, Hyderabad. To measure the return loss of the antenna, Vector Network Analyzer (AB Millimeter Wave's-MVNA-8-350) is calibrated in

single port and the return loss is tested at 60 GHz. To record the gain and radiation pattern, the VNA is calibrated in two port mode. The separation between the antennas is maintained to be greater than the far field requirement. The elliptical dielectric loaded antenna simulated and measured results of  $S_{11}$  parameter, gain and radiation pattern are shown in Figs. 13, 14 and 15. A slight difference is observed between the measured value and simulated value. The difference between the measured and simulated  $S_{11}$  of the antenna is caused by the microstrip to SIW transition. But the results from simulation and measurement are in good agreement.



Fig. 11. SIW based ETS antenna without dielectric loading.

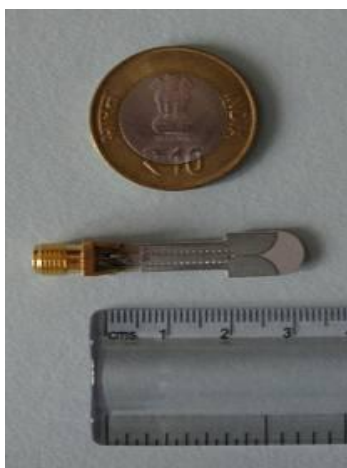


Fig. 12. SIW based ETS antenna with elliptical dielectric loading.

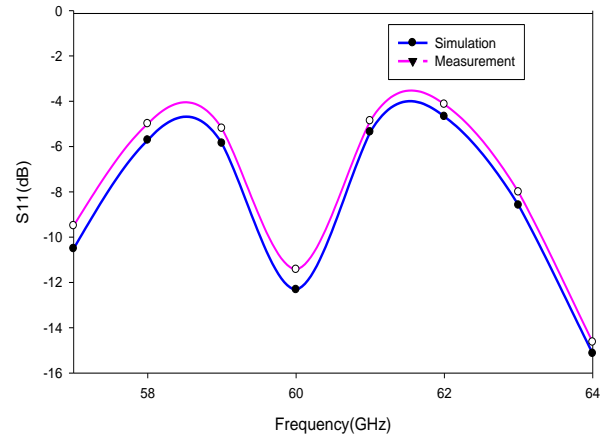


Fig. 13. Measured and simulated  $S_{11}$  parameter for antenna with elliptical dielectric loading.

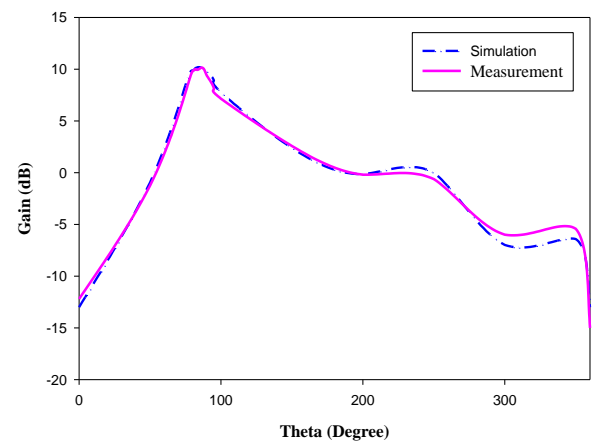


Fig. 14. Measured and simulated gain for antenna with elliptical dielectric loading.

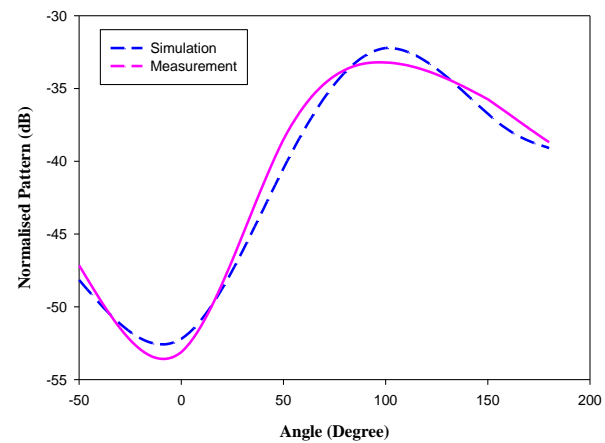


Fig. 15. Measured and simulated radiation pattern for antenna with elliptical dielectric loading.

### III. 1×2 PLANAR DIELECTRIC LOADED ETS ANTENNA ARRAY

A new Y-junction two way power divider is proposed to feed ETS array antenna. In the SIW Y-junction two way power divider, a metallic via as an inductive post, which is short circuited between two wide walls of the waveguide, is set to increase reflectance. Based on conventional waveguide transmission theory, the inductive post is equivalent to a parallel susceptance. Optimization of the inductive matching post diameter and position was performed in order to achieve a low return loss at 60 GHz. The Simulated  $S_{11}$  and  $S_{21}$  plots of the Y-junction two way power divider are shown in Fig. 16.

The ETS antenna array structure is fabricated in a single layer structure using Rogers RT Duroid 5880 with a thickness of 0.787 mm. Figure 17 shows the photograph of the fabricated elliptically dielectric loaded ETS antenna array. The simulated and measured  $S_{11}$  and gain of the antenna array are shown in Figs. 18 and 19. When compare simulated and measured  $S_{11}$  parameter of the antenna array, the simulation results show that much of the loss is caused by the dielectric loss effect at the feed network. The bandwidth of the antenna array covers the entire V-band, while the gain of the antenna is retained nearly constant within a wide bandwidth of the antenna array. The apparent difference between the simulated and measured gain might be due to the calibration related tolerance range of the antenna reference in the anechoic chamber.

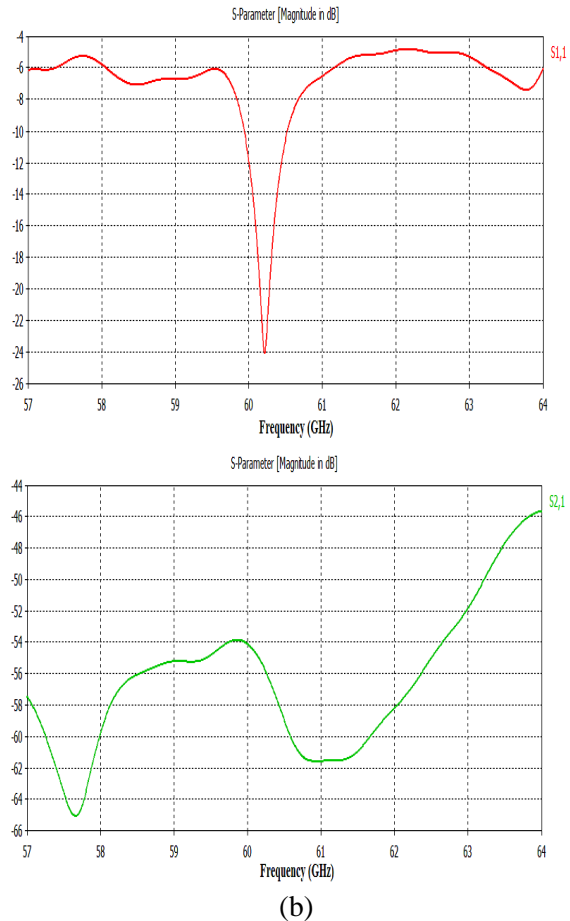
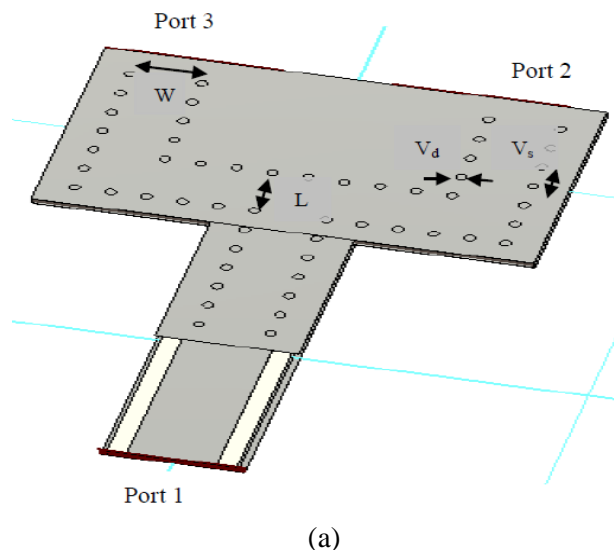


Fig. 16. (a) Geometry of power divider, and (b) simulated  $S_{11}$  and  $S_{21}$  of the Y-junction power divider;  $W=2$  mm,  $L=2$  mm,  $V_d=0.3$  mm, and  $V_s=0.7$  mm.

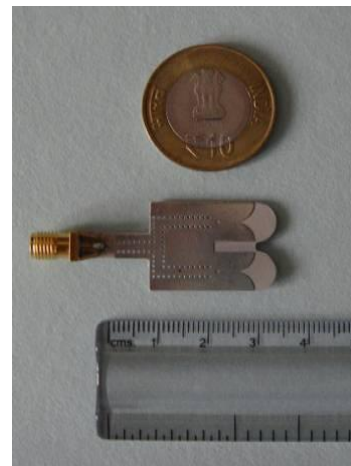


Fig. 17. Photograph of the fabricated ETS antenna array with elliptical dielectric loading.

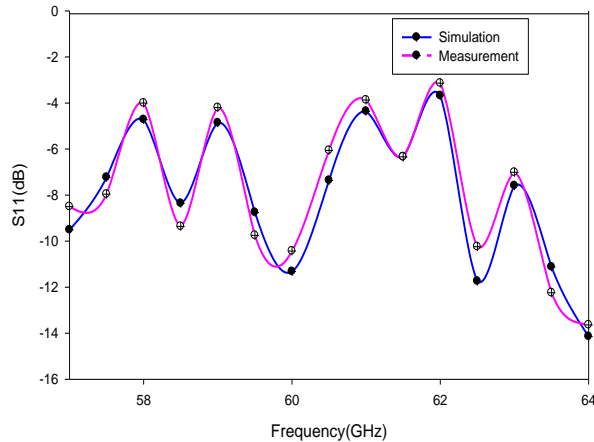


Fig. 18. Measured and simulated  $S_{11}$  Parameter comparison of elliptical dielectric loaded ETS antenna array.

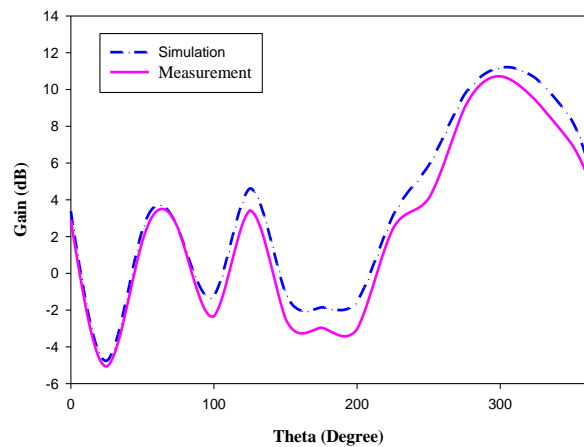


Fig. 19. Measured and simulated gain comparison of elliptical dielectric loaded ETS antenna array.

#### IV. CONCLUSION

The use of Mm wave techniques offers many advantages for short-range wireless communication systems compared to radio techniques at lower frequencies. Besides, a new adaptation between microstrip line and SIW is proposed, which is predominantly useful in V-band wireless communication applications. The SIW technology with emulated waveguides can be utilized to eliminate the unwanted radiations from feed, particularly when compared to similar structures built using microstrip lines. A novel configuration of SIW based ETS antenna with dielectric loading is designed, fabricated and measured. The proposed antenna measured gain of the single element antenna is 10.2 dB, return loss

is -12.23 dB, VSWR is 1.64 and main lobe direction is 84 degree at 60 GHz. While the gain of the  $1 \times 2$  antenna array is 11.2 dB, return loss is -7.36 dB, VSWR is 1.89 and main lobe direction is 120 degree at 60 GHz. It is also observed that with proper selection of dielectric structures and its parameters, marginally more gain with broader main lobe direction for the given antenna can be achieved. The reasonable agreement between the simulated and measured results shows that the designed antenna with elliptical dielectric loading is useful for the variety of wireless applications at Mm wave frequencies.

#### ACKNOWLEDGEMENT

Authors are very much grateful to the DRDO, Government of India for providing financial patronage in executing this research work.

#### REFERENCES

- [1] P. Smulders, "Exploiting the 60 GHz band for local wireless multimedia access: prospects and future directions," *IEEE Communications Magazine*, vol. 40, no. 1, pp. 140-147, 2002.
- [2] T. S. Rappaport, J. N. Murdock, and F. Gutierrez, "State of the art in 60-GHz integrated circuits and systems for wireless communications," *Proceedings of the IEEE*, vol. 99, no. 8, pp. 1390-1436, August 2011.
- [3] H. H. Meinel, "Commercial applications of millimeter waves-history, present status and future trends," *IEEE Transactions Microwave Theory Tech.*, vol. 43, no. 7, pp. 1639-1653, July 1995.
- [4] S. K. Yong and C. C. Chong, "An overview of multi gigabit wireless through millimeter wave technology: potentials and technical challenges," *EURASIP Journal on Wireless Communications and Networking*, volume 2007, article ID 78907, 2007.
- [5] H. Julien, T. Larbi, and N. Mourad, "60-GHz optically transparent microstrip antenna made of meshed AuGL material," *IET Microwaves, Antennas & Propagation*, vol. 8, iss. 6, April 2014.
- [6] N. Ghassemi and K. Wu, "Planar high-gain dielectric-loaded antipodal linearly tapered slot antenna for E and W-band gigabyte point-to-point wireless services," *IEEE Transactions on Antennas and Propagation*, vol. 61, no. 4, pp. 1747-1755, April 2013.
- [7] D. Deslandes and K. Wu, "Single-substrate integration technique of planar circuits and waveguide filters," *IEEE Transactions on Microwave Theory Tech.*, vol. 51, no. 2, 593-596, February 2003.

- [8] S. Cheng, H. Yousef, and H. Kratz, "79 GHz slot antennas based on substrate integrated waveguides (SIW) in a flexible printed circuit board," *IEEE Transactions on Antennas Propagation*, vol. 57, no. 1, 64-70, January 2009.
- [9] S. S. Lee, S. Yang, A. E. Fathy, and A. Elsherbini, "Development of a novel UWB vivaldi antenna array using SIW technology," *Progress In Electromagnetic Research*, vol. 90, 369-384, 2009.
- [10] K. Wu, Y. J. Cheng, T. Djerafi, and W. Hong, "Substrate-integrated millimeter-wave and terahertz antenna technology," *Proceedings of the IEEE*, vol. 100, no. 7, 2219-2232, July 2012.
- [11] A. Bakhtafrooz, A. Borji, and D. Busuioc, "Novel two-layer millimeter-wave slot array antennas based on substrate integrated waveguides," *Progress In Electromagnetics Research*, vol. 109, 475-491, 2010.
- [12] J. P. Gibson, "The vivaldi aerial," *Proceedings of 9<sup>th</sup> European Microwave Conference*, Brighton, U.K., 101-105, June 1979.
- [13] E. Gazit, "Improved design of the vivaldi antenna," *IEE Proceedings*, vol. 135, no. 2, 89-92, April 1988.
- [14] K. S. Yngvesson, T. Korzeniowski, Y. Kim, E. Kollberg, and J. F. Johansson, "The tapered slot antenna-a new integrated element for millimeter wave applications," *IEEE Transactions on Microwave Theory Tech.*, vol. 37, no. 2, 365-374, February 1989.
- [15] A. Z. Hood, T. Karacolak, and E. Topsakal, "A small antipodal vivaldi antenna for ultra wide-band applications," *IEEE Antennas Wireless Propagation Letters*, vol. 7, 656-660, 2008.
- [16] F. Xu and K. Wu, "Guided-wave and leakage characteristics of substrate integrated waveguide," *IEEE Transactions on Microwave Theory Tech.*, vol. 53, no. 1, 66-72, January 2005.
- [17] S. Costanzo, G. A. Casula, A. Borgia, G. Montisci, I. Venneri, G. Di Massa, and G. Mazzarella, "Synthesis of slot arrays on integrated waveguides," *IEEE Antennas and Wireless Propagation Letters*, vol. 9, 962-965, 2010.
- [18] R. Rezaiesarlak, M. Salehi, and E. Mehrshahi, "Hybrid of moment method and mode matching technique for full-wave analysis of SIW circuits," *Applied Computational Electromagnetics Society (ACES) Journal*, vol. 26, no. 8, pp. 688-695, August 2011.
- [19] S. E. Hosseininejad, N. Komjani, H. Oraizim, and M. T. Noghani, "Optimum design of SIW longitudinal slot array antennas with specified radiation patterns," *Applied Computational Electromagnetics Society (ACES) Journal*, vol. 27, no. 4, pp. 320-325, April 2012.
- [20] D. Deslandes and K. Wu, "Integrated microstrip and rectangular waveguide in planar form," *IEEE Microwave Wireless Comp. Letters*, vol. 11, no. 2, 68-70, February 2001.
- [21] D. Langley, P. Hall, and P. Newham, "Balanced antipodal vivaldi antenna for wide bandwidth phased arrays," *IEE Proc. Microwave Antennas Propag.*, vol. 143, no. 2, 97-102, April 1996.
- [22] Y. Yang, Y. Wang, and A. E. Fathy, "Design of compact vivaldi antenna arrays for UWB see through wall applications," *Progress In Electromagnetics Research*, vol. 82, 401-418, 2008.
- [23] A. Z. Hood, T. Karacolak, and E. Topsakal, "A small antipodal vivaldi antenna for ultra-wideband applications," *IEEE Antennas and Wireless Propagation Letters*, vol. 7, 556-560, 2008.
- [24] P. Shrivastava, D. Chandra, N. Tiwari, and T. R. Rao, "Investigations on corrugation issues in SIW based antipodal linear tapered slot antenna for wireless networks at 60 GHz," *Applied Computational Electromagnetics Society (ACES) Journal*, vol. 28, no. 10, 960-967, October 2013.
- [25] A. Kedar and K. S. Beenamole, "Wide beam tapered slot antenna for wide angle scanning phased array antenna," *Progress In Electromagnetics Research B*, vol. 27, 235-251, 2011.
- [26] N. Hamzah and K. A. Othman, "Designing vivaldi antenna with various sizes using CST software," *Proceedings of the World Congress on Engineering 2011*, vol. II, WCE 2011, London, U.K., July 6-8, 2011.
- [27] J. Nokedal and S. J. Wright, "Numerical optimization," *Springer*, August 2000.
- [28] S. Ramesh and T. R. Rao, "Dielectric loaded exponentially tapered slot antenna for wireless communications at 60 GHz," *Progress In Electromagnetics Research C*, vol. 38, 43-54, 2013.



**S. Ramesh** received his B.E. in Electronics and Communication Engineering from The University of Madras, Tamilnadu, India in 2001 and M.Tech in Communication Engineering from VIT University, Vellore, Tamil Nadu, India in 2004. Currently he is pursuing his Ph.D. from the Department of Telecommunication Engineering at SRM University, India. He is a Student member of IEEE Antennas & Propagation Society. He authored papers in reputed journals and international/national conferences. His area of interest includes Antennas and Propagation and

Wireless Communications.



**T. Rama Rao** is currently working as 'Professor & Head' of the Telecommunication Engineering Department, SRM University, Chennai, India. He received his Ph.D. degree on 'Radio Wave Propagation Studies for Fixed and Mobile Communications over Southern India' from Sri Venkateswara University, Tirupati, India. Rama Rao is a Member of the IEEE-USA; Member of WWRF; an IETE-India Fellow; Senior Member of the ACEEE, Member of IACSIT, Life Member of ISCA; Member of SEMCE-India and

Member of the ACM. He was the recipient of "Young Scientist" award for the XXVIth URSI GA, University of Toronto, Canada, August 1999. Rama Rao worked with Aalborg University, Denmark as 'Research Professor'; with Universidad Carlos III de Madrid, Spain and at the University of Sydney, Australia as 'Visiting Professor.' Also, worked as 'PostDoc Research Fellow' at National Chio Tung Univeristy, Hsinchu, Taiwan. His research interests are Antennas and its applications, Broadband Wireless Communications/Networks and Mobile Cellular Telecommunications. He authored papers in reputed journals/transactions and international/national conferences. Recently, he served as Co-Chair for the 7<sup>th</sup> edition of IEEE ANTS 2013.

# Modified Broadband Half Mode Substrate Integrated Waveguide Cruciform Coupler

Zahra Mansouri <sup>1</sup>, Mitsuyoshi Kishihara <sup>2</sup>, Ferdows B. Zarrabi <sup>3</sup>, and Fatemeh Geran <sup>4</sup>

<sup>1</sup>Department of Electrical and Computer Engineering  
Sciences and Research Branch, Islamic Azad University, Tehran, Iran  
zm.mansouri@gmail.com

<sup>2</sup>Faculty of Computer Science and System Engineering  
Okayama Prefectural University, Kuboki, Soja, Okayama 719-1197, Japan  
kishihara@c.oka-pu.ac.jp

<sup>3</sup>Faculty of Electrical and Computer Engineering  
University of Tabriz, Tabriz, Iran  
ferdows.zarrabi@yahoo.com

<sup>4</sup>Faculty of Electrical and Computer Engineering  
Shahid Rajaei Teacher Training University, Tehran, Iran  
f.geran@Srrtu.edu

**Abstract** — In this paper, a cruciform coupler with Half Mode Substrate Integrated Waveguide (HMSIW) structure is presented. The prototype coupler consists of four half mode SIW structures, which are crossing each other at right angles. Also, two metallic posts are inserted in free section of junction in order to make coupling properties. Compact size and broadband operation are the features of this coupler. The size of coupler is reduced 24% in comparison to previous HMSIW cruciform couplers. A fractional bandwidth of about 35% is obtained. The coupler is designed and simulated by HFSS13. Here, the simulation results are compared with experimental results.

**Index Terms** — Cruciform coupler, directional coupler, half mode SIW, millimeter wave, substrate integrated waveguide.

## I. INTRODUCTION

90 degree hybrids have been used in many applications in telecommunication circuits such as modulators, mixers, feed networks and other microwave devices. Branch line, Lange, Bethe hole, short slot and cruciform coupler are well-known conventional types of 90 degree hybrids

[1]. The cruciform couplers are attractive due to some advantages such as compactness, simplicity, planar structure, right-angled input/output ports, high power handling capability, flat coupling and broadband properties [2-3]. In designing cruciform couplers, realization of wide bandwidth and small size are two important goals.

A new structure called substrate integrated waveguide is useful for high frequency applications. It is a kind of rectangular waveguide in which sidewalls are replaced by a row of metallic posts. Low loss, high Q factor, and easy fabrication are the advantages of SIWs [4-5]. In the last decade, in the process of redeveloping rectangular waveguide components in the form of substrate integrated waveguides, some cruciform couplers have been designed and implemented [6-9]. In the rectangular waveguide cruciform coupler [3], the wide cross junction technique for wide bandwidth has been introduced for the first time and 28% bandwidth has been achieved. The original cruciform coupler tends to give flat coupling property at high frequency region. The wide cross junction can shift the flat frequency characteristics to the lower frequency region. Wide cross junction techniques have been applied to the SIW cruciform couplers in different

manners, such as bending the angel of cross junction [6] or changing the place of the vias in corners [7,8,9].

We need more compact and wider bandwidth couplers in some applications. A Half Mode SIW (HMSIW) cruciform coupler has been introduced by Wang, et al. [10]. In that structure, the size was reduced and a compact structure was achieved. But in that coupler, because of input/output arms bending for the impedance matching between HMSIW and cross region, a tradeoff exists between the width of cross junction and the bandwidth. If the size of cross region is decreased, the coupling factor will be improved, but the bandwidth will be reduced. Small size and low insertion loss are the advantages of the half mode SIW in comparison with SIW [11-12]. In recent years, some half mode SIW couplers have been designed. Size reduction is their common feature [13-14].

In this article, we propose a modified HMSIW cruciform coupler with smaller size and wide bandwidth. The size of coupler is reduced 24% in comparison to previous HMSIW cruciform couplers. Also, a fractional bandwidth is obtained about 35%. The half mode SIW is a modified structure of SIW to reduce its size. It is built by bisecting a SIW structure along the symmetrical center plane along the propagation direction. To this reason, when an SIW works only in dominant mode,  $TE_{10}$ , tangential E-field has maximum value and normal magnetic field is equal to zero in symmetrical plane along the propagation direction. Thus, we can assume the center symmetrical plane as a fictitious magnetic wall and bisect the SIW from this fictitious wall to two sections. Each half section has half of the field distribution, and the power leakage from open side is negligible because of its large width-to-height ratio (exceed 10).

## II. CIRCIFORM COUPLER DESIGN

The cruciform coupler is a type of 90 degree hybrids. It originally consists of two rectangular waveguides which are crossing each other at right-angle. Two metallic posts in cross region are used to make the coupling factors. Also, metallic posts are placed in each input arm for better matching. The height of structure is less than wavelength; thus, the electromagnetic field

is nearly constant in vertical direction. The wide cross junction technique leads to wider bandwidth in cruciform couplers [6-9].

A prototype 3-dB HMSIW cruciform coupler is designed by replacing the SIW waveguides by the half mode structures. Figure 1 shows the designed half mode cruciform coupler geometrical dimension at 24 GHz. The coupler is designed on a Rogers RT/duriod 5880 substrate. The height of substrate is 0.508 mm with  $\epsilon_r = 2.2$  (loss tangent 0.0009).  $r$  is the radius of vias,  $h$  is the thickness of substrate,  $a$  is the initial width of half mode SIW arms,  $d$  is the distance between two coupling via,  $c$  and  $m$  present coupling vias and matching vias, respectively. Width of the arms are shown by "a" in Fig. 1 and it is calculated by the formula presented in [11]. It is about  $\lambda/4$  wavelength and gives the cutoff frequency of the HMSIW. Also, the diameter  $r$  and spaces  $s$  between the vias are calculated by equations in [5]. Two metallic posts are inserted in cross region to generate and control the coupling factors. Here, the placements of coupling vias in Fig. 1 is presented with 90 degree rotation to Wang's half mode coupler design [10]. The Wang's structure is classified to a kind of short-slot coupler. By this change, the cross junction will be large enough for wide bandwidth and we don't need to sketch the arms of coupler similar to the pervious design by Wang, et al. Therefore, realization of a smaller coupler is expected. We also introduce the bending vias in corners and the tapering vias of input arms for better matching and apply widening technique for wide bandwidth (the vias are tapered with the rate of  $w=0.2$  mm). Coupling factors and good matching state can be adjusted by changing the radius and place of coupling vias. Space 'd' between the coupling vias and radius  $R_c$ , affect the coupling factors and bandwidth. Small distance leads to disturbance to matching state and also decreases the  $S_{11}$  and  $S_{41}$ . Increasing this space causes weaker coupling factor. In addition, if the position ( $U_c$ ,  $W_c$ ) is adjusted individually, the coupling factor can be controlled more precisely. Therefore, it is possible to design a 6 dB or 9 dB coupler, if the coupling factor, namely, the position of the coupling vias are optimized. Matching vias are

inserted in each input arms for better matching.

The size and place of coupling vias and the matching vias are optimized by full wave simulator software, HFSS 13. As a result, the dimensions of structure are determined as:  $\epsilon_r=2.2$ ,  $h=0.508$  mm,  $r=0.5$  mm,  $s=1.7$  mm,  $a=4.5$  mm,  $w=0.2$ ,  $R_c=0.85$  mm,  $R_m=0.35$  mm,  $(U_c, W_c)=(3.5, -3.5)$ ,  $(U_m, W_m)=(7, 1.5)$ .

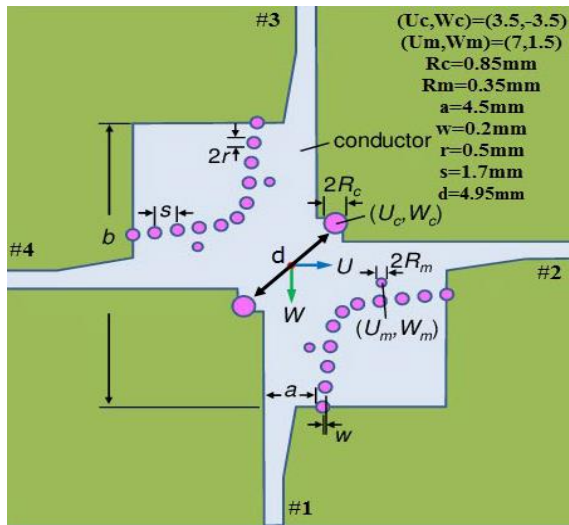


Fig. 1. Half mode cruciform coupler geometrical dimension.

### III. SIMULATION AND EXPERIMENTAL RESULTS

The coupler is simulated by HFSS13 with full wave simulation. Then, the simulation results are compared with experimental results. Figure 2 shows the current distribution at 24 GHz on the surface of half mode prototype coupler. It is found that the input signal from port 1 interacts with metallic posts in the cross region, and is coupled equally to port 2 and port 3. The S-parameters of the coupler obtained by HFSS are shown in Fig. 3. In the simulation, the conductor, dielectric, and radiation losses are considered.

From 20.5 GHz up to 29 GHz,  $S_{21}$  and  $S_{31}$  are between range of 4-6 dB. The values of  $S_{11}$  and  $S_{41}$  in the frequency range of 21-29 GHz are below -15 dB, 35% bandwidth is achieved by -15 dB isolation. The following typical values are obtained for the center frequency at 24 GHz:

$$\begin{aligned} S_{11} &= -33\text{dB} & S_{21} &= -4\text{dB}, \\ S_{31} &= -4\text{dB} & S_{41} &= -30\text{dB}. \end{aligned}$$

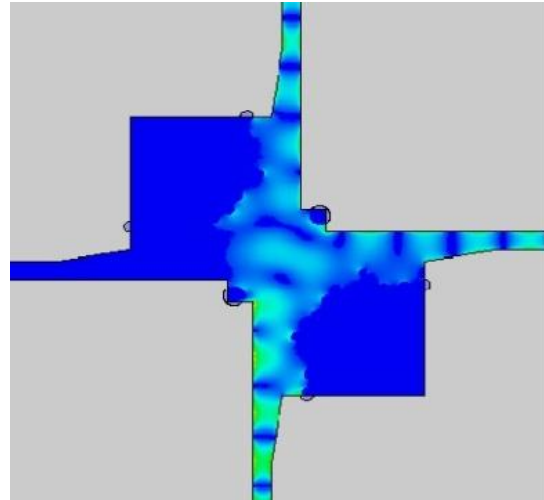


Fig. 2. Current distribution on the surface of half mode prototype coupler for 24 GHz.

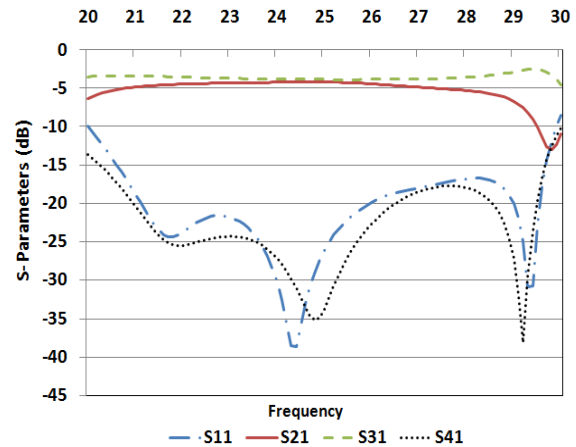


Fig. 3. S-parameters of half mode SIW cruciform coupler in HFSS.

Figure 4 shows the phase difference between ports 2 and 3 and it obviously shows 90-degree phase difference. The designed 3 dB coupler was fabricated and the S-parameters and phase difference were measured using Agilent's E8361C vector network analyzer. Figure 5 (a) shows the fabricated coupler. The measured magnitudes of the S-parameters and the output phase difference are presented in Figs. 5 (b), (c), and (d). A full 2-port 1.85 mm calibration was performed on the VNA electronically. The 1.85-3.5 mm adapters and the SMA connectors are necessary for the measurement. To exclude the insertion losses of microstrip lines, the SMA

terminals and the adapters, a straight section of 2-port microstrip line was fabricated. The insertion losses including terminal connectors are calibrated by using the measurement results of the 2-port microstrip straight section. It is obvious that both the simulated results and the measured results are in good agreement. The size of our prototype coupler is 24.0×24.0 mm without tapered microstrip sections. Considering the fact that the width of HMSIW is  $a=4.5$  mm (or about 1/4 wavelength), it is equal to about 6 times of the width (or 1.5 wavelengths) of HMSIW. It becomes 36.0×36.0 mm with tapered microstrip sections.

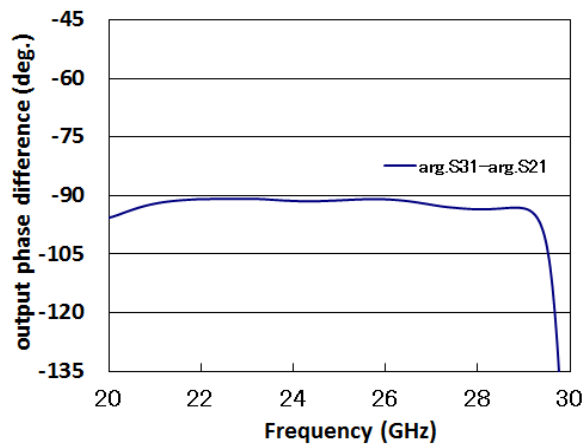


Fig. 4. Output phase difference between port 2 and 3 in HFSS.

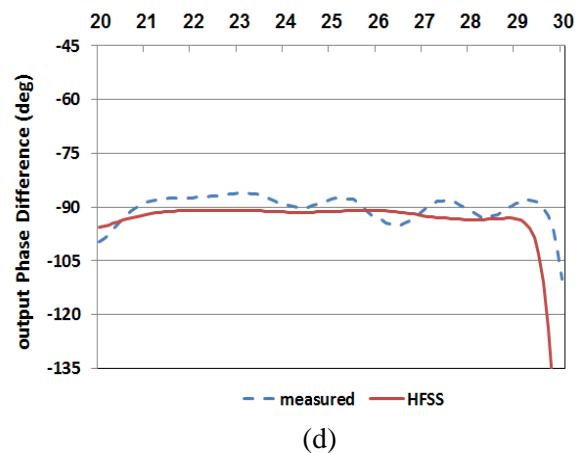
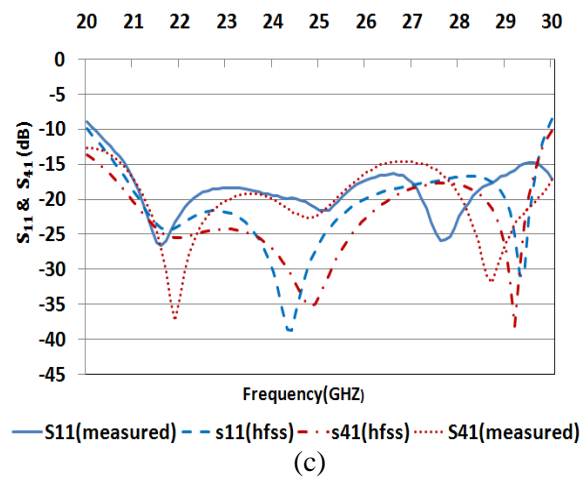
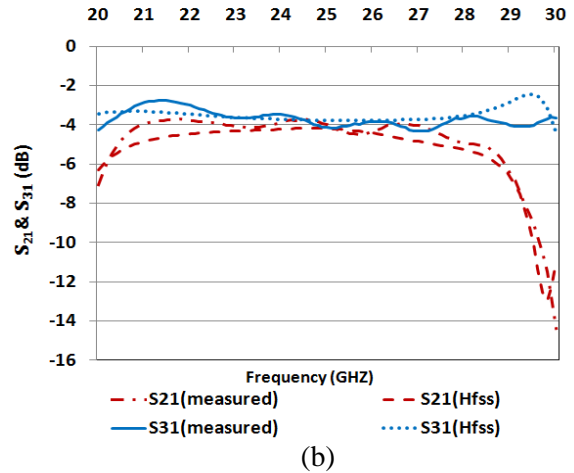
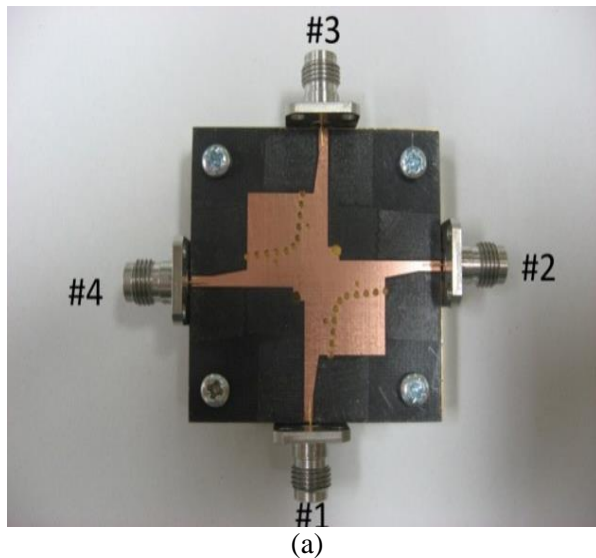


Fig. 5. Experimental results: (a) fabricated coupler, (b) measured and simulated  $S_{21}$  and  $S_{31}$ , (c) measured and simulated  $S_{11}$  and  $S_{41}$ , and (d) output phase difference.

First, the prototype coupler is compared with a broadband SIW cruciform coupler that is designed by Kishihara, et al. [6]. Their coupler has been designed for 21-28 GHz frequency and 30% bandwidth. The size of SIW cruciform coupler is 26.15×26.15 mm and it is equal to 3.89 widths or 1.95 wavelengths and with tapered microstrip sections it becomes 30.55×30.55 mm. One can conclude that the area of the present prototype is about 40% smaller and bandwidth of 35% is 5% broader than the one in [6]. Subsequently, another comparison is done with Wang's HMSIW cruciform coupler designed at 36 GHz [10]. The area of this HMSIW cruciform coupler is 15.5×15.5 mm without tapered sections it is equal to 6.89 widths or 1.72 wavelengths,

because the width of the HMSIW is around 2.25 mm or 1/4 wavelength. This comparison indicates that our proposed structure is 24% smaller than previous research by Wang, et al. In addition, the modified model has more than 35% bandwidth while the previous one has achieved only 22% bandwidth. This comparison results are shown in Table 1. Due to using half mode SIW and optimum arrangement of vias, the phase difference between ports 2 and 3 is around -90° with tapered microstrip sections from simulation and experimental. We have achieved a coupler with 24% smaller size in comparison to the HMSIW cruciform coupler and around 40% smaller than the SIW cruciform coupler.

Table 1: Comparison between our coupler and two models of previous one

	Frequency	Bandwidth	Size (Without Taper Microstrip Section)
Ref [6]	21-28 GHz	30%	26.15×26.15 mm <sup>2</sup> (1.95 wavelength)
Ref [10]	32-40 GHz	22%	15.5×15.5 mm <sup>2</sup> (1.72 wavelength)
Our design	20.5-29 GHz	35%	(24×24 mm <sup>2</sup> ) (1.5 wavelength)

#### IV. CONCLUSION

In this paper, a modified cruciform type coupler with half mode SIW structure is presented for millimeter wave applications. The bandwidth of about 35% is obtained in full wave simulation and experimental. Small size and broad bandwidth are the obtained features of this coupler.

#### REFERENCE

- [1] D. M. Pozar, "Microwave engineering," *John Wiley & Sons, Inc.*, second edition.
- [2] I. Ohta, Y. Yumita, K. Toda, and M. Kishihara, "Cruciform directional couplers in H-plan rectangular waveguide," *APMC2005 Proceedings*, 2005.
- [3] K. Toda, I. Ohta, and M. Kishihara, "H-plane crossed-waveguide hybrids," *Proceedings of the 36<sup>th</sup> European Microwave Conference*, 2006.
- [4] M. Bozzi, A. Georgiadis, and K. Wu, "Review of substrate-integrated waveguide circuits and antennas," *IET Microw. Antennas Propag.*, 2011.
- [5] F. Xu and K. Wu, "Guided-wave and leakage characteristics of substrate integrated waveguide," *IEEE Transaction on Microwave Theory and Techniques*, vol. 53 (1), January 2005.
- [6] M. Kishihara, I. Ohta, and K. Okubo, "Design of a broadband cruciform substrate integrated waveguide coupler," *IEICE Transactions on Electronics*, vol. E94-C, no. 2, pp. 248-250, February 2011.
- [7] K. Murai, H. Ikeuchi, T. Kawai, M. Kishihara, and I. Ohta, "Broadband design method of SIW directional couplers," *Microwave Conference Proceedings (CJMW)*, 2011.
- [8] T. D. Jerafi and K. Wu, "Super-compact substrate integrated waveguide cruciform directional coupler," *IEEE Microwave and Wireless Components Letters*, vol. 17, no. 11, November 2007.
- [9] T. D. Jerafi, M. Daigle, H. Boutayeb, X. Zhang, and K. Wu, "Substrate integrated waveguide six-port broadband front-end circuit for millimeter-wave radio and radar systems," *Proceedings of the 39<sup>th</sup> European Microwave Conference*, September 2009.
- [10] Y. Wang, X. Zhu, C. You, and G. Yang, "Design of ka-band half mode substrate integrated waveguide (HMSIW) mixer," *ICUWB 2009*, pp. 684-687, September 2009.
- [11] Q. Lai, C. Fumeaux, W. Hong, and R. Vahldieck,

“Characterization of the propagation properties of the half-mode substrate integrated waveguide,” *IEEE Transaction on Microwave Theory and Techniques*, vol. 57, no. 8, August 2009.

- [12] B. Liu, W. Hong, Y. Wang, Q. Lai, and K. Wu, “Half mode substrate integrated waveguide (HMSIW) 3-dB coupler,” *IEEE Microw. Wireless Components Letters*, vol. 17, no. 1, pp. 22-24, January 2007.
- [13] J. Chen, W. Hong, H. Tang, P. Yan, B. Liu, and

K. Wu, “A millimeter wave six-port network using half-mode substrate integrated waveguide,” *J. Infrared Milli. Terahz Waves* (2012), 33:348-356, DOI 10.1007/s10762-012-9880-3.

- [14] B. Liu, W. Hong, Y. Zhang, H. J. Tang, X. Yin, and K. Wu, “Half mode substrate integrated waveguide 180 3-dB directional couplers,” *IEEE Transaction on Microwave Theory and Techniques*, vol. 55, no. 12, December 2007.



**Zahra Mansouri** was born in Zanjan, Iran in 1987. She received her B.Sc. degree in Electrical Engineering (Telecommunication) from Zanjan University, Zanjan, Iran, in 2008 and her M.Sc. degree in Electrical Engineering (Telecommunication) from Islamic Azad University, Science and Research Branch, Tehran, Iran, in 2012. Her primary research interests are in microwave components such as couplers and power dividers, metamaterials and UWB antenna.



**Mitsuyoshi Kishihara** was born in Hyogo, Japan in 1973. He received his B.S. degree in Electrical Engineering from Setsunan University, Osaka, Japan, in 1996 and his M.S. and Ph.D. degrees in Electrical Engineering from Himeji Institute of Technology, Hyogo, Japan, in 1998 and 2002, respectively. In October 2000, he joined the Department of Communication Engineering, Faculty of Computer Science and System Engineering, Okayama Prefectural University, as a Research Associate. He is currently an Associate Professor. His main research area is microwave and millimeter-wave passive component such as directional couplers, multiport hybrids, power dividers, and the development of millimeter-wave three-dimensional integrated circuits. Kishihara is a member of IEEE.



**Ferdows B. Zarrabi** was born in Babol in 1983. He studied Electrical Engineering at the University of Tabriz in major of Communication Engineering in 2008. His major research interest is designing of antenna for wireless and UWB application for breast cancer detection radar, microwave devices, absorber, metamaterial, Plasmonic, Nano antenna and THz antenna. He is author and co-author of more than 18. He is currently work focused on fluid Plasmonic for bio-sensing, Cloak, Photocell development based on Nano-antenna. He is also Reviewer of the ACES Journal.



**Fatemeh Geran** was born in Ghaemshar, Iran in 1977. She received her B.Sc. degree in Electrical Engineering from Tehran University, Tehran, Iran, in 1999. Also, she received her M.Sc. and Ph.D. degrees in Electrical Engineering (Telecommunication) from Tarbiat Modares University, Tehran, Iran, in 2003 and 2009, respectively. Her main areas of interest in research are antenna design, microwave passive and active circuits and filters. She is currently an Assistant Professor in Electrical Engineering at Islamic Azad University-Science and Research Branch, Tehran, Iran.

# An Improved Combination of IE-ODDM and MLFMA

Jun Hu<sup>1,2</sup>

<sup>1</sup>School of Electronic and Optical Engineering  
Nanjing University of Science and Technology, Nanjing, 210094, China  
hujunwujin@gmail.com

<sup>2</sup>State Key Laboratory of Millimeter Waves  
Southeast University, Nanjing, 210096, China

**Abstract** — Domain decomposition methods are efficient for analyzing scattering problems with large-scale structures. In the present paper, an improved combination of Overlapped Domain Decomposition Method of Integral Equations (IE-ODDM) and Multilevel Fast Multi-pole Algorithm (MLFMA) is developed. Amount of independent MLFMA progresses of sub-domains are departed and re-integrated, such that the total CPU time of coupled effects in IE-ODDM can be saved. The proposed method developed minimal-completed sub-trees of sub-domains to reduce redundant aggregations of the MLFMA process blended in IE-ODDM. Numerical results and comparisons with the original method are provided, which suggest that the proposed combination integrates MLFMA with IE-ODDM better than the original combined method, and it can greatly improve the computational efficiency of coupled effects in IE-ODDM.

**Index Terms** — Improved combined method, method of moments, multilevel fast multipole algorithm, overlapped domain decomposition method of integral equations.

## I. INTRODUCTION

Method of Moments (MoM) for surface integral equations has been widely used [1], but the dense matrix makes it difficult for analyzing large-scale objects. In the past two decades, this problem has been circumvented by developments of sparse matrix methods and matrix partition iterative schemes. Sparse matrix method utilizes analytical or numerical low-rank matrix decompositions to

accelerate matrix-vector multiplication, like fast multipole method [2] and Multilevel Fast Multipole Algorithm (MLFMA) [3-11] based on plane-wave spectral approximation. Matrix partition iterative schemes divide and solve large problems, like forward-backward iterative scheme [12,13] and Overlapped Domain Decomposition Method for Integral Equations (IE-ODDM) [14,15]. Moreover, sparse matrix methods and matrix partition iterative schemes can be combined for higher performance, like the overlapped domain decomposition method based on MLFMA (IE-MLFMA-ODDM) [16-18] which was newly reported by many researchers [19-22].

In the original IE-MLFMA-ODDM, MLFMA processes are simply embedded in IE-ODDM iterative scheme to accelerate calculations of many matrix-vector multiplications in self-effects and coupled effects of sub-domains. Although the combined method is successful, the above combination of MLFMA and IE-ODDM is still primitive. In the original combined routine, there are many different and independent MLFMA processes of sub-domains, which consume most of CPU time and memory resources. All those MLFMA processes in the combined method are completed processes like the one without IE-ODDM. That is to say, MLFMA processes and IE-ODDM are isolated, and every MLFMA process utilizes too little information from IE-ODDM and other MLFMA processes. If decompositions consist of many sub-domains and all sub-domains are with amount of exterior unknowns, amount of MLFMA processes are still time-consuming.

In the present paper, an improved combination

is proposed. Compared with the original combined method, the proposed combination integrates MLFMA with IE-ODDM much better, and it optimizes MLFMA processes of sub-domains, which can greatly accelerate the calculation of coupled effects. It can be called IE-O-MLFMA-ODDM. The proposed IE-O-MLFMA-ODDM divides many completed and independent MLFMA processes consisting of aggregations, translations and disaggregations into segments, extracts and reuses their common information. Redundancies of many MLFMA processes are reduced, and those independent MLFMA processes and IE-ODDM are blended. Localized aggregations of sub-domains are introduced, and radiation patterns of coupled effects are saved and shared in IE-ODDM loops. The above localization/sharing mechanism can greatly improve the efficiency of IE-ODDM. However, everything has double folds. To support saving and sharing of radiation patterns, the proposed method needs more memory. In order to manage local radiation patterns efficiently, one data structure called minimal-completed sub-tree is introduced.

## II. THE ORIGINAL COMBINED METHOD

In order to find the distribution of current on perfect electrical conductors by MoM, one should build the following electric field integral equation [23]:

$$-\left[\int_{\Omega} \bar{\bar{G}}_{E,J}(r,r')\bar{J}(r')ds'\right]_{\tan} = \bar{E}^{\text{INC}}(r)|_{\tan}, \quad (1)$$

and magnetic field integral equation:

$$-\left[\int_{\Omega} \bar{\bar{G}}_{H,J}(r,r')\bar{J}(r')ds'\right]_{\tan} = \bar{H}^{\text{INC}}(r)|_{\tan}, \quad (2)$$

where  $\Omega$  represents the surface of objects and  $\bar{\bar{G}}$  represents the dyadic Green's function,  $\bar{J}$  is the surface current, and  $\bar{E}^{\text{INC}}$  and  $\bar{H}^{\text{INC}}$  are incident fields. The MoM matrices derived from the above integral equations or their combinations are usually dense, and the corresponding equations from large scale problems cannot be easily solved. Matrix partition iterative methods are useful methods for solving matrix equations with large scales. The domain decomposition methods for integral equations, one kind of matrix partition iterative method, decomposed the whole surface into many completed covering sub-domains  $\Omega = \bigcup \Omega_i$ , and solve Eq. (1) or Eq. (2) or their combined equation

on sub-domains recursively to update the entire current. This principle of domain decomposition methods is the simplest, but it isn't practicable as edge effects. Edge effects would make the iterative process of non-overlapped domain decomposition method unstable and divergent. So, modifications of the original domain decomposition method are necessary. One feasible approach is extending buffer domains like the method in IE-ODDM [14]. In IE-ODDM, Eq. (3) or Eq. (4) or their combined equation are solved on extend region  $\bar{\Omega}_i$ :

$$-\left[\int_{\bar{\Omega}_i} \bar{\bar{G}}_{E,J}(r,r')\bar{J}(r')ds'\right]_{\tan} = \bar{E}^{\text{INC}}(r)|_{\tan} + \left[\int_{\bar{\Omega}_i^c} \bar{\bar{G}}_{E,J}(r,r')\bar{J}(r')ds'\right]_{\tan}, \quad (3)$$

$$-\left[\int_{\bar{\Omega}_i} \bar{\bar{G}}_{H,J}(r,r')\bar{J}(r')ds'\right]_{\tan} = \bar{H}^{\text{INC}}(r)|_{\tan} + \left[\int_{\bar{\Omega}_i^c} \bar{\bar{G}}_{H,J}(r,r')\bar{J}(r')ds'\right]_{\tan}, \quad (4)$$

where extension includes original sub-domains and buffer domains. Parts of their results restricted on original sub-domains are saved to update the entire current. Compared with the unstable iterative scheme of non-overlapped domain decomposition method, this scheme of IE-ODDM has a great convergence.

Corresponding to the above physical principle, IE-ODDM has another matrix interpretation. After discretizations of Eq. (3) or Eq. (4) or their combination utilizing basis functions and test functions like Galerkin procedures in [24], one can obtain the following linear equations on  $\bar{\Omega}_i$ :

$$\sum_{j=1}^{N_{\bar{\Omega}_i}} Z_{ij}^{\bar{\Omega}_i} I_j^{\bar{\Omega}_i} = V_i^{\bar{\Omega}_i} - \sum_{j=1}^{N-N_{\bar{\Omega}_i}} Z_{ij'}^{\bar{\Omega}_i^c} I_{j'}^{\bar{\Omega}_i^c}, \quad (5)$$

where

$$Z_{ij}^{\bar{\Omega}_i} = Z_{g_i^{\bar{\Omega}_i} g_j^{\bar{\Omega}_i}}, \quad Z_{ij'}^{\bar{\Omega}_i^c} = Z_{g_i^{\bar{\Omega}_i} g_{j'}^{\bar{\Omega}_i^c}},$$

$g_i^{\bar{\Omega}_i}$  and  $g_{j'}^{\bar{\Omega}_i^c}$  are global indexes of the  $i$ -th and the  $j$ -th basis functions in the iterative and coupled domain, respectively. Matrices  $Z^{\bar{\Omega}_i}$  and  $Z$  are the local and global impedance matrices, and  $I^{\bar{\Omega}_i}$  is the local current coefficients. The first right-hand term represents the excitation from incident waves, and the second right-hand term represents the coupled effect from other sub-domains. Equation (5) suggests that IE-ODDM is one kind of matrix partition iterative methods.

In IE-ODDM, a loop like block Gauss-Seidel iteration method repeatedly scans all sub-domains and updates local current until the whole current becomes stable. For convenience, the IE-ODDM should classify all basis functions as “interior”, “edge”, “buffer” or “exterior” basis functions, where the interior, edge and buffer basis functions are iterative basis functions, and the exterior basis functions are coupled basis functions. The effects of coupled basis functions on the iterative basis functions are called coupled effects, and the effects of the iterative basis functions on the iterative basis functions are called self-effects. Coupled effects take on calculating right-hand terms of sub-problems, and self-effects take on solving the local current.

In order to accelerate IE-ODDM, MLFMA could be combined and utilized in matrix-vector multiplications of coupled effects and self-effects. The direct combinations are that original combined method IE-MLFMA-ODDM [16-18]. When the MLFMA is utilized in matrix-vector multiplication, the coupled effect in Eq. (5) is divided into the following two terms:

$$\sum_{j=1}^{N-N_{\text{DB}}} Z_{ij}^{\text{OC}} I_j^{\text{OC}} = \sum_{n^l \in \text{Neigh}(m_{s_k}^l)} \sum_{s_j^l \in n^l} Z_{ij}^{\text{OC}} I_j^{\text{OC}} + \sum_{n^l \in \text{Neigh}(m_{s_k}^l)} \sum_{s_j^l \in n^l} Z_{ij}^{\text{OC}} I_j^{\text{OC}}, \quad (6)$$

where

$$\sum_{n^l \in \text{Neigh}(m_{s_k}^l)} \sum_{s_j^l \in n^l} Z_{ij}^{\text{OC}} I_j^{\text{OC}} \approx \sum_p \bar{V}_{s_k, m_{s_k}^l}^{\text{F}}(k_p^L) \bar{W}_{m_{s_k}^l}^{\text{(DA,C)}}(k_p^L),$$

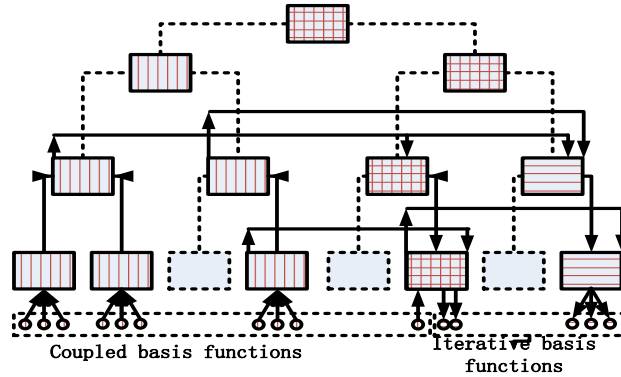


Fig. 1. The sketch of the MLFMA process in the original IE-MLFMA-ODDM. Keeping the critical processes, radiation patterns in coupled domain are aggregated from leaves to nodes, and translated to iterative nodes in the same level, and disaggregated in iterative domains from nodes to leaves. Since some nodes consist of coupled and iterative basis functions, they are both coupled and iterative nodes.

### III. THE IMPROVED COMBINED METHOD

In the MLFMA processes utilized for coupled

and

$$\bar{W}_{m_{s_k}^l}^{\text{(DA,C)}}(k_p^{l+1}) = \bar{W}_{m_{s_k}^l}^{\text{(T,C)}}(k_p^{l+1}) + \sum_t \left( C_{t+1}^p(t) e^{-jk_p^l \bar{r}_{m_{s_k}^l, m_{s_k}^l}} \bar{W}_{m_{s_k}^l}^{\text{(DA,C)}}(k_t^l) \right),$$

and

$$\bar{W}_{m_{s_k}^l}^{\text{(T,C)}}(k_s^l) = \sum_{n^l \in \text{HypoNeigh}(m_{s_k}^l)} \alpha_{m_{s_k}^l, n^l}^s(k_s^l, \hat{r}_{m_{s_k}^l, n^l}) \bar{W}_{n^l}^{\text{(A,C)}}(k_s^l),$$

and

$$\bar{W}_{n^l}^{\text{(A,C)}}(k_p^l) = \sum_{n^{l+1} \in \text{Child}(n^l)} \left( e^{-jk_p^l \bar{r}_{n^l, n^{l+1}}} \sum_t C_{t+1}^p(p) \bar{W}_{n^{l+1}}^{\text{(A,C)}}(k_t^{l+1}) \right).$$

In Eq. (6),  $m_k^l$  is the index of the father node of the  $k$ -th basis function in  $l$ -th level.  $\bar{V}$  is the receiver pattern.  $\bar{W}_m^{\text{(A,C)}}$ ,  $\bar{W}_m^{\text{(T,C)}}$ , and  $\bar{W}_m^{\text{(DA,C)}}$  are process patterns of aggregation, translation and disaggregation, respectively. Matrix  $C$  is the interpolating matrix of different level. Herein, we just list some critical equations of MLFMA. More details, please refer to [16] and references therein.

According to the above description, every MLFMA process in the original combination has an exclusive and completed oct-tree for the aggregation, translation and disaggregation. According to Eq. (6), leaves/nodes of those completed oct-trees should be marked and classified as iterative leaves/nodes and coupled leaves/nodes. Like in Fig. 1, the ones marked by horizontal lines are iterative leaves/nodes, and the ones marked by vertical lines are coupled leaves/nodes.

effects, radiation patterns of coupled leaves/nodes are aggregated from coupled leaves to coupled nodes, and disaggregated from iterative nodes to

iterative leaves. The whole processes have many redundant operations. In the aggregation, radiation patterns of useless iterative leaves are set zero and are also aggregated; while in the disaggregation process, radiation patterns of coupled leaves/nodes are not useful but are still disaggregated. For large-scale problems with many segments, these redundant processes waste a great of CPU time. That is to say, the original combined method just simply embeds MLFMA into IE-ODDM, which can be optimized.

In fact, there is another hidden redundancy. When the IE-ODDM loop serially scans sub-domains, the current coefficients of two steps are partly different. It is because that every step in the loop only renews the current on its sub-domain and keeps the current on other sub-domains. It is a redundancy that unchanged radiation patterns are aggregated again and again in the same IE-ODDM loop. For example, one can run an IE-ODDM loop for decomposition in Fig. 2, where Domain A, B and C are three different sub-domains. When the loop starts, only the current on Domain A is updated. After that, the loop comes to Domain B and calculates the coupled effect. Meanwhile, the unchanged radiation patterns on Domain C are aggregated again, which has been done when the loop in Domain A. The same phenomenon occurs when the loop comes to Domain C.

In order to reduce the above hidden redundancy, one can modify the aggregation processes and design an optimized routine. The optimized combination is simply called IE-OMLFMA-ODDM. Compared with the original

combined method, completed MLFMA processes in IE-ODDM loops are replaced by simplified processes which consist of some simplified aggregation, translation and disaggregation processes. Moreover, different from the classification in the original combination, basis functions are grouped according to the decomposition, and oct-trees for different sub-domains are also replaced by oct-trees for different group, where aggregation processes of all groups has their exclusive oct-trees like in Fig. 2. More details are shown as Fig. 3. Because of these optimized techniques, the CPU time can be greatly saved, and the efficiency for solving coupled effects can be improved.

Compared with the original combined method, the proposed scheme is more efficient, but it needs extra memory to support this acceleration. There is a balance between the CPU time and the memory requirement. Although, extra memory requirement may not be a big problem for hardware, we can still save some memory from the proposed method by using some special localized data structures such as minimal-completed sub-trees. Like in Fig. 2, the sub-tree with leaves/nodes marked by left diagonal lines is a minimal-completed sub-tree of Group A. Since the aggregation process of Group A only updates radiation patterns of its group, the redundant leaves/nodes can be cut-down. As most of memory is occupied by those leaves/nodes in higher levels and most of redundant leaves have been cut-down by sub-trees, the application of this technique can efficiently save memory.

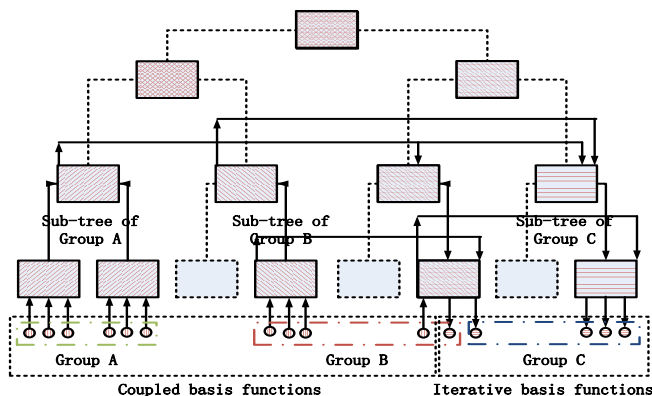


Fig. 2. Groups and their minimal-completed sub-trees. Different from the original MLFMA, leaves and nodes are grouped according to the decomposition. Sub-trees of groups are completed trees without a single node in one level. Because of the same original oct-tree, some nodes are of different sub-trees. Compared with direct aggregations, radiation patterns of groups are saved and reused.

1. Grouping basis functions as interior groups or edge group according to sub-domains;
2. Classifying oct-tree nodes as iterative or coupled nodes of each group;
3. IE-ODDM loop for scanning sub-domains and updating current repeatedly:
  - 3.1 Solving coupled-effect by the modified MLFMA:
    - 3.1.1 Aggregating radiation patterns of the edge group;
    - 3.1.2 Translating radiation patterns of other sub-domains to the iterative sub-domain;
    - 3.1.3 Aggregating, conversing and translating the radiation patterns of the buffer functions;
  - 3.2 Solving the self effect matrix equation by MLFMA;
  - 3.3 Updating the local current;
  - 3.4 Aggregating the radiation patterns of the interior function group of the current sub-domain;
4. Calculating the relative residual of the obtained result and the previous result;
5. Repeating Step 3 till the relative residual is satisfied.

Fig. 3. Detailed description of the proposed method.

#### IV. NUMERICAL RESULTS

In order to validate the correction and efficiency of the proposed IE-O-MLFMA-ODDM, the following three examples are considered.

##### Example I:

A PEC spherical object with a radius of  $5\lambda$  in Fig. 4 is considered, and the number of unknowns is 119,544. Its surface is divided into eight congruent sub-domains. The numbers of unknowns in iterative domains and coupled domains are 16,511 and 103,033, respectively. The CPU times for the calculation of coupled effects are listed in Table 1. It suggests that the CPU time utilized in the proposed method is about 25.0% of the time utilized in the original IE-MLFMA-ODDM. The extra memories for the radiation patterns of different groups are listed in Table 2. It suggests that the extra memory is about 1.2 times more than the memory utilized in the original IE-MLFMA-

ODDM. The RCS of two different methods are also shown as Fig. 4. The result of the proposed method agrees with the result of the original method, which validates the correction of the proposed method.

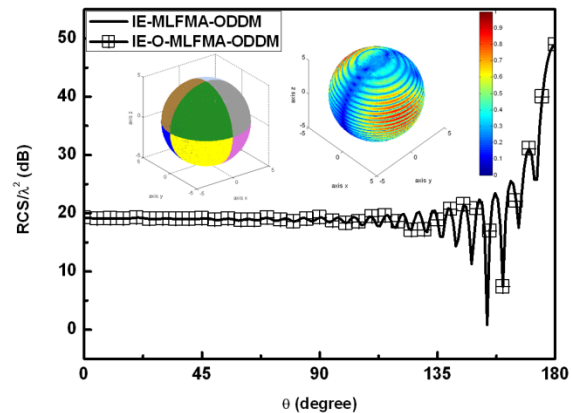


Fig. 4. The RCS and current of a spherical PEC object with a radius  $5\lambda$ .

Table 1: CPU time consumptions of coupled effects of a spherical PEC object

Sub-Domains	Unknowns		CPU Time of Coupled Effects (minutes)	
	Iterative	Coupled	Original Method	Proposed Method
D1	16,511	103,033	6.8530	1.6336
D2	16,511	103,033	6.6780	1.6198
D3	16,511	103,033	6.6892	1.6625
D4	16,511	103,033	6.6787	1.6233
D5	16,511	103,033	6.6990	1.6380
D6	16,511	103,033	6.7074	1.6408
D7	16,511	103,033	6.6962	1.6611
D8	16,511	103,033	6.6878	1.6520

Table 2: Memory requirements of coupled effects

Example	Unknowns	Memory Requirement of Coupled Effects (megabytes)	
		Original Method	Proposed Method
I	119,544	35.7432	43.7757
II	117,450	52.5482	85.4319
III	188,202	86.7601	145.506

**Example II:**

A PEC airplane-type object in Fig. 5 is considered, and the number of unknowns is 117,450. Its surface is divided into six sub-domains. The numbers of unknowns in iterative domains vary from 13,274 to 32,450, and the numbers of unknowns in coupled domains vary from 104,176 to 85,000. Table 3 lists the CPU time for the calculation of coupled effects, which suggests that the CPU time utilized in the proposed method is about 29.0% (varying from 23.7% to 37.3%) of the time utilized in the original IE-MLFMA-ODDM. Table 2 suggests that the extra memory is about 1.6 times more than the memory utilized in the original IE-MLFMA-ODDM. Figure 5 shows that two RCS from different methods can well agree with each other.

6 shows that two RCS from different methods can well agree with each other.

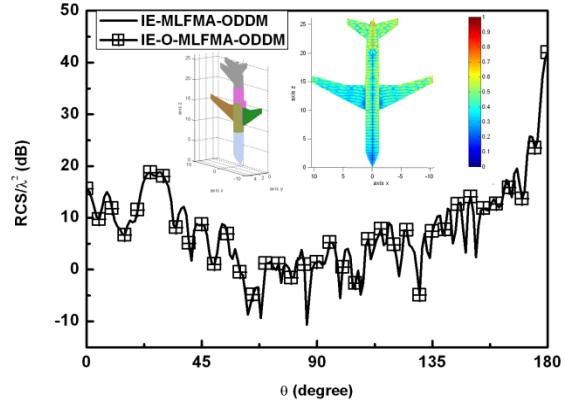


Fig. 5. The RCS and current of an airplane-type PEC object.

**Example III:**

A PEC missile-type object in Fig. 6 is considered, and the number of unknowns is 188,202. Its surface is divided into five sub-domains. The numbers of unknowns in iterative domains vary from 11,521 to 55,978, and the numbers of unknowns in coupled domains vary from 176,681 to 132,224. Table 4 lists the CPU time for the calculation of coupled effects, which suggests that the CPU time utilized in the proposed method is about 50.6% (varying from 31.5% to 62.8%) of the time utilized in the original IE-MLFMA-ODDM. Table 2 suggests that the extra memory is about 1.6 times more than the memory utilized in the original IE-MLFMA-ODDM. Figure

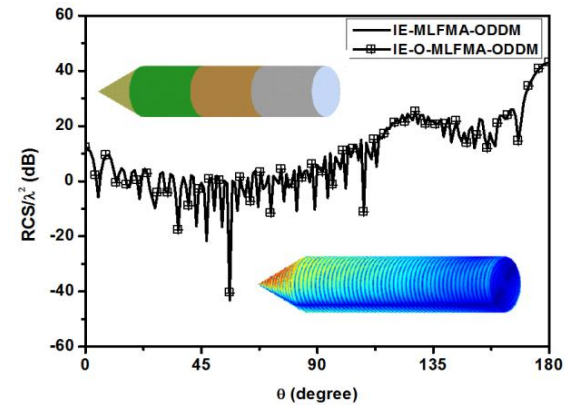


Fig. 6. The RCS and current of a missile-type PEC object.

Table 3: CPU time consumptions of coupled effects of an airplane-type PEC object

Sub-Domains	Unknowns		CPU Time of Coupled Effects (minutes)	
	Iterative	Coupled	Original Method	Proposed Method
D1	19,140	98,310	6.7515	1.8571
D2	32,450	85,000	7.2072	2.6894
D3	19,189	98,261	6.7760	1.9460
D4	19,495	97,955	6.6570	1.8158
D5	13,274	104,176	6.5534	1.5547
D6	20,941	96,509	6.9181	2.0461

Table 4: CPU time consumptions of coupled effects of a missile-type PEC object

Sub-Domains	Unknowns		CPU Time of Coupled Effects (minutes)	
	Iterative	Coupled	Original Method	Proposed Method
D1	11,521	176,681	3.5104	1.1057
D2	55,978	132,224	3.6260	1.9685
D3	52,986	135,216	3.6794	2.3107
D4	54,881	133,321	3.6226	2.2333
D5	22,615	165,587	3.5117	1.5016

The above numerical results and comparisons suggest that the proposed method can greatly improve the efficiency of combined method, and the improvement depends on the decomposition. More fine decomposition, more high performance. Moreover, we can find that the memory required to save the radiation patterns grows with the problem size, and the extra memory of saving radiation patterns is about 1.5 times more than the memory required in the original completed MLFMA process. Considering the good performance of MLFMA and the development of hardware, we think this extra memory requirement is meaningful and can be acceptable to improve a high computational efficiency.

## V. CONCLUSION

In the present paper, we improve the combined method of overlapped domain decomposition method and multilevel fast multi-pole algorithm. In the proposed method, amount of independent MLFMA processes for different sub-domains are departed, reduced redundancies and re-integrated with IE-ODDM loops, so that aggregations of sub-domains can be simplified and radiation patterns can be reused. Meanwhile, localized data structures of minimal-completed sub-trees are used to reduce memory redundancies. Numerical results show that the proposed method can improve the efficiency of combined method with acceptable extra memory.

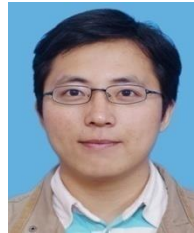
## ACKNOWLEDGMENT

This work was supported in part by National Natural Science Foundation of China (No. 61301019), and in part by State Key Laboratory of Millimeter Waves (No. K201306).

## REFERENCES

- [1] R. F. Harrington, "Field computation by moment method," *New York: McMillan*, 1968.
- [2] N. Engheta, W. D. Murphy, V. Rokhlin, et.al., "The fast multipole method (FMM) for electromagnetic scattering problems," *IEEE Trans. Antennas Propag.*, vol. 40, pp. 634-641, 1992.
- [3] J. M. Song and W. C. Chew, "Multilevel fast multipole algorithm for solving combined field integral equations of electromagnetic scattering," *Microwave Opt. Technol. Lett.*, vol. 10, pp. 14-19, 1995.
- [4] J. M. Song, C. C. Lu, and W. C. Chew, "Multilevel fast multipole algorithm for electromagnetic scattering by large complex objects," *IEEE Trans. Antennas Propag.*, vol. 45, pp. 1488-1493, 1997.
- [5] E. Bleszybski, M. Bleszynski, and T. Jaroszewicz, "AIM: adaptive integral method for solving large-scale electromagnetic scattering and radiation problems," *Radio Science*, vol. 31, pp. 1225-1251, 1996.
- [6] Y. Zhang, D. Huang, and J. Chen, "Combination of asymptotic phase basis functions and matrix interpolation method for fast analysis of monostatic RCS," *Applied Computational Electromagnetics Society (ACES) Journal*, vol. 28, pp. 49-56, 2013.
- [7] N. Carpentieri, Y. F. Jing, T. Z. Huang, W. C. Pi, and X. Q. Sheng, "Combining the CORS and BiCORSTAB iterative methods with MLFMA and SAI preconditioning for solving large linear systems in electromagnetics," *Applied Computational Electromagnetics Society (ACES) Journal*, vol. 27, pp. 102-111, 2012.
- [8] Z. N. Jiang, R. S. Chen, Z. H. Fan, S. G. Shen, and X. Q. Hu, "Efficient multilevel compressed block decomposition for large-scale electromagnetic problems using asymptotic phasefront extraction," *Applied Computational Electromagnetics Society (ACES) Journal*, vol. 26, pp. 876-885, 2011.
- [9] M. Chen, R. Chen, Z. Fan, and D. Ding, "Accelerating the multilevel fast multipole method with parallel preconditioner for large-scale scattering problems," *Applied Computational Electromagnetics Society (ACES) Journal*, vol. 26, pp. 815-822, 2011.
- [10] Z. N. Jiang, Z. H. Fan, D. Z. Ding, R. S. Chen, and K. W. Leung, "Preconditioned MDA-SVD-MLFMA for analysis of multi-scale problems," *Applied Computational Electromagnetics Society (ACES) Journal*, vol. 25, pp. 914-925, 2010.
- [11] H. Fangjing, N. Zaiping, and H. Jun, "An efficient

- parallel multilevel fast multipole algorithm for large-scale scattering problems,” *Applied Computational Electromagnetics Society (ACES) Journal*, vol. 25, pp. 381-387, 2010.
- [12] M. R. Pino, et al., “The generalized forward-backward method for analyzing the scattering from targets on ocean-like rough surfaces,” *IEEE Trans. Antennas Propag.*, vol. 47, pp. 961-969, 1999.
- [13] C. Brennan, P. Cullen, and M. Condon, “A novel iterative solution of three dimensional electric field integral equation,” *IEEE Trans. Antennas Propag.*, vol. 52, pp. 2781-2784, 2004.
- [14] W. D. Li, W. Hong, and H. X. Zhou, “Integral equation-based overlap domain decomposition method for the analysis of electromagnetic scattering of 3D conducting object,” *Microwave Opt. Technol. Lett.*, vol. 49, pp. 265-274, 2007.
- [15] J. Hu, W. Hong, H. X. Zhou, W. D. Li, and Z. Song, “An overlapped domain decomposition method for solving electromagnetic surface integral equations,” *International Conference on Computational Problem-Solving (ICCP)*, Lijiang, pp. 1-4, 2010.
- [16] W. D. Li, W. Hong, and H. X. Zhou, “An IE-ODDM-MLFMA scheme with DILU preconditioner for analysis of electromagnetic scattering from large complex objects,” *IEEE Trans. Antennas Propag.*, vol. 56, pp. 1368-1380, 2008.
- [17] W. D. Li, W. Hong, and H. X. Zhou, “A cube-based scheme of IE-ODDM-MLFMA for electromagnetic scattering problems,” *IEEE Antennas and Wireless Propagation Letters*, vol. 8, pp. 630-633, 2009.
- [18] J. Chen, S. Li, and Y. Song, “Analysis of electromagnetic scattering problems by means of a VSIE-ODDM-MLFMA method,” *Applied Computational Electromagnetics Society (ACES) Journal*, vol. 27, pp. 660-667, 2012.
- [19] A. A. Kucharski, “Efficient solution of integral-equation based electromagnetic problems with the use of macromodels,” *IEEE Trans. on Antennas Propag.*, vol. 56, pp. 1482-1487, 2008.
- [20] L. Carin, “Fast electromagnetic solvers for large-scale naval scattering problem,” *Final Report for Office of Naval Research*, September 2008.
- [21] P. Yla-Oijala and M. Taskinen, “Electromagnetic scattering by large and complex structures with surface equivalence principle algorithm,” *Waves in Random and Complex Media*, vol. 19, pp. 105-125, 2009.
- [22] L. M. Jaime, “Técnicas de descomposición de dominios con ecuación integral para el análisis eficiente de problemas electromagnéticos,” *Tesis Doctoral, Universidad De Oviedo*, April 2010.
- [23] J. A. Kong, “Electromagnetic wave theory,” *New York: Wiley*, 1981.
- [24] S. M. Rao, D. R. Wilton, and A. W. Glisson, “Electromagnetic scattering by surfaces of arbitrary shape,” *IEEE Trans. Antennas Propag.*, vol. 3, pp. 409-418, 1982.



**Jun Hu** received the B.S., M.S. and Ph.D. degrees from Southeast University, Nanjing, in 2004, 2007 and 2011, respectively. Now, he is with Nanjing University of Science and Technology, Nanjing, China. His current interests include Green's functions in layered medium, domain decomposition methods, and optimization algorithms for passive component designing. He is a Member of IEEE and ACES, and also serves as Reviewer of IEEE T-AP.

# Real-Time Implementation of UWB-OFDM SAR Imaging System Using Shared Memory Based FPGA

Md Anowar Hossain, Ibrahim Elshafiey, and Majeed A. S. Alkanhal

Department of Electrical Engineering  
King Saud University, Riyadh, Kingdom of Saudi Arabia  
ahossain@ksu.edu.sa, ishafiey@ksu.edu.sa, majeed@ksu.edu.sa

**Abstract**— This paper presents a novel technique for FPGA based implementation of high-resolution SAR system using UWB-OFDM architecture. Greater computation time and larger memory requirement are the main difficulties in processing large amount of raw data in real-time SAR imaging. Significant part of the computation time is related to range and azimuth compression of raw SAR data which in turns heavily depends on computing FFT, IFFT and complex multiplication. A shared memory based FPGA model is developed using Xilinx block-set that provides real-time SAR imaging with higher accuracy and less computation time. The design procedures are straightforward and can be applied to practical SAR system for real-time imaging. The model is designed as hardware co-simulation using Xilinx system generator and implemented on Xilinx Virtex-6 ML605 FPGA.

**Index Terms** — Field Programmable Gate Array (FPGA), Orthogonal Frequency Division Multiplexing (OFDM), Synthetic Aperture Radar (SAR), Ultra-Wideband (UWB).

## I. INTRODUCTION

Synthetic Aperture Radar (SAR) is used to achieve high-resolution images of a terrain. SAR transmits signals at spaced intervals called Pulse Repetition Intervals (PRI). The reflections at each PRI are processed together to reconstruct a radar image [1]. In general, high-resolution SAR imaging is obtained using UWB waveforms as radar transmitted pulse. UWB pulses (500-MHz bandwidth and above) can enhance the range resolution considerably [2].

OFDM is a digital modulation scheme that

shows a great potential to be used as radar waveforms. OFDM signal consists of several orthogonal sub-carriers, emitted over a single transmission path simultaneously. Each sub-carrier contains a small portion of the entire signal bandwidth [3]. Technology advances facilitates higher sampling speed, allowing accurate generation of UWB-OFDM waveforms. This results in a diverse signal that is capable of high resolution imaging.

Although OFDM has been studied and implemented in the digital communication field, it has not yet been widely considered by the radar scientific community rather than few efforts [4,5].

FPGA implementation of SAR imaging is presented in [6]. However, the processing steps were too complicated using both C++ and HDL platform. Real-time SAR imaging by FPGA is introduced in [7] and the processing result of a frame of airborne SAR data is demonstrated. The computation time of 12.8 ns for 1024-point FFT has been achieved using Altera Stratix II FPGA. FPGA implementation of synthetic aperture radar application is shown in [8] and reasonable speedup has been achieved when compared to a software solution. SAR processing with General-Purpose Graphics Processing Units (GPGPUs) is described in [9]. GPU-based *omega-k* tomographic processing by 1D non-uniform FFTs is introduced in [10]. However, incorporating GPU hardware into systems adds expense in terms of power consumption, heat production, and cost.

Greater computation time is a characteristic of SAR imaging algorithms that poses a particularly serious problem for real-time

application. Advances in the operating speed of the FPGA allow signal processing applications to be solved in commercially available hardware. Because of their highly parallel nature, a 10 to 20 times increase in SAR processing speed is expected using modern FPGAs compared to multi-node RISC processors such as the PowerPC. Historically, FPGAs were much harder to program than a processor. Recently, system generator for DSP from Xilinx® has made FPGA technology accessible to DSP engineers. Xilinx System Generator pioneered the idea of compiling an FPGA program from a high-level Simulink model based on Xilinx block-sets [11].

## II. UWB OFDM SIGNAL GENERATION

UWB-OFDM signal is generated by randomly populating the digital frequency domain vector as:

$$\Psi_{\omega} = [\Pi_{ns} \ \Pi_0 \ \Pi_{ps}], \quad (1)$$

where  $\Pi_{ps}$  and  $\Pi_{ns}$  represent the positive and negative sub-carriers respectively, whereas  $\Pi_0$  represents the baseband DC value. IFFT is then applied to  $\Psi_{\omega}$  to obtain the discrete time-domain OFDM signal as:

$$\Psi_{tx}(t) = F^{-1}[\Psi_{\omega}]. \quad (2)$$

For example, UWB-OFDM waveform can be generated using the following parameters: number of OFDM sub-carriers=256, sampling time,  $\Delta t_s=1$  ns results in baseband bandwidth,  $B_0=1/2\Delta t_s=500$  MHz, dividing by a factor of two to satisfy Nyquist criterion. When  $\Pi_{ps}$  is randomly populated and modulation scheme is chosen as BPSK, the waveform is noise-like as shown in Fig. 1.

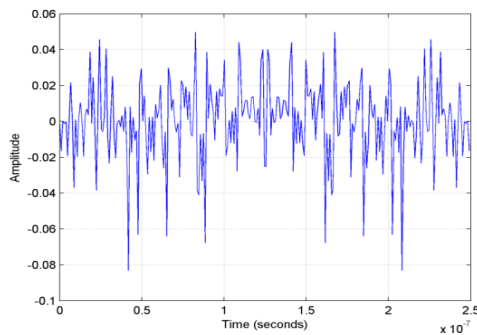


Fig. 1. UWB-OFDM signal using random sub-carriers.

## III. RAW DATA GENERATION

Raw SAR data are generated based on simulation parameter shown in Table 1, using a gray-scale image of a ‘battle tank’ as a target profile. The input image is converted to a matrix. The position of each element is considered as the range and cross-range of the point target while the normalized value of each element of the matrix is used as reflectivity of the target.

At each synthetic aperture position, UWB-OFDM waveform is transmitted and the time-delayed signals reflected from the target are stored to form the raw SAR image space as shown in Fig. 2. The received radar signal is given as:

$$\Psi_{rx}(t, u) = \sum_{n=1}^N \sigma_n \Psi(t - t_{dn}) + \eta(t), \quad (3)$$

where  $N$ ,  $\sigma_n$  and  $t_{dn}$  are the number of targets, reflectivity and round-trip time delay associated with  $n^{th}$  target respectively. The term  $\eta(t)$  denotes the AWGN. The round-trip delay  $t_{dn}$  is given by:

$$t_{dn} = \frac{2}{c} \sqrt{(X_c + x_n)^2 + (y_n - u)^2}, \quad (4)$$

where  $X_c$  is the range distance to the center of the swath and  $(x_n, y_n)$  represents the location of the  $n^{th}$  target. The term  $u$  and  $c$  represents the synthetic aperture positions in azimuth direction and speed of light respectively.

Table 1: Simulation parameters

Parameter	Symbol	Value
Pulse Repetition Frequency	PRF	1024 Hz
Duration of flight	Dur	4 seconds
Velocity of the platform	$V_p$	200 m/s
Baseband bandwidth	$B_0$	500 MHz
Carrier frequency	$f_c$	7.5 GHz
Number of OFDM sub-carrier	$N_{sub}$	256
Range distance to center of swath	$X_c$	20 Km
Half target area width	$X_0$	200 m

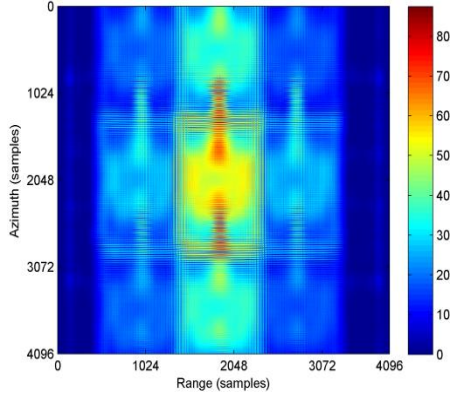


Fig. 2. Raw SAR image (battle tank).

#### IV. RANGE AND AZIMUTH COMPRESSION

Different imaging algorithms such as Range-Doppler algorithm and Omega-k algorithm can be used to process raw SAR data to reconstruct the final SAR image [12]. Almost all imaging algorithms perform matched filtering separately in range and cross-range domains. Range compression is performed by match filtering between each row of raw data and range reference signal as:

$$\Psi_{Mx}(t, u) = F^{-1} \left[ \Psi_{rx}(\omega, u) \Psi_{ref}^*(\omega, u) \right]. \quad (5)$$

The range reference signal  $\Psi_{ref}(\omega, u)$  is an ideal echo signal from a unit reflector at the center of the current range swath and is given in time-domain by:

$$\Psi_{ref}(t, u) = \Psi(t - t_{d0}), \text{ where } t_{d0} = \frac{2X_c}{c}. \quad (6)$$

Azimuth compression is obtained by match filtering in frequency domain between each column of the range compressed data and azimuth reference signal. IFFT is then applied to reconstruct the final SAR image. Azimuth reference signal is an ideal return from a unit reflector located at the center of the swath, i.e.,  $(x_n, y_n) = (X_c, 0)$  and is given as:

$$\Psi_{azref}(\omega, u) = e^{-j \frac{2\omega}{c} \sqrt{X_c^2 + u^2}}. \quad (7)$$

#### V. FPGA IMPLEMENTATION

Shared memory based FPGA model is designed to reduce the computation time in range and azimuth compression and to achieve real-time SAR imaging. The prominent blocks used in

the developed FPGA model from Xilinx block-set are introduced in the following subsections.

##### A. System generator

System Generator block provides control of system and simulation parameters, and is used to invoke the code generator. This block is also referred as System Generator “token” because of its unique role in the design. Every Simulink model containing any element from the Xilinx Block-set must contain at least one System Generator block. Once a System Generator block is added to a model, it is possible to specify how code generation and simulation should be handled. System Generator automatically compiles designs into low-level representations. Designs are compiled and simulated using the System Generator block. When the type is a variety of hardware co-simulation, then System Generator produces an FPGA configuration bit-stream that is ready to run in an actual hardware based on FPGA platform. System Generator also produces a hardware co-simulation block to which the bit-stream is associated. This block is able to participate in Simulink simulations. In a simulation, the block delivers the same results as those produced by the portion, but the results are computed in actual hardware, which speed up the computation time dramatically.

##### B. Shared memory

Xilinx shared memory block implements a Random Access Memory (RAM) that can be shared among multiple designs or sections of a design. A shared memory block is uniquely identified by its name. Instances of shared memories of same name within the same model automatically share the same memory space. These interfaces make it possible for hardware-based shared memory resources to map transparently to common address spaces on a host PC. System generator’s hardware co-simulation interfaces allow shared memory to be compiled and co-simulated in FPGA hardware. Shared memories facilitate high-speed data transfers between the host computer and FPGA, and bolster the tool’s real-time hardware co-simulation capabilities. The access to the shared memory can either be Lockable or Unprotected. An unprotected memory has no restrictions concerning when a read or write can occur. In a

locked shared memory, the block can only be written to when granted access to the memory. When the grant port outputs a 1, access is granted to the memory and the write or read request can proceed. The depth specifies the number of words in the memory. The word size is inferred from the bit width of the data input port.

### C. Shared memory write/shared memory read

The Xilinx shared memory write block facilitates a high-speed interface for writing data into a Xilinx shared memory object. The shared memory write block is driven by the vector or matrix signal containing the data to be written into the shared memory object.

## VI. FPGA MODEL FOR RANGE/AZIMUTH COMPRESSION

The schematic block diagram of the proposed FPGA model shown in Fig. 3 includes: input buffer subsystem, FFT and IFFT block, complex multiplier and output buffer subsystem. The developed FPGA model based on Xilinx block-set is presented in Fig. 4. The design consists of two subsystems that implements input and output buffer storage, named input and output buffer storage, named input and output buffer subsystem as shown in Figs. 5 and 6 respectively.

Each buffering subsystem consists of two

shared memory blocks to provide the buffer storage for real and imaginary part of the raw data and output data respectively. Each shared memory is wrapped by logic circuitry (Counter, SR Flip-flops, delay and relational blocks) that controls the flow of data from the host computer, through the FPGA interface, and back to the host computer. This circuitry enables high-speed transfers of the memory data when the FPGA acquires or releases lock of the shared memory. It takes advantage of the lockable shared memory mutual exclusion to implement a high speed I/O buffering interface for hardware co-simulation. The Fast Fourier Transform block computes the FFT of the SAR raw data and the FFT of reference data is computed in MATLAB<sup>®</sup> for resource optimization as it is a row (column) matrix with fewer samples. The output of FFT block and the output of the shared memories of reference data are fed to the complex multiplier. Inverse Fast Fourier Transform block then computes IFFT of the data found after complex multiplication. Finally, the real and imaginary part of the output data is separately stored in two shared memories named shared memory (Real\_out) and shared memory (Imag\_out) inside the output buffer subsystem.

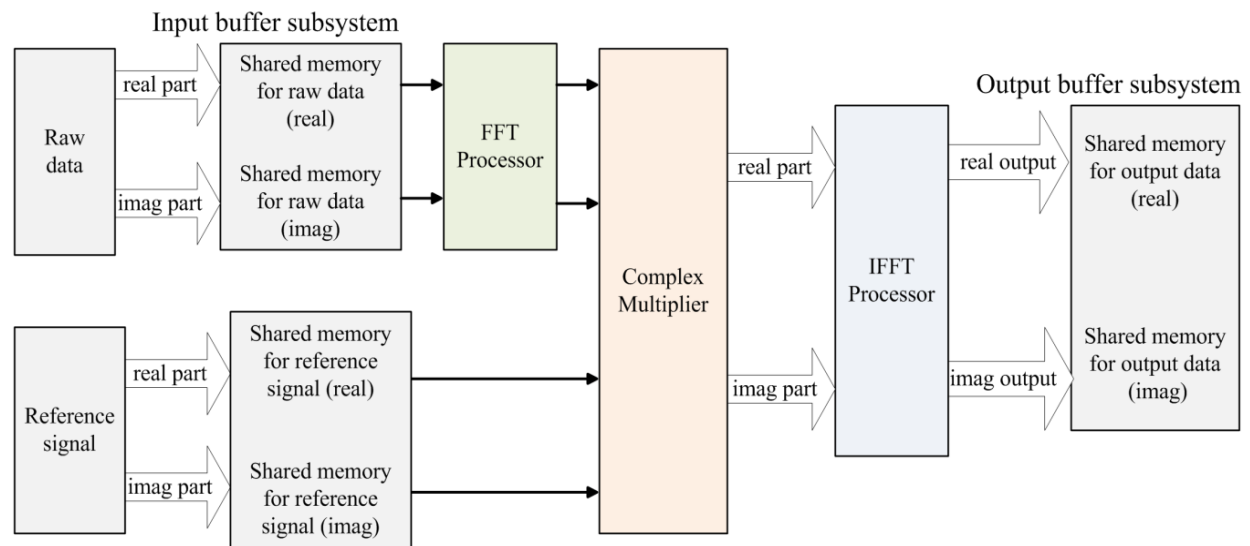


Fig. 3. Schematic block diagram of the proposed FPGA model.

Shared Memory based FPGA Model for Range/Azimuth Compression

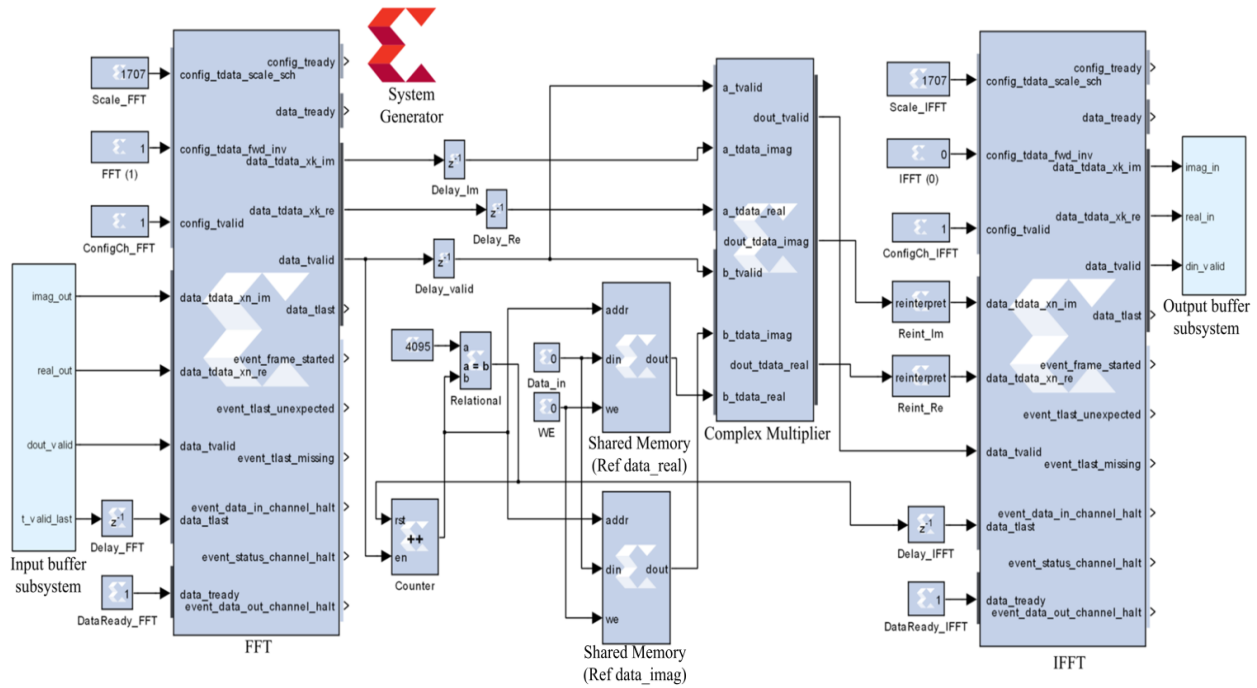


Fig. 4. FPGA model for real-time SAR imaging.

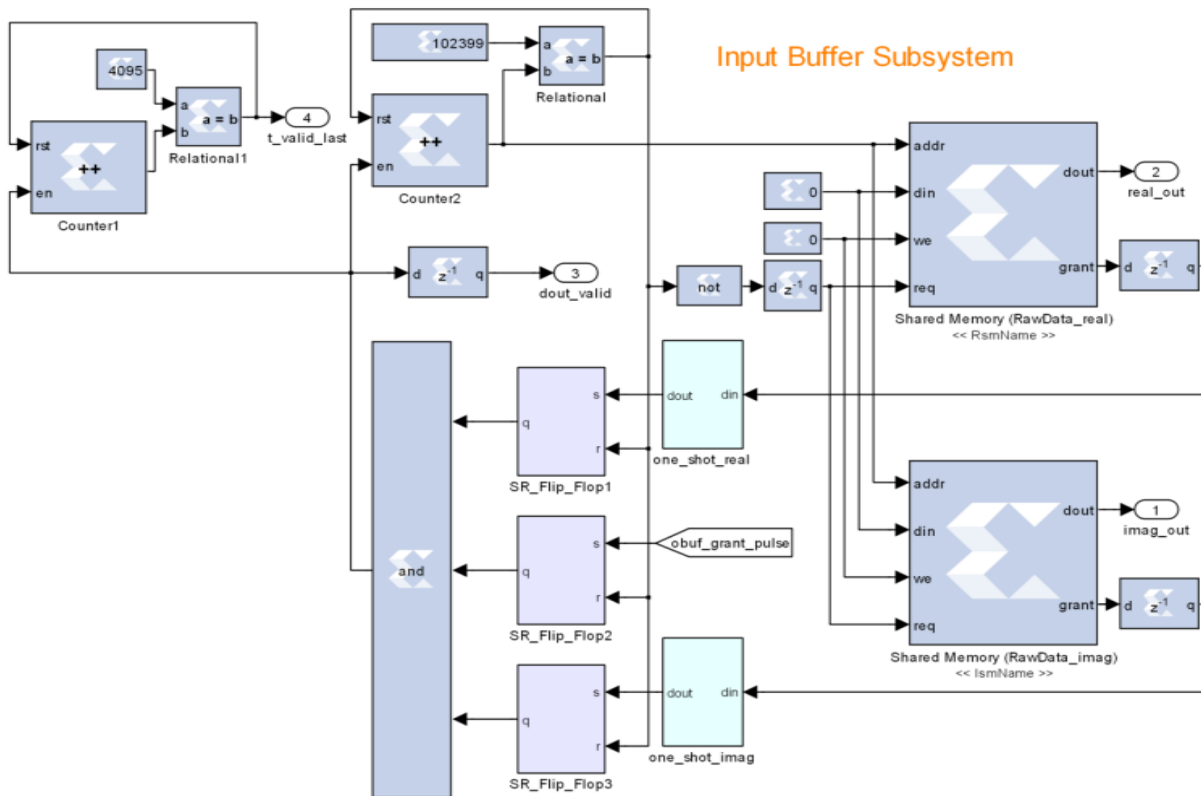


Fig. 5. Input buffer subsystem.

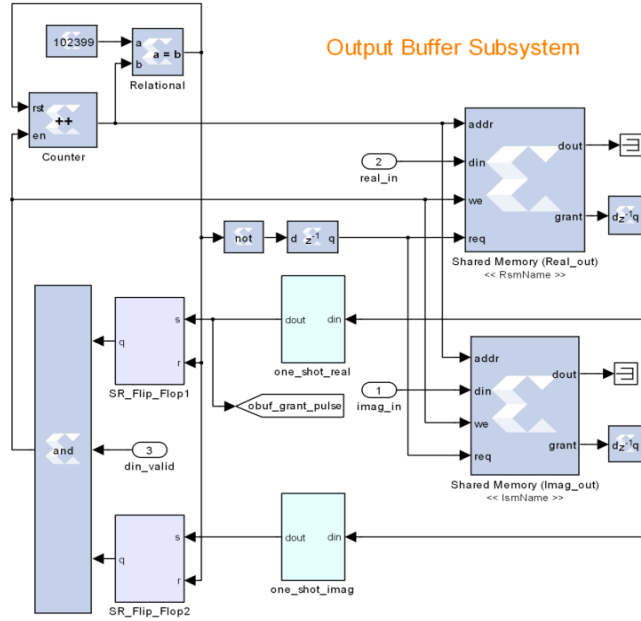


Fig. 6. Output buffer subsystem.

**VII. TESTBENCH MODEL**

The FPGA model shown in Fig. 4 is then compiled using system generator to generate hardware co-simulation block. A testbench model shown in Fig. 7 is designed which includes the hardware co-simulation block. The test-bench model includes a ‘From Workspace’ block from Simulink to read the SAR raw data from a \*.MAT file. The real and imaginary part of the data is separated and written to two lockable shared memories named shared memory write (Real\_data) and shared memory write (Imag\_data). Similar name is used for the shared memories inside the input buffer subsystem so that the data are shared to the FPGA hardware.

Finally, the real and imaginary part of the FPGA processed output data are stored into shared memory write blocks named shared memory write (Real\_out) and shared memory write (Imag\_out). To control the data processing flow shown in Fig. 8, the blocks provided in the testbench model is pre-configured with appropriate priorities for proper wake-up sequence such as: shared memory write (1), hardware co-simulation block (2) and shared memory read (3). The operation of the model is described as follows: (a) Shared memory write blocks wake up and request a lock of the input buffer lockable shared memories. Once lock is granted, the blocks write the data into lockable shared memories and release the lock. (b) The hardware co-simulation block then wakes up and the host computer shared memory data are transferred to the FPGA. The FPGA processes the input buffer data and writes the output into the output buffer shared memories. Finally, the FPGA releases lock, causing the FPGA shared memory data to be transferred back to the host computer. (c) Shared memory read blocks wake up and request a lock of the output buffer lockable shared memories. The blocks read data from output buffer and drive its output port with the processed output data. The experimental test is then performed using the raw data generated by

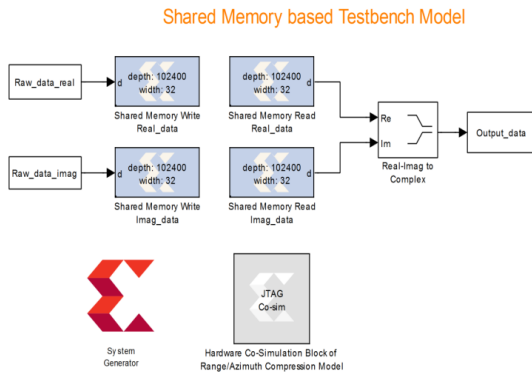


Fig. 7. Testbench Model.

using gray-scale image of a ‘battle tank’ as a target profile. Range compression is performed by feeding raw data to testbench model and running the model on Xilinx Virtex-6 ML605

FPGA [11]. Figure 9 shows the SAR image after range compression. Finally, azimuth compression is accomplished by using the same model to reconstruct the final SAR image shown in Fig. 10.

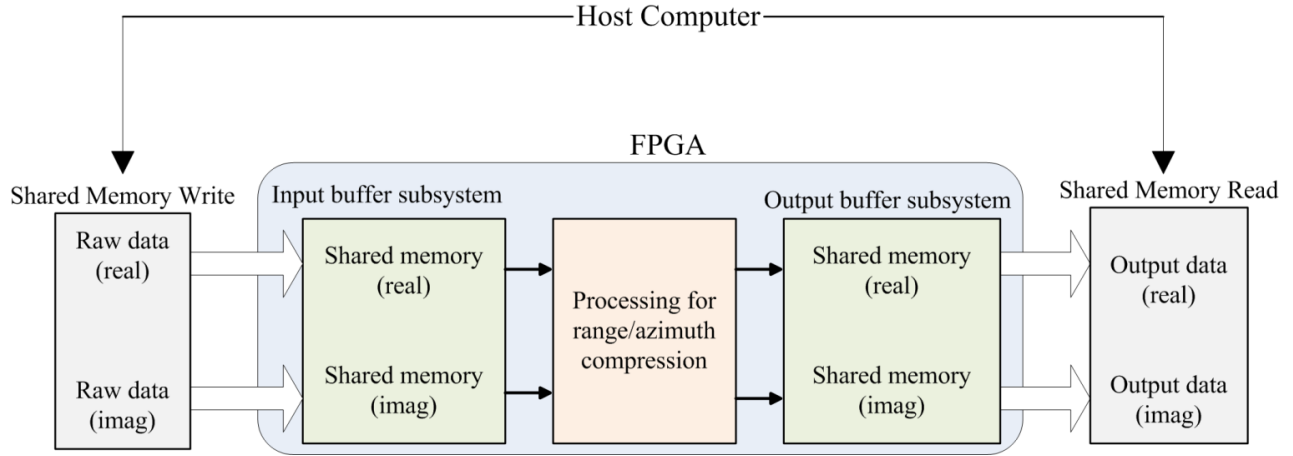


Fig. 8. Data Processing flow.

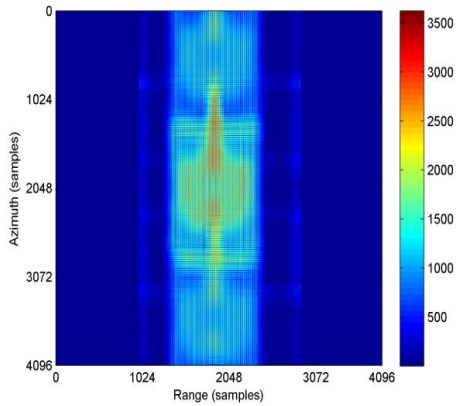


Fig. 9. SAR image after range compression.

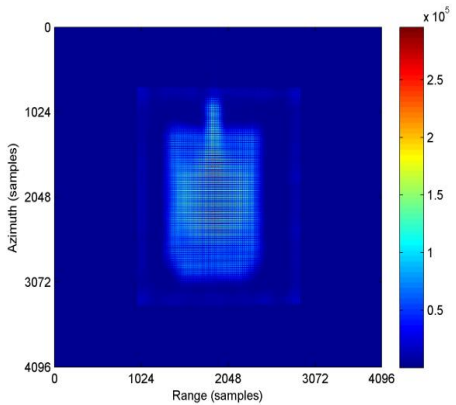


Fig. 10. Final SAR image after azimuth compression.

### VIII. RESULTS AND DISCUSSIONS

The error level of FPGA output in comparison with MATLAB® results is shown in Fig. 11. As the difference between MATLAB results and FPGA output are extremely low, these results are computed by subtracting the FPGA output from MATLAB® output. It is observed that very low error fluctuated between 0 and .0001, i.e., at 4<sup>th</sup> decimal place which is negligible. Significant parts of the errors arise from the truncation at the complex multiplier output. The reason behind the FPGA output with lower error is that the raw data is converted into integer format before feeding to FPGA.

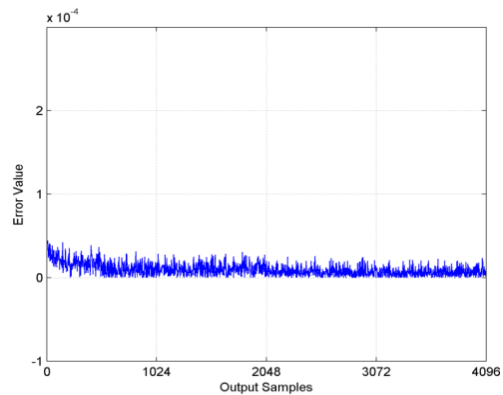


Fig. 11. Error level comparison of FPGA output and MATLAB® simulated results.

Data can be written to or read from unprotected shared memory blocks at any time. This type of memory has no mutual exclusion. Data transfers to and from an unprotected shared memory occurs a single-word at a time, unlike the high-speed data transfer mode used by lockable shared memories. The computation time and maximum frequency for both lockable and unprotected shared memory are compared and tabulated in Table 2. It is observed that the lockable shared memory requires less computation time as compared to unprotected shared memory.

Table 2: Computation time and frequency

Shared Memory Type	FPGA Clock	Maximum Frequency
Lockable	2.97 ns	335.68 MHz
Unprotected	3.99 ns	250.43 MHz

The significant reduction in computation time can be achieved by taking the advantage of parallel processing of FPGA, i.e., by running several hardware co-simulation blocks simultaneously. However, the major drawback is the memory I/O time. Table 3 shows the speedups with FPGA against a typical CPU using MATLAB for different image sizes. It is observed that FPGA processing achieves better speeds against CPU processing as the amount of data (image size) increases.

Table 3: Comparison of processing time for different image size

Image Size	CPU Processing (MATLAB)	FPGA Processing
4096×4096	4.24 sec	2.98 ns
8192×8192	8.96 sec	5.18 ns
16384×16384	18.27 sec	9.68 ns

Table 4 summarizes the resource estimation. It is observed that the lockable shared memory requires more resources than unprotected shared memory because it uses some logic circuitry to handle mutual exclusions. On the other hand, lockable shared memory requires less

computation time as shown in Table 2. Thus, lockable shared memory is the best choice for the proposed FPGA model.

Table 4: Resource estimation

Component	Shared Memory Type	
	Lockable	Unprotected
Flipflop	6%	5%
LUTs	8.5%	7%
BRAM	3.6%	3.6%
IOB	73%	72.5%
DSP48s	12.5%	10%

## IX. CONCLUSION

Real-time imaging of UWB-OFDM SAR system has been investigated using the high speed Xilinx Virtex-6 ML605 FPGA. FPGA output of the FFT/IFFT and complex multiplications as part of match filtering are compared with simulated results obtained under standard CPU (MATLAB<sup>®</sup>) processing. Experimental results show that FPGA implementation using shared memory approach is effective to implement SAR imaging algorithm and provides a real-time tool for SAR imaging.

## ACKNOWLEDGEMENTS

This work is funded in part by the National Plan for Science and Technology, Saudi Arabia, under project number: 08-ELE262-2. The research is also supported by the Deanship of the Scientific Research and the Research Center at the College of Engineering, King Saud University, Saudi Arabia.

## REFERENCES

- [1] M. Soumekh, "Synthetic aperture radar signal processing," *A Wiley-Interscience Publication*, United States of America, 1999.
- [2] J. D. Taylor, "Ultra-wideband radar technology," *CRC Press*, 2000.
- [3] L. Hanzo, M. Münster, B. Choi, and T. Keller, "OFDM and MC-CDMA," *Wiley*, March 2004.
- [4] M. A. Hossain, I. Elshafiey, and M. A. Alkanhal, "High resolution UWB SAR based on OFDM architecture," *2011 3<sup>rd</sup> International Asia-Pacific Conference on Synthetic Aperture Radar (APSAR)*, pp. 1-4, 2011.
- [5] M. A. Hossain, I. Elshafiey, M. A. Alkanhal, and A. Mabrouk, "Anti-jamming capabilities of UWB-OFDM SAR," *2011 European Radar*

- Conference (EuRAD)*, pp. 313-316, 2011.
- [6] C. Le, S. Chan, F. Cheng, W. Fang, M. Fischman, S. Hensley, R. Johnson, M. Jourdan, M. Marina, and B. Parham, "Onboard FPGA-based SAR processing for future spaceborne systems," 2004.
- [7] X. Xiao, R. Zhang, X. Yang, and G. Zhang, "Realization of SAR real-time processor by FPGA," *In IGARSS 2004 IEEE International Geoscience and Remote Sensing Symposium*, pp. 3942-3944, 2004.
- [8] J. Greco, G. Cieslewski, A. Jacobs, I. A. Troxel, and A. D. George, "Hardware/software interface for high-performance space computing with FPGA coprocessors," *In Aerospace Conference, 2006 IEEE*, p. 10, 2006.
- [9] M. Di Bisceglie, M. Di Santo, C. Galdi, R. Lanari, and N. Ranaldo, "Synthetic aperture radar processing with GPGPU," *Signal Processing Magazine, IEEE*, vol. 27, pp. 69-78, 2010.
- [10] A. Capozzoli, C. Curcio, and A. Liseno, "GPU-based  $\omega$ -k tomographic processing by 1D non-uniform FFTs," *Progress In Electromagnetics Research M*, vol. 23, pp. 279-298, 2012.
- [11] Xilinx Inc. (January, Xilinx Website. [Online], "Xilinx ISE design suite 13.4," <http://www.xilinx.com/>.
- [12] I. G. Cumming and F. H. C. Wong, "Digital processing of synthetic aperture radar data: algorithms and implementation," *Artech House*, 2005.



**Md Anwar Hossain** received his B.S. degree in Computer and Communication Engineering from International Islamic University Chittagong (IIUC), Bangladesh in 2005 and his M.S. degree in Electrical Engineering from King Saud University, Saudi Arabia in 2012. He has been working as a Researcher in the Department of Electrical Engineering, King Saud University, from October 2008 till now. Currently, he is pursuing his Ph.D. degree in Electrical Engineering at King Saud University. His research interests include UWB radar, Synthetic Aperture Radar (SAR) imaging, radar jamming and anti-jamming, radar signal processing and FPGA based real-time signal processing.



**Ibrahim Elshafiey** received his B.S. degree in Communications and Electronics Engineering from Cairo University in 1985. He obtained his M.S. and Ph.D. degrees from Iowa State University in 1992 and 1994, respectively. He is currently a

Professor in the Electrical Engineering Department, King Saud University, on loan from the Electrical Engineering Department, Fayoum University, Egypt. His research interests include computational electromagnetics, biomedical imaging and nondestructive evaluation.



**Majeed A. S. Alkanhal** received his B.S. and M.S. degrees from King Saud University, Riyadh, Saudi Arabia, in 1984 and 1986 respectively, and the Ph.D. degree from Syracuse University, Syracuse, NY, in 1994, all in Electrical Engineering. He is presently a Professor in the Electrical Engineering Department at King Saud University, Riyadh, Saudi Arabia. His research interests are in antennas and propagation, computational electromagnetics, and microwave engineering.

# Normal Directional NURBS Arithmetic of Conformal PML

Y. J. Zhang and X. H. Zhang

School of Aeronautics  
Northwestern Polytechnical University, Xi'an, 710072, P. R. China  
zyj19191@nwpu.edu.cn

**Abstract** — Conformal Perfectly Matched Layer (PML) is a high-efficiency absorbing boundary condition for the finite element analysis of electromagnetic fields. Accurate calculation of normal direction of conformal PML is essential for the geometric modelling of conformal shell elements and constitutive parameters of conformal PML, especially for sophisticated and arbitrary shape scatterers. Consequently, a Non-Uniform Rational B-Splines (NURBS) arithmetic is proposed for describing the conformal surface accurately in this study. Based on the NURBS arithmetic, four weighted average formulas are presented for calculating the common normal direction of adjacent surface elements of conformal shell. Numerical experiments show the availability of NURBS arithmetic and precision of weighted average formulas in the geometrical modelling of conformal PML.

**Index Terms** — Common normal direction, conformal PML, finite element modeling, NURBS arithmetic.

## I. INTRODUCTION

As an efficient artificial absorbing media, conformal Perfectly Matched Layer (PML) has been attracting more and more attention since the half-space Cartesian PML is extended into conformal absorbing boundary of cylindrical and spherical geometries in approximate PML formulations by Kuzuoglu and Mittra [1]. The conformal mesh truncation defined by exact PML formulations [2-4], which encloses the scatterer a small distance away, is very advantageous for saving spatial scattering elements, especially in the Finite Element Method (FEM). In curvilinear coordinates and general orthogonal curvilinear

coordinates, numerical efficiency of absorbing boundary conditions of complex geometries are improved by conformal PML with grid generation technique [5]. The dynamic stability of the Cartesian, cylindrical, spherical and conformal PMLs is analyzed and presented in [6] and [7]. Some basic conclusions have played an important role on the design of conformal PMLs. However, how to mesh the conformal shell elements well is still a basic issue for realizing and developing the conformal PML [8-10]. Accurate calculation of normal direction of conformal PML is a basic requirement for meshing the conformal elements, especially for the high-fidelity mapped shell (hexahedron) elements. Fortunately, Non-Uniform Rational B-Splines (NURBS), which possesses the excellent characteristics on defining the complicated surfaces and generating the curvilinear elements [11-13], is a valid scheme for describing the conformal surface and calculating the normal direction of conformal PML.

The contents of this paper include the normal directional NURBS arithmetic of conformal PML, arithmetic implementation and numerical experiments, which demonstrate both the availability and precision of the arithmetic.

## II. FEM IMPLEMENTATION OF CONFORMAL PML

In the FEM for electromagnetic scattering problems, the PML is an efficient mesh truncation boundary. As a more efficient absorbing boundary condition, the conformal PML is introduced for solving the computational scale problem of large-size scatterer. The basic implementation steps of applying the conformal PML into FEM are presented as follows.

**Step 1.** Mesh the outer surface of scatterer and

generate the basic surface elements of scatterer. (When the shape of scatterer is arbitrary or unknown, the basic surface of scatterer should be reconstructed accurately by the surface elements. NURBS in Section III is advantageous for this situation.)

**Step 2.** Calculate the normal directions of nodes of basic surface elements and create the nodes of conformal surface along the normal directions, shown in Fig. 1. Because the precision and quality of conformal PML elements depend largely on these normal directions, this step is fundamental and key for computational accuracy and numerical efficiency of conformal PML.

**Step 3.** Based on the nodes of conformal surface, generate one layer of shell elements of conformal PML, similarly generate multilayer of shell elements of conformal PML.

**Step 4.** According to the geometric information of shell elements, compute the constitutive parameters  $\bar{\mu} = \mu_r \bar{\Lambda}$  and  $\bar{\varepsilon} = \varepsilon_r \bar{\Lambda}$  of conformal PML [2]. The matrix of  $\bar{\Lambda}$  in local coordinate system  $(u, v, w)$  is given by:

$$\bar{\Lambda}_{u,v,w} = \begin{bmatrix} \frac{s_2 s_3}{s_1} & 0 & 0 \\ 0 & \frac{s_1 s_3}{s_2} & 0 \\ 0 & 0 & \frac{s_1 s_2}{s_3} \end{bmatrix}. \quad (1)$$

Where  $s_1 = \frac{r_{01} + \int_0^w s(\zeta) d\zeta}{r_1}$ ,  $s_2 = \frac{r_{02} + \int_0^w s(\zeta) d\zeta}{r_2}$ ,  $s_3 = s$ ,  $s$  is the complex stretching variable [9,10] in the  $w$ -direction.  $r_1$  and  $r_2$  are principal radii [9,10] on the nodes of shell elements.

**Step 5.** Apply the constitutive parameters of conformal PML to vector wave equations of scattering field:

$$\nabla \times \left( \frac{1}{\mu_r} \bar{\Lambda}^{-1} \cdot \nabla \times \mathbf{E}^s \right) - k_0^2 \varepsilon_r \bar{\Lambda} \cdot \mathbf{E}^s = \mathbf{0}. \quad (2)$$

Where  $\mathbf{E}^s$  is scattering electric field. After interface boundary conditions of conformal PML are applied, the conformal absorbing boundary is completed in the FEM.

In the above implementation steps of conformal PML, the key step is to calculate accurately the normal directions of nodes of basic surface elements because the normal directions

control the geometric shapes of conformal shell elements and constitutive parameters of conformal PML. Therefore, the calculation arithmetic of normal direction of conformal PML is presented in detail in the following sections.

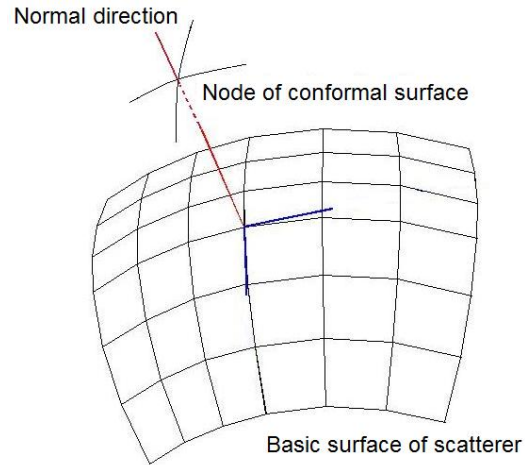


Fig. 1. Normal direction of conformal PML.

### III. NURBS SURFACE

Since the Non-Uniform Rational B-Splines (NURBS) is introduced into the computational electromagnetic applications by Valle, Rivas and Citedra [14], it is always a quite sophisticated geometrical modelling method of arbitrary shape bodies and complex scatterers. As a quite powerful modelling tool, NURBS plays a fundamental role in integral and differential methods of computational electromagnetics. Presently, the rapid development of complex curve/surface construction and grid generation technique largely depends upon the progress of NURBS.

In view of the advantage on the geometric description, NURBS shows great promise as an ideal discrete approximation for the complex surface, especially on the large curvature surface. Generally, numerical accuracy and efficiency of NURBS are very high for describing and constructing the basic surface of arbitrary shape scatterers. Therefore, in our work the NURBS is employed to describe the basic surface of scatterer and convex surface of conformal PML.

In this section, we start by reviewing the basic definition of NURBS surface [15]; only the equations relevant to our implementation are presented.

If a NURBS surface is  $p$ th order on  $u$  direction

and  $q$ th order on  $v$  direction, its piecewise rational vector function is expressed as:

$$S(u, v) = \frac{\sum_{i=0}^n \sum_{j=0}^m N_{i,p}(u) N_{j,q}(v) w_{i,j} \mathbf{P}_{i,j}}{\sum_{i=0}^n \sum_{j=0}^m N_{i,p}(u) N_{j,q}(v) w_{i,j}}, \quad 0 \leq u, v \leq 1. \quad (3)$$

Where  $\{\mathbf{P}_{i,j}\}$  define control points on  $u$  and  $v$  directions,  $\{w_{i,j}\}$  are weighting factors,  $\{N_{i,p}(u)\}$  and  $\{N_{j,q}(v)\}$  are nonrational B-splines basis functions defined on vector  $\mathbf{U}$  and  $\mathbf{V}$  respectively [15],

$$\begin{cases} \mathbf{U} = \left\{ \underbrace{0, \dots, 0}_{p+1}, u_{p+1}, \dots, u_{r-p-1}, \underbrace{1, \dots, 1}_{p+1} \right\} \\ \mathbf{V} = \left\{ \underbrace{0, \dots, 0}_{q+1}, u_{q+1}, \dots, u_{s-q-1}, \underbrace{1, \dots, 1}_{q+1} \right\} \end{cases}. \quad (4)$$

Where  $r = n + p + 1$ ,  $s = m + q + 1$ .

In (3), the numerator and denominator of piecewise rational vector function are respectively rewritten as:

$$\mathbf{A}(u, v) = \sum_{i=0}^n \sum_{j=0}^m N_{i,p}(u) N_{j,q}(v) w_{i,j} \mathbf{P}_{i,j}, \quad (5)$$

$$w(u, v) = \sum_{i=0}^n \sum_{j=0}^m N_{i,p}(u) N_{j,q}(v) w_{i,j}. \quad (6)$$

Hence, first order partial derivative [15] of piecewise rational vector function is given by:

$$S_\alpha(u, v) = \frac{A_\alpha(u, v) - w_\alpha(u, v) S(u, v)}{w(u, v)}. \quad (7)$$

Where  $\alpha$  indicates  $u$  or  $v$  partial derivative of  $S(u, v)$ .

#### IV. NURBS ARITHMETIC OF COMMON NORMAL DIRECTION

Using the NURBS, we generate accurately the basic surface elements of scatterer in step 1 (in Section II). Otherwise, the normal direction definition of nodes of basic surface elements becomes a very knotty problem when the shell elements of conformal PML will be generated in step 2 (in Section II). As following Fig. 2, the normal directions of adjacent surface elements are different on the common node  $O$ . For instance, on the common node  $O$ , the normal direction  $\mathbf{Z}_1$  of element no.1 is defined by two tangential directions  $S_{u1}$  and  $S_{v1}$  of element no.1. Similarly,

the normal directions of other adjacent surface elements are also obtained.

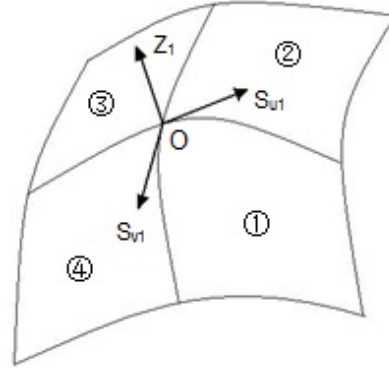


Fig. 2. Normal direction of adjacent surface elements.

In consideration of the conciseness of representation, the normal direction of the  $i$ th surface element on the node  $O$  is unitized as:

$$\mathbf{Z}_i(u, v) = \frac{S_{ui}(u, v) \times S_{vi}(u, v)}{\left| S_{ui}(u, v) \times S_{vi}(u, v) \right|_{(u_0, v_0)}}. \quad (8)$$

Where  $\mathbf{Z}_i(u, v)$  is the unit normal direction of the  $i$ th surface element on the common node  $O$ .  $S_{ui}$  and  $S_{vi}$  are two tangential directions of the  $i$ th surface element on the common node  $O$  respectively.

For calculating accurately the common normal direction of adjacent surface elements, four weighted average formulas are proposed. In these formulas, different weighting factors are introduced to present the contribution of normal directions of adjacent elements to the common normal direction. Moreover, some geometric and discretization impacts are also considered. The detailed weighted average formulas are described as following.

- (i) If the common normal direction is expressed as a simple average of normal directions of adjacent elements, the common normal direction is defined as:

$$\mathbf{Z}_0(u, v) = \frac{\sum_{i=1}^n \mathbf{Z}_i(u, v)}{n}. \quad (9)$$

Where  $n$  is total number of adjacent surface elements. Actually, the weighting factor is 1.0 in (9).

- (ii) Considering that the shapes of adjacent surface elements are important factors for the common normal direction, area percentages of adjacent elements are introduced as the weighting factors. Thus, the common normal direction is defined as:

$$\mathbf{Z}_0(u, v) = \frac{\sum_{i=1}^n \Omega_i \mathbf{Z}_i(u, v)}{\sum_{i=1}^n \Omega_i}. \quad (10)$$

Where  $\Omega_i$  is the area of the  $i$ th element. The area percentage  $\Omega_i / \sum_{i=1}^n \Omega_i$  is the weighting factor of the  $i$ th element. This means that the common normal direction will be close to the normal directions of big elements.

- (iii) Considering that the geometric curvatures of adjacent surface elements are also important factors for the common normal direction, Gauss curvatures of surface elements are introduced as the weighting factors. Thus, the common normal direction is defined as:

$$\mathbf{Z}_0(u, v) = \frac{\sum_{i=1}^n \rho_i \mathbf{Z}_i(u, v)}{\sum_{i=1}^n \rho_i}. \quad (11)$$

Where  $\rho_i$  is Gauss curvature of the  $i$ th surface element on the common node  $O$ . The curvature percentage  $\rho_i / \sum_{i=1}^n \rho_i$  is the weighting factor of the  $i$ th element. This means that the common normal direction will be close to the normal directions of large curvature elements.

- (iv) In order to ensure the geometric shape and computational precision of finite element, the size of conformal shell element must be so fine (1/10 wavelength) that the geometric information of element is enough for the discrete approximation on the large curvature domain. Therefore, area percentages and curvatures of surface elements should be considered globally. Based on the harmonic average formula, the common normal direction is defined as:

$$\mathbf{Z}_0(u, v) = \frac{\sum_{i=1}^n \frac{\rho_i}{\Omega_i} \mathbf{Z}_i(u, v)}{\sum_{i=1}^n \frac{\rho_i}{\Omega_i}}. \quad (12)$$

Where  $\rho_i$  is Gauss curvature of the  $i$ th surface element.  $\Omega_i$  is the area of the  $i$ th surface element.

The mixed percentage  $\frac{\rho_i}{\Omega_i} / \sum_{i=1}^n \frac{\rho_i}{\Omega_i}$  is the weighting factor of the  $i$ th element. This means that the common normal direction will be close to the normal directions of large curvature (unsmooth) and small elements.

## V. NUMERICAL EXPERIMENTS

In this section, in order to verify the modelling accuracy of NURBS arithmetic, we implement the arithmetic in two classical experiments.

- (1) Sphere, its diameter is 2 cm, as following Fig. 3.
- (2) Ellipsoid, its major axis is 4 cm, its minor axis is 2 cm, as following Fig. 4.

In the above experiments, all programs are developed in Matlab2009 compiled language.

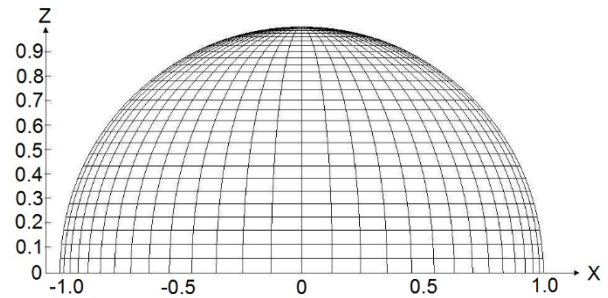


Fig. 3. Sphere.

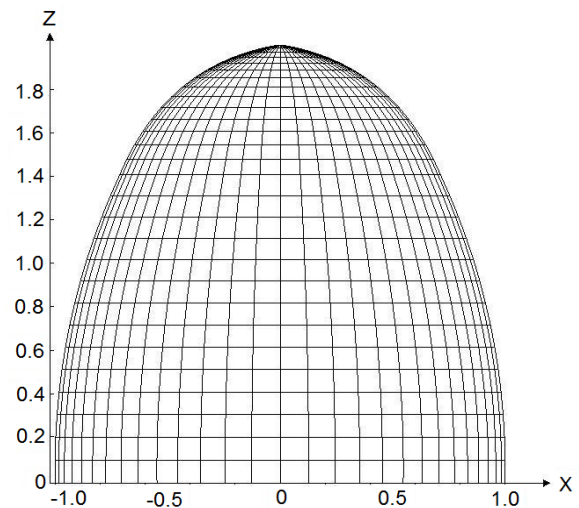


Fig. 4. Ellipsoid.

In Table 1, we compare the common normal directions calculated by four weighted average formulas with the analytic normal direction on the common node. The analytic normal direction and calculated common normal directions are expressed as the vector format. The spherical coordinate system ( $\theta$  and  $\varphi$ ) is employed for describing the conformal surface conveniently.

The unit of spherical coordinates  $\theta$  and  $\varphi$  is the degree. In consideration of the generality of four adjacent surface elements, division of surface is controlled by the angular intervals of spherical coordinates  $\theta$  and  $\varphi$  in every case (in Table 1) like the longitude and latitude of the earth.

Table 1: Calculation results of common normal directions

Model	Mesh Sizes ( $^{\circ}$ )	Analytic Normal Vector	Formula (i)	Formula (ii)	Formula (iii)	Formula (iv)
Sphere	$\theta$ : 20, 30, 40 $\varphi$ : 1, 10, 20	0.150384 0.086824 0.984808	0.150388 0.086837 0.984806	0.15044 0.086878 0.984794	0.150388 0.086837 0.984806	0.150334 0.086795 0.984818
	$\theta$ : 0, 10, 20 $\varphi$ : 20, 30, 40	0.492404 0.086824 0.866025	0.49239 0.086814 0.866034	0.49241 0.086817 0.866022	0.49239 0.086814 0.866034	0.492369 0.086811 0.866046
	$\theta$ : 0, 10, 40 $\varphi$ : 20, 50, 60	0.754406 0.133022 0.642788	0.751913 0.13369 0.645565	0.751475 0.133856 0.64604	0.751988 0.133681 0.645479	0.752624 0.133381 0.6448
	$\theta$ : 20, 50, 60 $\varphi$ : 1, 10, 40	0.111619 0.133022 0.984808	0.112833 0.133589 0.984593	0.11316 0.133792 0.984527	0.112797 0.133582 0.984598	0.111965 0.132882 0.984787
	$\theta$ : 30, 70, 90 $\varphi$ : 5, 30, 60	0.17101 0.469846 0.866025	0.173981 0.468775 0.866014	0.175156 0.469796 0.865224	0.173793 0.46882 0.866028	0.172363 0.467737 0.866898
	$\theta$ : 5, 30, 60 $\varphi$ : 30, 70, 90	0.813798 0.469846 0.34202	0.811349 0.469217 0.348638	0.81086 0.469319 0.349637	0.811438 0.469277 0.348351	0.811996 0.469193 0.347161
Ellipsoid	$\theta$ : 20, 30, 40 $\varphi$ : 1, 10, 20	0.288022 0.16629 0.943075	0.292844 0.169097 0.941089	0.294023 0.169771 0.9406	0.292393 0.168845 0.941274	0.291268 0.168202 0.941738
	$\theta$ : 0, 10, 20 $\varphi$ : 20, 30, 40	0.744445 0.131266 0.654654	0.748462 0.131963 0.649916	0.748397 0.131952 0.649993	0.748539 0.131985 0.649822	0.748601 0.131996 0.649749
	$\theta$ : 0, 10, 40 $\varphi$ : 20, 50, 60	0.908121 0.160126 0.38688	0.917875 0.163196 0.361763	0.918985 0.163692 0.358708	0.919571 0.163598 0.357246	0.918558 0.162952 0.360135
	$\theta$ : 20, 50, 60 $\varphi$ : 1, 10, 40	0.213778 0.25477 0.943075	0.238914 0.282892 0.92892	0.244353 0.288933 0.92564	0.233345 0.276594 0.932226	0.21844 0.259424 0.940735
	$\theta$ : 30, 70, 90 $\varphi$ : 5, 30, 60	0.258543 0.710341 0.654654	0.272015 0.73291 0.62358	0.273087 0.732454 0.623646	0.270861 0.733465 0.623428	0.269443 0.73418 0.623202
	$\theta$ : 5, 30, 60 $\varphi$ : 30, 70, 90	0.852031 0.49192 0.179044	0.854928 0.494413 0.157015	0.854999 0.494862 0.155202	0.855228 0.495324 0.152444	0.855205 0.494868 0.154045

The calculation errors of four weighted average formulas are shown in Table 2. The calculation errors are defined as the angles between the analytic normal direction and calculated common normal directions, as following equation (13). The unit of error is the degree.

$$\theta_{error} = 180 \arccos \left( \frac{\mathbf{Z}_a \cdot \mathbf{Z}_{0i}}{|\mathbf{Z}_a| |\mathbf{Z}_{0i}|} \right) / \pi. \quad (13)$$

Where  $\mathbf{Z}_a$  is the analytic normal direction.  $\mathbf{Z}_{0i}$  is the common normal directions calculated by the  $i$ th formulas.  $\arccos()$  is arc cosine function.

Although, the element size is very fine (1/10 wavelength) in the FEM of electromagnetic problems actually, the large size elements are proposed to show obviously the calculation errors between the analytic and numerical solution. In Table 2, the results show that the calculation errors of four weighted average formulas are very small, and the calculation errors of formula (iv) are almost less than those of other formulas, especially on the large curvature domain. This means that the weighted average approach to the analytic normal direction will be very accurate in the FEM of actual electromagnetic problems.

Table 2: Calculation errors of common normal directions

Model	Mesh Sizes ( $^{\circ}$ )	Formula (i) Error ( $^{\circ}$ )	Formula (ii) Error ( $^{\circ}$ )	Formula (iii) Error ( $^{\circ}$ )	Formula (iv) Error ( $^{\circ}$ )
Sphere	$\theta$ : 20, 30, 40 $\varphi$ : 1, 10, 20	0.0008	0.00456	0.00078	0.00334
	$\theta$ : 0, 10, 20 $\varphi$ : 20, 30, 40	0.0011	0.00054	0.0011	0.00247
	$\theta$ : 0, 10, 40 $\varphi$ : 20, 50, 60	0.2172	0.2553	0.2107	0.1553
	$\theta$ : 20, 50, 60 $\varphi$ : 1, 10, 40	0.0778	0.1000	0.0757	0.0214
	$\theta$ : 30, 70, 90 $\varphi$ : 5, 30, 60	0.1809	0.2420	0.1699	0.1520
	$\theta$ : 5, 30, 60 $\varphi$ : 30, 70, 90	0.4059	0.4687	0.3885	0.3144
Ellipsoid	$\theta$ : 20, 30, 40 $\varphi$ : 1, 10, 20	0.3393	0.4220	0.3079	0.2291
	$\theta$ : 0, 10, 20 $\varphi$ : 20, 30, 40	0.3582	0.3523	0.3652	0.3707
	$\theta$ : 0, 10, 40 $\varphi$ : 20, 50, 60	1.5538	1.7421	1.8312	1.6529
	$\theta$ : 20, 50, 60 $\varphi$ : 1, 10, 40	2.3084	2.8107	1.7908	0.4005
	$\theta$ : 30, 70, 90 $\varphi$ : 5, 30, 60	2.3321	2.3360	2.3356	2.3460
	$\theta$ : 5, 30, 60 $\varphi$ : 30, 70, 90	1.2811	1.3869	1.5474	1.4537

## VI. CONCLUSION

For calculating accurately the common normal direction of conformal PML elements, we develop the NURBS arithmetic of conformal surface and

four weighted average formulas of common normal direction. In view of its precision in the experiments, the NURBS arithmetic shows high availability as an ideal approach for the common

normal direction of conformal PML.

### ACKNOWLEDGEMENT

This work was supported by National Science Foundation for Distinguished Young Scholars of China (11201375), Specialized Research Fund for the Doctoral Program of Higher Education of China (20106102120001) and Postdoctoral Science Foundation of China (201003680).

### REFERENCES

- [1] M. Kuzuoglu and R. Mittra, "Investigation of nonplanar perfectly matched absorbers for finite-element mesh truncation," *IEEE Transactions on Antennas and Propagation*, vol. 45, no. 3, pp. 474-486, March 1997.
- [2] F. L. Teixeira and W. C. Chew, "Analytical derivation of a conformal perfectly matched absorber for electromagnetic waves," *Microwave and Optical Technology Letters*, vol. 17, no. 4, pp. 231-236, March 1998.
- [3] O. Ozgun and M. Kuzuoglu, "Non-maxwellian locally-conformal PML absorbers for finite element mesh truncation," *IEEE Transactions on Antennas and Propagation*, vol. 55, no. 3, pp. 931-937, March 2007.
- [4] B. Donderici and F. L. Teixeira, "Conformal perfectly matched layer for the mixed finite element time-domain method," *IEEE Transactions on Antennas and Propagation*, vol. 56, no. 4, pp. 1017-1026, April 2008.
- [5] K. P. Hwang and J. M. Jin, "Application of a hyperbolic grid generation technique to a conformal PML implementation," *IEEE Microwave and Guided Wave Letters*, vol. 9, no. 4, pp. 137-139, April 1999.
- [6] F. L. Teixeira and W. C. Chew, "On causality and dynamic stability of perfectly matched layers for FDTD simulations," *IEEE Transactions on Microwave Theory and Techniques*, vol. 47, no. 6, pp. 775-785, June 1999.
- [7] F. L. Teixeira, K. P. Hwang, W. C. Chew, and J. M. Jin, "Conformal PML-FDTD schemes for electromagnetic field simulations: a dynamic stability study," *IEEE Transactions on Antennas and Propagation*, vol. 49, no. 6, pp. 902-907, June 2001.
- [8] Y. J. Zhang and Q. Sun, "Layer-based integration arithmetic of conformal PML," *Applied Computational Electromagnetics Society Journal*, vol. 24, no. 5, pp. 518-522, October 2009.
- [9] P. Liu, J. D. Xu, and W. Wan, "A finite-element realization of a 3-D conformal PML," *Microwave and Optical Technology Letters*, vol. 30, no. 3, pp. 170-173, August 2001.
- [10] P. Liu and Y. Q. Jin, "Numerical simulation of bistatic scattering from a target at low altitude above rough sea surface under an EM-wave incidence at low grazing angle by using the finite element method," *IEEE Transactions on Antennas and Propagation*, vol. 52, no. 5, pp. 1205-1210, May 2004.
- [11] R. Sevilla, S. Fernandez-Mendez, and A. Huerta, "3D NURBS-enhanced finite element method (NEFEM)," *International Journal for Numerical Methods in Engineering*, vol. 88, no. 2, pp. 103-125, October 2011.
- [12] B. Lai, H. B. Yuan, and C. H. Liang, "Analysis of NURBS surfaces modeled geometries with higher-order mom based aim," *Journal of Electromagnetic Waves and Applications*, vol. 25, no. 5-6, pp. 683-691, 2011.
- [13] L. Z. Liu and J. Yang, "Analysis of electromagnetic scattering with higher-order moment method and NURBS model," *Progress in Electromagnetics Research-Pier*, vol. 96, pp. 83-100, 2009.
- [14] L. Valle, F. Rivas, and M. F. Citedra, "Combining the moment method with geometrical modelling by NURBS surfaces and bezier patches," *IEEE Transactions on Antennas and Propagation*, vol. 42, no. 3, pp. 373-381, March 1994.
- [15] L. A. Piegl and W. Tiller, "The NURBS book," 2<sup>nd</sup> edition, *Springer-Verlag*, New York, 1997.



**Y. J. Zhang** Received his Ph.D. degree from Northwestern Polytechnical University, Xi'an, P. R. China, in 2009. Since 2013, he has been an Associate Professor at Aeronautics School of Northwestern Polytechnical University, P. R. China. He has co-authored more than 20 papers appeared in international journals and conferences. His current research interest includes electromagnetic scattering computation and finite element methods.

# Diamond Shaped Ring Antenna for UWB Applications with Inherent Band-Notched Functionality

Majid Shokri<sup>1</sup>, Zhaleh Amiri<sup>1</sup>, Somayeh Asiaban<sup>1</sup>, and Bal Virdee<sup>2</sup>

<sup>1</sup> Young Researchers and Elite Club, Urmia Branch  
Islamic Azad University, Urmia, Iran  
majed.shokri@gmail.com

<sup>2</sup> Faculty of Life Sciences and Computing, Center for Communications Technology  
London Metropolitan University, London, UK

**Abstract** — In this Letter, a novel printed monopole antenna design is described that operates across a wideband frequency band and exhibits band-notch characteristic necessary to suppress interference signals. The prototype antenna consists of a radiating patch in the configuration of a diamond shaped ring that has attached within it an inverted T-shaped resonant structure that controls the notch frequency. The antenna is excited with a microstrip feed-line and includes an elliptically shaped ground-plane that is defected with a dielectric notch in the vicinity of the patch to enhance the antenna's impedance bandwidth. The antenna exhibits an inherent stop-band function at the WLAN frequency band. The proposed antenna configuration is simple and compact with dimensions of  $30 \times 30 \times 1.6 \text{ mm}^3$ . The measured impedance bandwidth exceeds the Ultra-Wideband (UWB) spectrum defined between 3.06-15.96 GHz, for  $VSWR \leq 2$  that corresponds to a fractional bandwidth of 135.6%. The radiation characteristic of the proposed antenna is approximately omni-directional.

**Index Terms** — Band-notched antenna, microstrip fed antenna, monopole antenna, UWB.

## I. INTRODUCTION

Latest progress in wireless technology employs several communication standards to enable various systems; e.g., satellite, ultra-wideband, and WLAN systems, to operate over a common platform. Such systems necessitate the integration of various sub-systems and the use of a

single antenna to enable wireless communications. The antenna therefore needs to be designed so that its impedance bandwidth is sufficiently wide enough to cover the operating frequency spectrum of multiple wireless communication systems. UWB systems have a 10 dB bandwidth of 7.5 GHz between 3.1-10.6 GHz as defined by Federal Communications Commission (FCC). Such systems have become the de facto standard of high data rate, high capacity and low power transmission for short range indoor applications. In fact, the effective isotropic radiated power spectral density of UWB is restricted to -41.3 dBm/MHz [1]. Since printed monopole antennas have attractive characteristics including: (i) relatively large impedance bandwidth, (ii) ease of manufacture using conventional Microwave Integrated Circuit (MIC) technology, and (iii) acceptable radiation properties, hence these types of antenna find application in UWB systems [2-7]. The UWB spectrum includes within it other wireless narrowband standards, such as WLAN bands (5.15-5.35 GHz and 5.725-5.825 GHz) that will interfere with the operation of UWB systems. Hence, to avoid interference, the UWB systems need to employ filters with stop-band functionality. Unfortunately, the inclusion of filters would unnecessarily increase the overall size, weight and cost of the UWB systems. In order to save space, UWB antennas possessing a notch function across the band 5.15-5.825 GHz would provide the solution. Several band-notched antennas have been recently proposed for UWB systems including: using H-shaped conductor-

backed plane [8], etching two modified U-shaped slots on the patch [9], inserting two rod-shaped parasitic structures [10], embedding a resonant cell within the feed-line [11], using a fractal tuning stub [12], and utilizing a resonant patch [13].

In this paper, a novel WLAN band-notched antenna is proposed for UWB applications that uses a radiating patch consisting of a diamond shaped ring structure in which is embedded an inverted T-shaped resonance element. The diamond ring determines the center frequency of the notch band.

### II. ANTENNA STRUCTURE

The proposed monopole antenna was constructed on a low-cost commercial FR-4 substrate with relative permittivity of 4.4,  $\tan\delta=0.02$  and thickness of 1.6 mm. Figure 1 shows the geometry of the proposed UWB antenna. The antenna is terminated with a 50  $\Omega$  SMA connector for signal transmission and reception. The width of the feed-line is fixed at 2.8 mm, which corresponds to a characteristic impedance of 50  $\Omega$ . The optimized dimensions of the antenna are shown in Fig. 1. The antenna's structure includes a ground-plane with a notch in the shape of a semi-ellipse in the vicinity of the radiating patch. Within the patch is embedded an inverted T-shaped resonance element.

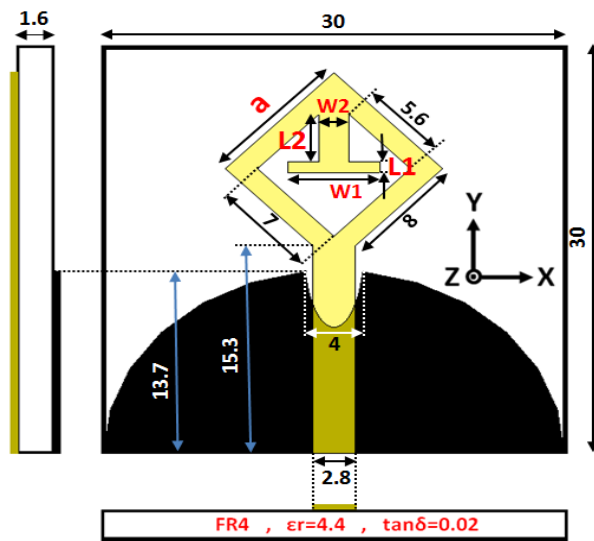


Fig. 1. Geometry of the proposed antenna (optimized dimensions in mm).

The notched band defined between 5-6 GHz is determined by the dimensions of this resonance element. Figure 2 shows the three steps employed to implement the antenna structure. The first step includes the radiating patch in the configuration of a diamond shaped ring, and a truncated ground-plane in the shape of a rectangle. In order to extend the impedance bandwidth to cover the UWB spectrum, in the second step the rectangular ground-plane is modified into a semi-elliptical shape with a semi-elliptical notch next to the patch. The notch-band is created by adding an inverted T-shaped resonance element, as the third step in Fig. 2 depicts. The antenna's VSWR response in Fig. 2 is wider than previous antennas [2-21].

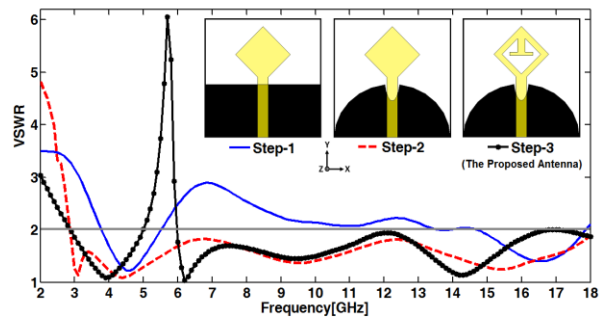


Fig. 2. Simulated VSWR characteristic of the antenna in the various steps to create the final proposed structure.

### III. SIMULATION AND MEASUREMENTS RESULTS

In this Section, the affect of the various parameters on the band-notched antenna are studied. Numerical and experimental results of the impedance bandwidth, radiation characteristics, gain, surface current distribution, and group delay are presented and discussed. The affect of the various parameters defining the proposed UWB antenna are studied by changing them one at a time while keeping all others fixed. Full-wave analysis on the proposed antenna configuration was performed using Ansoft HFSS (ver 11.1). As shown in Fig. 3, the width ( $W_1$ ) of the inverted T-shaped resonance element affects the antenna's notch frequency. However, the thickness of the inverted T-shaped element ( $W_2$ ) greatly affects the frequency of the notch band as shown in Fig. 4.

The thickness of the horizontal section ( $L_1$ ) and vertical section ( $L_2$ ) of the inverted T-shaped element also affects the notch's center frequency as shown in Figs. 5 and 6, respectively.  $L_1$  and  $L_2$  changes the notch frequency by approximately 1 GHz, for  $L_1$  change between 0.8-1.5 mm and  $L_2$  change between 3.5-4.5 mm.

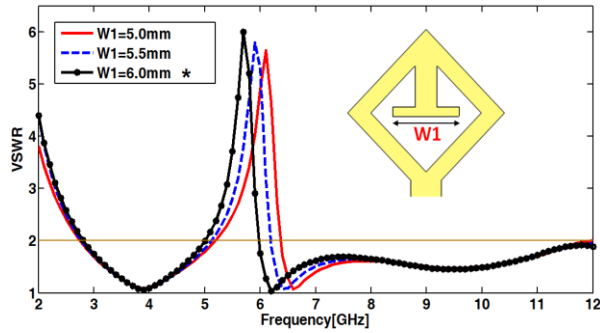


Fig. 3. Simulated VSWR characteristics of the proposed antenna for various dimensions of parameter  $W_1$ .

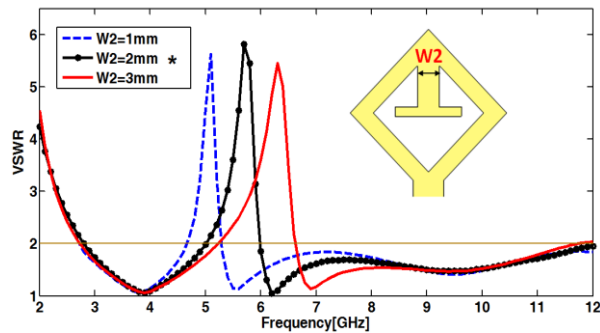


Fig. 4. Simulated VSWR characteristics of the proposed antenna for various dimensions of parameter  $W_2$ .

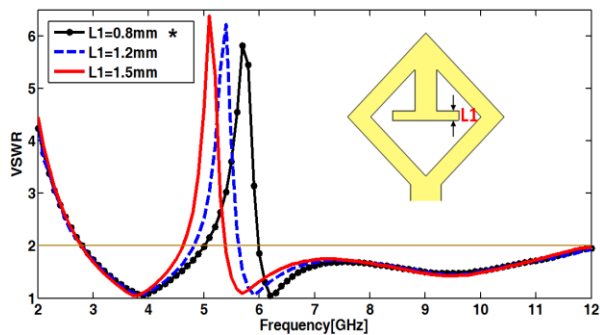


Fig. 5. Simulated VSWR characteristics of the proposed antenna for various dimensions of parameter  $L_1$ .

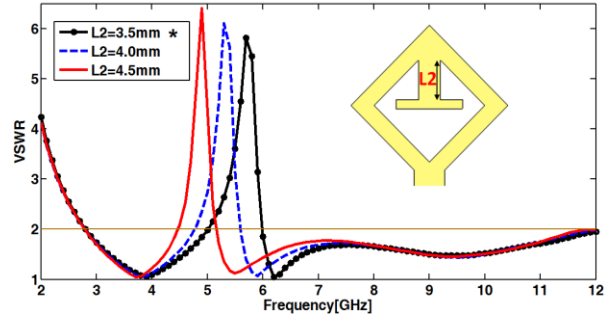


Fig. 6. Simulated VSWR characteristics of the proposed antenna for various dimensions of parameter  $L_2$ .

Figure 7 shows the simulated radiation patterns of the proposed antenna with the co- and cross-polarization in the H-plane ( $x$ - $z$  plane) and E-plane ( $y$ - $z$  plane). It can be observed that the radiation patterns in  $x$ - $z$  and  $y$ - $z$  plane are nearly omni-directional and bidirectional, respectively, at the frequencies of 3.8 GHz and 8 GHz. The measured and simulated gain of the proposed antenna over the antenna's operating bandwidth is shown in Fig. 8. The graph shows that the measured gain is optimum of about 4 dBi between 2-3.5 GHz and 10.8-11 GHz. The gain as required drastically drops across the notch band.

The process contributing towards the UWB and notch-band is explained by the current distribution density over the antenna.

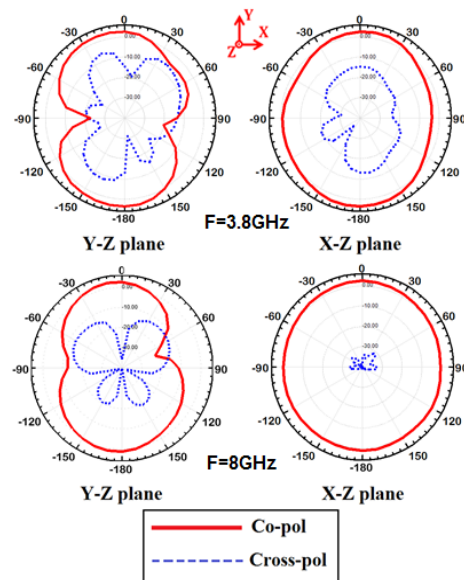


Fig. 7. Radiation patterns of the proposed antenna at: (a) 3.9 GHz, and (b) 8 GHz.

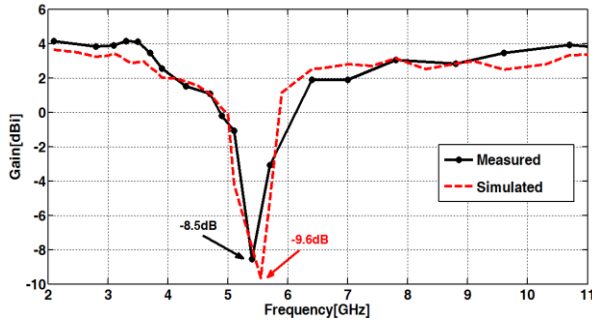


Fig. 8. Measured and simulated gain of the antenna.

Figure 9 shows the current distribution at the notch's center frequency of 5.8 GHz which is intense over the feed-line, the diamond ring and the base of the inverted T-shaped element. The concentration is also strong in the ground-plane in the vicinity of the feed-line. The current emanating from the inverted T-shaped element flowing over the top of the ring is in the opposite direction to the current flow in the bottom half of the ring. This results in the attenuation at 5.8 GHz.

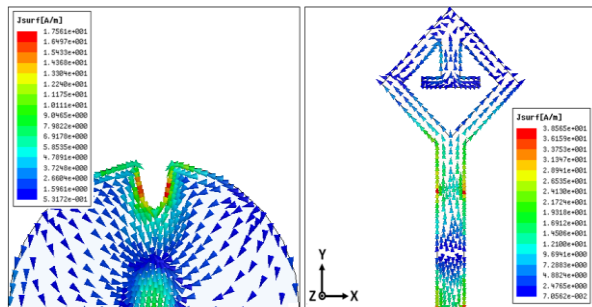


Fig. 9. Surface current distribution at 5.8 GHz over the defected ground-plane, feed-line and the patch.

Group delay is an important parameter in UWB antenna design, which represents the degree of distortion of pulse signal. To evaluate the dispersion performance of the proposed antenna, group delay was measured. The measured group delay between two identical antennas separated by 50 cm is shown in Fig. 10. The variation in the group delay is within about 2 ns, which verifies the proposed antenna is suitable for UWB communication systems. The measured VSWR, shown in Fig. 11, not only verifies its performance up to 15.96 GHz but also shows a close

correspondence between the measured and simulated curves. The photograph of the proposed antenna is inset in Fig. 11. Both the impedance bandwidth and radiation patterns were measured by using the Agilent 8722ES network analyzer in its full operational span (3.06-15.96 GHz).

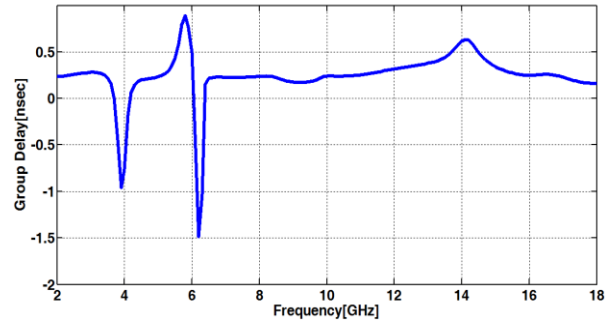


Fig. 10. Measured group delay of the proposed antenna.

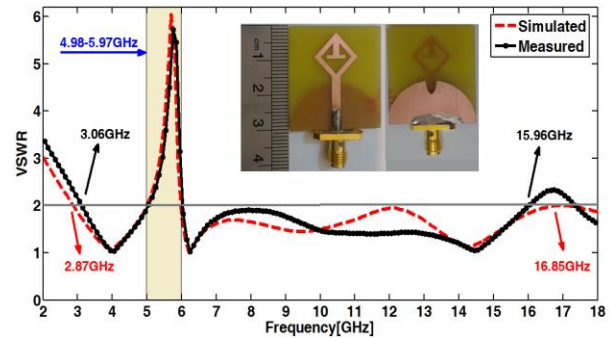


Fig. 11. Measured and simulated VSWR of the proposed optimized antenna. Inset is the photograph of the front and back side of the antenna.

#### IV. CONCLUSION

Proof of concept is reported of a novel compact printed monopole antenna for UWB application. The antenna has an inherent band-notch characteristic which is necessary to mitigate interfering signals with the UWB spectrum. The antenna has the following features: ease of pre-manufacture tuning of the notch-band, compact size, ease of fabrication and low cost. The measured results verify the antenna operation exceeds the UWB frequency range (3.06-15.96 GHz), rejection band between 5-6 GHz, and good radiation patterns across the UWB band. These characteristics make the antenna feasible for UWB

wireless systems.

### ACKNOWLEDGMENT

The authors would like to thank the Antenna Measurement Laboratory at Iran Telecommunication Research Center (ITRC), for fabricating and testing the antenna presented in this paper.

### REFERENCES

- [1] *Federal Communications Commission*: "First report and order, revision of part 15 of the Communication's rules regarding ultra-wideband transmission system," 2002.
- [2] J. Pourahmadazar, C. Ghobadi, J. Nourinia, and H. Shirzad, "Multiband ring fractal monopole antenna for mobile devices," *IEEE Ant. Wireless Propag. Lett.*, vol. 9, pp. 863-866, 2010.
- [3] M. Shokri, C. Ghobadi, J. Nourinia, H. Shirzad, S. Asiaban, and Z. Amiri, "Tiny circularly polarized printed slot antenna for UWB usage," *Life Science Journal*, vol. 9, pp. 2288-2291, 2012.
- [4] J. Pazar, H. Shirzad, C. Ghobadi, and J. Nourinia, "Using a MAM and genetic algorithm to optimize UWB microstrip monopole antenna with FEM and HFSS," *2010 5<sup>th</sup> International Symposium on Telecommunications (IST'2010)*.
- [5] M. Shokri, C. Ghobadi, J. Nourinia, H. Shirzad, Z. Amiri, and S. Asiaban, "Compact circularly polarized printed slot antenna with a wrench shaped patch for UWB application," *Int. Journal of Natural and Engineering Sciences*, vol. 1, pp. 60-63, 2013.
- [6] J. Pourahmadazar, C. Ghobadi, J. Nourinia, N. Felegari, and H. Shirzad, "Broadband CPW-fed circularly polarized square slot antenna with inverted-L strips for UWB applications," *IEEE Antennas Wireless Propag. Lett.*, vol. 10, pp. 369-372, 2010.
- [7] J. Zhang, H. Yang, and H. Liang, "Band-notched split-ring resonators loaded monopole antenna for ultra-wideband applications," *Applied Computational Electromagnetics Society (ACES) Journal*, vol. 28, no. 2, pp. 137-142, February 2013.
- [8] R. Zaker, C. Ghobadi, and J. Nourinia, "Novel modified UWB planar monopole antenna with variable frequency band-notch function," *IEEE Antennas Wireless Propag. Lett.*, vol. 7, pp. 112-114, 2008.
- [9] M. Ojaroudi, G. Ghanbari, N. Ojaroudi, and C. Ghobadi, "Small square monopole antenna for UWB application with variable frequency band-notch function," *IEEE Antennas Wireless Propag. Lett.*, vol. 8, pp. 1061-1064, 2009.
- [10] M. Rostamzadeh, S. Mohamadi, J. Nourinia, C. Ghobadi, and M. Ojaroudi, "Square monopole antenna for UWB applications with novel rod-shaped parasitic structures and novel V-shaped slots in the ground plane," *IEEE Antennas and Wireless Propag. Lett.*, vol. 11, pp. 446-449, 2012.
- [11] S. W. Qu, J. L. Li, and Q. Xue, "A band-notched ultra-wideband printed monopole antenna," *IEEE Antennas Wireless Propag. Lett.*, vol. 5, pp. 495-498, 2006.
- [12] W. J. Lui, C. H. Cheng, Y. Cheng, and H. Zhu, "Frequency notched ultra-wideband microstrip slot antenna with fractal tuning stub," *Electron. Lett.*, vol. 41, no. 6, pp. 294-296, 2005.
- [13] K. G. Thomas and M. A. Sreenivasan, "A simple ultra wideband planar rectangular printed antenna with band dispensation," *IEEE Trans. Antennas Propag.*, vol. 58, no. 1, pp. 27-34, 2010.
- [14] N. P. Agrawal, G. Kumar, and K. P. Ray, "Wide band planar monopole antennas," *IEEE Trans. Antenna Propag.*, vol. 46, pp. 294-295, 1998.
- [15] E. Lee, P. S. Hall, and P. Gardner, "Compact wide band planar monopole antenna," *Electron. Lett.*, vol. 35, pp. 2157-2158, 1999.
- [16] Y. Roh, K. Chung, and J. Choi, "Design of a microstrip-fed ultra wideband monopole antenna having band rejection characteristics," *IEEE 2B*, pp. 556-559, 2005.
- [17] S. W. Su, K. L. Wong, and C. L. Tang, "Ultra wideband square monopole antenna for IEEE802.16a operation in the 2-11 GHz band," *Micro. Opt. Technol. Lett.*, vol. 42, pp. 463-466, 2004.
- [18] G. Kumar and K. P. Ray, "Broadband microstrip antennas," *Artech House*, Norwood, MA, 2003.
- [19] Y. X. Guo, K. M. Luk, K. F. Lee, and R. Q. Lee, "A broad-band U-slot rectangular patch antenna on a microwave substrate," *IEEE Trans. Antenna Propag.*, vol. 48, pp. 954-960, 2000.
- [20] Y. J. Kim and D. H. Kwon, "Planar ultra wideband slot antenna with frequency band notched function," *IEEE Int. Symp. on Antenna and Propag.*, Monterey, CA, vol. 2, pp. 1788-1791, 2004.
- [21] T. Mandal and S. Das, "Ultra wideband printed hexagonal monopole antennas with WLAN band rejection," *Micro. Opt. Technol. Lett.*, vol. 54, no. 6, pp. 1520-1525, 2012.

# Electromagnetic Force Calculation of Conductor Plate Double Halbach Permanent Magnet Electrodynamic Suspension

Yin Chen and Kunlun Zhang

Key Laboratory of Magnetic Suspension Technology and Maglev Vehicle Ministry of Education  
Chengdu Sichuan 610031, China  
chenyin\_swjtu@126.com, zhangkunlun@263.net

**Abstract** — In order to solve the problem of high drag force in traditional Permanent Magnet Electrodynamic Suspension (PM-EDS) and increase the levitation-drag force ratio, this paper proposes a new suspension system composed of conductor plates and a double Halbach permanent magnet array, and calculates its electromagnetic force. The eddy current distribution equation for the conductor plate and the analytic calculation formula for the electromagnetic force of the device are derived by solving the differential equations for the magnetic vector potential in space. Verifying the analytic method using the finite element method, the maximum and mean relative errors of the results were calculated to be 4% and 1.7%, respectively. This paper also compares the levitation-drag force ratio of the new suspension system with that of the traditional system and concludes that the new system can substantially reduce the drag force and power loss.

**Index Terms** — Analytic calculation, conductor plate, double Halbach array, electromagnetic field, Halbach permanent magnet electrodynamic suspension.

## I. INTRODUCTION

The traditional PM-EDS structure is composed of conductor plates and a single Halbach permanent magnet array. One issue with this structure is its high electromagnetic drag force and power loss at the low speeds, making it unsuitable for urban rail transit. To overcome this disadvantage, the USA's GA developed a "null-current electrodynamic levitation system" composed of a Halbach array and independent

coils [1-2]. This system can indeed reduce drag force considerably, but it is exceedingly complex and very difficult to manufacture. More importantly, its rail is composed of many independent coils, resulting in a discontinuous levitation force, which means an uncomfortable ride for passengers. In order to overcome these issues, this paper proposes the conductor plate double Halbach permanent magnet electrodynamic suspension.

Such suspension system consists of a non-magnetic conductor plate and two sets of Halbach arrays provided on the upper and lower sides of the conductor plate, respectively; when the upper and lower air gaps are unequal, the conductor plate will generate the induced current, thus, giving rise to levitation force. Its nature is the dynamic characteristics between the permanent magnet and metal plate, and when studying such electromagnetic device, it's often to employ the numerical computation [3-7]. Usually, the numerical computation results are accurate, but fail to reflect the inherent relations among different parameters. While studying such issues with the analytic method, due to the complexity of electromagnetic field calculations, the conductor plate is often supposed to be infinitely thick or thin, for the purpose of simplifying the study [8-9]. Yet, the current skin depth is a function of the speed, and hence, the speed range that can be studied using this method is rather limited. The literature [8] has, when studying the single Halbach permanent magnet electrodynamic suspension, regarded the conductor plate to be infinitely thin, and therefore, replace the volume current by surface current; however, this method only coincides

with the experimental results in a small medium speed range. Literature [10] takes into account the effect of conductor plate thickness, but the model boundary selected makes the equation too complex and the expression for the eddy current in the conductor plate cannot be derived from it. Another common analytic method is the equivalent circuit model; i.e., to create an equivalent circuit of the electromagnetic device and calculate the electromagnetic force based on the energy conversion theory [11-12]. Since the equivalent inductance of the plate-type device is difficult to solve, such method is only suitable for the suspension system consisting of coils and permanent magnets. What's more, permanent magnet linear motors have the similar electromagnetic property, but the permanent magnet motors are characterized by active control systems and constant secondary current, so its electromagnetic force calculation is simple, greatly different from the electromagnetic system studied in this paper [13-15].

Based on previous research, this paper proposes the conductor plate double Halbach PM-EDS scheme and investigates its electromagnetic property and electromagnetic force. The differential equation for magnetic vector potentials throughout the interior of the system is obtained and used to derive the magnetic field and eddy current distribution equation and the analytical expression for the electromagnetic force calculation. By verifying the analytic calculation result using the ANSYS and comparing the levitation-drag force ratio of the new suspension system with that of the traditional single Halbach PM-EDS, we conclude that the new system is indeed superior.

## II. SUSPENSION MODLE

The cross section of the double Halbach suspension train, studied herein, is shown in Fig. 1.

The suspension system has a structure as shown in Fig. 2, where  $L$  is the thickness of non-magnetic conductor plate,  $\tau$ ,  $h$  and  $l$  are the polar distance, height of permanent magnet array and the thickness of the conductor plate, and  $d_1$  and  $d_2$  are the upper and lower air gaps.

If,

$$d_1 \neq d_2,$$

then, the air gap field

$$B_y \neq 0.$$

It will induce current in the metal plate and further give rise to electromagnetic force along the  $d_1=d_2$  direction; thus, the system is able to achieve self-stabilized suspension. And as can be seen from the figure, as for the magnetic field generated in the air gap by the two sets of permanent magnet arrays, the  $Y$  components are offset, but  $X$  components are superimposed; hence, it can generate a greater levitation-drag force ratio than the single Halbach suspension [16].

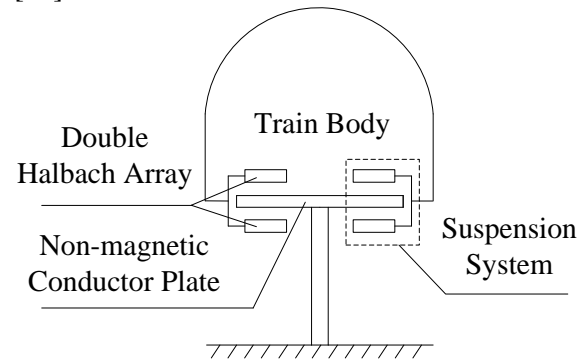


Fig. 1. Cross section of the conductor plate double Halbach PM-EDS train.

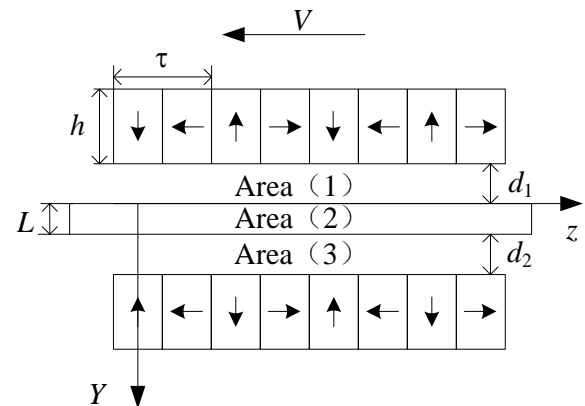


Fig. 2. Sketch diagram of conductor plate double Halbach PM-EDS train suspension system.

## III. ELECTROMAGNETIC CALCULATION

### A. Analytic calculation

The space magnetic field of permanent magnet Halbach array is expressed as [17]:

$$\begin{aligned} B_{y0} &= B_{m0} e^{j(pz+\omega t)} \\ B_{z0} &= B_{m0} e^{j(pz-\pi/2+\omega t)}, \end{aligned} \quad (1)$$

where,  $p = \frac{\pi}{\tau}$ , and

$$\begin{cases} B_{m0} = B_0 e^{-ps} \\ B_0 = B_r (1 - e^{-ph}) \sin\left(\frac{\pi}{m}\right) / \left(\frac{\pi}{m}\right) \end{cases} \quad (2)$$

Here,  $B_r$  is the remanence of permanent magnet,  $m$  means the number of modules contained in a pair of poles (Fig. 1 shows a 4-module structure,  $m=4$ ),  $s$  stands for the distance from one point in the air gap to the lower surface of permanent magnet. The air gap field of double Halbach permanent magnet array may be expressed as:

$$\begin{cases} B_{sy} = B_0 (e^{-p(y+d_1)} - e^{-p(-y+d_2+l)}) e^{j(pz+\omega t)} \\ B_{sz} = B_0 (e^{-p(y+d_1)} + e^{-p(-y+d_2+l)}) e^{j(pz-\pi/2+\omega t)} \end{cases}, \quad (3)$$

where,  $B_0$  may be determined by Equation (2), and for the convenience of expression, make:

$$\begin{cases} B_{ym} = B_0 (e^{-p(y+d_1)} - e^{-p(-y+d_2+l)}) \\ B_{zm} = B_0 (e^{-p(y+d_1)} + e^{-p(-y+d_2+l)}) \end{cases} \quad (4)$$

When the conductor plate in Fig. 1 moves in the +Z direction at a relative speed of  $v$ , the surface density of eddy current generated in the conductor plate can be expressed as:

$$\begin{cases} \mathbf{J}_s = \gamma \mathbf{E}_s \\ \mathbf{E}_s = \mathbf{v} \times \mathbf{B} \end{cases} \quad (5)$$

The Equation above may be shown as a scalar equation:

$$J_s = -\gamma v B_{sy} \quad (6)$$

Based upon the Lorenz Gauge [18],

$$\nabla \mathbf{A} - \frac{k^2}{j\omega} \varphi = 0 \quad (7)$$

Obtain the magnetic vector potential equation,

$$\nabla^2 \mathbf{A} + k^2 \mathbf{A} = -\mu \mathbf{J}_s \quad (8)$$

In the two-dimensional model, the magnetic vector potential  $\mathbf{A}$  only has  $X$  component, and thus, for Areas (1)-(3) indicated in Fig. 1, the equation above may, based on the scalar equation, be expressed as:

$$\begin{cases} \nabla^2 A_{ix} + k_i^2 A_{ix} = 0 & (i=1,3) \\ \nabla^2 A_{ix} + k_i^2 A_{ix} = -\mu_0 J_s & (i=2) \end{cases}, \quad (9)$$

where,  $k_i$  is a propagation function [19],

$$k_i^2 = -j\omega\mu_0(\gamma_i + j\omega\epsilon) \quad (10)$$

Here,  $\gamma_i$  is the conductivity of air ( $i=1,3$ ) and the conductor plate ( $i=2$ ). Formula (9) is partial differential equations, the solution to which requires the establishment of boundary condition equations [20] against different area joint faces.

(1) Infinity boundary condition:

$$\begin{cases} \lim_{y \rightarrow -\infty} A_{1x} = 0 \\ \lim_{y \rightarrow +\infty} A_{3x} = 0 \end{cases} \quad (11)$$

(2) Inner boundary condition of joint face:

$$\begin{cases} A_{1x} = A_{2x} & (y=0) \\ A_{2x} = A_{3x} & (y=L) \end{cases} \quad (12)$$

(3) Tangential boundary condition of magnetic field:

$$\begin{cases} H_{1z} - H_{2z} = K_0 & (y=0) \\ H_{2z} - H_{3z} = K_L & (y=L) \end{cases}, \quad (13)$$

where,  $K_0$  and  $K_L$  are the linear current density at joint faces, and the surface current density in the conductor plate is  $J_e$ , then,

$$\begin{cases} K_0 = \int_{0^-}^{0^+} J_e dy = 0 \\ K_L = \int_{L^-}^{L^+} J_e dy = 0 \end{cases} \quad (14)$$

And according to the relation between the magnetic field intensity and magnetic vector potential,

$$H_{iz} = -\frac{1}{\mu_0} \frac{\partial A_{ix}}{\partial y} \quad (15)$$

Taking (14) and (15) into (13) may obtain:

$$\begin{cases} -\frac{\partial A_{1x}}{\partial y} - \left(-\frac{\partial A_{2x}}{\partial y}\right) = 0 & (y=0) \\ -\frac{\partial A_{2x}}{\partial y} - \left(-\frac{\partial A_{3x}}{\partial y}\right) = 0 & (y=L) \end{cases} \quad (16)$$

And the general solution of Formula (9) is [18]:

$$\begin{cases} A_{1x} = (C_1 e^{-R_1 y} + C_2 e^{R_1 y}) e^{j(pz+\omega t)} \\ A_{2x} = (C_3 e^{-R_2 y} + C_4 e^{R_2 y} + \theta(y)) e^{j(pz+\omega t)}, \\ A_{3x} = (C_5 e^{-R_3 y} + C_6 e^{R_3 y}) e^{j(pz+\omega t)} \end{cases} \quad (17)$$

where,

$$\begin{cases} R_i = \sqrt{p^2 - k_i^2} \\ \theta(y) = \frac{\mu_0 \gamma v B_{ym}(y)}{k_2^2} \end{cases} \quad (18)$$

$C_1$ - $C_6$  are undetermined constants, and it can, based upon the boundary conditional expressions (11), (12) and (16), be determined that the magnetic field in the plate is the superposition of static magnetic field and induced magnetic field generated by the permanent magnet. As a result, the electromagnetic field and eddy current in the space may be expressed as:

$$\begin{cases} B_y = B_{sy} + \frac{\partial A_{2x}}{\partial z} \\ B_z = B_{sz} + \left(-\frac{\partial A_{2x}}{\partial y}\right) \\ J_e = -\gamma v B_y = -\gamma v (B_{sy} + j p A_{2x}) \end{cases} \quad (19)$$

Levitation force and drag force may be expressed as:

$$\begin{cases} F_y = -\frac{1}{2} \operatorname{Re} \left( \int_{2\tau}^L \int_0^L J_e B_z^* dy dz \right) \\ F_z = \frac{1}{2} \operatorname{Re} \left( \int_{2\tau}^L \int_0^L J_e B_y^* dy dz \right) \end{cases}, \quad (20)$$

where,  $B_y^*$  and  $B_z^*$  are the conjugate complex numbers of magnetic fields in  $Y$  and  $Z$  directions.

## B. Finite element calculation

With ANSYS, this paper has established the conductor plate double Halbach PM-EDS finite element models. The model parameters are shown in Table 1 below.

Table 1: Model parameters

Parameters	Symbol	Values
Polar distance	$\tau$	100 mm
Remanence	$B_r$	1.277 T
Height of magnet	$h$	50 mm
Thickness of plate	$L$	3 mm
Resistivity of plate	$\rho$	$3.92e^{-8} \Omega m$
Upper air gap	$d1$	26 mm
Lower air gap	$d2$	32 mm
Width of model	$L_x$	100 mm

The element is PLANE53, and in view of the fact that materials in the model are of linear characteristics, it is hence to adopt the SOLVE linear solving method. The number of nodes generated totals 81573, and that of elements is up to 26962. The distribution of magnetic induction lines at 200 km/h is shown in Fig. 3.

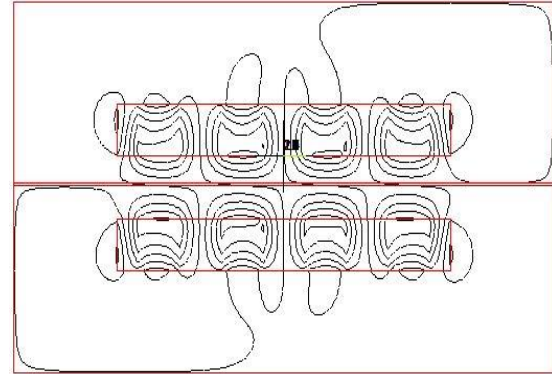


Fig. 3. Distribution of magnetic induction lines at 200 km/h.

To verify the validity of models, analytic and finite element methods are employed respectively to calculate the levitation force arising from the suspension system at 0-200 km/h under the parameters given in Table 1, as shown in Fig. 4.

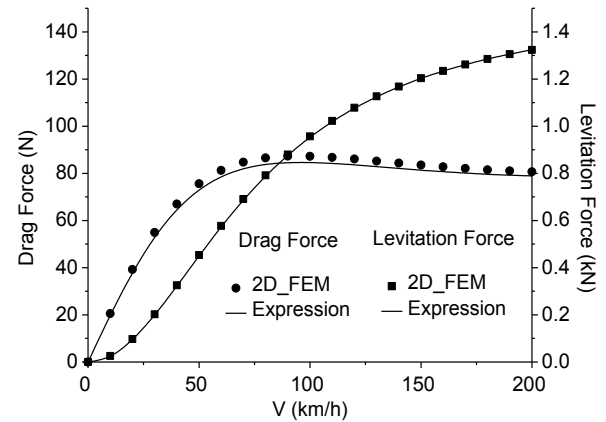


Fig. 4. Relations of electromagnetic force with the speed changes.

Figure 5 shows the relative errors between the analytic and finite element calculations at different speeds. It can be seen from the figure

that the maximum relative error is 4%, with a mean relative error of 1.7% only. Moreover, the maximum levitation error is just 1.2%.

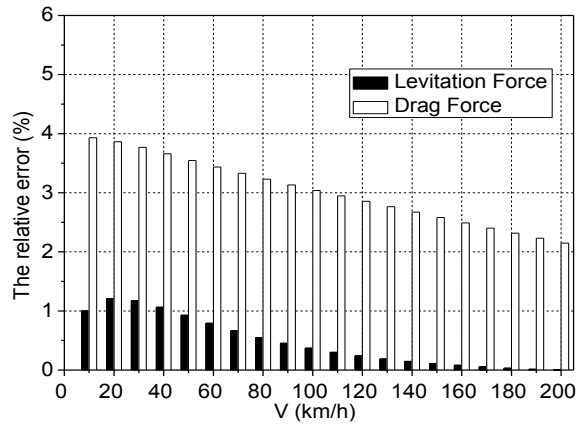


Fig. 5. Relative errors between the analytic and finite element methods.

#### IV. COMPARISON WITH THE TRADITIONAL SINGLE HALBACK PM-EDS

This paper proposes the conductor plate double Halbach PM-EDS scheme in order to increase the levitation-drag force ratio. To demonstrate its effectiveness, levitation-drag force ratio of both systems was calculated at different speeds. The parameters are shown in Table 2 and the structures of the single/double Halbach suspension systems are shown in Figs. 2 and 6 [10]. The single Halbach system has no permanent magnet array below it, so  $d_2$  is ignored. All other parameters are the same.

Table 2: Parameters of the single/double Halbach systems

Parameters	Symbol	Values
Polar distance	$\tau$	800 mm
Remanence	$B_r$	1.277 T
Height of magnet	$h$	300 mm
Thickness of plate	$L$	10 mm
Resistivity of plate	$\rho$	$3.92e^{-8} \Omega m$
Upper air gap	$d_1$	15 mm
Lower air gap	$d_2$	60 mm

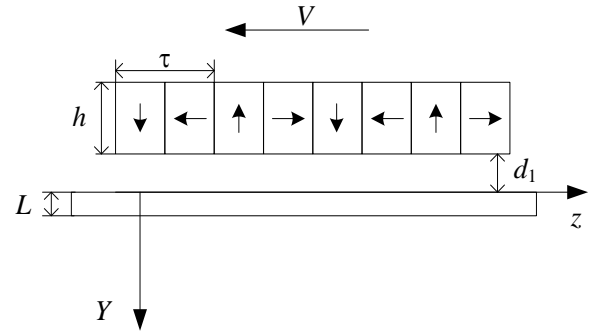


Fig. 6. Sketch diagram of conductor plate single Halbach suspension system.

The curve in Fig. 7 shows how the levitation-drag force ratio of the single and double Halbach suspension systems changes with speed. The figure indicates that, compared with the traditional single Halbach system, the double Halbach system considerably increases the levitation-drag force ratio. In applied engineering, when a maglev train is in a suspension state, the levitation force is equal to the gravity, which is a constant. Therefore, a greater levitation-drag force ratio means a smaller drag force and less power loss. This demonstrates the superiority of this new suspension system.

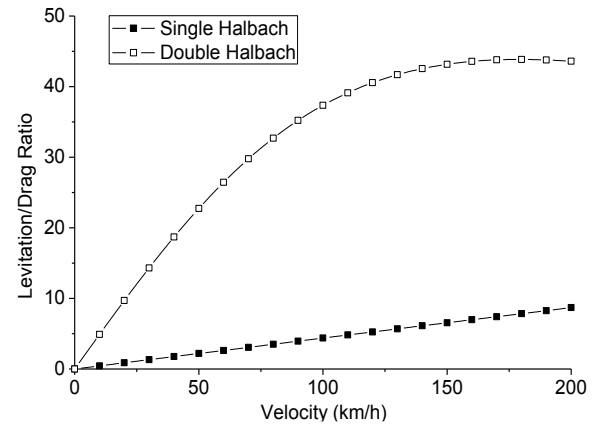


Fig. 7. Comparison of levitation-drag force ratios of single and double Halbach PM-EDS systems.

If  $\eta_1$  and  $\eta_2$  represent the levitation-drag force ratios of the single and double Halbach PM-

EDS systems,  $\eta_1/\eta_2$  changes with speed as shown in the curve in Fig. 8.

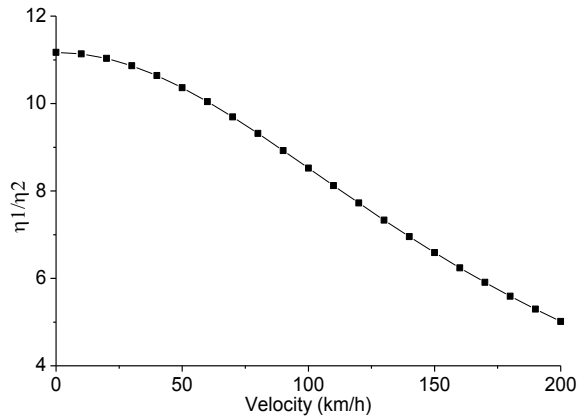


Fig. 8. Improvement of levitation-drag force ratio.

At different speeds, the double Halbach suspension system can increase the levitation-drag force ratio 5 to 11 times. Since the levitation-drag force ratio improvement decreases as speed increases, this improvement is more significant at low speeds. Therefore, the double Halbach system is more suitable for low-speed urban rail transit.

## V. CONCLUSION

Based on the reference to relevant studies, this paper proposes the conductor plate double Halbach permanent magnet electrodynamic suspension to address issues with the existing system, provides the analytic calculation method applicable to this suspension model and proves the accuracy of this analytic method using the finite element method. Finally, this paper compares the levitation-drag force ratios of the two suspension systems to demonstrate that the double Halbach system can solve the problem of low levitation-drag force ratio and high drag force in the single Halbach system, and therefore, has positive significance for further research into electrodynamic suspension.

## ACKNOWLEDGMENT

This material is based upon work supported by the Fundamental Research Funds for the Central Universities (2682013ZT18) and Doctor Innovation Funds of SWJTU (2014).

## REFERENCES

- [1] R. Kratz and R. F. Post, "A null current electrodynamic levitation system," *IEEE Transactions on Applied Superconductivity*, vol. 12, no. 1, pp. 930-932, 2002.
- [2] Y. Wu, L. Yan, and S. Xu, "Inductrack technology and its application in maglev transport," *Electric Application*, vol. 25, no. 1, pp. 1-3, 2006.
- [3] S. M. Jang, S. H. Lee, and S. S. Jeong, "Characteristics analysis of eddy-current brake system using the linear halbach array," *IEEE Transactions on Magnetics*, vol. 38, no. 8, pp. 2994-2996, 2002.
- [4] S. M. Jang, S. S. Jeong, and S. D. Cha, "The application of linear halbach array to eddy current rail brake system," *IEEE Transactions on Magnetics*, vol. 37, no. 7, pp. 2627-2629, 2001.
- [5] Z. Tan and Y. Li, "Development of flywheel energy storage system control platform based on dual-DSP," *Power System Protection and Control*, vol. 40, no. 11, pp. 127-139, 2012.
- [6] P. Tang, Y. Qi, G. Huang, and T. Li, "Eddy current loss analysis of iron-less flywheel electric machine's winding," *Transactions of China Electrotechnical Society*, vol. 25, no. 3, pp. 27-32, 2010.
- [7] Y. Huang, B. Fang, and J. Sun, "Simulation research on the microgrid with flywheel energy storage system," *Power System Protection and Control*, vol. 39, no. 9, pp. 83-113, 2011.
- [8] C. Li, Y. Du, P. Xia, and L. Yan, "Analysis and experimental testing of EDS maglev with linear halbach and conducting sheet," *Transactions of China Electrotechnical Society*, vol. 24, no. 1, pp. 18-22, 2009.
- [9] J. Wang, Y. Li, and L. Yan, "Study on applying the linear halbach array to eddy current brake system for maglev," *Electric Drive*, vol. 40, no. 5, pp. 8-11, 2010.
- [10] H. W. Cho, H. S. Han, J. S. Bang, H. K. Sung, and B. H. Kim, "Characteristic analysis of electrodynamic suspension device with permanent magnet halbach array," *Journal of Applied Physics*, vol. 105, no. 7, pp. 3141-3143, 2009.
- [11] R. F. Post and D. D. Ryutov, "The inductrack: a simpler approach to magnetic levitation," *IEEE Transactions on Applied Superconductivity*, vol. 10, no. 1, pp. 901-904, 2000.
- [12] M. Toshiaki and H. Hitoshi, "Electromagnetic analysis of inductrack magnetic levitation," *Electrical Engineering in Japan*, vol. 142, no. 1, pp. 67-74, 2003.
- [13] X. Huang, Q. Zhang, and G. Zhou, "Halbach permanent magnet iron-less linear motors," *Transactions of China Electrotechnical Society*, vol. 25, no. 6, pp. 1-6, 2010.

- [14] P. Meng, X. Qiu, and W. Lin, "Study of the dynamic characteristics of directly driven permanent magnet synchronous wind turbine," *Power System Protection and Control*, vol. 40, no. 14, pp. 38-43, 2012.
- [15] J. Fan, J. Wu, C. Li, et al., "Solution of permanent magnet synchronous motors with partition between poles halbach magnet," *Transactions of China Electrotechnical Society*, vol. 28, no. 3, pp. 36-42, 2013.
- [16] Y. Zhang, D. Qiao, and J. Gao, "Current research on and applications of halbach permanent magnet array," *Analytical Instrumentation*, vol. 1, no. 2, pp. 5-10, 2010.
- [17] J. F. Hoburg, "Modeling maglev passenger compartment static magnetic field from linear halbach permanent magnet arrays," *IEEE Transactions on Magnetics*, vol. 40, no. 1, pp. 59-64, 2004.
- [18] Y. Chena and K. Zhang, "Calculation and analysis of the forces created by halbach permanent magnet electrodynamic suspension," *Applied Mechanics and Materials*, vol. 229, pp. 440-443, 2012.
- [19] Y. Lei, "Analytic calculation of harmonic electromagnetic field," Beijing, China, 2000.
- [20] C. Feng and X. Ma, "Introduction of engineering electromagnetic field," Beijing, China, 2000.

# A Novel Fractal Monopole Antenna with Wide Bandwidth Enhancement for UWB Applications

Bahman Heydari<sup>1</sup>, Zakarya Sanaati<sup>1</sup>, Vorya Waladi<sup>1</sup>, and Yashar Zehforoosh<sup>2\*</sup>

<sup>1</sup>Department of Electrical Engineering, Science and Research Branch  
Islamic Azad University, Urmia, Iran  
bahman.heydari1@gmail.com, sanaatilgboukan@yahoo.com, v.waladi@gmail.com

<sup>2\*</sup>Department of Electrical Engineering, Urmia Branch  
Islamic Azad University, Urmia, Iran  
y.zehforoosh@srbiau.ac.ir

**Abstract** — A novel wideband fractal monopole antenna with a semi-elliptical ground plane is presented. In this letter, by inserting a fractal shape in the conventional circular ring, much wider impedance bandwidth and new resonances are generated. By only increasing the fractal iterations, larger bandwidth is attained. The designed antenna has a compact size of  $25 \times 25 \times 1$  mm<sup>3</sup> and operates over the frequency band between 2.2 and 17 GHz for  $VSWR < 2$ . The process of improving the impedance bandwidth and measured results are presented and discussed.

**Index Terms** — Fractal, monopole antenna, Ultra-Wideband (UWB).

## I. INTRODUCTION

With the development of wireless technology, satellite navigation systems, wireless LANs, Ultra-Wideband systems (UWB) and some combinations of them are introduced. Therefore, a single antenna with stable radiation properties and wide impedance Bandwidth (BW) enough to cover the multiple wireless communication systems is respectable [1-4].

During the recent years, various types of monopole antennas using modified patch and ground plane or feeding structure have been discussed in order to achieve more improvement of the BW [1-6] and radiation characteristics [6-8]. In addition, reducing the antenna size with keeping the

previous features such as wide BW, good matching and stable radiation characteristics is more beneficial.

In this letter, a wideband fractal monopole antenna is presented. Fractal geometry has been useful to design small, multiband, and high-directive elements [9-13]. Effects of the fractal iterations and a semi-elliptical ground plane will be shown. Here, we show that by increasing of the fractal iterations, impedance bandwidth is between 2.2 to 17 GHz and can support most of the communication standards such as IEEE802.11a in the US (5.15-5.35 GHz, 5.725-5.825 GHz), HIPERLAN/2 in Europe (5.15-5.35 GHz, 5.47-5.725 GHz) and UWB (3.1-10.6 GHz). The proposed antenna design, simulation and measured results are shown and discussed.

## II. ANTENNA DESIGN

The geometry of the proposed antenna which consist of fractal patch with a semi-ellipse shaped ground plane is illustrated in Fig. 1. The scale factor for converting the first iteration to second iteration is 0.5 and etc. The construction procedure of the antenna is illustrated in Fig. 3. The final fractal shape of radiating patch is achieved by inscribing the first iteration of koch fractal within the circular radiating patch, and repeating this three times. More iterations aren't implemented because of negligible effect on impedance bandwidth of proposed antenna.

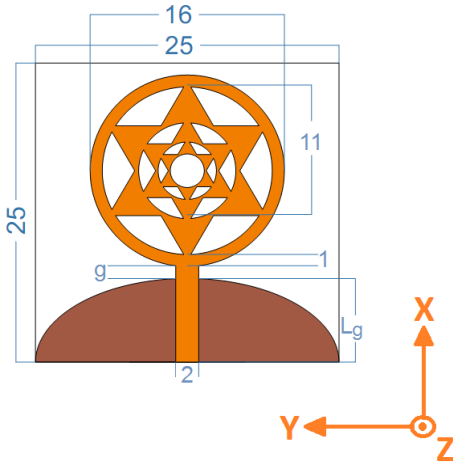


Fig. 1. Configuration and parameters of the proposed antenna (unit: millimeters).

The proposed fractal antenna with specified dimension of  $25 \times 25$  is printed on FR4 substrate with relative permittivity of 4.4, loss tangent of 0.02 and thickness of 1 mm. To achieve a better impedance matching that results in bandwidth enhancement, the technique of loading a rectangular notch with dimension of  $2 \times 2 \text{ mm}^2$  at the feeding position in the ground plane is used [1]. The proposed shape of the truncation in the ground-plane acts as an effective impedance matching network to realize an antenna with a wide impedance bandwidth. This is because the truncation creates capacitive loading that neutralizes the inductive nature of the patch to produce nearly pure resistive impedance present at the antenna’s input [14-16]. The width  $W_f$  and length  $L_f$  of the microstrip feed line to achieve  $50 \Omega$  characteristic impedance are fixed at 2 and 8 mm, respectively.

Due to the increasing fractal iteration on the fractal patch, it is expected that the bandwidth of antenna will be increased [1]. The fractal patch is printed on the top surface of the substrate, has the distance of  $g=0.5$  mm to the ground plane.

The dimension of the ground plane is  $L_g=7.5$  mm and the width of  $W_g=25$  mm. The final optimal values of the parameters of the antenna are shown in Fig. 1. Moreover, the structure of the antenna is symmetrical with respect to the longitudinal direction. The height of the feed gap between the main patch and the ground ( $g$ ) is also an important parameter to control the impedance bandwidth. Since  $g$  is the gap between the ground plane and the

patch, in a broad sense, the ground plane serves as an impedance matching circuit and it also turns the resonant frequency [1]. By adjusting  $g$ , the electromagnetic coupling between the lower edge of the patch and ground plane can be properly controlled [3].

### III. SIMULATED AND MEASURED RESULTS

The parameters of the proposed antenna are studied by changing one parameter at a time while fixing the others. To fully understand the behavior of the antenna’s structure and to determine the optimum parameters, the antenna was analyzed using Ansoft HFSS (ver. 13). In this section, we have presented the simulated results for the first three iterations of the proposed antenna, and different values of  $L_g$  and  $g$  based on the third iteration of the proposed fractal antenna. Eventually, the simulation and measured of proposed fractal antenna are presented.

The simple semi-ellipse Ground (GND) plane acts as an impedance matching circuit [5]. The parameters  $L_g$  and  $g$ , is the two prominent factors of the third iteration of the proposed fractal antenna, which are optimized to attain the most impedance bandwidth and better impedance matching. The simulated  $S_{11}$  curves for the third iteration of fractal antenna with different values of  $L_g$  and  $g$  are plotted in Fig. 2.

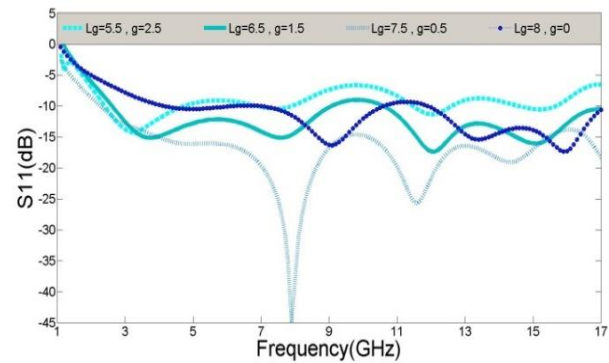


Fig. 2. Simulated  $S_{11}$  curves for the third iteration of the fractal antenna with different  $L_g$  and  $g$ .

When the ground length  $L_g$  enlarges, the impedance bandwidth increases up. As shown in Fig. 2, the small changes in the width of the gap between the fractal patch and the ground plane,  $g$ , has an impressive effect on the impedance

matching of the third iteration of the fractal antenna. By decreasing  $g$  up to 0.5 mm, the ellipticity of the ground plane improves the impedance matching of the proposed antenna. Also, with increasing  $L_g$  to 8 mm and decreasing  $g$  to 0 mm simultaneously, unprincipled results will be obtained. Consequently, the optimum value for  $L_g$  and  $g$  are 7.5 and 0.5 mm, respectively. Simulated  $S_{11}$  for the first three iterations of the fractal is framed in Fig. 3. From the simulation results in Fig. 3, it is observed that by increasing fractal iteration on the fractal patch impedance bandwidth will be increased and new resonances attained.

The measured results of  $S_{11}$  parameter of the designed antenna is presented in Fig. 4. The 10-dB bandwidth of the proposed antenna is 2.2~17 GHz. From the simulation and measured results, it is observed that the impedance bandwidth increases in the measurement.

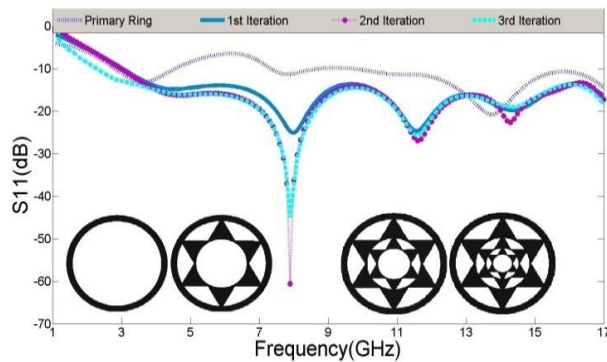


Fig. 3. The simulated  $S_{11}$  curves for the first three iterations of the fractal antenna and primary ring.

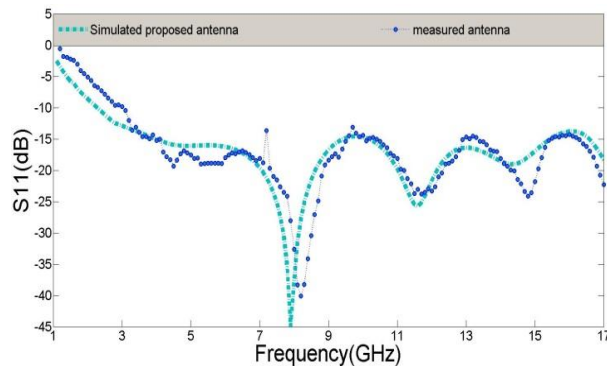


Fig. 4. The  $S_{11}$  curves of the simulated proposed fractal antenna and measured antenna.

The proposed fractal antenna have not only been simulated, but additionally fabricated as printed monopoles using common Printed Circuit Board (PCB) methods (Fig. 5). The impedance bandwidth of the antenna is measured using the Agilent 8722ES Network Analyser. In this part of the paper, we have presented the measured results for a fabricated model of the proposed fractal antenna using optimum simulated design parameters. Measured results of the radiation patterns of the corresponding proposed antenna at 4.5, 6, 9, and 13 GHz are depicted in Fig. 6. It is seen that the fractal antenna provides omnidirectional radiation patterns in the H-plane (y-z plane) and stable patterns in the form of figure-eight in the E-plane (x-z plane).

The Simulated and measured results of radiation efficiency and peak gain variation of proposed fractal antenna are displayed in Fig. 7. Here, a raising gain from 2.2 to 17 GHz is manifest with small fluctuation in simulation. As shown in Fig. 7, the simulated peak gain is stable along 2.2-17 GHz of the antenna operating band. Also, the measured peak gain has an increasing procedure from 2.2 to 12 GHz with small frequency variation. Also, radiation efficiency in Fig. 7 is presented. We see that good adjustment is available between simulated and measured results. The real and imaginary parts of the antenna input impedance for the proposed fractal antenna are simulated and presented in Fig. 8.

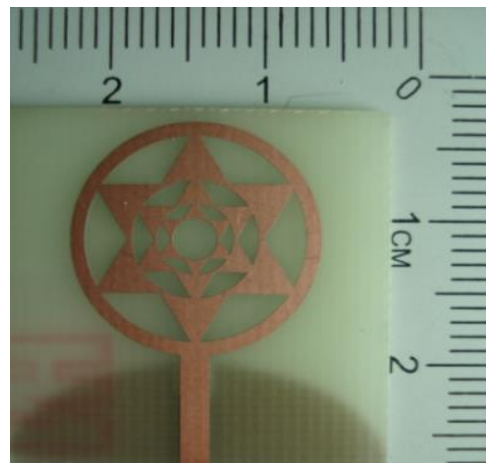


Fig. 5. Photograph of the fabricated prototype fractal antenna.

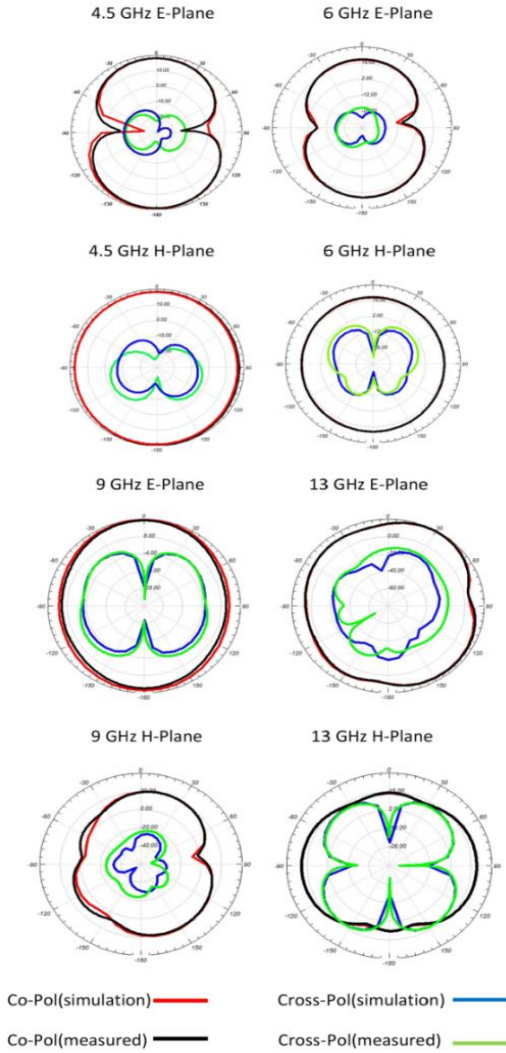


Fig. 6. Simulated & measured E-plane (x-z) and the H-plane (y-z) radiation patterns of proposed fractal antenna at 4.5, 6, 9 and 13 GHz.

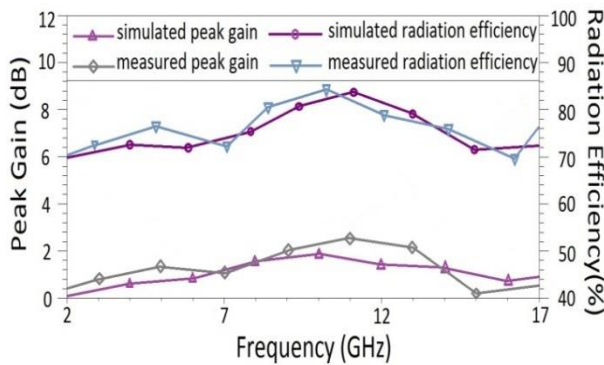


Fig. 7. Simulated and measured results of radiation efficiency and peak gain variation of proposed antenna.

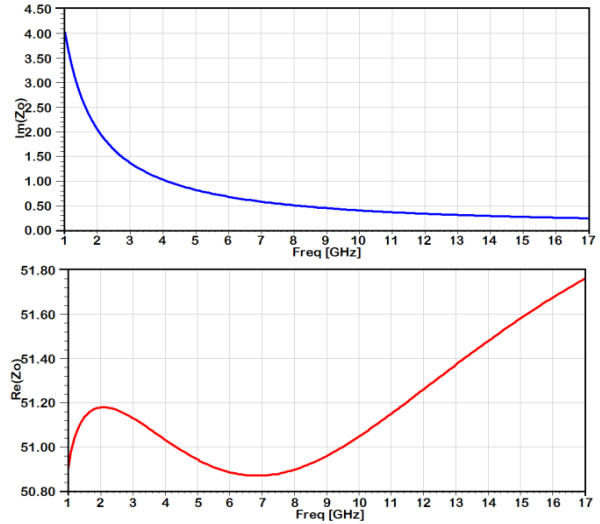


Fig. 8. Simulated antenna input impedance ( $\Omega$ ) curves versus frequency for the proposed antenna.

#### IV. CONCLUSION

A novel fractal monopole antenna with a compact size was presented and investigated. We showed that by increasing the fractal iteration and optimizing antenna parameters with proper values, a very good impedance matching and improvement bandwidth can be obtained. This would be the results of special layout properties. The operating bandwidth of the proposed fractal antenna covers the entire frequency band from 2.2 to 17 GHz. Both measured and simulated results had been suggested that the proposed fractal antenna can be suitable for UWB communication applications.

#### REFERENCES

- [1] V. Waladi, N. Mohammadi, Y. Zehforoosh, A. Habashi, and J. Nourinia, "A novel modified star-triangular fractal (MSTF) monopole antenna for super-wideband applications," *IEEE Antennas Wireless Propag. Lett.*, vol. 12, pp. 651-654, 2013.
- [2] K. J. Venoy, J. K. Abraham, and V. K. Varadan, "Fractal dimension and frequency response of fractal shaped antennas," *In Proc. IEEE Antennas Propag. Soc. Int. Symp.*, vol. 4, pp. 222-225, June 2003.
- [3] M. J. Ammann and Z. N. Chen, "Wideband monopole antennas for multi-band wireless systems," *IEEE Antennas Propag. Mag.*, vol. 45, no. 2, pp. 146-150, April 2003.
- [4] S. R. Best, "The effectiveness of space filling fractal geometry in lowering resonant frequency," *IEEE Antennas Wireless Propag. Lett.*, vol. 1, pp. 112-115, 2002.

- [5] S. S. Zhong, X. L. Liang, and W. Wang, "Compact elliptical monopole antenna with impedance bandwidth in excess of 21:1," *IEEE Trans. Antennas Propag.*, vol. 55, pp. 3082-3087, November 2007.
- [6] E. S. Angelopoulos, A. Z. Anastopoulos, D. I. Kaklamani, A. A. Alexandridiss, F. Lazarakis, and K. Dang, "Circular and elliptical CPW-fed slot and microstrip-fed antennas for ultra-wideband applications," *IEEE Antennas Wireless Propag. Lett.*, vol. 5, pp. 294-297, 2006.
- [7] T. G. Ma and S. K. Jeng, "Planar miniature tapered-slot-fed annular slot antennas for ultra-wideband radios," *IEEE Trans. Antennas Propag.*, vol. 53, no. 3, pp. 1194-1202, March 2005.
- [8] Y. Zehforoosh, M. Naser-Moghadasi, R. A. Sadeghzadeh, and C. Ghobadi, "Miniature fractal monopole antenna with inscribed arrowhead cuts for UWB applications," *IEICE Elect. Expr.*, vol. 9, no. 24, pp. 1855-1860, 2012.
- [9] J. Anguera, C. Puente, C. Borja, and J. Soler, "Fractal-shaped antennas: a review," *In Wiley Encyclopedia of RF and Microwave Engineering*, vol. 2, pp. 1620-1635, 2005.
- [10] C. T. P. Song, P. S. Hall, and H. Ghafouri Shiraz, "Multiband quasi-fractal multiple ring monopole antenna," *IEEE Transactions on Antennas and Propagation*, 51 (4): 722-729, 2003.
- [11] J. P. Gianvittorio and Y. Rahmat-Samii, "Fractal antennas: a novel antenna miniaturization technique, and applications," *IEEE Antennas and Propagation Magazine*, vol. 44, n. 1, pp. 20-36, February 2002.
- [12] J. Anguera, J. P. Daniel, C. Borja, J. Mumbrú, C. Puente, T. Leduc, N. Laeveren, and P. Van Roy, "Metallized foams for fractal-shaped microstrip antennas," *IEEE Antennas and Propagation Magazine*, vol. 50, n. 6, pp. 20-38, December 2008.
- [13] J. Anguera, E. Martínez, C. Puente, C. Borja, and J. Soler, "Broad-band triple-frequency microstrip patch radiator combining a dual-band modified sierpinski fractal and a monoband antenna," *IEEE Transactions on Antennas and Propagation*, vol. 54, n. 11, pp. 3367-3373, November 2006.
- [14] A. A. Eldek, "Numerical analysis of a small ultra wideband microstrip fed tap monopole antenna," *Prog. Electromagn. Res.*, 65, 59-69, 2006.
- [15] M. Naser-Moghadasi, G. R. Dadashzadeh, M. Abdollahvand, Y. Zehforoosh, and B. S. Virdee, "Planar triangular monopole antenna with multioctave bandwidth," *Microw. Opt. Technol. Lett.*, 53: 10-14, 2011.
- [16] R. A. Sadeghzadeh, Y. Zehforoosh, and N. Mirmotahhary, "Ultra-wideband monopole antenna with modified triangular patch," *Microw. Opt. Technol. Lett.*, 53: 1752-1756, 2011.



**Bahman Heydari** was born in Boukan, Iran. He received his B.Sc. degree in Electrical Engineering Telecommunication from the Urmia Branch of Islamic Azad University, Urmia, Iran, in 2011 and his M.Sc. degree in Electrical Engineering Telecommunication from the Urmia Branch of Islamic Azad University, Urmia, Iran, in 2013. His primary research interests are in antenna design, filters, and microwave component.



**Zakarya Sanaati** was born in Boukan, Iran. He received his B.Sc. degree in Electrical Engineering Telecommunication from the Urmia Branch of Islamic Azad University, Urmia, Iran, in 2012. He is currently working towards his M.Sc. degree in Electrical Engineering Telecommunication from the Urmia Branch of Islamic Azad University, Urmia, Iran. His primary research interests are in antenna theory and microwave component.



**Vorya Waladi** was born on September 21, 1986 in Sanandaj, Iran. He received his B.Sc. degree in Electrical and Electronic Engineering from Jahad Daneshgahi University, Hamedan, Iran, in 2011 and his M.Sc. degree in Electrical and Telecommunication Engineering from the Urmia Branch of Islamic Azad University, Urmia, Iran, in 2013. He is currently working towards his Ph.D. degree in Communication Engineering Fields and Waves. Since 2009, he has taught courses in Communication Circuits, Microwave Engineering, Antenna Theory, and Fields & Waves at Jahad Daneshgahi University. His research interests include antenna theory, electromagnetic structures, microwave component and filters.



**Y. Zehforoosh** was born in Urmia Iran in 1981. He received his Ph.D. degree from Urmia Islamic Azad University in 2012 in Telecommunication Engineering Fields and Waves. Also, he is a Faculty with the Electrical Engineering Department of Urmia Branch of Islamic Azad University, Urmia, Iran since 2009 where he is currently Head of the Technical Department and also Member of Central Research Council. His research interests include broadband antennas, electromagnetic structures and UWB systems.

# 60-GHz 3-D Cavity Bandpass Filter for V-Band Gigabit Wireless Systems

Gang Zhang, Jianpeng Wang, Hui Gu, and Xin Xu

Ministerial Key Laboratory of JGMT

Nanjing University of Science and Technology, Nanjing 210094, China

elegzhang@gmail.com, eejpwang@gmail.com, guhuinjust@gmail.com, xuxinnjust@gmail.com

**Abstract** — In this paper, a compact 60-GHz Three-Dimensional (3-D) SIW-based bandpass filter is presented using Low-Temperature Co-fired Ceramic technology (LTCC). The filter is composed of four cavities. The coupling scheme is made up of three direct coupling and one cross coupling between the first and the fourth SIW cavities. By using the cross coupling technology and the cavity transformation property, two Transmission Zeros (TZs) are introduced outside the passband to increase the filtering selectivity. Both simulated and measured results are presented in good agreement.

**Index Terms** — 60-GHz, bandpass filter, compact, Low-Temperature Co-fired Ceramic (LTCC).

## I. INTRODUCTION

As the demand for compact, low-loss Bandpass Filters (BPFs) increases in 60-GHz multigigabit-per-second wireless transceiver systems, integrating on-package cavity filters, based on the standard Substrate Integrated Waveguide (SIW) using multilayer Low-Temperature Co-fired Ceramic (LTCC) technology, has emerged as an attractive solution [1-5]. The LTCC based SIW cavity filters have a relatively high quality factor  $Q$ , a high power-handling capability compared to planar filter structures, and less interference from other circuits integrated in package.

Three LTCC bandpass filters with standard Chebyshev responses which exhibit poor out-of-band rejection are presented in [1,2,3]. Thus, to enhance the filtering selectivity, LTCC bandpass filters with quasi-elliptic responses which can

introduce two transmission zeros outside the passband [4-5] are proposed. However, due to the mechanism of generating transmission zeros adopted in these designs, the circuit size is not compact. Therefore, the design of a LTCC millimeter-wave bandpass filter with a compact size and a high selectivity is meaningful.

The motivation of this paper is to propose a SIW-based LTCC 60-GHz bandpass filter, which can be fully integrated into miniaturized V-band LTCC transceiver modules. By introducing the cross-coupling mechanism and vertically coupled structure, a high filtering selectivity and a compact circuit size are both achieved. The design principles and processes are illustrated in detail. To verify the validity of the design method, both simulated and measured results are presented.

## II. STRUCTURES AND DESIGN PROCESSES

Figure 1 shows the geometric configuration of the proposed SIW quasi-elliptic filter, consisting of four SIW cavity resonators which occupy substrate layers 2-5. And the filter is directly excited by the open-ended microstrip feedlines via coupling slots etched on the first/fourth cavity. The schematic topology of this filter is shown in Fig. 2, where  $k_{ij}$  represents the coupling coefficient between the  $i$ - and  $j$ th resonator cavity, while the solid and dashed lines indicate the main and cross-coupling paths, respectively. To achieve the quasi-elliptic function with a pair of attenuation poles at finite frequencies, it is essential that the signs of the coupling coefficients  $k_{12}$ ,  $k_{23}$ ,  $k_{34}$  should be opposite to  $k_{14}$ . However, it does not matter which

one of them is positive, as long as their signs are opposite. For convenience, it is assumed that  $k_{12}$ ,  $k_{23}$ ,  $k_{34}$  are positive while  $k_{14}$  is negative. To realize this negative coupling of  $k_{14}$ , the  $TE_{201}$ -mode is excited in cavity 3 using the cavity transformation property while the other three cavities are resonating at the  $TE_{101}$ -mode.

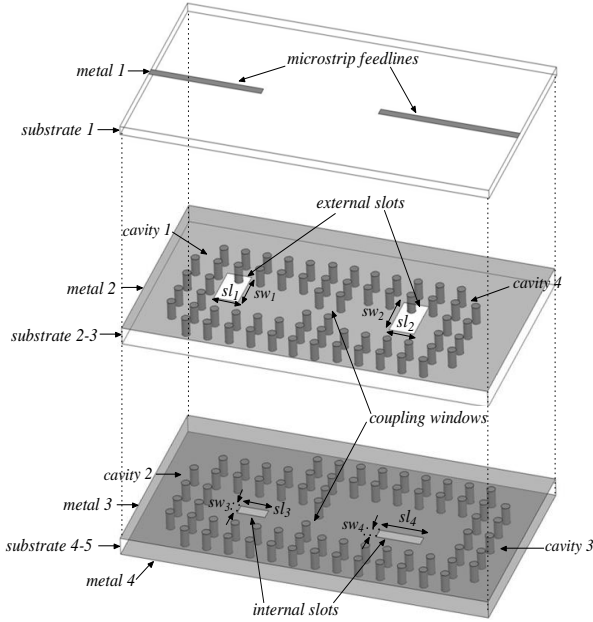


Fig. 1. Geometric configuration of the proposed SIW cross-coupled filter.

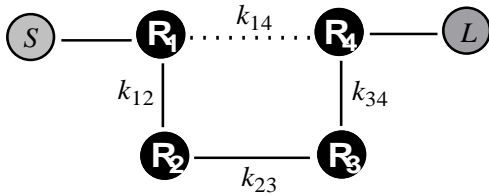


Fig. 2. Equivalent schematic topology of the proposed SIW cross-coupled filter.

### A. Circuit synthesis

The designed quasi-elliptic filter is centered at 59 GHz with 25 dB return loss in the passband while two normalized TZs are at  $\pm 2.27j$ . To achieve this design, we should firstly synthesize a low-pass prototype, which meets the given specification and determines an appropriate coupling matrix as well. Generally speaking, the synthesis of the filter has three steps. Firstly, the zeros and poles of the transfer function should be

obtained according to the specification of the filter. Secondly, generalized coupling matrix or generalized element values of the low-pass prototype can be obtained. Finally, we can calculate the design parameters by denormalizing the generalized element values. Based on the approach to the synthesis of cross-coupled resonators filter using the analytical gradient-based optimization technique [6], the generalized coupling matrix coefficients referred in Fig. 2 can be synthesized as shown in Table 1.

Table 1: Coupling matrix coefficients

Nonzero Entries	Normalizing Value
$M_{S1} = M_{S1}$	1.1413
$M_{12} = M_{12}$	0.9972
$M_{14} = M_{14}$	-0.1866
$M_{23} = M_{23}$	0.8375
$M_{34} = M_{34}$	0.9972
$M_{4L} = M_{4L}$	1.1413

The generalized coupling matrix is denormalized by using the following formula [7]:

$$k_{ij} = FBWM_{ij}, Q_e = 1/(FBWM_{S1}^2), FBW = BW/f_0. \quad (1)$$

Where  $FBW$  is the relative bandwidth,  $BW$  is the absolute bandwidth, and  $f_0$  is the center frequency. Then the design parameters of the proposed filter are given as:  $k_{12}=0.0399$ ,  $k_{23}=0.0334$ ,  $k_{34}=0.0399$ ,  $k_{14}=-0.0075$ ,  $Q_e=19.2$ .

### B. SIW cavity size

The SIW cavity resonator is constructed by a stacked LTCC substrate with a relative permittivity of 5.7, metal surfaces at the outer layers and via arrays. The SIW cavity size is determined by the corresponding resonant frequency using the following formula [8]:

$$f_{TE_{m0q}} = \frac{C_0}{2\sqrt{\epsilon_r}} \sqrt{\left(\frac{m}{W_{eff}}\right)^2 + \left(\frac{q}{L_{eff}}\right)^2}, \quad (2)$$

$$L_{eff} = L - \frac{d^2}{0.95p}, W_{eff} = W - \frac{d^2}{0.95p}. \quad (3)$$

Where  $W$  and  $L$  are the width and length of the cavity, respectively.  $d$  and  $p$  are the diameters of metalized via-holes and center-to-center pitch between two adjacent via-holes.  $C_0$  is the light velocity in vacuum.  $\epsilon_r$  is the relative permittivity of the substrate.

### C. External-coupling

In the proposed filter, the external quality factor  $Q_e$  can be controlled by the position and size of the coupling slots etched in the top metal layer (metal 2) of the cavities [9]. To determine the dimensions of the slots, the coupling slots are initially located at the position of a quarter of the cavity length and a short circuit is realized at the center of each slot by terminating the feedlines with  $\lambda_g/4$  open stubs to maximize the coupling [10]. Then, the slots width is varied with constant  $\lambda_g/4$  slot length, where  $\lambda_g$  is the guided wavelength at  $f_0$ . The external quality factor  $Q_e$  is calculated following the relationship below [7]:

$$Q_e = \frac{f_0}{\Delta f_{\pm 90^\circ}}. \quad (4)$$

Where  $\Delta f_{\pm 90^\circ}$  is the frequency difference between the  $\pm 90^\circ$  phase responses of  $S_{11}$ .

### D. Internal coupling

The internal couplings are realized by broad-wall slots in different layers and a narrow-wall window at the same layer. The coupling coefficient of the broad-wall slot is affected by the length and position of the slot. To get strong direct coupling, the slot should be located as close to the sidewall of the cavity as possible. The coupling coefficient of the narrow-wall window is controlled by the separation degree between the via pair. All the internal couplings have been extracted (using full-wave simulation) according to the following equation [7]:

$$k_{ij} = \pm \frac{f_{c1}^2 - f_{c2}^2}{f_{c1}^2 + f_{c2}^2}. \quad (5)$$

In (5),  $f_{c1}$  and  $f_{c2}$  are defined as the high and low resonance frequencies, respectively.  $k_{ij}$  represents the coupling coefficient between the two SIW cavity resonators. The sign of the  $k_{ij}$  is dependent on the physical structure of the coupled resonators.

In addition, the principal mechanism of implementing the internal negative coupling coefficient between cavities 1 and 4, i.e., and  $k_{14}$  has been clarified below. As mentioned above, TE<sub>201</sub>-mode is excited in cavity 3 using the cavity transformation property while the other three cavities are resonating at the TE<sub>101</sub>-mode. The magnetic field distributions functioning in the proposed configuration is clearly depicted in Fig.

3. It is not difficult to find that the field direction within TE<sub>101</sub>-mode cavity 4 determines the sign of the cross coupling  $k_{14}$ . This relationship is intrinsically determined by the TE<sub>201</sub>-mode cavity 3 and the coupling slot location between cavities 3 and 4. As it is illustrated in Fig. 3, the magnetic fields between cavities 1 and 4 will be reversed when the coupling slot between cavities 3/4 is selectively located at the right half of cavity 3, resulting in the negative coupling coefficient [7]. Alternatively, if the coupling slot is arranged at the left half of cavity 3, the  $k_{14}$  will be positive, which can be further utilized to construct a filter with liner phase characteristics [11].

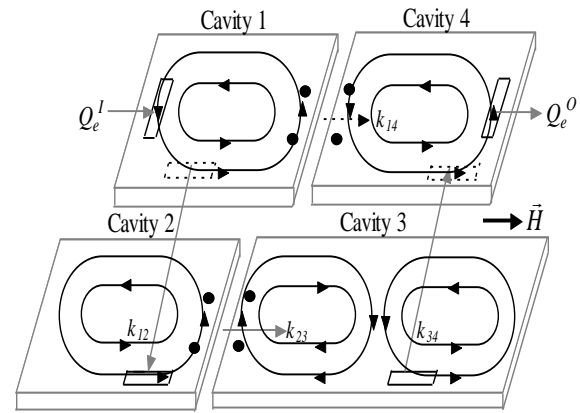


Fig. 3. Principal magnetic field patterns.

Based on the theory and process mentioned above, the initial dimensions of this filter could be deemed as optimal variables and they are well tuned to achieve the desired frequency response using High Frequency Structure Simulator (HFSSv12). The diameter of the metallic via hole is 0.15 mm and the space between two adjacent via holes is around 0.4 mm. The final dimensions of the filter illustrated in Figs. 1, 4 and 5 are the following:  $w_m=0.13$  mm,  $w_1=1.3$  mm,  $w_2=1.3$  mm,  $w_3=1.46$  mm,  $w_4=1.54$  mm,  $w_5=1.71$  mm,  $l_t=4.29$  mm,  $l_1=1.93$  mm,  $l_2=1.97$  mm,  $l_3=1.95$  mm,  $l_4=2.73$  mm,  $sp_1=0.46$  mm,  $sp_2=0.575$  mm,  $sp_3=0.975$  mm,  $sp_4=0.905$  mm,  $sw_1=0.69$  mm,  $sw_2=0.84$  mm,  $sw_3=0.2$  mm,  $sw_4=0.2$  mm,  $sl_1=0.39$  mm,  $sl_2=0.46$  mm,  $sl_3=0.5$  mm,  $sl_4=0.82$  mm,  $sh_1=0.275$  mm,  $sh_2=0.275$  mm,  $p_1=0.66$  mm,  $p_2=0.74$  mm,  $r_1=1.135$  mm,  $r_2=0.965$  mm,  $r_3=0.965$  mm,  $r_4=0.965$  mm,  $g_1=0.375$ ,  $g_2=0.355$  mm.

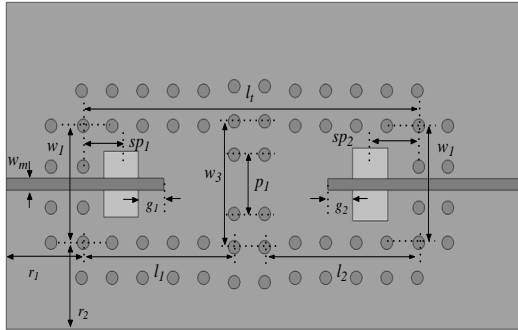


Fig. 4. Geometric parameters of top view of the substrate layers 2-3 and metal 1.

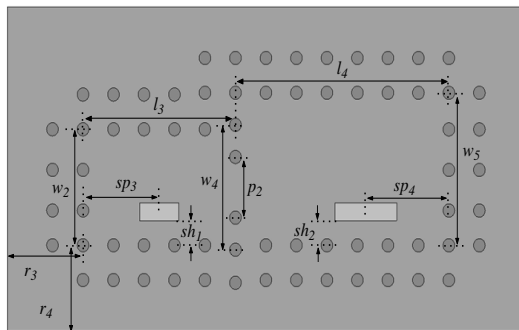


Fig. 5. Geometric parameters of top view of the substrate layers 4-5.

### III. FABRICATION AND MEASUREMENT

The designed filter is fabricated on LTCC substrate characterized by  $\epsilon_r=5.7$ ,  $\tan \delta=0.002$ , whose thickness is 0.1 mm. By connecting ZVA-75 frequency converts with a ZVA-50 vector network analyzer, we can convert the original frequency range of ZVA-50 vector network analyzer (10 MHz-50 GHz) to a new frequency range of 50-75 GHz. Therefore, the measurement frequency range can successfully cover the passband range of the filter through this method.

The photograph of the fabricated circuit is indicated in Fig. 6. Figure 7 shows the simulated and measured results of the proposed filter. The fabricated circuit exhibits an electrical size (including the CPW measurement pads) of  $1.28 \lambda_g \times 3.15 \lambda_g$ . The measured (simulated) center frequency of the passband is 59.48 GHz (58.85) with a 3-dB bandwidth of 2.1 (2.2) GHz. The minimum in-band insertion loss is 2.7 (2.2) dB approximately while the return loss is better than

14.7 (25.2) dB. Two TZs can be clearly identified at 56.5 and 61.6 GHz with rejection levels higher than 45 and 40 dB, respectively. These two TZs result in a high filtering selectivity. And the variation of the group time delay is smaller than 1% over 70% of the pass band around the central frequency as shown in Fig. 8, thus, implying good linearity in this bandpass filter. The shift of the centre frequency is mainly caused by the tolerance in the substrate permittivity at a high frequency and the misalignment between substrate layers. The higher insertion loss may be due to the loss tangent deviation at a high frequency, and the radiation loss from the ‘thru’ line that could not be well embedded because of the nature of the SOLT calibration and fabrication tolerance.

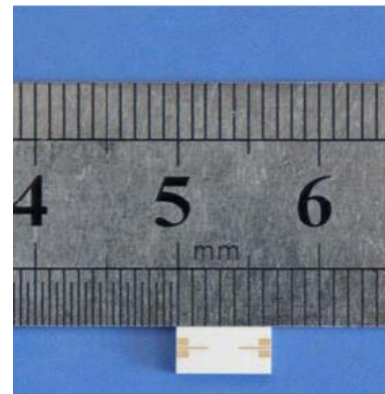


Fig. 6. Simulated and measured performances of the proposed filter including the insert photograph of the fabricated circuit.

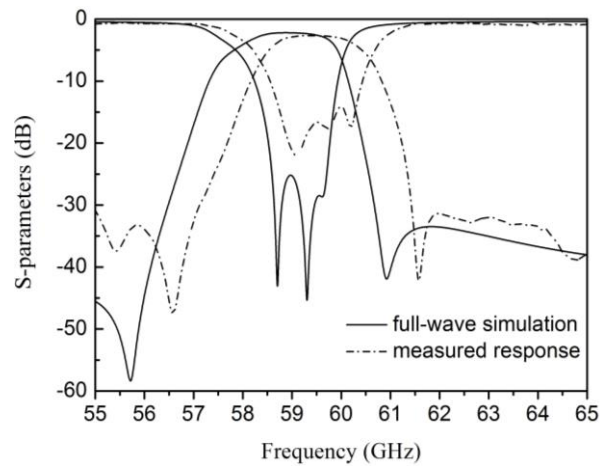


Fig. 7. Simulated and measured performances of the proposed filter of the fabricated circuit.

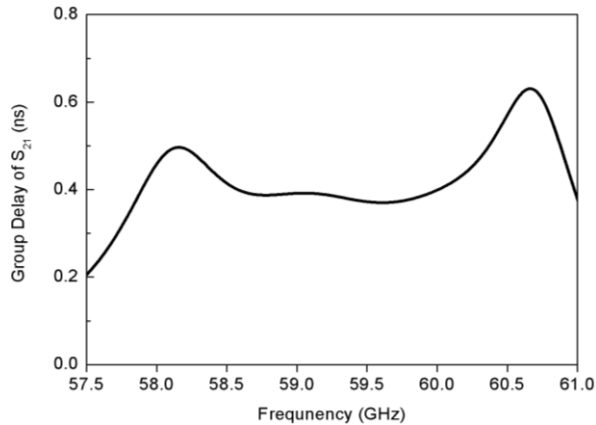


Fig. 8. The group time delay of the proposed filter.

#### IV. CONCLUSION

This paper presents a compact quasi-elliptic 60-GHz bandpass filter with a good performance using the LTCC technology. The design principle is given to reveal the realization of quasi-elliptic function responses. The proposed structures can be well integrated into miniaturized LTCC transceiver modules for V-band WPAN gigabit wireless communication systems.

#### ACKNOWLEDGEMENT

This work was supported by the Nature Science Foundation of China under Grant No. 61101047 and the Specialized Research Fund for the Doctoral Program by the Ministry of Education of China under Grant No. 20113219120015.

#### REFERENCES

- [1] J. H. Lee, S. Pinel, J. Papapolymerou, J. Laskar, and M. M. Tentzeris, "Low-loss LTCC cavity filters using system-on-package technology at 60 GHz," *IEEE Trans. Microw. Theory Tech.*, vol. 53, no. 12, pp. 3817-3824, December 2005.
- [2] J. H. Lee, N. Kidera, G. DeJean, S. Pinel, J. Laskar, and M. M. Tentzeris, "A V-band front-end with 3-D integrated cavity filters/duplexers and antenna in LTCC technologies," *IEEE Trans. Microw. Theory Tech.*, vol. 54, no. 7, pp. 2925-2936, July 2006.
- [3] D. Dancila, X. Rottenberg, H. A. C. Tilmans, W. De Raedt, and I. Huynen, "57-64 GHz seven-pole bandpass filter substrate integrated waveguide

(SIW) in LTCC," *2011 IEEE MTT-S Int. Microw. Symp. Dig.*, pp. 200-203, September 2011.

- [4] H. Chu, Y. X. Guo, and X. Q. Shi, "60 GHz LTCC 3D cavity bandpass filter with two finite transmission zeros," *Electron. Lett.*, vol. 47, no. 5, pp. 324-326, March 2011.
- [5] G. H. Lee, C. S. Yoo, Y. H. Kim, J. Y. Kim, Y. H. Park, J. G. Yook, and J. C. Kim, "A 60 GHz embedded SIW (substrate integrated waveguide) BPF considering the transition effect," *APMC Microw. Conf.*, Singapore, pp. 1192-1195, December 2009.
- [6] S. Amari, "Synthesis of cross-coupled resonator filters using an analytical gradient-based optimization technique," *IEEE Trans. Microw. Theory Tech.*, vol. 48, no. 9, pp. 1559-1564, September 2000.
- [7] J. S. Hong and M. J. Lancaster, "Microstrip filters for RF/microwave applications," Wiley, New York, USA, 2001.
- [8] Y. Cassivi, L. Perreggini, P. Arcioni, M. Bressan, K. Wu, and G. Conciauro, "Dispersion characteristics of substrate integrated rectangular waveguide," *IEEE Microw. Wireless Compon. Lett.*, vol. 12, no. 2, pp. 333-335, February 2002.
- [9] D. M. Pozar and D. H. Schaubert, "Microstrip antennas," *Piscataway, NJ: IEEE Press*, 1995.
- [10] M. J. Hill, R. W. Ziolkowski, and J. Papapolymerou, "Simulated and measured results from a Duroid-based planar MBG cavity resonator filter," *IEEE Microw. Wireless Compon. Lett.*, vol. 10, no. 12, pp. 528-530, December 2000.
- [11] X. P. Chen, W. Hong, T. J. Cui, J. X. Chen, and K. Wu, "Substrate integrated waveguide (SIW) linear phase filter," *IEEE Microw. Wireless Compon. Lett.*, vol. 15, no. 11, pp. 787-789, November 2005.



**Gang Zhang** received his B.S. degree in Electronics and Information Engineering from NJUST, Nanjing, China, in 2010. He is currently working in Electromagnetic Field and Microwave Technology with NJUST. His research interest is the design of miniaturized high performance microwave/millimeter-wave passive device and numerical methods in electromagnetics.



**Jianpeng Wang** received his M. Sc. and Ph. D. degrees from UESTC, Chengdu, China, in 2004, and 2007, respectively, both in Electronic Engineering. Since January 2008, he has been with the Ministerial Key Laboratory of JGMT, School of Electronic and Optical Engineering, NJUST, where he is currently an Associate Professor. His research interests include the high performance microwave/millimeter-wave passive components, circuits and systems realized on PCB, LTCC, etc.



**Hui Gu** received his B.S. degree in Electronics and Information Engineering from HNU, Huaian, China, in 2012. He is currently working towards his master degree in Communication and Information System with NJUST. His research interests include the

high performance microwave/millimeter-wave passive device realized on PCB, LTCC, etc.



**Xin Xu** received his B.S. degree in Electromagnetic Field and Radio Technology from UESTC, Chengdu, China, in 2010. He is currently working towards his Ph.D. degree in Electromagnetic Field and Microwave Technology with NJUST. His research interests include the high performance microwave/millimeter-wave passive device realized on PCB, LTCC, etc.